UNIVERSITÉ PARIS-EST
École doctorale de Sciences, Ingénierie et Environnement

THÈSE

présentée pour obtenir le grade de

DOCTEUR DE L'UNIVERSITÉ PARIS-EST

Spécialité : Structures et Matériaux

Présentée par

Sarah SOUHEIL GEBAI

Sujet de la thèse

Optimization of passive cantilever-type tuned mass damper to reduce the hand postural tremor

Soutenue le 8 juillet 2020 devant le jury composé de

Laurence CHEZE	Université Claude Bernard Lyon 1	Président du jury
Emeline SADOULET-REBOUL	Université de Franche-Comté	Rapporteur
Frédéric MARIN	Université de Technologie de Compiègne	Rapporteur
Xavier CHIEMENTIN	Université de Reims Champagne Ardenne	Examinateur
Jean-Luc DION	Institut supérieur de mécanique de Paris	Examinateur
Gilles FORET	École des ponts ParisTech	Directeur de thèse
Gwendal CUMUNEL	École des ponts ParisTech	Co-directeur de thèse
Mohammad HAMMOUD	Lebanese International University	Co-directeur de thèse
Elodie HAINQUE	Département de Neurologie, Hôpital Pitié-Salpêtrière AP-HP	Invitée

Acknowledgments

I am very grateful to each person who stood by my side and helped me to carry out this doctoral work.

I would like to express my gratitude to my thesis director Professor **Gilles FORET**. Thank you very much for the help and all kinds of support you provided me during our work together. Thanks because you made me spend a very smooth and enjoyable time which I needed to overcome the difficult days faced during this work. I want to offer my sincerest gratitude to my supervisor Doctor **Mohammad HAMMOUD**. I think that the words are not enough to express how thankful I am because you believed in me and guided me to reach what I am on right now. Thank you for proposing the topic of my doctoral thesis. You were always there leading and directing me to the right way, and provided me with all the motivation needed to continue the work. The deepest respect and appreciation goes out to my supervisor Doctor **Gwendal CUMUNEL** who spent great effort to add a thoughtful work full of rich details and insights gained from his wide experience, it was a pleasure to work with you. Thanks for the great recommendations and all the information you provided me.

I would like to thank the Department of Nervous System Diseases at Hôpital Pitié-Salpêtrière who accepted to share this cooperative work between the Lebanese International University (LIU) and École des ponts ParisTech (ENPC). Thanks for Professor **Emmanuel FLAMAND-ROZE** for being interested in the proposed work, and for providing us with the useful information needed to proceed in this research. I would greatly thank Doctor **Elodie HAINQUE** for the hard work and the precious time you had considered for the project, for providing us a large number of measurements of the patient's signals, and for answering all our questions. Thanks to Professor **Emmanuelle APARTIS** for your contribution in the measurement of the patient's signals.

I would like to thank all the members of the jury for their appreciated support and helpful recommendations. Thank you Professor **Laurence CHEZE** for accepting to be the president of the work, your kind presence made me feel very comfortable. I want to thank the reporters Professors **Emeline SADOULET-REBOUL** and **Frédéric MARIN** for the valuable time they spent to read the manuscript, for their interest in the work, and their helpful corrections and suggestions. Thanks for the examiners Professors **Xavier CHIEMENTIN** and **Jean-Luc DION** for your essential comments, and inspirational questions.

I would like to express my gratitude to Mrs. **Marie-Francoise KASPI** for taking care of all my administrative tasks and for her kindness. I will not forget to extend my gratitude and express my respect to the great Doctors **Ali SHAITO** and **Ali HALLAL**.

I would like to thank my family, with a special thanks that goes out to my brother **Hussein GEBAI**. Thank you for being in my life, and for giving me half of your heart before I came here. I want to give a very big thanks to the lovely colleagues in our "warm" office, Doctor **Le Hung TRAN**, **Benjamin CLAUDET**, Doctor **Tien HOANG**, and **Truong Son PHAM**. Thanks for the nice days we spent together, and for all your help. Thanks for my friends: **Hussien ISSA**, and Doctors **Abdul-Karim JAMAL-EDDINE**, and **Mazen ERFAN**.

ABSTRACT

This work aims to develop a tuned mass damper (TMD) in order to achieve a passive vibration absorber to reduce the amplitudes of postural tremor. This absorber, of simple design, consists of a thin cantilever beam to which a mass is attached along its longitudinal axis. For this, experimental measurements of postural tremor were first carried out on patients in different conditions in order to understand the characteristics of the tremor and to collect information on the amplitude of the tremor and the frequency ranges. A biodynamic model of the upper limb excited by the measured muscle signal was then used to perform a parametric study of TMD and to examine its behavior with numerical simulations. The semi-analytical formula used to calculate the natural frequency of the TMD has been verified experimentally for each mass position along the beam. A rectangular steel beam experimentally representing the arm was excited using a dynamic exciter reproducing the muscle signal in order to test the behavior of TMD experimentally and compare the results with those of the numerical study. Several absorber configurations were then tested, the configuration using 3TMD offering the best performance. Each TMD has a mass of approximately 13.75 g and selected natural frequencies close to the patient's muscle excitation frequency. In order to improve the results, it would be interesting to replace the material used for the beam, made of stainless steel, by materials capable of providing a higher damping ratio, such as for example 3D printing plastic materials which can moreover be easily shaped.

RÉSUMÉ

Ce travail vise à développer un amortisseur à masse accordée (AMA) dans le but de réaliser un absorbeur passif des vibrations permettant de réduire les amplitudes de tremblement postural. Cet amortisseur, de conception simple, consiste en une poutre mince encastrée-libre de laquelle est fixée une masse le long de son axe longitudinal. Pour cela, des mesures expérimentales du tremblement postural ont tout d'abord été effectuées sur des patients dans différentes conditions afin de comprendre les caractéristiques du tremblement et de recueillir des informations sur l'amplitude du tremblement et les plages de fréquence. Un modèle biodynamique du membre supérieur excité par le signal musculaire mesuré a ensuite été utilisé pour réaliser une étude paramétrique du TMD et examiner son comportement avec des simulations numériques. La formule semi-analytique utilisée pour calculer la fréquence naturelle du TMD a été vérifiée expérimentalement pour chaque position de masse le long de la poutre. Une poutre en acier rectangulaire représentant expérimentalement le bras a été excité à l'aide d'un pot vibrant reproduisant le signal musculaire afin de tester expérimentalement le comportement du TMD et faire une comparaison avec les résultats de l'étude numérique. Plusieurs configurations d'amortisseur ont ensuite été testées, la configuration utilisant 3TMD offrant les meilleures performances. Chaque TMD a une masse d'environ 13,75 g et des fréquences naturelles choisies proches de la fréquence d'excitation musculaire du patient. Afin d'améliorer les résultats, il serait intéressant de remplacer le matériau utilisé pour la poutre, en acier inoxydable, par des matériaux capables de fournir un taux d'amortissement plus élevé, comme par exemple des matériaux plastiques d'impression 3D pouvant de plus être aisément mis en forme.

Keywords : Tremor measurements, upper limb model, vibration absorber, experimental testing.

ACRONYMS

ADVA :	Active dynamic vibration absorber
AMD :	Active mass driver
ATMD :	Active tuned mass damper
D :	Dimensional
DBS :	Deep brain stimulation
DC:	Direct current
DOF :	degrees-of-freedom
DVA :	dynamic vibration absorber
ECR :	Extensor carpi radialis
EM :	Electromagnetic
EMG :	Electromyography
ET :	Essential tremor
EVA :	electrical vibration absorber
FCR :	Flexor carpi radialis
HAVS :	Hand-arm vibration syndrome
IFFT :	Inverse fast Fourier transform
IMU :	Inertial measurement unit
KT :	Kinetic tremor
MDOF :	Multi degrees-of-freedom
MTMD :	Multi tuned mass damper
PD :	Parkinson disease
PI :	proportional–integral

PID :	proportional–integral–derivative
PPF :	positive position feedback
PT :	Postural tremor
RT :	Rest tremor
SD :	Standard deviation
TMs :	Target modes
TMD :	Tuned mass damper

TABLE OF CONTENTS

LIST OF FIGURES

LIST OF TABLES

CHAPTER 1. GENERAL INTRODUCTION

The joint torque, having spring-like properties in the human musculoskeletal system, contributes to our interaction with the environment by neural feedback systems and motor commands. Involuntary oscillatory activity in a body part can cause social embarrassment and functional disability due to the movement disorder. It can occur on hand, feet, or head. Diagnosing the pathophysiology for different tremor disorders is still not possible since their causes are far from being completely understood. Tremor can be described as the back-and-forth rhythmic movement, which starts at one finger and propagates to affect the whole hand.

1.1. Pathological tremor

Human body can sustain certain level of vibration, but for over a long period of time deterioration will begin and natural process of the system will fail. Vibrational energy waves in human body are absorbed by tissue, organs, and skeletal systems before it is being dissipated leading to voluntary and involuntary contraction of muscles. Vibration at resonant frequency can cause tissue degeneration, organ failure, severe discomfort, and reduction in the ability to perform accurate motor movement. Local muscle fatigue occurs when muscles try to react against vibrational energy to maintain the balance at resonance. The induced vibration disorder in vascular and nonvascular structures in human hand-arm is referred as hand-arm vibration syndrome (HAVS) [1]. HAVS is associated with blood circulation (vascular effects), nerves signals (neurological effects), and injuries in bones and joints known as white finger phenomenon.

Tremor is a semi-rhythmic, involuntary, and oscillatory movement of a body part which results from alternating simultaneous contractions of antagonistic muscle group [2]. Physiological tremor is present in each healthy person. It can occur in all voluntary muscle groups and can be rarely visible to the eye. Tremor can be associated to neurological disorders and is referred as pathological tremor, like cerebellar, essential, and Parkinsonian tremors [3]. Physiological and pathological tremors behave differently in terms of amplitude and frequency [4,5]. Their effect is high at the upper limbs. The negative correlation between amplitude and frequency is demonstrated by several studies [6-9], where high amplitudes are displayed in low frequency tremors and vice versa, which is due to the low-pass filtering properties of muscles and limbs.

1.1.1. Classification

James Parkinson published in 1817 the first well defined description of Parkinson disease (PD) in his article titled ‘An Essay on the Shaking Palsy’ [10]. Parkinsonism is a slowly progressive degenerative disorder of the central nervous system characterized by the low level of dopamine in the brain. Initial symptoms may initiate early in life, but tremor progresses with time and becomes significant to physician when the patient is elderly. The disease can be detected for patients above 40 years with an estimated 5–10% of all Parkinson patients. Symptoms are mostly diagnosed in the age of 60–70 with an average age of 59 years.

People suffering from PD around the world were around 6.3 millions in 2004 [11]. Tremor in hand of PD patients makes them suffer while performing their daily tasks and they can feel embarrassed to face other people. The age of the PD patient and the disease duration are not associated with its severity [12]. The level of severity of PD can be determined using the spiral drawing test shown in Figure 1.1 since no instrumental method is able to monitor the PD symptoms [14]. The tremor severity is described by tremor frequency range, since the dominant frequency has no direct relation with its severity [15].

PD is related to rest tremor (RT) (3–7 Hz) and postural tremor (PT) (5–12 Hz) [16], presented in Figures 1.2a and 1.2b. PD tremor increases highly with emotions and stress. Resting hand tremor is the most recognizable sign of PD [17]. It affects usually the upper limbs and can affect the chin, lips, legs, and trunk. Parkinson’s tremor usually appears at the rest conditions and disappears with movement. The PD tremor can usually start from one finger and expand to affect the whole arm. The rest condition involves fully supported limbs against gravity with no voluntary contraction. The PT in patients with PD can be found in the enhanced physiological tremor, clonus, or can coexist with essential tremor (ET) patients.

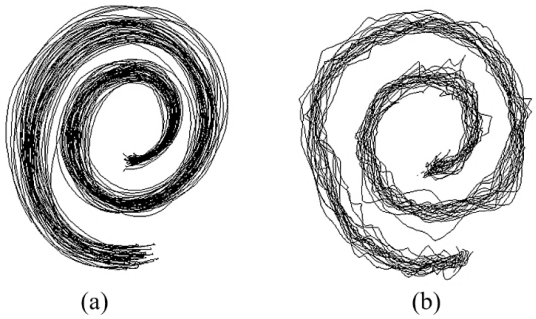

Figure 1.1: Spiral drawing test of (a) healthy person and (b) PD patient [13]

ET is slowly progressive mono-symptomatic disorder which is a bilateral of PT and kinetic tremor (KT). It is a single frequency phenomenon that ranges between 4–12 Hz [18,19], and affects the upper limbs and head. It was estimated in 2014 that the ET affects

7 millions people living in the U.S. [20,21]. KT appears during movement of a body part towards a target as shown in Figure 1.2c. KT is usually greater than PT and increases as the body part reaches the target. ET is characterized initially by a low amplitude, which increases dramatically with age as the tremor frequency is decreasing. ET becomes severe when it occurs at rest, but this may also represent the coexistence of PD and ET. The severity of bradykinesia and rigidity in the affected patient are tested by performing the tasks presented in Figures 1.2d and 1.2e, respectively.

Table 1.1 summarizes the most common types of involuntary tremor and their characteristics. The voluntary or intentional motion has frequency which ranges from 0–2 Hz [26].

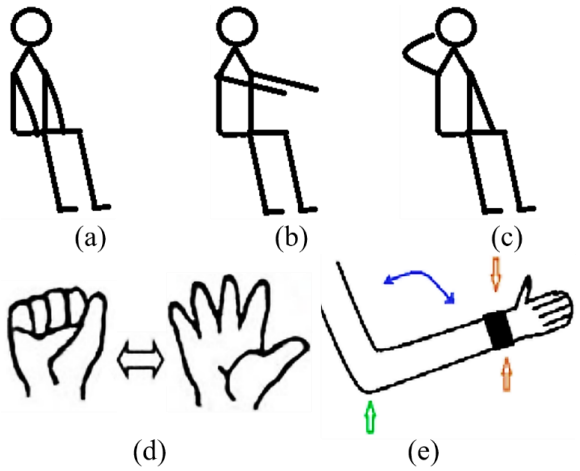

Figure 1.2: Tasks used to check the severity of (a) RT, (b) PT, (c) KT, (d) bradykinesia test, and (e) rigidity test [14]

Table 1.1: Classification of involuntary tremor

Involuntary tremor	Categories	Bandwidth	Emergence
Physiological	–	8–12 Hz [22,23]	Any movement, for healthy people
Pathological	**RT**	3–7 Hz [16]	- Fully supported limbs against gravity without voluntary contraction [16], for 75% of PD [16] - May exists in severe ET
	PT	5–12 Hz [16]	- Body part voluntary maintained against gravity [16,24], for 60% PD [16] - Persists during movement for ET [24]
	KT	3–10 Hz [25]	Target or any form of voluntary movement for patients with ET [24]

1.1.2. Surgery and medication

There is no treatment that can cure patients and control tremor completely, but there are different methods that can lessen tremor to improve life quality. Several researches were conducted to investigate and control human hand tremor. Pharmacological treatments can be applied to different types of tremor. Levodopa drug and propranolol can be used to reduce the RT, primidone and propranolol for hand PT, beta-blockers for KT, and primidone and anticholinergic medication for ET. Medication can decrease tremor progress, but it has withdrawal symptoms and side effects like addiction [27]. In case of non-responsive, brain stereotactic surgery can be applied. These treatments are like lesioning surgery, Gamma-Knife radiosurgery, and deep brain stimulation (DBS). DBS may reduce tremor, but it has a direct impact on the influences of neuronal activity patterns in the basal ganglia loops. Medication and neurosurgical procedures can have diverse effects like: ataxia, confusion, muscle paralysis, hallucinations, speech impediment, stroke, hemiparesis, and brain hemorrhage. In addition, positive effects of those treatments are temporary and 25% of patients can lose their life quality if they do not respond to drugs or neurosurgery treatments [22,28]. Each method has its weakness and may have high risks involving brain operation which points to the need for an alternative approach to reduce the vibration. As a result, mechanical treatment may be used as a good solution to suppress the tremor instead of using medical and surgical methods. Such devices can treat Parkinsonism mechanically and avoid fatigue, sleepy, nausea, poor vision, and muscle paralysis side effects of medications [29].

1.2. Plan of thesis

The work carried out during the thesis emphasizes the need to find alternatives to the medical treatments, which are expected to help the neurodegenerative disordered patients during their daily life and reduce the effect of slipping, falls, and faults. The medical and surgical treatments can cause negative effects on their life quality and increase their involuntary tremor vibration level with time. Mechanical vibration absorber used to reduce the undesired vibration of buildings, bridges, and machines, are designed to be as compact and light as possible and bearable solution for the affected patients.

The document is organized as follows:

- Chapter 1 is the introductory chapter, which includes the main context of the study.
- Chapter 2 provides a wide literature review to better understand the problem, detect the project’s needs. The review is related to different fields like: measurements and sensors used to obtain the muscles and upper limb signals of pathological tremor patients, the available biodynamic modeling of the upper

limb at the musculoskeletal level, and the passive and active control methods used to reduce the undesired vibration.

- Chapter 3 contains the analysis of experimental datasets for several patients and healthy people measured using a triaxial accelerometer and inertial measurement unit (IMU), along with the muscles Electromyography (EMG) signals for different hand tasks repeated several time to determine the shifting in the tremor properties.
- In Chapter 4, a biodynamic modeling of the upper limb is provided, where its equations of motion are derived in addition to several TMDs at the forearm or the palm segment. TMD's designs as pendulum or cantilever-type TMD are included. A parametric study to show the effect of the TMD parameters on their efficiency is performed on the dynamic model with the measured patient's signals as an input.
- Chapter 5 verifies the derived analytical formula of the fundamental frequency of the TMD composite system for rectangular and circular cross-sectional areas of the beam. The analytical and experimental frequencies are compared for each position of the TMD's proof mass along the beam. The response of the TMD is tested experimentally on a rotating beam, and the results are compared to those obtained numerically.
- Finally, the manuscript is closed by a general conclusion in Chapter 6 and several possible perspectives for this study.

CHAPTER 2. LITERATURE REVIEW

THIS chapter includes a literature review about several subjects that introduce the concept and objectives, identify the problematic, and give an overview about the previous studies which can help in the current work. The measurement methods used to track the active muscle's behavior that are driving the tremor are presented, in addition to the available sensors used to monitor the health of the patients. The chapter lists the proposed upper limb dynamic models and the designated muscles model, which are used together to construct the musculoskeletal upper limbs models. Finally, it defines the control strategies used to reduce the undesired vibration of a structure, and how the controllers were used to reduce the hand tremor as a replacement to medications and surgical treatments.

Plan of Chapter 2

2.1. Introduction

This chapter presents a literature review of the most available data related to the project using relevant papers. This review serves in understanding the dynamics of human hand at the musculoskeletal level in order to model his upper limb. It provides a brief description about the characteristics of the Pathological tremor and holds a review related to several areas including the sensors used to track the tremor, tremor behavior, biomechanical behavior of human hand, and active and passive control methods. On the other hand, a detailed review is done on the different types of used controllers by showing their applications, advantages, and disadvantages. Then, a suitable type of controller can be selected and designed to reduce the pathological tremor at the hand of the patient. This can be reached by improving the performance of the controller that needs no power consumption and designed using with low cost materials.

2.2. Muscles signal measurement

It is sometimes difficult to separate clinically between the PD and ET as both can occur at the rest conditions, with posture or intentional movement and with aging. It is important to quantify the quasi-sinusoidal tremor movement in a mathematical modeling with a high degree of fidelity. In order to diagnose what type of these tremors the patient is experiencing, quantified analysis can be used like: tremor amplitude ratios during different clinical tasks, side-to-side frequency relationship, reflex responses, and EMG topography. Tremor activity can be recorded using EMG, accelerometric, force, or gyroscopic measurements. Most biological tremors have frequency of concern less than 25 Hz [30], which must be considered while performing the signal processing.

EMG can be used to obtain information of the muscles activity which are generating the tremor. EMG can record the information using wire electrodes, needle, or surface electrodes overlying the active muscles [31]. Motor unit recruitment and synchronization of muscles can be provided from the EMG [7,32]. It can also explain the relationship between the muscles involved in the tremor to know if the tremor is produced from the antagonist muscles which are working at the same time or alternately.

EMG profile of PD patient suffering from RT is depicted in Figure 2.1 [30]. The first four curves in Figure 2.1a show the surface EMG signals of the forearm muscles: the left and the right flexor carpi radialis (FCR), and extensor carpi radialis (ECR) muscles. The EMG signals show that the presented muscles have alternating, or less commonly, synchronous contraction, this behavior of PD tremor is shown for a frequency below 6 Hz as shown in Figure 2.1b, where gray line is for the left hand and the black line for the right hand. The last two curves in Figure 2.1a, represented by the dark lines, show relatively

sinusoidal displacements resulting from the accelerometric signals for the left and the right hand.

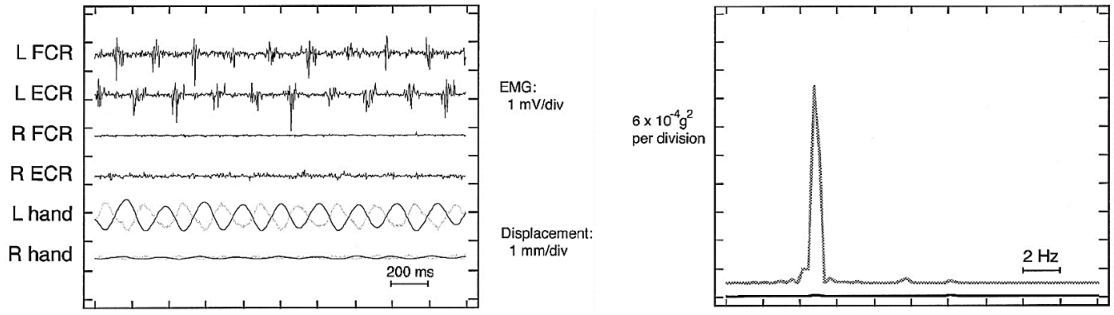

(a) (b)

Figure 2.1: RT in a PD patient (a) the EMG profile and hands displacement and (b) the frequency spectrum of tremor displacements [30]

Figure 2.2 shows the EMG profile for an ET patient having PT when his arms are extended [30]. Figure 2.2a shows the surface EMG signals of the forearm muscles: the left and right FCR, and ECR muscles. The last two curves represented by dark color, are the displacements derived from accelerometric measurements. The ET (Figure 2.2) is more irregular than the PD tremor (Figure 2.1). The frequency spectrum presented in Figure 2.2b reveals that tremor displacement peaks of both hands (gray line is for the left hand and the black line for the right hand) occur between 4–8 Hz.

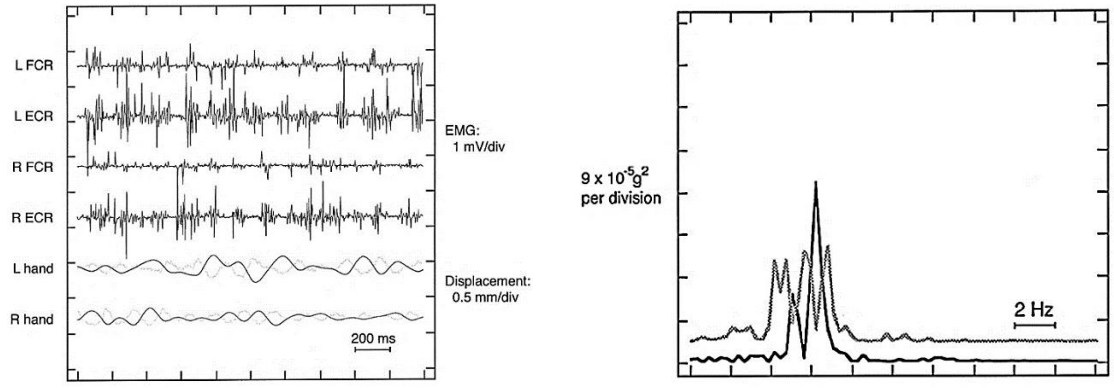

(a) (b)

Figure 2.2: PT in an ET patient (a) the EMG profile and hands displacement and (b) the frequency spectrum of tremor displacements [30]

According to the single oscillator theory, it was assumed that one single oscillator is able to govern all the tremulous activity of ET and PD tremor. Hunker and Abbs [33] supported this theory by showing that the tremor frequency is the same in different muscles of a patient. Hurtado et al. [34] reported that more complexity is required for tremor modeling by providing models with multiple oscillators. Raethje et al. [35] found that a group of muscles can oscillate with a nearly same frequency, however, with no significant coherence.

2.3. Limbs tremor measurement

It is important to have precise and comfortable sensors to track continuously the daily pathological tremor of affected patients. Tremor tracking devices that were used in some research works are video tracking, infrared cameras, digital drawing tablets, EMG, and digital drawing tablets [2,30,34,36-38]. However, such devices have limited usage in clinical applications because of their large dimensions which can be uncomfortable for the patients when it is located on their body, feet, or arm [12]. Research interest is being shifted to the usage of Micro-Electro-Mechanical Systems (MEMS) inertial sensors that provide smaller circuit board and easier signal processing for continuous monitoring of PD tremor [34].

Different sensors are used to track the tremor of the patient, like the accelerometer, gyroscopes, goniometers, IMU, and MEMS technology.

2.3.1. Accelerometer

Accelerometer measures the acceleration force along the sensor's sensitive axis based on Newton's law. It has three main categories: piezoelectric, piezoresistive, and capacitive. The difference between each type is shown in Table 2.1. Accelerometers measure the linear acceleration, but the articular motion is usually based on the rotational motion at the level of the joints. However, accelerometer is simple and can still be a relatively reliable and convenient sensor used to measure the oscillation's amplitude and frequency of the body segments [13].

Table 2.1: Comparison between accelerometer types which are adapted from Wong et al. [39]

Parameter	Piezoelectric	Piezoresistive	Capacitive
Gravitational component	No	Yes	Yes
Bandwidth	Wide	Low to moderate	Wide
Impedance	High	Low	Very high
Signal level	High	Low	Moderate
Ruggedness	Good	Moderate	Good
Cost	High	Low	High

2.3.2. Gyroscopes

Gyroscope is an angular velocity sensor based on the measurement of the Coriolis force. It has three basic types: ring gyroscope, spinning rotor, and the vibrating mass. Vibrating mass gyroscope, which includes a constantly vibrating internal mass, plays an important role in portable applications. It holds many advantages related to its weight, size, low power consumption, and cost. Gyroscopes are usually selected for the wearable exoskeletons application and used for measuring the amplitude of the lower limbs joint angle, trunk motion displacement, and the trunk rotation angular velocity [40]. The advantage of gyroscopes is their long term stability which eliminates the need of a periodic recalibration. Its long-term performance is ensured by the stability and fixed behavior under the temperature changes.

2.3.3. Goniometers

Goniometer is an interesting type of strain gauges that can be used as a flexible angular sensor to measure dynamically the joint angle. Its output voltage signal is proportional to the angle. Such sensors are usually used for rehabilitation and sport applications, but are not widely being used in the tremor studies [13,41]. Flexible springs are included in some goniometer in order to compensate the joint migration due to movement.

Rahimi et al. [42] used the four motion sensors shown in Figure 2.3 to track the angular displacements of the upper limbs motion in different directions for different rest and posture positions. An electro-goniometer (SG150, Biometrics Ltd) was used and placed at the wrist to measure its flexion-extension, and radial-ulnar relative angular displacements with respect to the forearm. A torsiometer (Q150, Biometrics Ltd) provides third angular displacement of the wrist, i.e. the pronation-supination, when placed at the dorsal of the forearm. An electro-goniometer is placed at the elbow to measure its flexion-extension angular motion. Another electro-goniometer is placed at the shoulder to measure the flexion-extension and adduction-abduction motions. In addition, accelerometer sensors were used to collect the acceleration data.

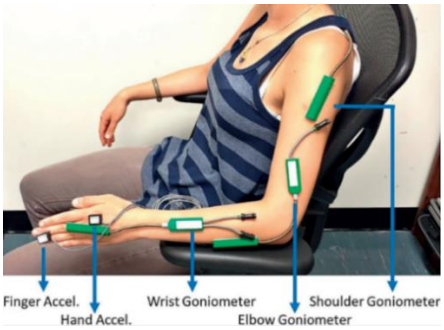

Figure 2.3: Kinematic sensors used to assess tremor by Rahimi et al. [42]

2.3.4. IMU

Buki et al. [43] measured the tremor using three IMUs (Xsens Company, the Netherlands), each includes 3-axis gyroscope and 3-axis accelerometer. The IMUs are attached to the wrist, middle of the forearm, and middle of the shoulder as shown in Figure 2.4. The tremor was measured for the free hand and 260 g and 500 g rings to see the effect of the load on the system. This was done in order to investigate the effect of the Vib-bracelet, which is manufactured to have 280 g and used for tremor attenuation.

Figure 2.4: IMU used to measure the tremor by Buki et al. [43]

2.3.5. MEMS technology

A major work is to monitor the tremor and detect the disease in early stage before the tremor becomes evident and begins to influence the patient's common activities. This increases the importance of tremor measuring sensors. As a result, Rovini et al. [36] conducted a review using 136 relevant publications out of 1,429 in order to have a wide overview about the wearable devices used to measure the motor performance of PD between the years 2006–2016. The distribution of these papers by years is shown in Figure 2.5a, which confirms the recent increase of interest on the wearable tremor measuring sensors. Figure 2.5b shows that the majority of papers were concentrated on the sensors used for body motion analysis. It was concluded that the most appropriate way for tremor measurement is represented by the MEMS technology and specially by the wearable inertial sensors that can acquire data using a high sampling rate [36]. The MEMS sensors

have a light weight, are portable, unobtrusive, inexpensive, can be easily used, and provide accurate measurements. The wearable inertial sensors can provide an optimal solution for healthcare applications and the tremor data used for early diagnosis of the PD, for body motion analysis, motor fluctuations, and long-term monitoring.

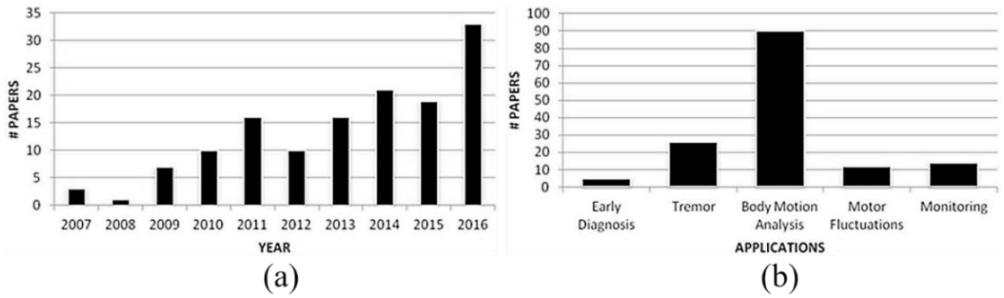

Figure 2.5: Publications of wearable tremor measuring sensors (a) trends per year and (b) distribution per application as reported by Rovini et al. [36]

Dai et al. [44] used the glove monitoring system shown in Figure 2.6 to quantify the tremor, bradykinesia, and rigidity during DBS surgery of PD. Two 6-axis MEMS IMU (MPU6150, InvenSense Inc.) are used, each IMU consists of a 3-axis gyroscope, and a 3-axis accelerometer combined together on a $4\ mm \times 4\ mm \times 0.9\ mm$ silicon chip. One IMU is placed at the middle finger, and the other one at the wrist, as shown in Figure 2.6a to assess the tremor and bradykinesia. The comparative experiments done between the glove prototype (Figure 2.6b), and an electromagnetic (EM) motion tracking system revealed that the prototype was reliable for the determination of tremor amplitude, the measurement of movement angles, and the measurement of passive movement resistance. In addition, it was found that the tremor calculation using the power spectral density (PSD) estimation is influenced by the inconsistent tremor movements.

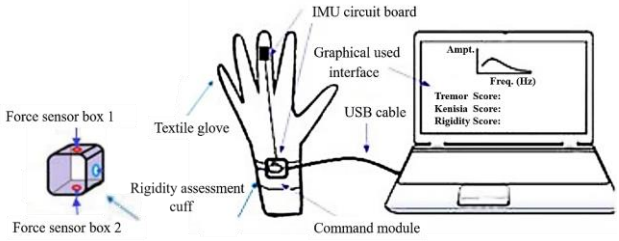

(a)

(b)

Figure 2.6: (a) System diagram of the glove monitoring system and (b) its prototype by Dai et al. [44]

Abbasi et al. [45] used the wearable tremor measuring system shown in Figure 2.7 to measure the vibration for hand tremor of PD patients. This system is made up of 6-axis IMU (MPU6050, InvenSense Inc., San Jose, CA, USA) placed at the back of the hand, and a module which sends the sensors data through a USB cable to a computer.

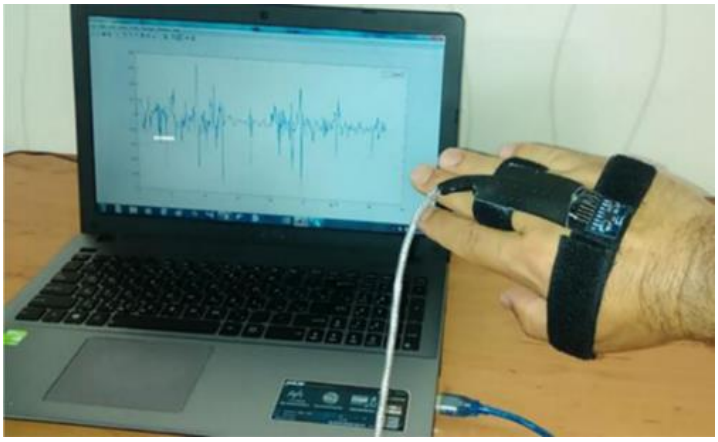

Figure 2.7: Device used to capture hand tremor by Abbasi et al. [45]

The measured signals can be analyzed to detect the tremor characteristics, where different descriptions are provided by the researchers.

2.4. Pathological tremor behavior

Physiological tremor is characterized by a linear second order stochastic process driven by white noise originated from uncorrelated moto-neuron firing [46,47]. On the other hand, pathological tremor is characterized by a non-linear oscillation which is not strictly periodic [48].

Gresty and Buckwell [49] modeled the pathological tremor behavior as harmonic oscillators with variable amplitude and/or frequency. Timmer et al. [48] analyzed data of high-quality ET and PD tremor signals shown in Figure 2.8, and suggested that the tremor behavior deviates from being periodic due to the second-order non-linear stochastic oscillator. Gao and Tung [50] analyzed the same dataset of Timmer et al. [48] and found that the pathological tremor can be modeled as diffusional processes. Gao [51] used a sample from each of ET and PD datasets, and concluded that the variation of the period for the pathological tremor can be similar to white noise, but its amplitude is proportional to the variation of $1/f^{\alpha}$ of the noise, where f is its frequency, and α is a constant. Besides, the period's variation in the ET is observed to be slightly larger than that of the PD tremor.

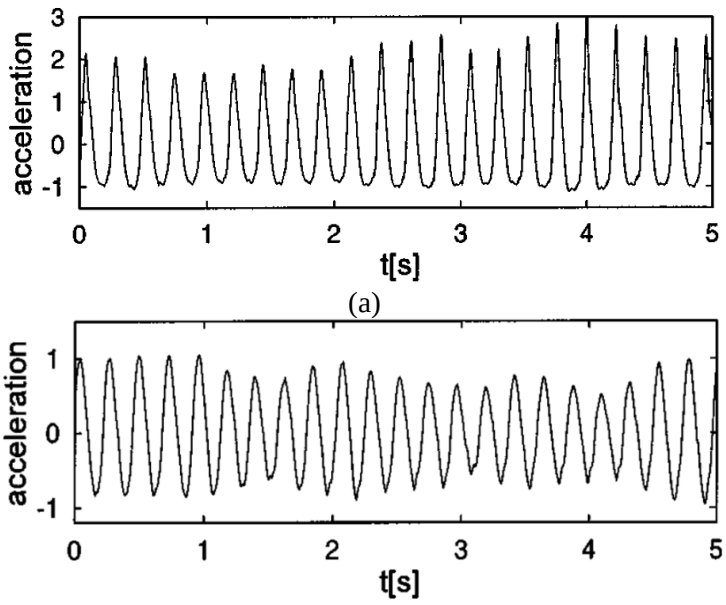

Figure 2.8: Time series measured using piezoresistive accelerometers attached at the dorsum of the out-stretched hand for patient with (a) ET and (b) PD by Timmer et al. [48]

Gao [51] used the acceleration of an ET data measured by piezoresistive accelerometer attached to the dorsum of an outstretched hand. It was used to present the time series of Figure 2.9a, which reveals that the pathological tremor can be modeled as a Gaussian noise source as suggested by Gresty and Buckwell [49], and Buckwell and Gresty [52]. The spectrum of Figure 2.9b is somehow broadened unlike the general observation of one clear peak for the ET, and distinct side bands peaks for the PD tremor. Figure 2.9c and 2.9d can be used to identify the amplitude $A(i)$ and period $T(i)$ variations over each period of oscillation.

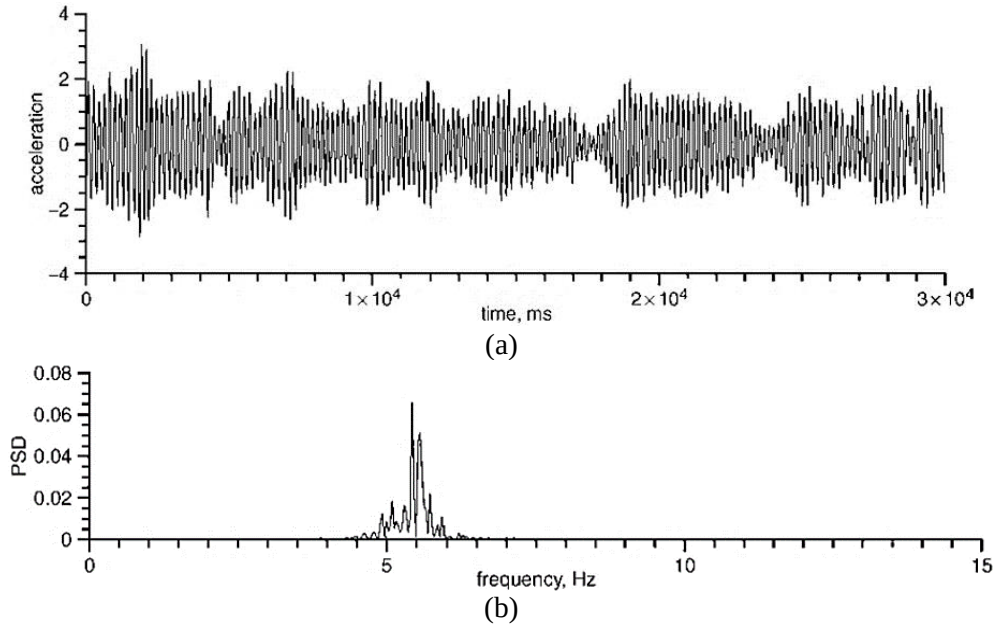

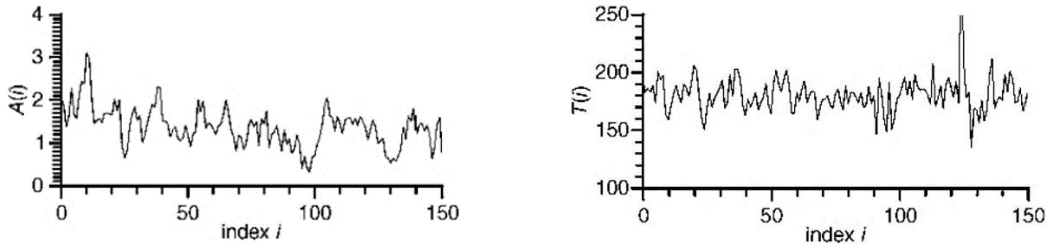

(c) (d)

Figure 2.9: (a) Time series for an ET dataset, (b) its spectrum, (c) amplitude variation, and (d) period variation used by Gao [51]

Buki et al. [43] recorded the tremor data, at the wrist using IMU, for 12 PD patients, and choose 4 PD patients having a consistent tremor behavior. The tremor measurement for one of these four patients tracked during 90 s and 4.5 s extracted from this signal are shown in Figure 2.10a. The PSD is represented in Figure 2.10b.

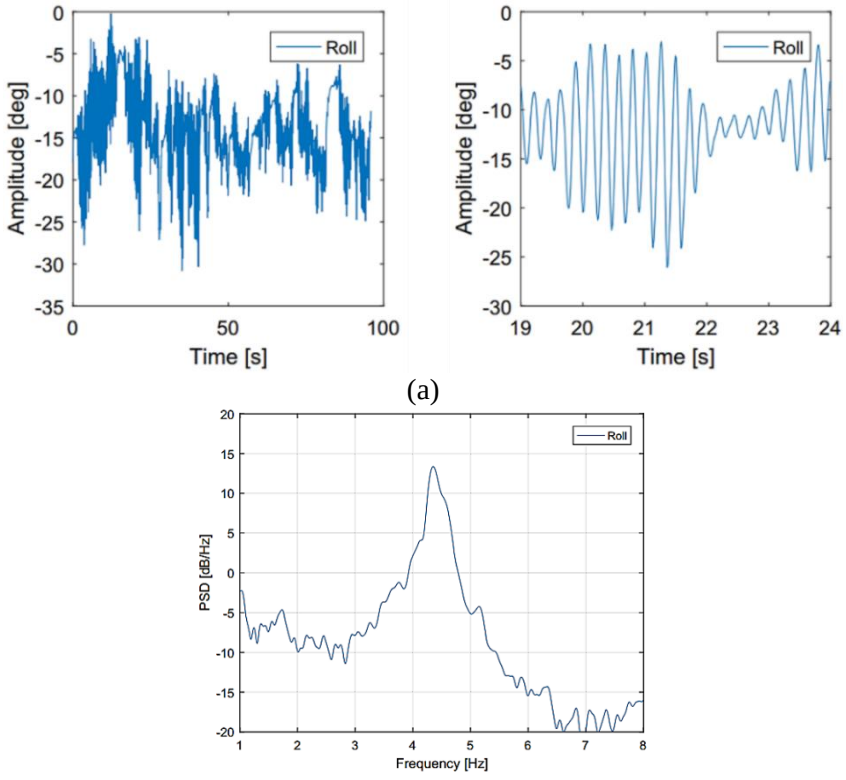

(a)

(b)

Figure 2.10: Tremor measured at the wrist of a PD patient (a) the time-amplitude plot and (b) the PSD measured by Buki et al. [43]

Abbasi et al. [45] provided data of the hand tremor acceleration for 6 PD patients as shown in Figure 2.11. These patients have different sex, and are between 62–84 years old. The tremor was measured using an IMU circuit.

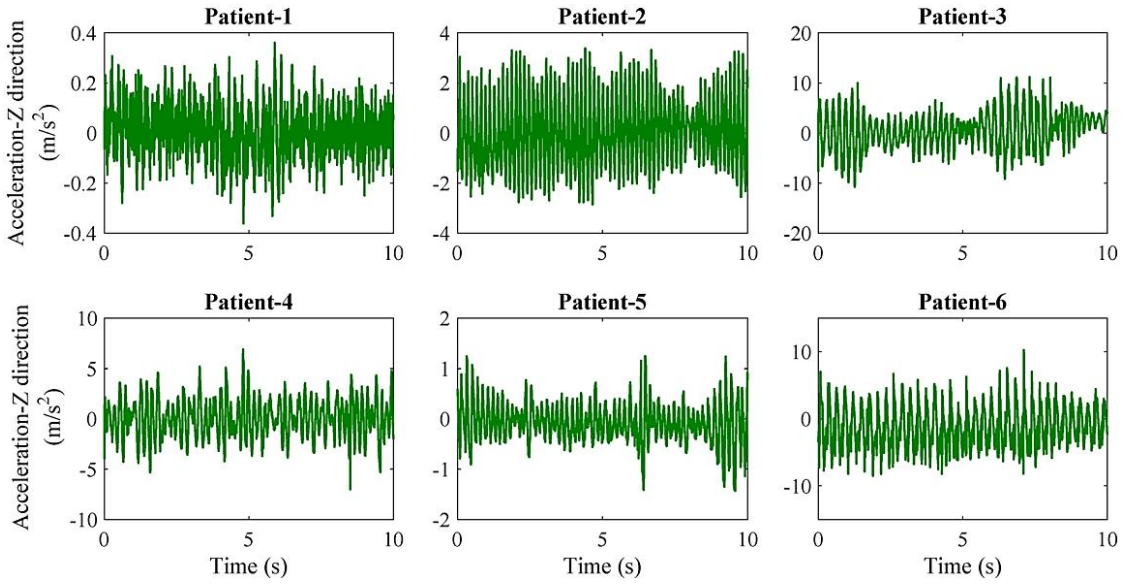

Figure 2.11: Acceleration in z-direction for six PD patients as provided by Abbasi et al. [45]

Each patient has his own tremor behavior characterized by different amplitude level. The pathological tremor behavior was modeled differently by each researcher, even the same measured tremor dataset was provided by different descriptions. So, it is confusing to decide the exact description of the tremor. This make it difficult to provide an analytical representation for the force exerted by the muscles, which is needed an as input for a modeled upper limb system, to obtain a descriptive behavior of the model's tremor response.

2.5. Musculoskeletal dynamic models

The hand model should reflect the tremulous motion in order to design numerically the parameters of the optimized absorber, and analyze its effect on the modeled hand before being manufactured. Oscillations can be translated into the movements of masses and springs due to the nature of the complex joint-muscle-tendon system [40]. Most researchers have agreed on modeling bones and corresponding soft tissues as rigid bodies connected by frictionless joints with fixed axes or centers of rotation [53-55]. The stiffness of the elbow joint can be approximated anywhere on the forearm in a range between 7–200 N.m/rad [56]. Active inputs can be described as muscular activity [57,58] and can be considered as sinusoidal function(s) [59]. The directions of hand's angular motion is shown in Figure 2.12. Usually, the adduction-abduction (or radial-ulnar) movement of the fingers and flexion-extension movement of the palm exists.

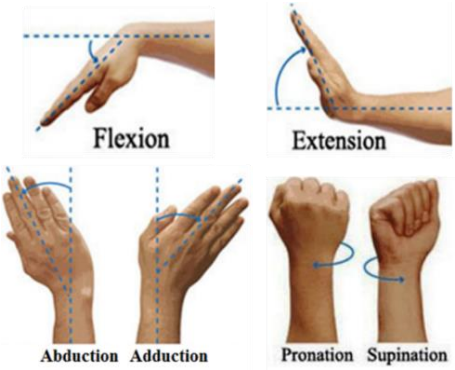

Figure 2.12: Angular hand motion

2.5.1. Upper limbs models

Several models were proposed in Literature based on different facts and assumptions, which are listed in the chronological order as follows:

a. Model A

Murray et al. [60] showed that movements occur outside the sagittal plane. However, a 2-dimensional (2D) model is adequate for showing the main features of upper limb movement during locomotion. Jackson et al. [61] modeled human upper limbs as two pivoted straight rods (the upper arm and the forearm together with the hand) with concentrated mass at the centroid of each segment as shown in Figure 2.13. The hand is modeled in sagittal plane during locomotion and flexion-extension planar motion at joints is considered. Active inputs to the model are described as the result of shoulder pivot acceleration. Muscular activity and resistive torques are modeled by elastic and viscous stiffness at the joints. Resistive torque is used to reflect the elbow locking at full extension of forearm. The angular displacements of the mechanical system rotating around pivot points are derived using the Lagrangian formalism [62]. The described model shows similar results to the available data on the movement of the upper limb during locomotion. Similar 2D models were also presented by Flanagan et al. [63] and Corradini et al. [64].

Jackson et al. [61] describes the muscular torque, during locomotion, as coming from four sources:

- Applied muscular activity at shoulder (H) and elbow joint (J)

$$\text{Torque} = 0.11 f_t \text{ in } N.m \tag{2.1}$$

where f_t is the rate at which motor unit impulses are recorded from a muscle (impulses/sec).

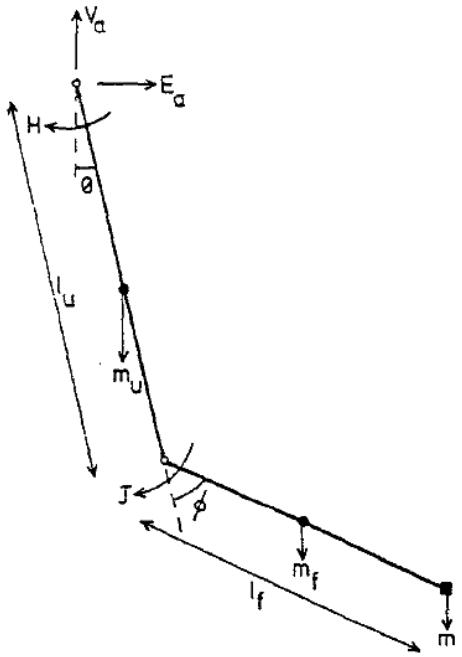

Figure 2.13: Hand model proposed by Jackson et al. [61]

- Resistive torques at the shoulder (D_T) and elbow joint (D_P)

$$D_T = \psi(-0.9\theta - 0.1\dot{\theta}), \qquad \psi = [0.1\,, 10]\ N.m/rad \tag{2.2}$$

$$D_p = \psi(-0.9\phi - 0.1\dot{\phi}), \qquad \psi = [0.1\,, 10]\ N.m/rad \tag{2.3}$$

where, the value of the spring stiffness ψ used by Goddard et al. [65] is 5.74 N.m/rad. θ and $\dot{\theta}$ are the angular displacement and velocity at the shoulder joint, respectively. ϕ and $\dot{\phi}$ are the angular displacement and velocity at the elbow joint.

- Elbow locking torque (T_r) preventing the forearm to be extended beyond longitudinal axis of the upper arm.

$$T_r = 0.1\psi e^{-\frac{180p}{\pi}(\phi-\phi_0)}, \qquad \psi = [0.1\,, 10]\ N.m/rad \text{ and } p = [0.27, 2.43] \tag{2.4}$$

where, p is a parameter controlling steepness of elbow locking, and ϕ_0 is the initial elbow joint angle. The locking torque falls rapidly to zero when $\phi > \phi_0$. If a very large value of p is used, then T_r will affect θ and will have no effect on ϕ. For very low value of p, T_r is not sufficient to prevent the elbow from extending beyond the upper arm's longitudinal axis. So, Jackson et al. [61] find that $p = [0.27\,, 2.43]$ compromizes the two extreme values, and they decided to use $p = 1$. The initial values of θ and ϕ used by Jackson et al. [61] are 0° and 15°, respectively. They quoted that changing this starting point causes no effect on the model's angular motion, since their effect disappears very quickly.

- Horizontal (E_a) and vertical (V_a) acceleration of the shoulder joint.

The model considers the forearm, palm, and any mass hold by the palm as one simple pendulum of mass m' and effective length l'. Then, the total torques at the shoulder (H') and elbow (J') joints are:

$$H' = H + m_u a_u E_a \cos\theta + D_T \tag{2.5}$$

$$J' = J + m'l'E_a \cos(\theta + \phi) + D_P + T_r \tag{2.6}$$

The equations of motion of the second ordered non-linear differential equations for the upper arm (2.7) and forearm (2.8) are:

$$\begin{aligned}\left[I_u + m'l'^2 + m'l_u^2 + 2m'l'l_u\cos\phi\right]\ddot{\theta} + \left[m'l'^2 + m'l'l_u\cos\phi\right]\ddot{\phi} \\ - [2m'l'l_u\sin\phi]\dot{\theta}\dot{\phi} - [m'l'l_u\sin\phi]\dot{\phi}^2 \\ + (g - V_a)[m_u a_u\sin\theta + m'l_u\sin\theta + m'l'\sin(\theta+\phi)] = H'\end{aligned} \tag{2.7}$$

$$\begin{aligned}\left[-m'l'^2 + m'l'l_u\cos\phi\right]\ddot{\theta} + \left[m'l'^2\right]\ddot{\phi} - [m'l'l_u\sin\phi]\dot{\theta}\dot{\phi} \\ + \left[m'l'l_u\dot{\theta}\sin\phi\right]\left(\dot{\theta} + \dot{\phi}\right) + (g - V_a)[m'l'\sin(\theta+\phi)] = J'\end{aligned} \tag{2.8}$$

where, I_u, m_u, and l_u are the inertia, mass, and length of the upper arm, respectively. a_u is the distance from the shoulder joint to the center of mass of the upper arm. g is the gravitational acceleration.

b. Model B

Damping and stiffness coefficient of muscles are assumed to be linearly proportional [66]. Based on this fact, Hashemi et al. [67] proposed a two degrees-of-freedom (2DOF) biodynamic model of upper limb with distributed mass and inertia, as shown in Figure 2.14. The hand is modeled in horizontal plane as two rigid segments fixed to the trunk. Equations of motion were derived using the Lagrangian formalism. The model describes the flexion-extension planar motion of the frictionless elbow and shoulder joints. Muscles are assumed to be regulated independently. Simulations and experimental results of the prototype arm showed good correlation. Later, Hosseini et al. [68] and Rahnavard et al. [69] used the same 2D hand modeling.

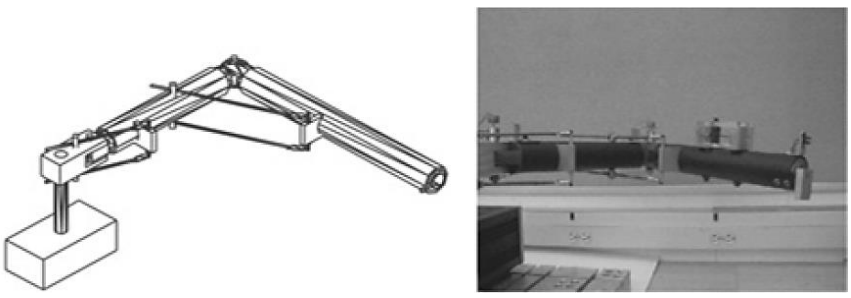

Figure 2.14: Design and front view of experimental arm [67]

The 2DOF linear differential equation for the model provided by Hashemi et al. [67] is:

$$\begin{aligned}[(I_1 + m_1a_1^2) + (I_2 + m_2a_2^2) + m_2l_1^2 + m_b(l_1^2 + l_2^2) + m_3(l_1^2 + l_3^2)]\ddot{\theta}_1 \\ + [(I_2 + m_2a_2^2) + m_bl_2^2 + m_3l_3^2]\ddot{\theta}_2 + c_1\dot{\theta}_1 + k_1\theta_1 = 0 \\ [(I_2 + m_2a_2^2) + m_bl_2^2 + m_3l_3^2](\ddot{\theta}_1 + \ddot{\theta}_2) + c_2\dot{\theta}_2 + k_2\theta_2 = f_2\end{aligned} \tag{2.9}$$

where, $M,\ C,$ and K are the inertia, damping, and stiffness matrices, respectively. $I_i,\ m_i,$ $l_i,$ and a_i are the inertia, mass, length, and position from proximal joint to centroid, respectively, for the upper arm $(i = 1)$ and forearm $(i = 2)$. $\theta_i, k_i,$ and c_i are the relative angular displacement, muscle stiffness coefficient, and muscle damping coefficient at the shoulder joint $(i = 1)$ and elbow joint $(i = 2)$. Hashemi et al. [67] included in his model, the effect of the absorber's casing mass m_3, and the exciter mass m_b which is set at distance l_3 and l_b away from the elbow joint along the forearm, respectively.

c. Model C

Hirashima [70] presented a 2DOF hand modeling, with two joints, in the vertical plane to describe the flexion-extension planar motion as shown in Figure 2.15. The model doesn't consider the existence of the palm. Its second ordered non-linear differential equations are:

$$\begin{aligned}[(I_1 + m_1a_1^2) + (I_2 + m_2a_2^2) + m_2l_1^2 + 2m_2l_1a_2\cos\theta_2]\ddot{\theta}_1 \\ + [(I_2 + m_2a_2^2) + m_2l_1a_2\cos\theta_2]\ddot{\theta}_2 - [m_2l_1a_2\sin\theta_2]\dot{\theta}_2^2 \\ - [2m_2l_1a_2\sin\theta_2]\dot{\theta}_1\dot{\theta}_2 \\ - g[(m_2l_1 + m_1r_1)\cos\theta_1 + m_2r_2\cos(\theta_1 + \theta_2)] = \tau_1\end{aligned} \tag{2.10}$$

$$\begin{aligned}[(I_2 + m_2a_2^2) + m_2l_1a_2\cos\theta_2]\ddot{\theta}_1 + [I_2 + m_2a_2^2]\ddot{\theta}_2 \\ = \tau_2 - [m_2l_1a_2\sin\theta_2]\dot{\theta}_1^2 - g[m_2r_2\cos(\theta_1 + \theta_2)]\end{aligned} \tag{2.11}$$

where, θ_i is the joint's relative angular displacement, I_i the moment of inertia, a_i the distance from the proximal joint of a segment to its center of mass, l_i the length, and τ_i the joint torque. $i = 1$ refers to the upper arm and $i = 2$ refers to forearm.

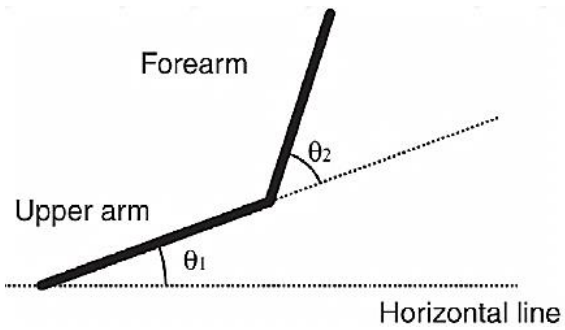

Figure 2.15: Two-joint system in a vertical plane [70]

d. Model D

Buki et al. [43] modeled the forearm as an inertial rod excited using direct current (DC) motor with a four-bar linkage mechanism as presented in Figure 2.16 to reflect the pronation-supination tremor of PD. The used inertia of the forearm is $2.89 \times 10^{-3}\ kg.m^2$ which is the upper range of adults [71]. The forearm system was manufactured to have a natural frequency which belongs to the frequency range of the tremor 4.4–5.7 Hz, measured using IMU. The forearm model was dynamically illustrated as a SDOF mass-spring-damper linear dynamic system attached to a vibrating base.

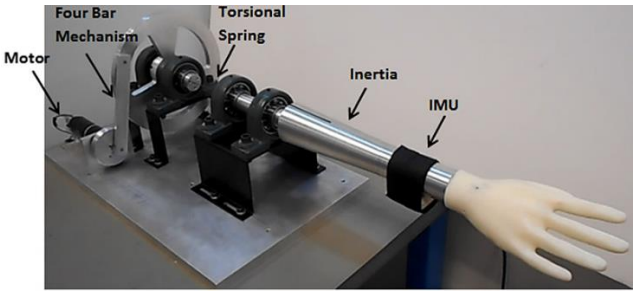

Figure 2.16: Forearm system designed to reflect the pronation/supination tremor [43]

2.5.2. Muscles models

In order to build a muscle model, the viscoelastic behavior of soft tissue is described by introducing series and parallel connection of muscle's mechanical elements (spring and damper). For soft tissues subjected to compressive and tensile loads, the Maxwell (Figure 2.17a), Voigt (Figure 2.17b), and Kelvin (Figure 2.17c) passive models can be used [72]. In addition, "active state" muscles can be represented as the Hill (Figure 2.17d), and modified Hill (Figure 2.17e) models, including a force generator [73].

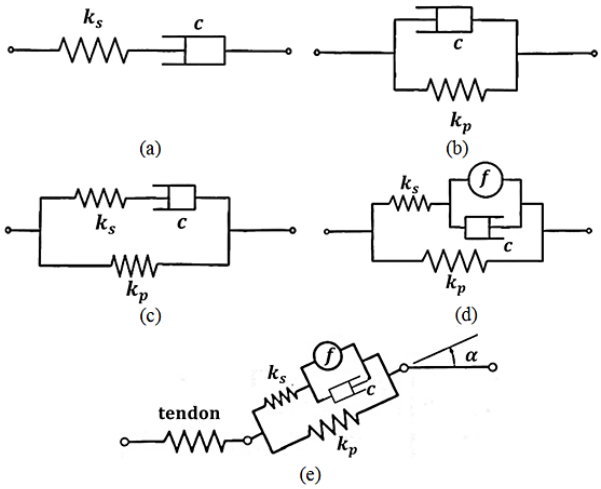

Figure 2.17: Muscular Models (a) Maxwell, (b) Voigt, (c) Kelvin, (d) Hill, and (e) modified Hill (k_s: series-connected spring, k_p: parallel-connected spring, c: damper and f: active generator force) [72]

Kazi et al. [74] modeled the human hand as a SDOF vibratory system subjected to a harmonic excitation, and incorporating a Voigt muscle model shown in Figure 2.18. The Voigt model is represented by a purely viscous damper connected in parallel to an elastic spring.

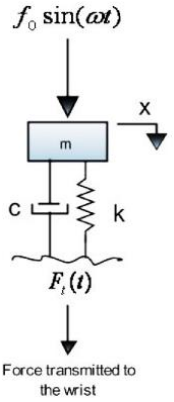

Figure 2.18: Voigt muscle model [74]

Hence, identifying the tremulous motion and attenuating it without adding resistance to the patient's intentional motion is a challenging task. Different simple and complex hand models are proposed, each with different accuracy. So, the hand modeling that reflects a realistic behavior must be considered, and based on it, a suitable vibration absorber can be designed.

2.6. Vibration control methods

Structural control and biomechanical tremor mitigation methods can be passive, active, or semi-active. They are classified according to their energy consumption. Passive absorber is a low cost device used in many applications since it doesn’t require any energy consumption. Many studies are interested in improving passive control method due to its advantages. Passive absorber has fixed characteristics and can tune the structure at specific frequencies. Its weakness comes when dealing with structures for which the determination of natural frequencies is not clear. Other shortcoming of the passive absorber exists when the fundamental frequency of the structure changes with time or due to an extreme dynamic event. This motivates the use of smart structures for controlling the vibration effectively.

Smart structures, including smart materials, are considered as one of the most exciting area of research in structural engineering. In addition, it is the field of interest for many mechanical, electrical, and material engineers. A structure is called “smart” when it includes sensors able to sense the dynamic loading and modify the real time behavior. It aims to make the structure an intelligent machine which can adapt the environmental changes dynamically [75,76], by placing actuators to apply the required compensate force, and reduce its vibration [77]. So, a smart structure includes the actively controlled

members: sensor, feedback loop, and actuator [78-80]. The sensor is responsible of the measurement. The feedback loop determines the required correction force to be applied by the actuator. It is also required to specify the needed algorithm which permits the calculation of the magnitude of the real time control force. Other strategies may exist, but all aim to minimize vibration at any time with an effective control algorithm.

The reduction caused by the damped passive vibration absorbers may be decreased due to insufficient mass ratio, below 1% [81], and when the modal properties of the system of interest changes due to environmental impacts. Pathological tremor tends to have constant frequency with small variations [5]. RT decreases with any deliberate muscle activation [2,82], i.e. with target directed movement. RT has been reported to stay obvious even during posture or movement [83-85], or re-emergent in the postural position after a delay and referred as the "re-emergent tremor" [86]. There are some indications which reveal that the frequency of ET decreases with time [8,19], and amplitude can change depending on the hand position. This causes the detuning of the passive vibration absorber due to the aforementioned problems and thus introduces the need of the active and semi-active alternative control strategies to minimize the displacement response of a complex hand model.

Passive absorber seeks to reduce all the motion instead of reducing the undesired motion only. However, active control methods can be used as in which the unintentional vibration only can be attenuated. Most researchers tend to use the active controllers to reduce the symptoms of the tremor despite of its disadvantages.

2.6.1. Active controllers

In this technique, the muscular force generating the tremor is counteracted by a force out-of-phase of the same magnitude and frequency of excitation. Hewit proposed the use of the active control force in the early 80's [74]. The active control forces are developed depending on the feedback information from a sensor measuring the structure's response and/or feedforward information from another sensor measuring the external excitation, as shown in Figure 2.19. The recorded measurements are monitored by a controller (computer) to determine the appropriate control signal needed for the operation of the actuator.

The main effort of some of the active control systems tested experimentally was done to modify the level of damping with a minor modification of stiffness [88,89]. The appropriate actuator type of the active controller is a challenging task for many researchers. The active control forces may be supplied by electro-hydraulic or electro-mechanical actuators which require a very large power source to achieve precise feedback to the

undesired vibration. The required power is tens of kW from small structures and up to MW for large structures [90]. Figure 2.20 shows the electro-mechanical model of an actuator.

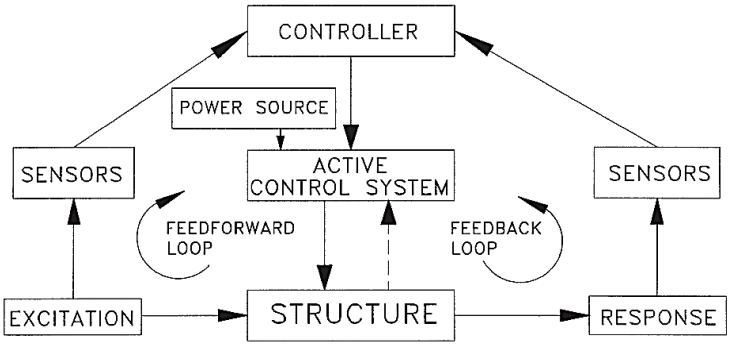

Figure 2.19: Block diagram of active structural control systems [87]

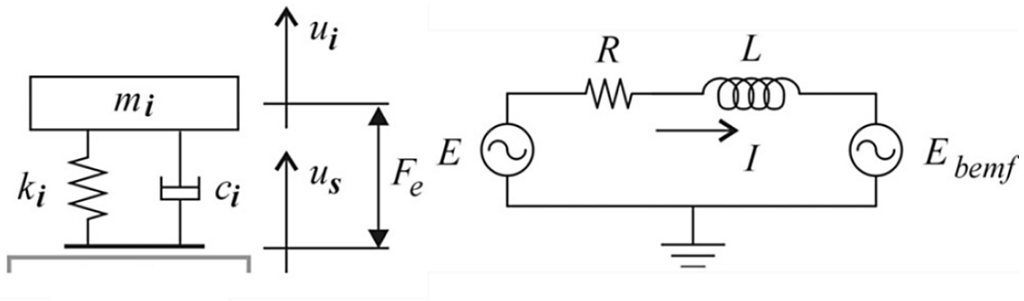

Figure 2.20: Electro-mechanical model of an actuator [91]

Passive DVA is attached to an actuator to form the active dynamic vibration absorber (ADVA) or the electrical vibration absorber (EVA). The advantages of EVA over DVA are that its design parameters (mass, spring, and damper) are easy to control, heavy mass can be imposed without actually loading the setup (i.e., without increasing the total mass of the system) and multiple vibration modes can be conveniently controlled by a single actuator using multiple filters. The disadvantages of the EVA are: high energy consumption, very complex structure, and the need for a large actuating force. Several control laws can be used to determine the actuator's force, such as: proportional–integral–derivative (PID) [92], robust [93], positive position feedback (PPF) [94], and fuzzy control [95]. However, inserting the active controller to the flexible structure leads to many problems which affect its performance especially in multi-modal systems. Despite this, active controllers are used by several researchers to reduce the involuntary tremor in patients with pathological tremor.

Leblanc [96] proposed a mechanical device that is more effective than drugs in suppressing the ET. He used the proportional–derivative (PD-controller) consisting of four linear actuators to actively control the tremor when attached to a patient's wrist. Stone et al. [97] built a test stand to simulate the lower arm of a patient with ET simulated in the horizontal plane by an electro-dynamic shaker (Figure 2.21). They used the idea of Leblanc [96] to model a superior device consisting of a single linear inertial actuator with a moving

mass as a mechanical device to reduce the tremor. The feasibility of the used adaptive PID device was tested on the built stand. They used 0.12 kg H2W linear voice coil actuator to generate the control force using coil's electrical current. The measured parameters of the lower arm are shown in Table 2.2. The PID-controller suppresses 20–60% of physiological vibration level in 6–13 Hz band.

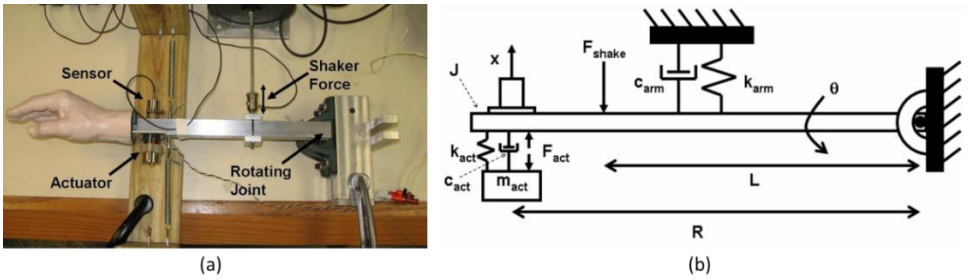

Figure 2.21: (a) The test stand forearm including the accelerometer and actuator attached at the end of the aluminum bar and the shaker attached near the midpoint and (b) the lumped parameters of the forearm [96]

Table 2.2: Measured parameters used for the model test stand by Stone et al. [97] **compared to the forearm parameters determined using the static testing for rotation around forearm by Bennett et al.** [98]

Forearm parameters	**Stone et al.** [97]	**Bennett et al.** [98]
$J_{arm}(kg.m^2)$	0.11	0.07
$k_{arm}(N.m/rad)$	210	16.3–17.3
$c_{arm}(N.m.s/rad)$	1.2	0.62

$J_{arm}, k_{arm},$ and c_{arm} are the measured lower arm's rotational mass moment of inertia around elbow joint, rotational stiffness, and rotational damping coefficient

Huen et al. [29] have manufactured a 350 g wearable exoskeleton, as shown in Figure 2.22, used to suppress the pronation-supination of forearm at elbow joint, and the flexion-extension of the palm at the wrist joint. It was designed as an active controller actuated by electrical geared motors to reduce PD or ET above 3 Hz. The flexion-extension motion at the hand of the volunteer was selected to be simulated at 3 Hz to reflect the tremor movement. The wearable robot prototype can reduce 65% of the simulated tremor amplitude when its power is off, and 77% when activated, as shown in Figure 2.23.

Figure 2.22: Design and configuration of the wearable robotic device for the tremor control of the upper limb motions [29]

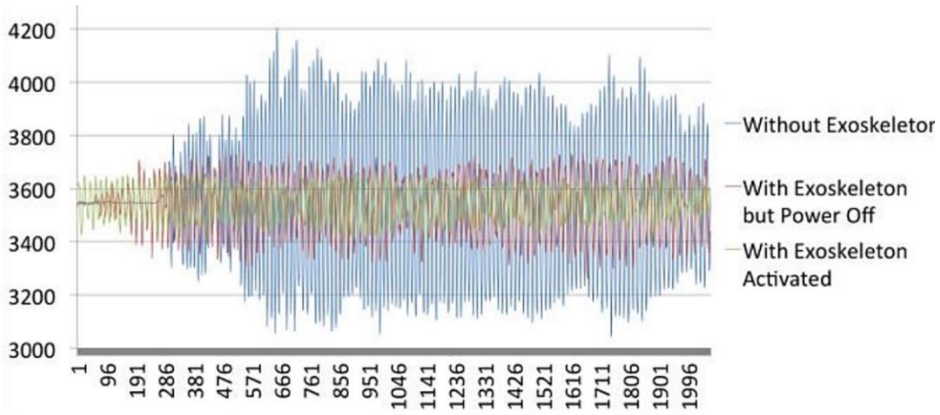

Figure 2.23: Raw signals from gyroscope detecting the simulated tremor motion acquired from the researcher [29]

Recently, Lopez and Morales [99] designed an orthotic system where its schematic is presented in Figure 2.24a. It adjusts its frictional coefficient to reduce the PT of a PD patient. A proportional–integral (PI) controller was proposed to reduce the tremor behavior of the wrist joint, which provides the results shown in Figure 2.24b. Its response is based on a mathematical model developed to reflect the biomechanical dynamics simulated on MATLAB. In addition, they obtain simulated results comparable to those obtained by Gebai et al. [100].

(a)

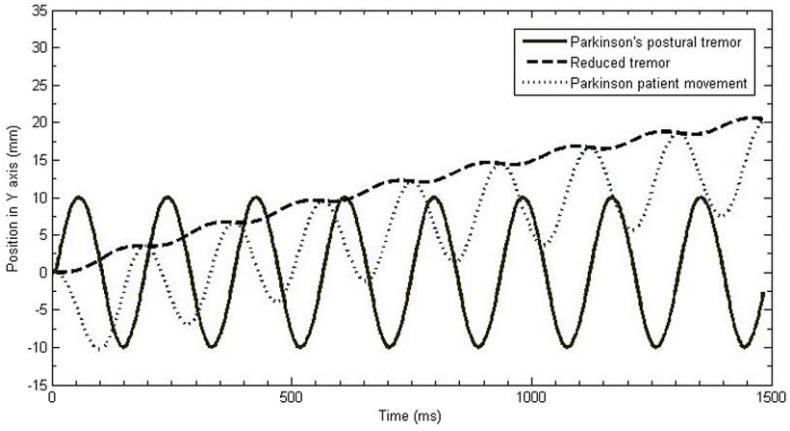

(b)

Figure 2.24: (a) 3D model of the orthosis and (b) simulation of Parkinson Disease patient's behavior with Postural tremor (continuous line), and tremor with (dashed line) and without (dotted line) control while moving the limbs upward [99]

Active controllers have the ability to counteract the tremulous motion by applying a load of the same magnitude, opposite sense, and of the same frequency at each instant. However, a stability problem is found in most of the active controller, and must be considered while designing it. In addition, the high-power required to activate this controller has led researchers look for another type of controller. Several papers have toward on the use of passive absorbers because they have very simple design, inexpensive, and don't require any external power source.

2.6.2. Passive absorbers

Passive absorbers are characterized by their ability to apply a reaction force to the structure without the need the external power source. Its reaction forces are produced depending on the response of the structure itself as represented in Figure 2.25. The dynamic vibration absorber (DVA) is a passive vibration control device widely used to attenuate troublesome resonance. The undamped DVA or the classical tuned mass damper (classical TMD) consists of a proof mass and a spring. It was first invented by Frahm [101] in 1909, but this device was only effective over a narrow and fixed frequency bandwidth. The absorber's spring transfers energy to the proof mass, which must be able to withstand the full force of excitation and its corresponding deflection. The proof mass absorbs the vibrational energy of the primary system. Its mass and spring are chosen to satisfy the tuning condition, so that the structure doesn't feel any undesired transmitted force. Den Hartog and Ormondroyd [102] introduced the TMD or the conventional DVA in 1928 with a broadened frequency range by the addition of a viscous damper, it is also called the Voigt DVA. The suspension's connection (spring and damper) affects the performance of the absorber. A relative motion is produced within the passive devices due to the vibration of the structure, and the absorber in return dissipates the structure's energy using its damper which converts this mechanical energy into heat. On the other hand, the tuned Voigt DVA's parameters are chosen so that the vibration of the structure is close to zero, which can't be exactly zero due to the damper.

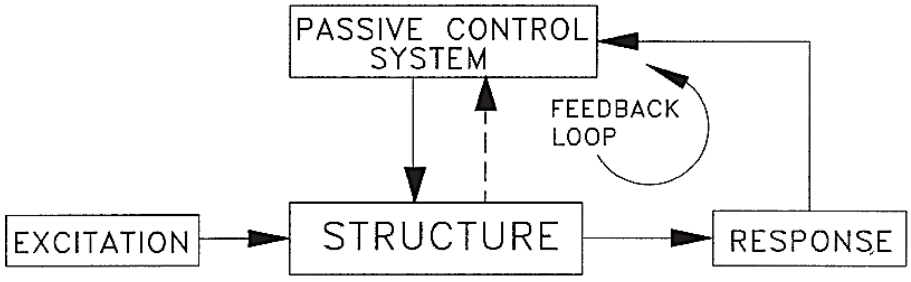

Figure 2.25: Block diagram of passive structural control systems [87]

The conventional DVA has been widely used in passive structural control despite its shortcomings. The TMDs can be used to attenuate the undesired vibration in many practical implementations like machines and buildings [103,104]. They can absorb the

vibration level of a building against earthquake, of a bridge against high speed or turbulence wind, and of airplanes wing flutter. Researchers exerts lots of effort trying to improve the performance of the SDOF passive absorbers.

2.6.2.1. Passive structural control

a. 2DOF absorber

Snowdon et al. [105] were the first to introduce the idea of using a 2TMDs connected in parallel and provided different design guidelines in 1984. Zuo and Nayfeh [106] carried out a detailed study about 2DOF tuned vibration absorber (TVA) connected to a SDOF base excited system by two connecting planar masses. They optimized the two sets of spring and damper to minimize the H_2 and H_∞ norms of transmissibility. Results reveal that a 2DOF TVA has better performance than the two separated SDOF TVAs of the same total mass.

Zainulabidin and Jaini [107] conducted an experimental study of 2DOF DVA modeled as a flexible beam with two masses placed symmetrically on both ends of a static frame. The absorber is proposed to reduce the vibration of clamped-clamped beam structure. They aimed to determine the best location of the proof masses along the beam by trying four different conditions: each DVA on one side (condition 1), first DVA on one side and the other in the center (condition 2), both DVAs in the center (condition 3), and first DVA in the center and the other on the side (condition 4). Only the first two natural frequencies of the structure were tested for tuning the absorber as shown in Figure 2.26. The influence of the 2DOF DVA in reducing the displacement amplitude at the first two natural frequencies is provided by Table 2.3.

(a)

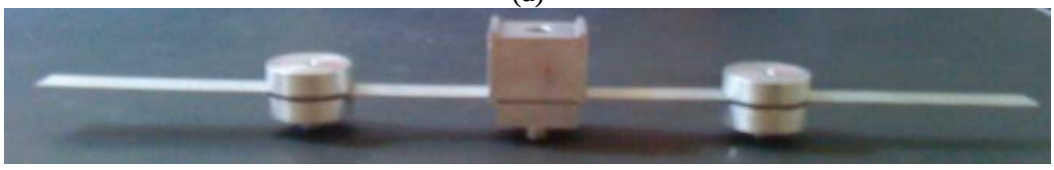

(b)

Figure 2.26: Dynamic vibration absorber (a) tuned to the first mode and (b) tuned to the second mode [107]

Table 2.3: Peak values of beam amplitudes and reduction percentage [107]

Mounting	First DVA (first mode)		Second DVA (second mode)	
	Peak Value (m)	Reduction (%)	Peak Value (m)	Reduction (%)
Without absorber	0.0022	reference	0.0021	reference
Condition 1	0.0009	59	0.00007	99
Condition 2	0.0005	77	0.00003	98
Condition 3	0.0001	95	0.00002	99
Condition 4	0.0002	91	0.00003	98

The concept behind using a 2DOF DVA is to improve the control behavior of the 1DOF conventional DVA. The design of the 2DOF passive absorber can open the door to design of the 2DOF active absorber and the Multi-DOF (MDOF) passive absorber. Many systems in real world applications are excited by multiple central frequencies. However, few studies have considered the control strategies of a MDOF system in comparison to the available studies on controlling SDOF systems. Most researchers studied the application of absorbers on systems with a single harmonic excitation frequency.

b. MDOF absorber

Igusa and Xu [108] studied multiple mass dampers tuned within a frequency range. This technique was more robust than a TMD with the same total mass. Brennan [109] used parallel multiple absorbers tuned to slightly different frequencies, which results in an improved broadband device. In a study done by Zuo and Nayfeh [110], the multiple tuned DVAs shown in Figure 2.27a were more effective than a SDOF TVA of the same total mass. Zuo [111] proposed a multiple mass vibration absorber connected in series. Later on, this new configuration, which is shown in Figure 2.27b was named the series TMD. Thus, the multiple passive vibration absorbers were suggested to replace the conventional SDOF absorbers attached to a MDOF vibratory system.

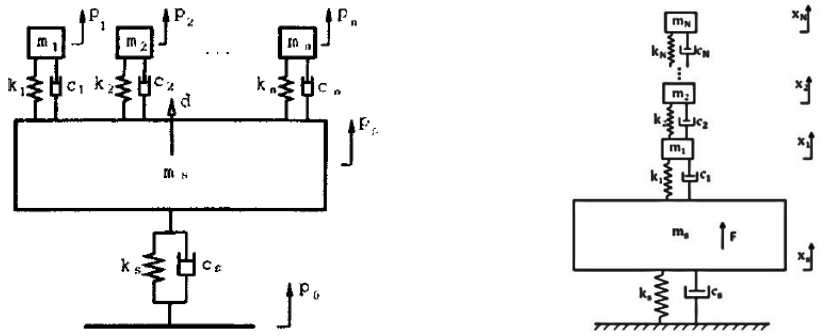

(a) (b)

Figure 2.27: Structure with (a) parallel TMD [110] **and (b) series TMD** [111]

Multiple DVA's [110] and beam structures [112] can be used to overcome the problem of single DVA, and to cancel vibrations with multiple excitation frequencies. However, the addition of the passive absorber(s) to the primary system increases the number of the resonance frequencies of the overall structure.

Some research works [113-115] have toward a modified suspension's connection of the SDOF absorber, and formed uncommon types of DVAs in order to increase their efficiency.

c. Absorber's suspension

Snowdon [113] has designed a three-element absorber which is formed from a spring and damper connected in series and this configuration is connected in parallel with another spring element. The three-element absorber shows better perform than the conventional absorber tested on an undamped structure. Later on, Asami and Nishihara [114] investigated that the three-element DVA has superior performance compared with the Voigt model. Anh et al. [115] in 2013 were the first to use the three-element DVA, shown in Figure 2.28a, while attached to a damped primary system. They presented an approximated analytical solution using the H_∞ optimization. Figure 2.28b shows that this device was more effective than the conventional DVA.

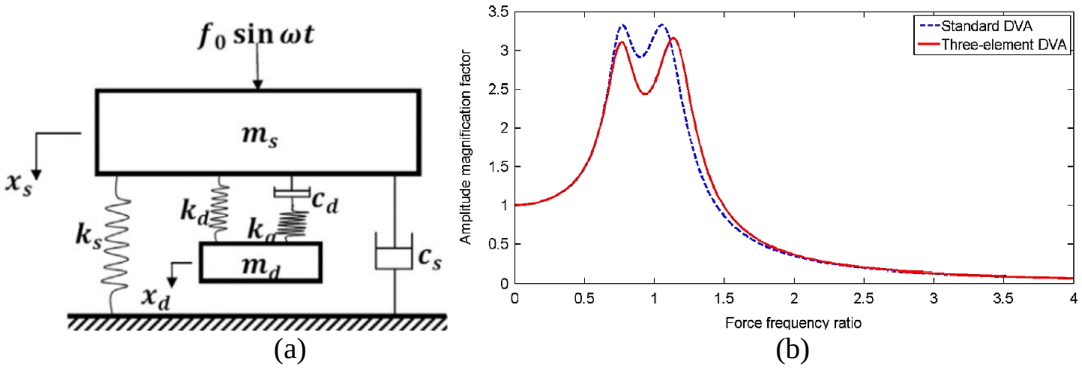

(a) (b)

Figure 2.28: (a) Configuration of the three-element DVA attached to a damped primary structure and (b) comparison between the amplitude magnification factor due to the conventional DVA and the three-element DVA [115]

Other researchers [110,111,116-119] were interested in studying the influence of the passive single, dual, and multiple absorbers parameters (mass, spring, and damper) on its performance.

d. Absorber's parametric study

Zuo and Nayfeh [110] studied the mass distribution, number of dampers, total mass ratio, and system parameters uncertainties of multiple tuned DVAs to reduce the vibration of a SDOF primary system. The numerical study shows that the optimal design can be obtained by using non-uniformly spaced tuning frequencies with optimized stiffnesses and

non-identical, but optimized, damping coefficients. They verified that the displacement of the controlled primary system decreases as the total mass of the conventional MDOF TVAs increases, as shown in Figure 2.29. Results concerning the number of dampers and the effect of the mass distribution of the absorbers are shown in Figure 2.30. Zuo and Nayfeh [110] proved numerically that the variation in the masses distribution of the MDOF DVAs leads to slight improvement in performance beyond uniform masses. On the other hand, Li [119] proved in his study that changing the masses distribution causes leads to better efficiency than varying the stiffness for systems with equally spaced tuning frequencies.

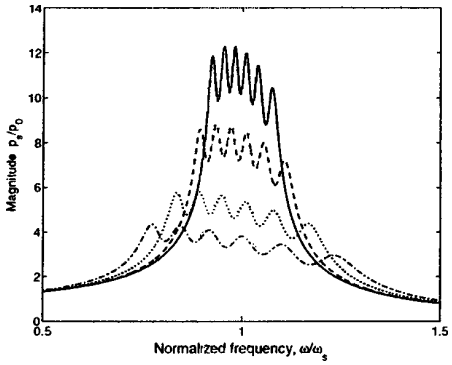

Figure 2.29: Harmonic response of the displacement of an undamped primary system to base excitation for $n = 5$ with $\mu = 1\%$ (solid), $\mu = 2\%$ (dash), $\mu = 5\%$ (dot), and $\mu = 10\%$ (dash-dot) (n is the number of dampers and μ is the mass ratio) [110]

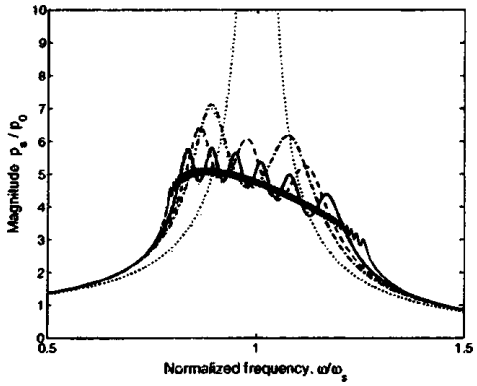

Figure 2.30: Harmonic response of the displacement of an undamped primary system to base excitation for $\mu = 5\%$ with $n = 0$ (dot), $n = 1$ (dash-dot), $n = 2$ (dash), and $n = 5$ (thick dash) (n is the number of dampers and μ is the mass ratio) [110]

Due to the need for using the absorber in real application, MDOF absorbers have been recommended to reduce the vibration a structure with multiple frequencies. Further improvements were done to increase the performance of the absorber by modifying the classical suspension's connection of the TMD. The effect of each absorber's parameter was also studied.

Passive tremor control methods apply to the human limb a velocity–proportional damping force. The addition of the damping element, inertia, and gyroscopic stabilization

are considered passive technologies, and can be used to mechanically reduce tremor [120,121].

2.6.2.2. Passive tremor control

Hashemi et al. [67] used the conventional DVA to reduce the RT of the 2DOF model hand system of PD patient as shown in Figure 2.31. They tried to tune the parameters of the conventional absorber modeled as a cantilever beam with 8.5 cm length and 0.13 kg proof mass, but used an absorber with 300 g mass in the experimental study. Experimental results at the shoulder, and elbow joints, using that manufactured absorber, are shown in Figure 2.32. Numerical and experimental studies show qualitatively similar results. Rouhollah et al. [68] used the multi-objective optimization design of the TMD to minimize displacement as well as acceleration variance and tested it on the same hand model as used by Hashemi et al. [67] (Figure 2.14). It was reported that the developed vibration absorber generated numerical results comparable to those of similar studies.

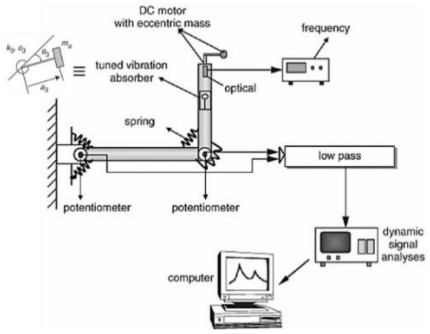

Figure 2.31: Experimental instrumentation for the 2DOF modeled hand system [67]

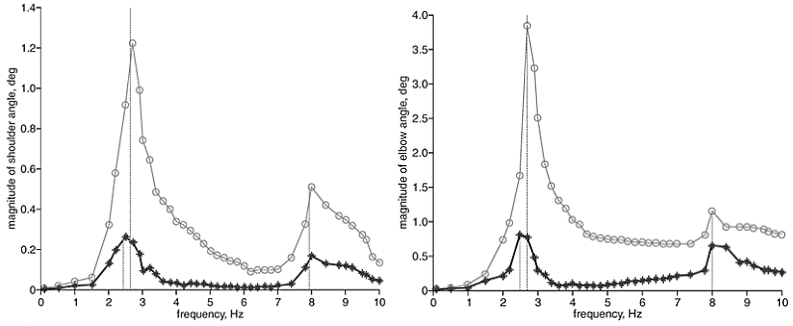

(a) (b)

Figure 2.32: Experimental frequency response results at (a) shoulder joint and (b) elbow joint; (-○-○-○-) uncontrolled and (-∗-∗-∗-) controlled [67]

Rahnavard et al. [69] tried to improve the absorber's performance of Hashemi et al. [67]. They designed an optimal cantilever beam TMD with 20 cm length and 0.375 kg attached mass. They used the H_2 optimization criterion, which is applied to reduce the total vibration energy of the system for the overall frequencies. It reduces the flexion motion at the first and second natural frequencies of the elbow joint response by 98% and 80%. Two

types of random inputs were also considered separately. In one type, the absorber causes 60% and 39% reduction of flexion motion at the shoulder and elbow joints in time domain, and in the other, 33% and 50%.

Buki et al. [43] used a single degrees-of-freedom (SDOF) passive vibration absorber to reduce the pronation-supination tremor of PD with the SDOF modeled forearm system shown in Figure 2.33a. The 280 g Vib-bracelet shown in Figure 2.33b was manufactured to reduce tremor using two concentric rigid rings with three round leaf springs tuned to the resonance frequency of the system. The wrist tremor amplitude simulated on ADAMS software is represented in Figure 2.34a. The results show that the maximum amplitude at 4.5 Hz was reduced by 88%. The results based on ten repeated experiments are represented in Figure 2.34b, which shows that the maximum amplitude at 4.75 Hz was reduced by 86%.

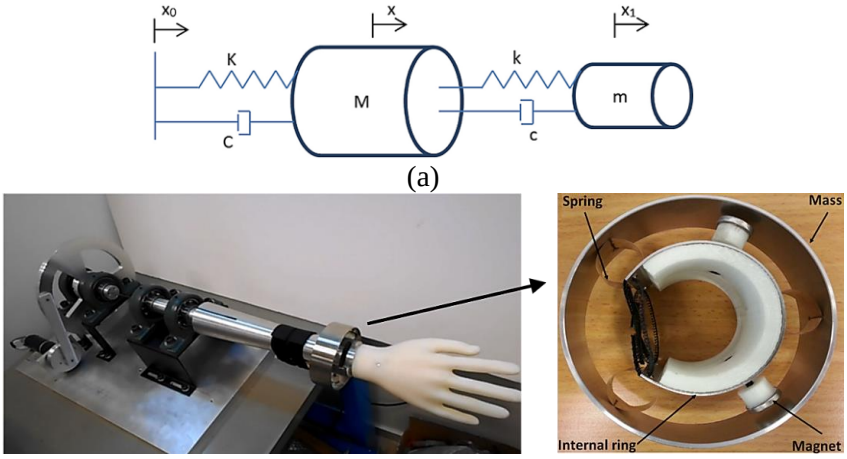

Figure 2.33: (a) The modeled two DOF controlled system and (b) the manufactured passive absorber [43]

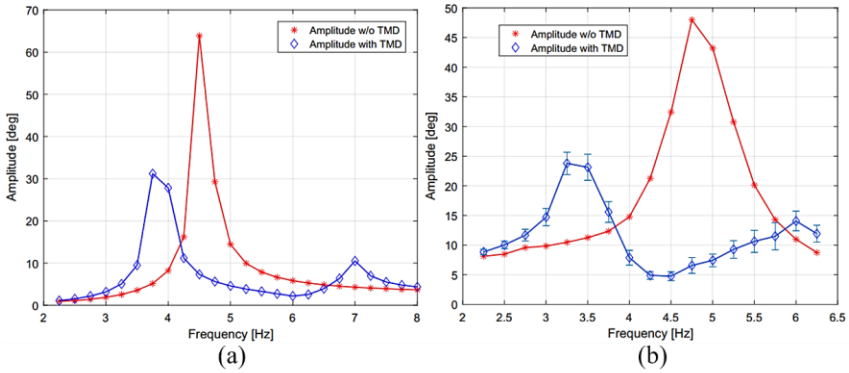

Figure 2.34: Tremor data at the wrist with and without the Vib-bracelet (a) simulated on ADAMS software and (b) measured experimentally by Buki et al. [43]

Therefore, SDOF vibration absorbers have been suggested as a mechanical treatment to reduce the tremor vibration of the hand joints. The well-tuned absorbers show

their numerical and experimental ability to reduce tremor's amplitude. However, passive SDOF absorbers are able to reduce the tremor at a narrow and fixed frequency and their use is still limited by the researchers. This requires the development of a conventional type of passive absorbers, for research directed at tremor control, as they have the advantage of operating without power requirements.

2.7. Conclusion

Different types of pathological tremor exist for the neurodegenerative disordered patients, which appear depending on the performed hand tasks and muscle's situation. However, they can be hardly separated and identified clinically. Frequency ranges are an acceptable method used to identify the involuntary tremor type. Researchers have provided a different description of the behavior of upper limbs tremor signals. Tremor requires accurate and comfortable sensors to monitor the health of the patient. The measured EMG signals of the muscles can be used as an active input for the musculoskeletal dynamic models of the hand to reflect a more realistic response tremor behavior of the patient, and to overcome existing contradictions in the tremor behavior description and the proposition of experimentally non validated models of the hand. Most existing tremor control strategies shift to the use of active control methods which require mainly large input power and present stability problems. Developments in the passive tremor control type with an improved performance can be classified as being of great importance.

This thesis work focuses on the development of a light, simply designed, and optimized passive vibration absorber that can reduce the angular displacement amplitude of the PT for a specific patient. A parametric study of a single TMD of several TMDs is carried out to improve its performance in reducing the tremor. The EMG signals of the patient are measured and used as an input for a proposed 3DOF upper limb model, which is described by the flexion-extension motion at the shoulder, elbow, and wrist joints. The passive elements of the muscles were used based on reliable values provided from the literature. The equations of motion of such a system are derived in addition to the equations obtained after the addition of multi-TMDs (MTMDs) at the forearm or palm segments. The scaling level of the EMG voltage signal of the muscles required to reflect the input torque of the model was based on the values required to reach the measured PT tremor amplitude. Measurement of the PT of different patient is done and repeated for several days with different hand positions to realize whether the critical tremor frequency will shift within a wide or a narrow bandwidth. The acceleration, displacement, and angular displacement ranges are collected from each measured dataset. An improvement proposed for the passive vibration absorbers according to the range of PT frequency shifting deduced from the measurements.

CHAPTER 3. TREMOR SIGNAL MEASUREMENT ANALYSIS

THE measurements are done using an accelerometer, IMU, and EMG. In order to fill the information gap about the pathology and physiology of the hand's postural tremor and obtain useful information to design an absorber, measurements carried out at Hôpital Pitié-Salpêtrière were post-processed. Tremor behavior is recorded for the forearm, palm, and finger's tremor, in addition to the forearm flexor carpi radialis and extensor carpi radialis muscles. The measured signals are analyzed in time and frequency domains to provide information, under different tested clinical tasks, as the tremor signals amplitude range, the power spectral density critical amplitude, and the corresponding frequency of the hand's postural tremor.

Plan of Chapter 3

3.1. Introduction

This chapter presents the tremor measurements conducted for several patients affected by the hand PT. The EMG recording is done for the ECR and FCR muscles at the forearm. A tri-axial accelerometer is used to measure the tremor behavior at the index finger for different postural tasks. Tremor measurements are repeated several times for different days to determine the change in the tremor characteristics. Tremor signals are then processed to collect data from the measurements. The acceleration and integrated displacement signal's amplitude range at the finger is determined for each patient, as well as the PSD's dominant peak frequency and amplitude. A comparison between the PSD obtained from the muscle's EMG and accelerometer measurements is presented. Depending on the amplitude and width of the muscles PSD peak, the damping ratio of each EMG PSD is identified. IMU measurements are also used to identify the tremor and compare the palm's and forearm's physiology and pathology.

3.2. Experiment protocol

Four patients with neurological disorders ("Patient 1", "Patient 2", "Patient 3", and "Patient 4") participated in this study. Tremor measurements are conducted by Dr. Emmanuel Flamand-Roze, Elodie Hainque, and Emmanuelle Apartis from the Department of Nervous System Diseases in Hôpital Pitié-Salpêtrière (Paris). They did the measurements, at the left hand of each patient, for two different clinical hand posture tasks. In "Task 1", the arms are extended and palms raised (Figure 3.1a). In "Task 2", the elbows are bent so that the dorsum are facing each other (Figure 3.1b). Measurements are done while the patients are sitting in these two tasks. The measurements of each task are done for four different hand angular positions: "Pos. 1", "Pos. 2", "Pos. 3", and "Pos. 4", and repeated twice along three days. Each measurement dataset includes 3-directional acceleration signals of the index finger, measured using a lightweight tri-axial accelerometer (PCB Piezotronics, Model 356A32), and the muscles activation signals for the ECR and FCR of the forearm, using EMG. The datasets of the tremor measurements are distributed as 10 datasets for "Patient 1", 25 datasets for "Patient 2", 24 datasets for "Patient 3", and 24 datasets for "Patient 4", respectively, for each task.

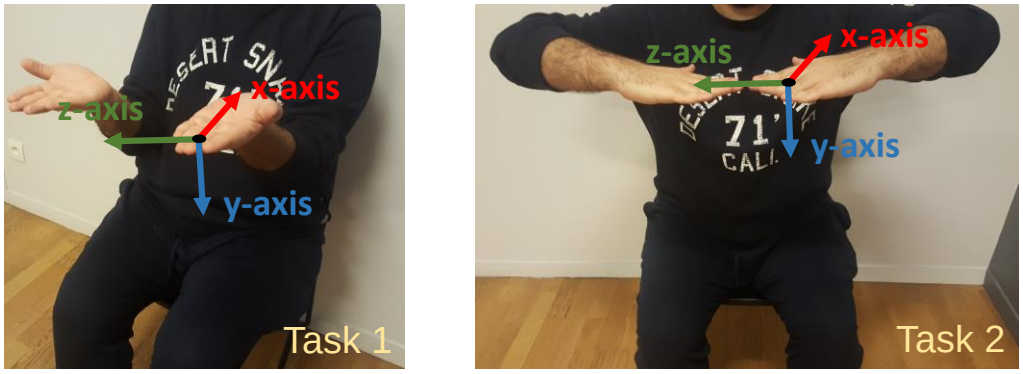

(a) (b)

Figure 3.1: Hand Posture (a) extended arms with raised palms and (b) bent elbows so that the dorsum are facing each other, which represent the clinical tasks used by Hôpital Pitié-Salpêtrière

Measurements are also done to obtain the tremor behavior at the forearm and palm segments of a PT patient ("Patient 5") and four healthy subjects ("Healthy 1", "Healthy 2", "Healthy 3", and "Healthy 4") for the "Task 1" hand position, as shown in Figure 3.2. Tremor signals are recorded using an IMU to obtain the 3-directional acceleration and 3-directional angular velocity signals for the affected patient and healthy people.

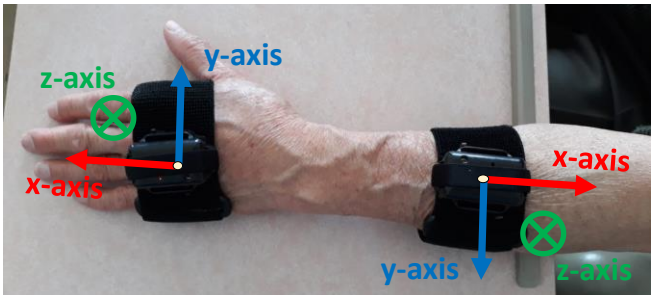

Figure 3.2: IMU measurements at the forearm and palm for a "Task 2" postural position

3.3. Data acquisition

Tremor data was recorded using the tri-axial accelerometer at the index finger and EMG for the ECR and FCR muscles for 60 s with a sampling frequency of 5 kHz. The raw data for "Patient 4" under "Task 1" clinical hand position are shown in Figures 3.3a and b. Their PSD determined using the Welch's method with Hamming window of 256 points, 80% overlap, and 5 kHz sampling frequency is shown in Figure 3.3c. Prior to analysis, signal processing is required to interpret the tremor time signal so that it can provide more information in the frequency domain than the untreated waveform [13].

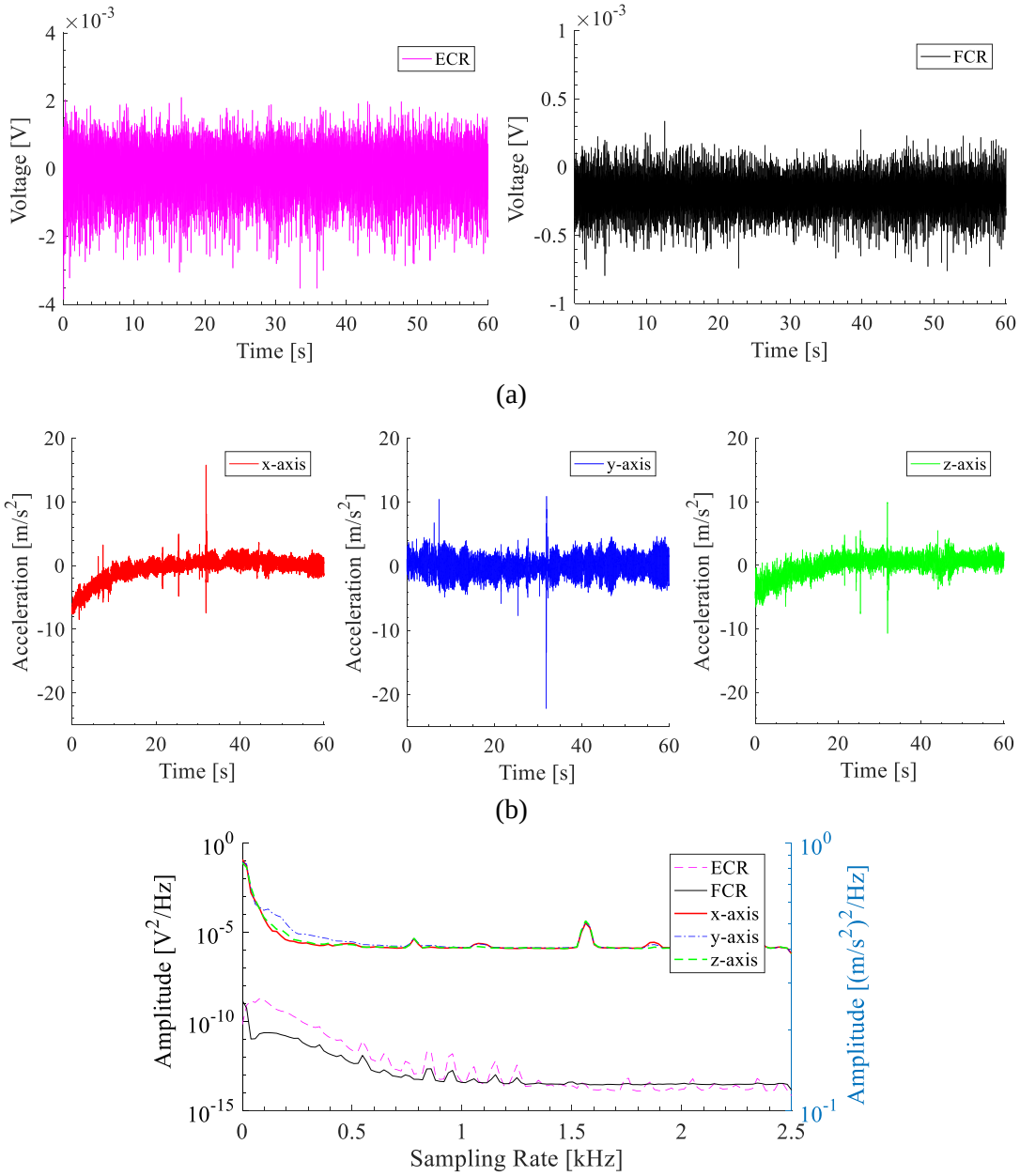

Figure 3.3: Measured raw data of (a) EMG activity for the ECR and FCR forearm muscles, (b) x-, y-, and z-axis accelerometer's signals at the index finger, and (c) PSD of (a) and (b) voltage signals for "Patient 4" with "Task 1" position

The time signals are downsampled by a ratio of 100 to obtain a sampling frequency of 50 Hz, which is more than twice the upper limit of the frequency of interest. The frequency response information is obtained by means of the Welch's method with Hamming window of 256 points, 80% overlap, and 50 Hz sampling frequency. The DC component effect component effect at low frequencies is reduced by a high-pass filter with a cut-off frequency of 1.5 Hz. The EMG and accelerometer's signals after their processing are shown in Figure 3.4a and b, and the PSD of each is shown in Figure 3.4c.

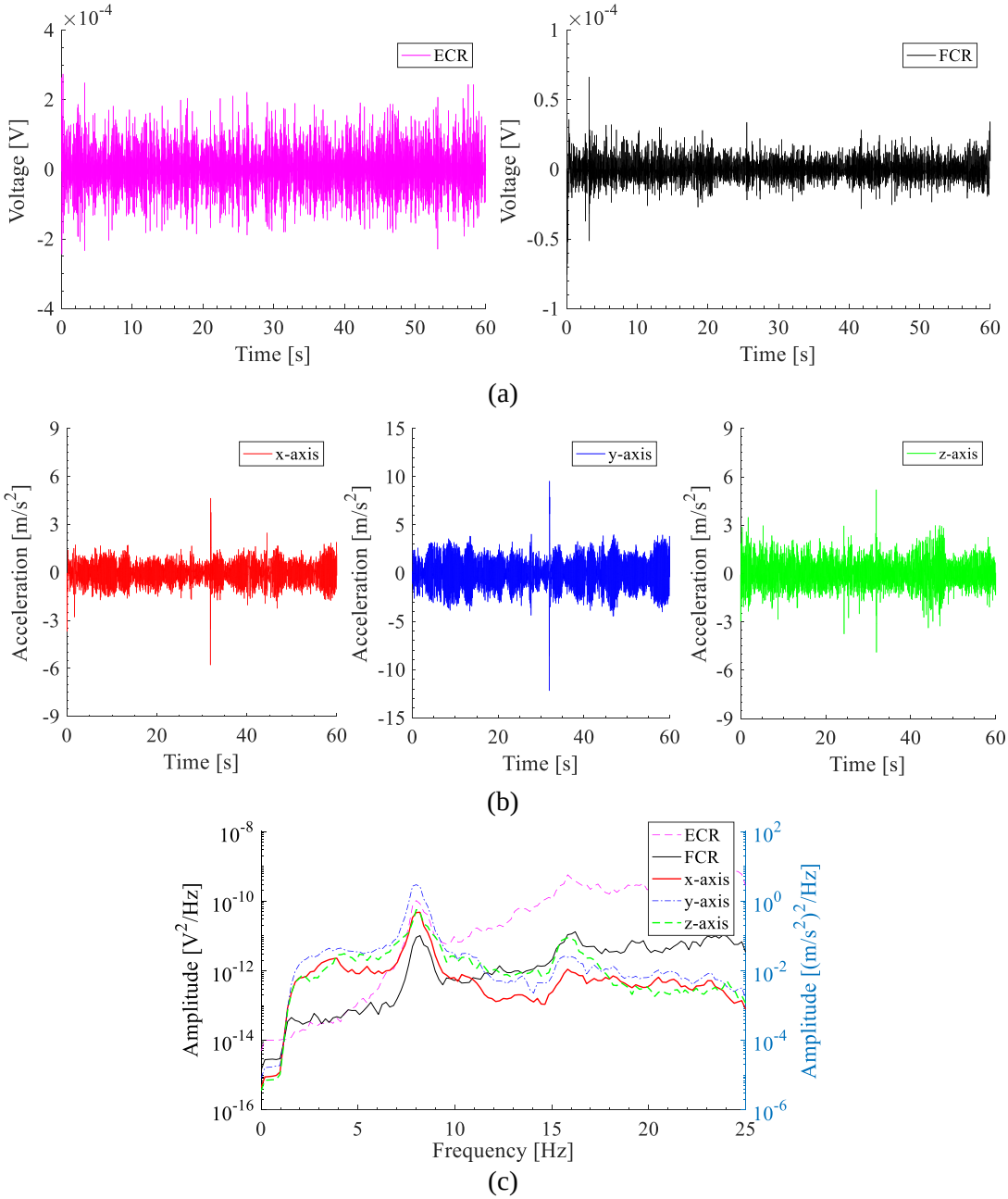

Figure 3.4: Tremor signals after signal processing of (a) EMG activity for the ECR and FCR forearm muscles; (b) x-, y-, and z-axis accelerometer's signals at the index finger; (c) PSD of (a) and (b) voltage signals for "Patient 4" with "Task 1" position

The processed acceleration signals are integrated twice to obtain the displacement signals along the three axes for "Patient 4" with "Task 1" postural position (Figure 3.5). Similar processing steps are done for the rest of the patients under different tasks.

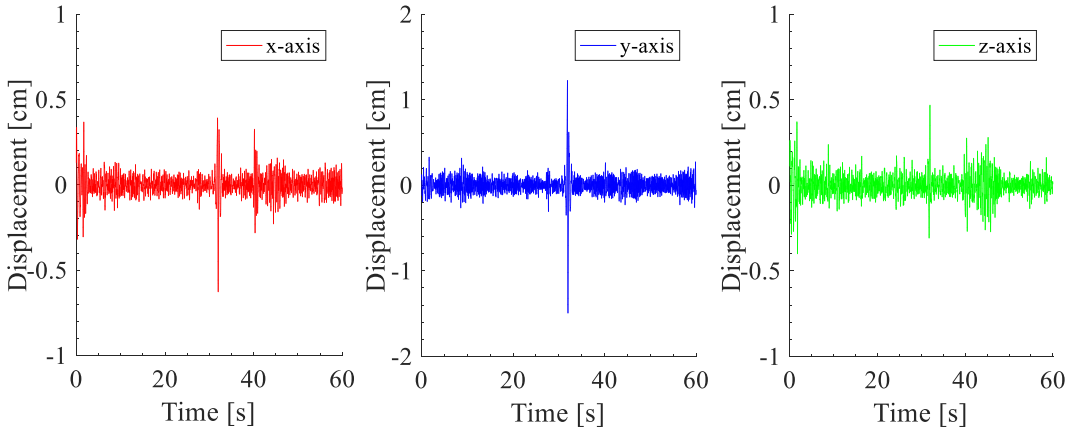

Figure 3.5: X-, y-, and z-axis displacement signals obtained after integrating twice the acceleration signals at the index finger for "Patient 4" with "Task 1" position

In the same manner, the IMU acceleration and angular velocity signals were processed. The tremor data was recorded for 60 s with a sampling frequency of 1.3 kHz for the acceleration and 800 Hz for the angular velocity. The acceleration and angular velocity signals were downsampled by a ratio of 25 and 16, respectively, to obtain a sampling frequency around 50 Hz. The Welch's method with Hamming window of 512 points, 90% overlap, and 53 Hz sampling frequency is used for the signals PSD. The processed IMU 3-axis acceleration and angular velocity signals at the forearm of "Healthy 1" under "Task 2" clinical test, in addition to their PSD, are shown in Figure 3.6 and Figure 3.7, respectively.

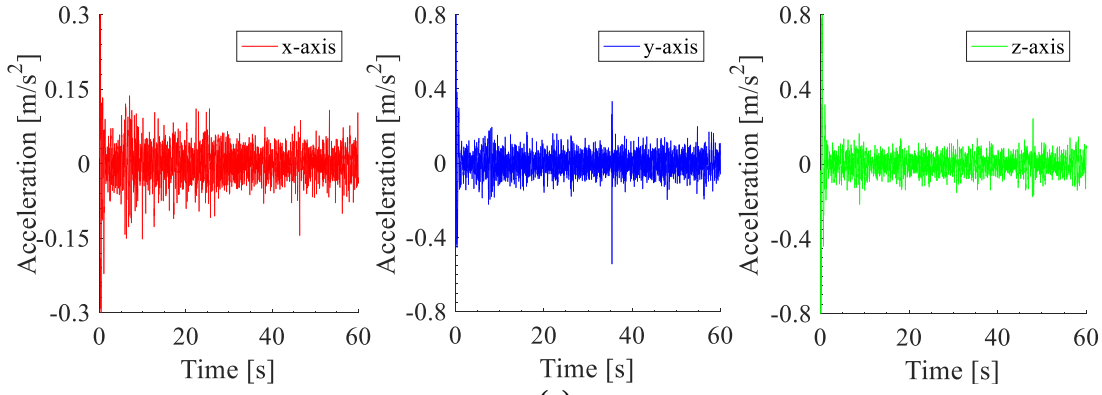

(a)

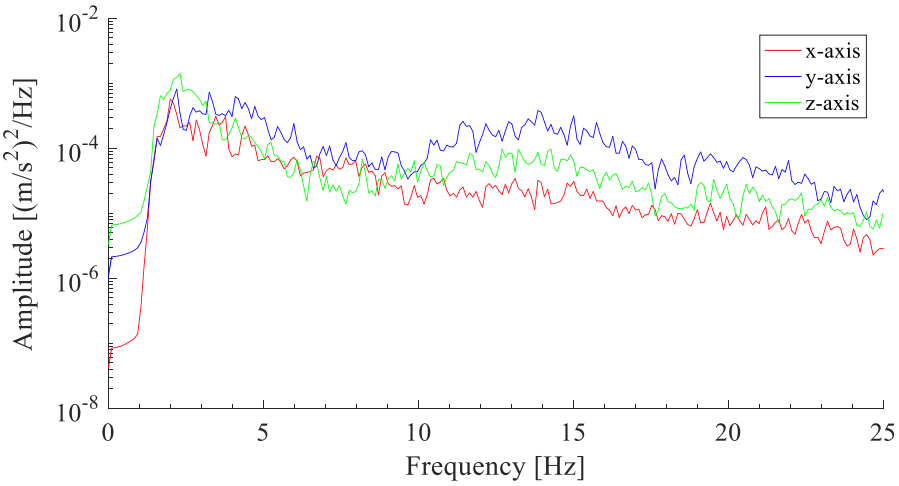

(b)

Figure 3.6: (a) IMU x-, y-, and z-axis processed acceleration signals measured at the forearm and their (b) PSD for "Healthy 1" with "Task 2" hand position

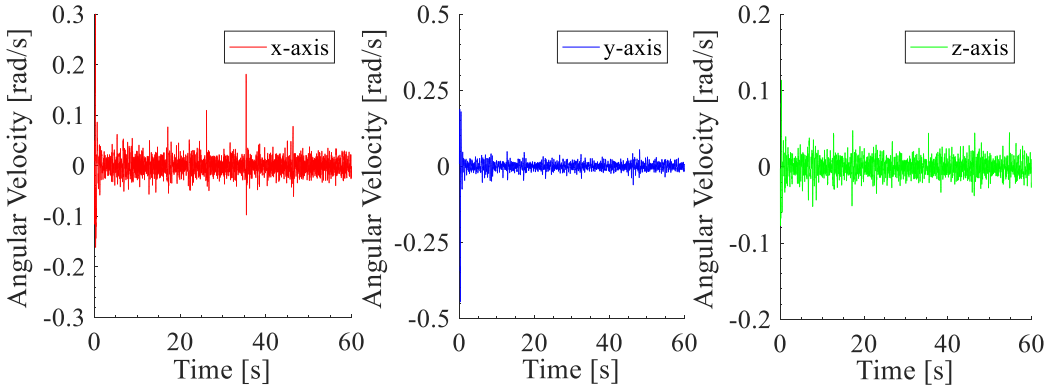

(a)

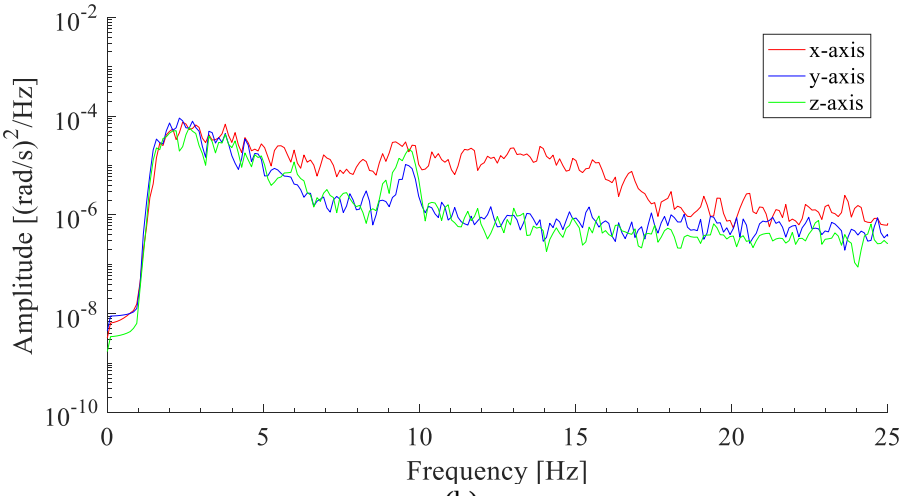

(b)

Figure 3.7: (a) IMU x-, y-, and z-axis processed angular velocity signals measured at the forearm and their (b) PSD for "Healthy 1" with "Task 2" hand position

The processed IMU 3-axis acceleration and angular velocity signals at the palm of "Healthy 1" under "Task 2" clinical test, in addition to their PSD, are shown in Figure 3.8 and Figure 3.9, respectively.

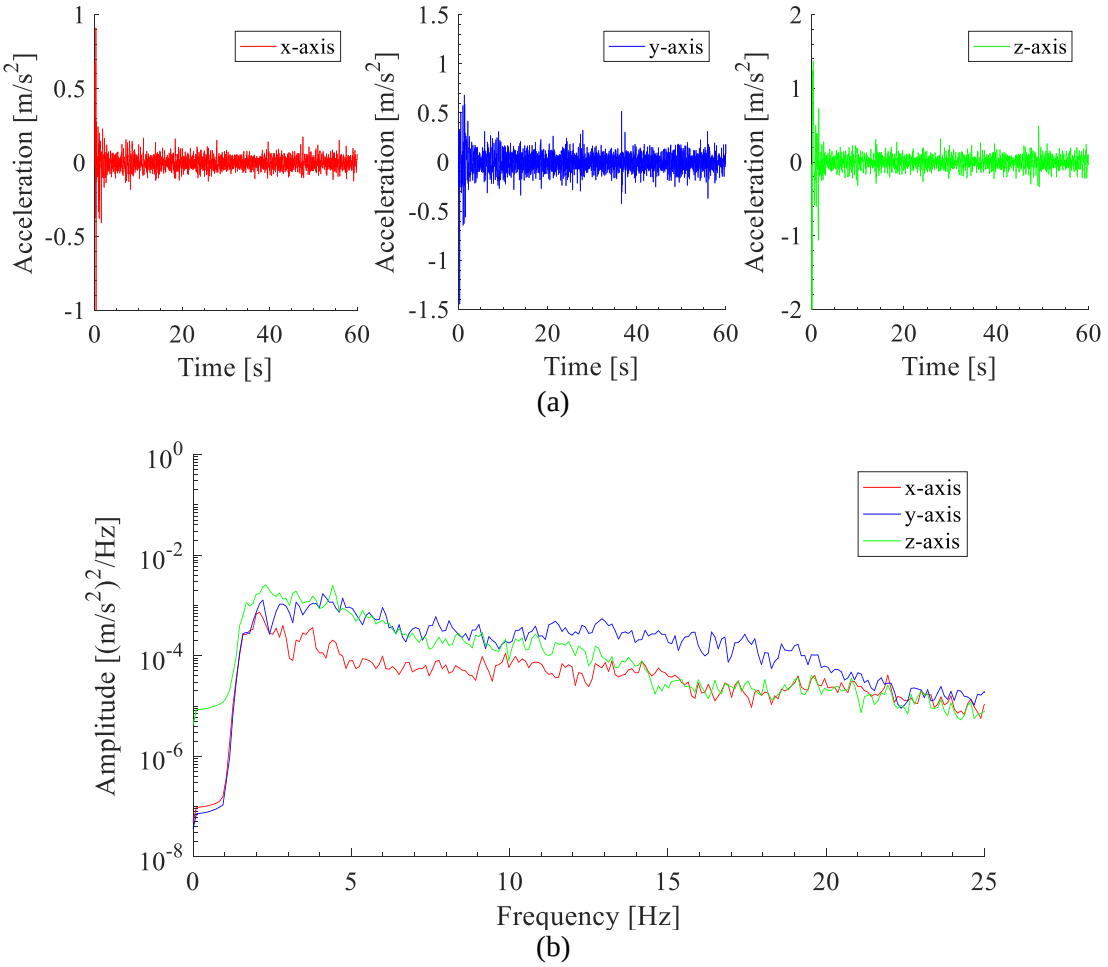

Figure 3.8: (a) IMU x-, y-, and z-axis processed acceleration signals measured at the palm and their (b) PSD for "Healthy 1" with "Task 2" hand position

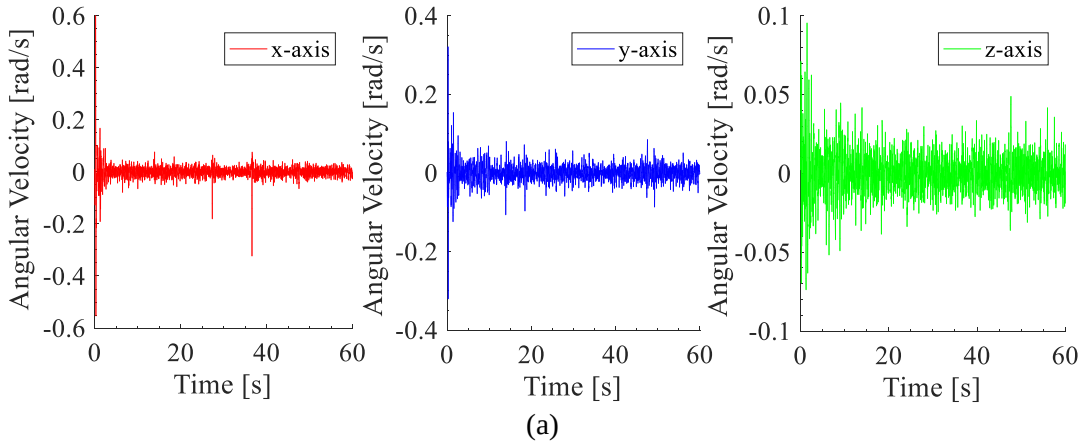

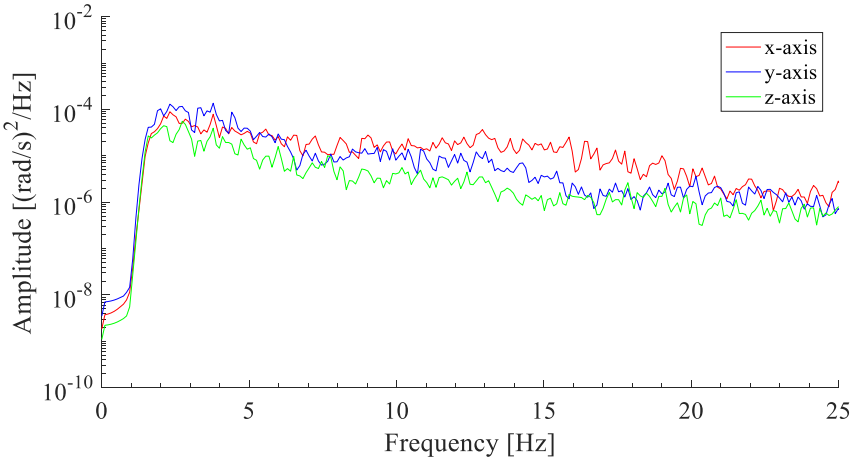

(b)

Figure 3.9: (a) IMU x-, y-, and z-axis processed angular velocity signals measured at the palm and their (b) PSD for "Healthy 1" with "Task 2" hand position

The IMU acceleration signals are integrated twice to obtain the 3-axis displacement signals and the angular velocity signals are also integrated to obtain the 3-axis angular displacement signals at the forearm and the palm. Similar processing steps are done for the healthy participants and "Patient 5" signals measured using the IMU.

3.4. Tremor analysis

The tremor is measured using an accelerometer to obtain the pathological tremor behavior at the finger index for "Task 1" and "Task 2" hand positions. The EMG measurements are also done for both tasks to obtain the corresponding pathological tremor behavior of the ECR and FCR muscles at the forearm. Moreover, the IMU measurements are done to obtain the pathological and physiological tremor behaviors at the forearm and the palm at "Task 2" hand position.

3.4.1. Accelerometer and EMG measurements

The tremor behavior at the index finger in x-, y-, and z-axis is similar in the frequency domain but with different amplitudes for all datasets, as presented for "Patient 4" with "Task 2" in Figure 3.4. Peaks occur at the same frequencies in the three axes. The vertical response (y-axis) captures a higher contribution from the tremor. The peak frequencies of the finger's PSD correspond to peak frequencies of the ECR and/or FCR active muscles, which means that these muscles are causing the tremor.

Figure 3.10a–d shows the y-axis acceleration signals for different patients measured with "Task 1" postural test for 60 s. The tremor's behavior of each patient is different with different amplitude levels. The PSD of these signals is presented in Figure

3.10e. For each patient, the PSD shows a critical peak that occurs at different frequencies, but within the range of the PT.

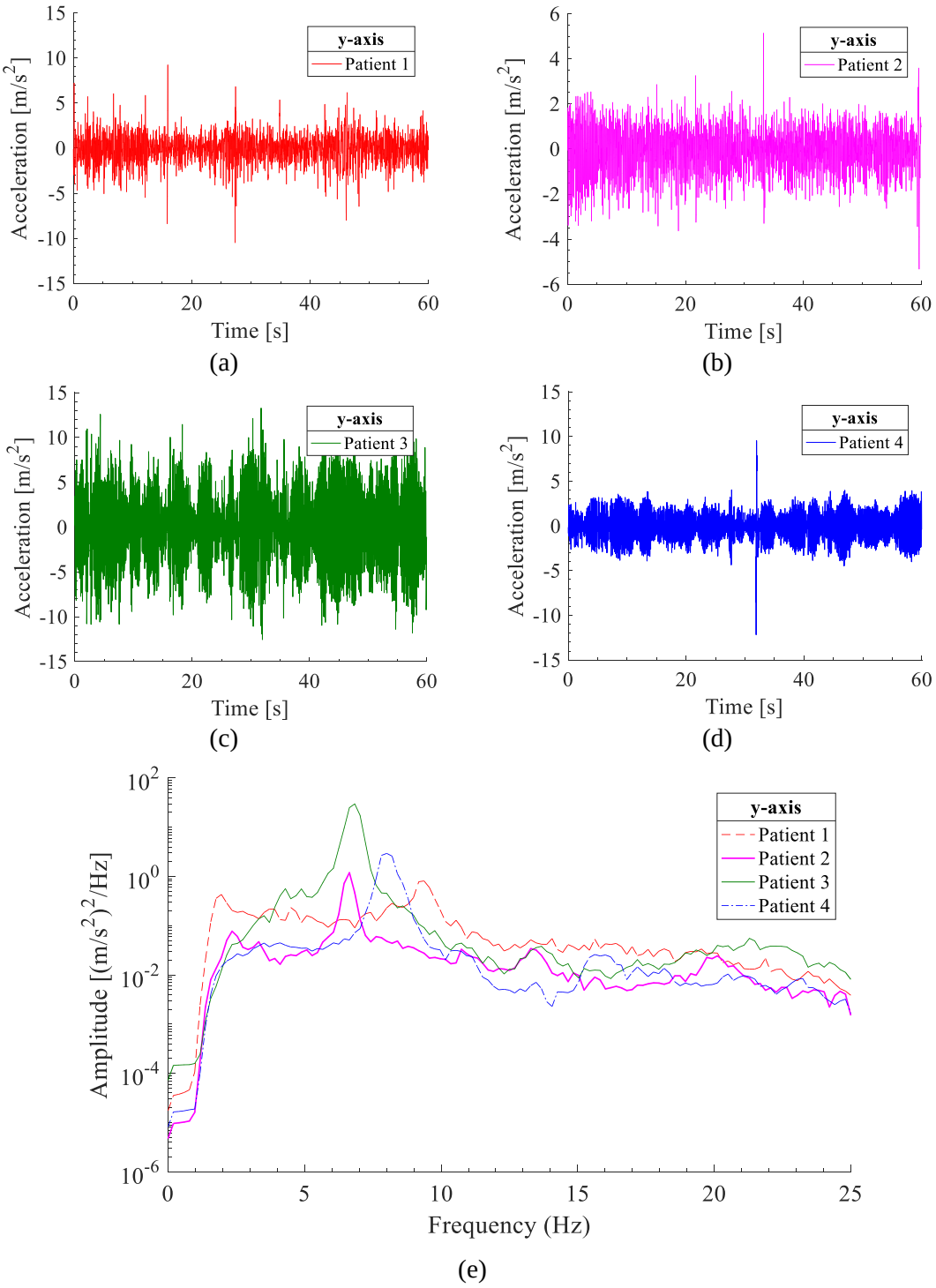

Figure 3.10: Y-axis acceleration signals at the index finger under clinical "Task 1" hand position in for (a) "Patient 1", (b) "Patient 2", (c) "Patient 3", and (d) "Patient 4" and their (e) corresponding PSD

Figure 3.11 shows the PSD of the y-axis acceleration signal compared to that of the amplified ECR signal for the four patients and the hand's "Task 1" position. It shows that the critical peak of the finger's PSD occurs at the driving frequency of the muscles.

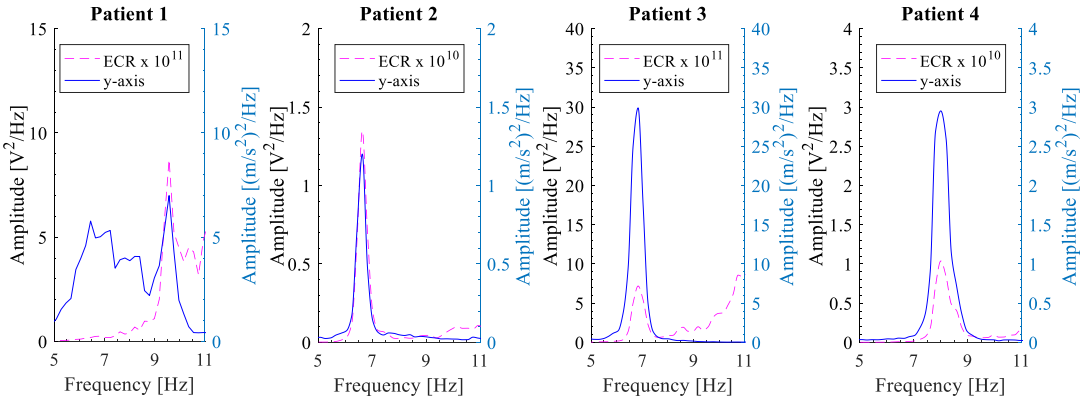

Figure 3.11: PSD for the y-axis index finger and ECR signals of the four patients under "Task 1" clinical test

In order to test the finger's behavior with respect to the muscle's behavior, Figure 3.12 is represented for "Patient 4" with postural "Task 1". Figure 3.12a shows the PSD of the y-axis acceleration signal of the finger for "Pos. 1", "Pos. 2", "Pos. 3", and "Pos. 4" within the same days, compared to the corresponding PSD of ECR signal. Measurements for each position were repeated twice. The finger's (upper curves) and muscle's (lower curves) curves show almost similar behavior for different hand positions, with slight changes in the amplitude and small shifting in the frequency. PSD obtained for the different hand positions show that the finger's critical frequency reflects the muscle's critical frequency. Figure 3.12b illustrates the PSD of the y-axis finger (upper curves) and the FCR (lower curves) signals for the same hand's position, repeated twice, but measured for three different days. The curves also show that the finger's critical frequency corresponds to the muscle's operating frequency. It is not necessary to obtain clear EMG signals for all the muscles simultaneously, where one may be more active that the other. Researchers usually choose those providing useful information among several measurements done. So, the representation of the ECR or FCR signal in Figure 3.12 was chosen depending on those which have more clear frequency contents.

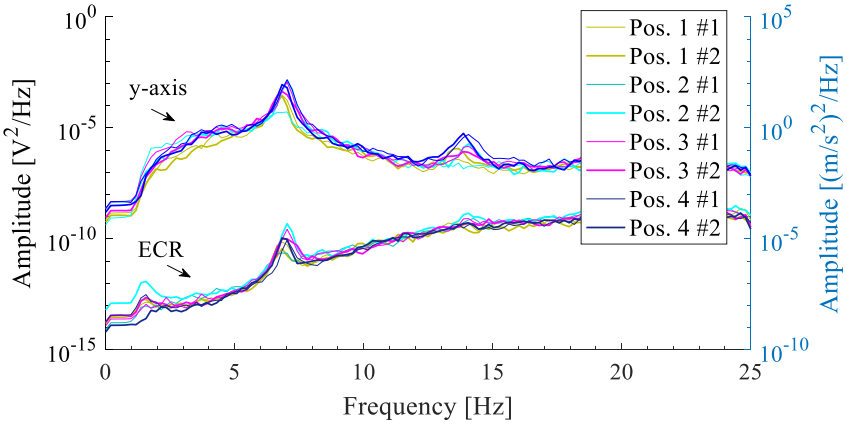

(a)

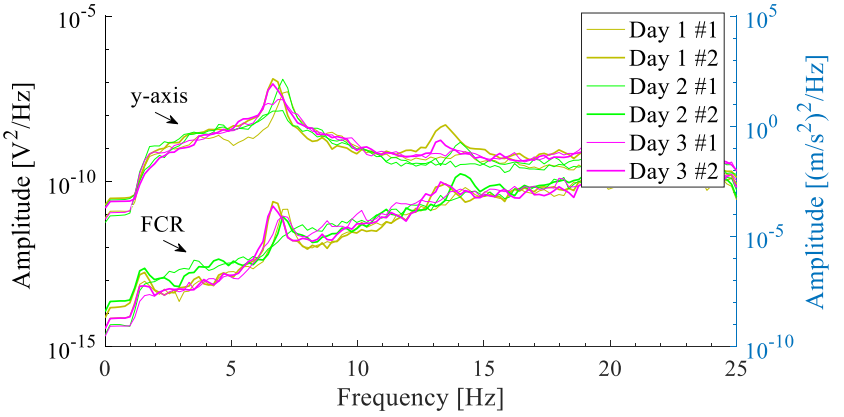

(b)

Figure 3.12: PSD of "Patient 3" for "Task 1" clinical test for (a) four different hand's positions repeated twice in the same day and (b) the same hand's position repeated twice each day (upper curves for y-axis acceleration at the index finger and lower curves for (a) ECR (b) FCR signals)

As it is more meaningful to deal with the tremor's displacement, the acceleration signals are integrated twice to obtain the displacement motion at the index finger. The displacement signals of the graphs presented in Figure 3.10 are shown in Figure 3.13. In order to design a passive TMD for a specific patient, it is important to study the variations in the tremor's amplitude and the shift in tremor's frequency for each patient. So, the acceleration and displacement signal's amplitude levels for each patient will be collected, in addition to the PSD's critical peak frequency and amplitude.

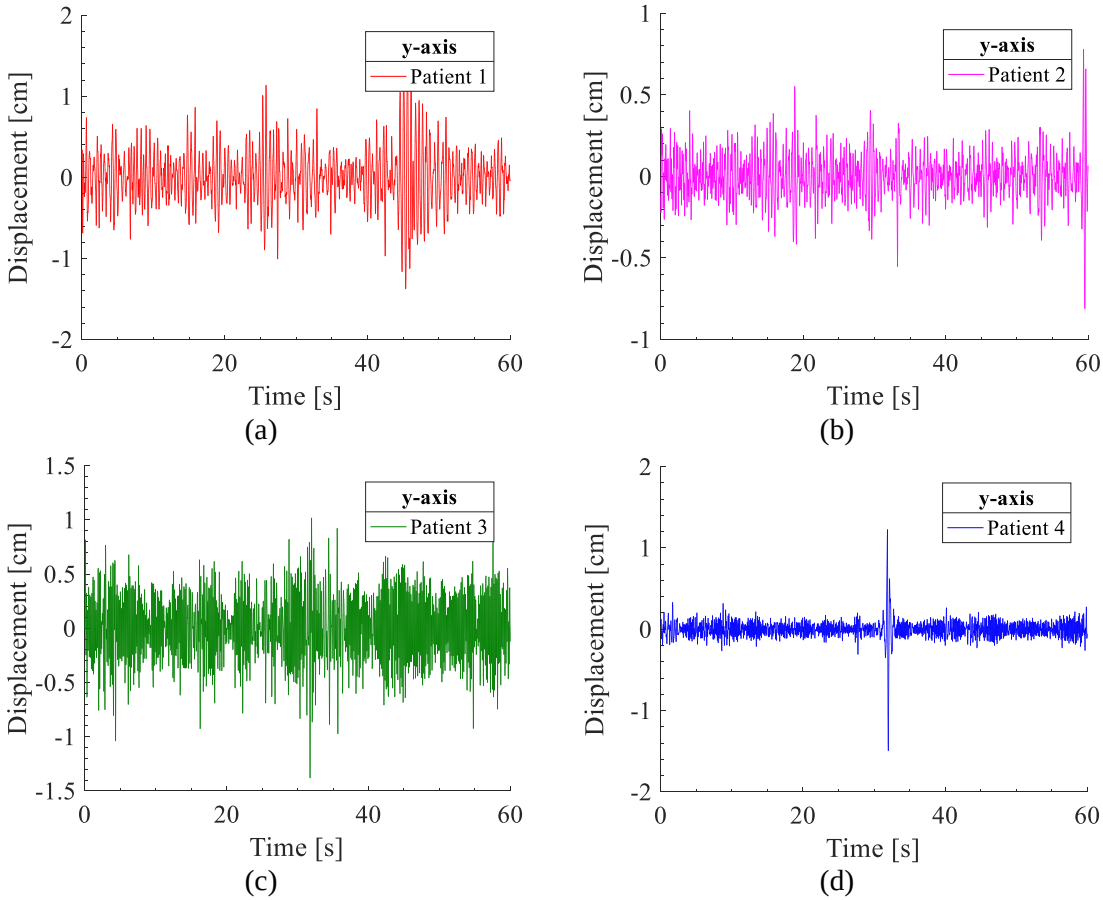

Figure 3.13: Y-axis displacement signals at the index finger of (a) "Patient 1", (b) "Patient 2", (c) "Patient 3", and (d) "Patient 4" for clinical "Task 1" hand position

3.4.2. IMU measurements

A PT affected patient and four healthy people participated in tremor measurement tests to obtain the pathological and physiological behavior at the forearm and the palm. The IMU in Figure 3.2 is used to determine the 3-axis acceleration and 3-axis angular velocity signals for the "Task 2" clinical test shown in Figure 3.1b.

3.4.2.1. Pathological tremor

The 3-axis acceleration signals measured using the IMU at the forearm and the palm of "Patient 5" are shown in Figure 3.14. Figure 3.15 shows the corresponding angular velocity measurements. Both figures show that the forearm and the palm have different amplitude level.

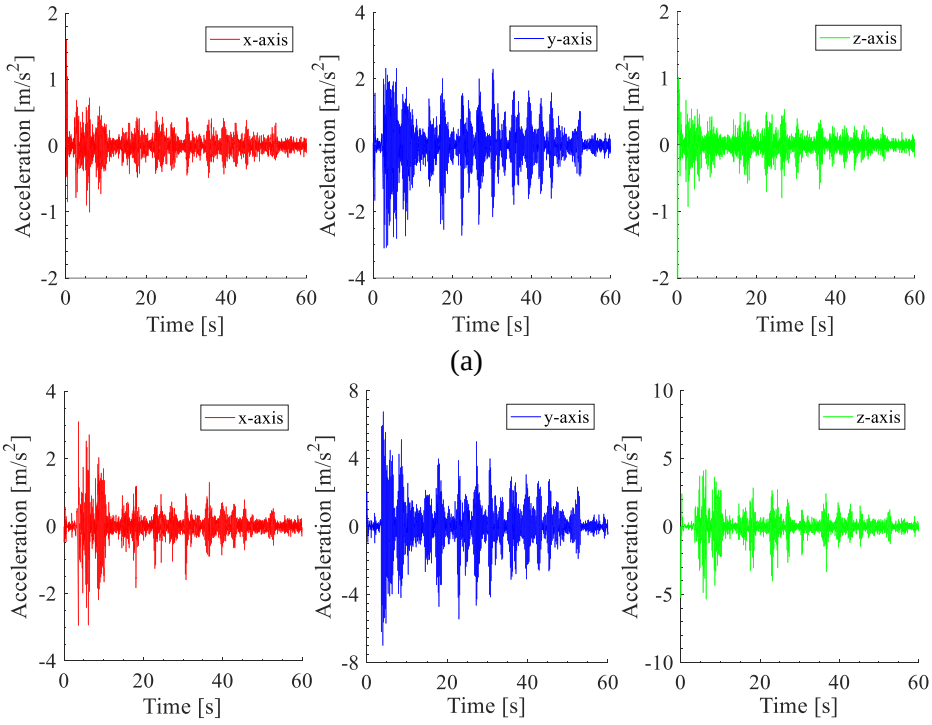

Figure 3.14: IMU x-, y-, and z-axis acceleration signals measured at the (a) forearm and (b) palm of "Patient 5" for clinical "Task 2"

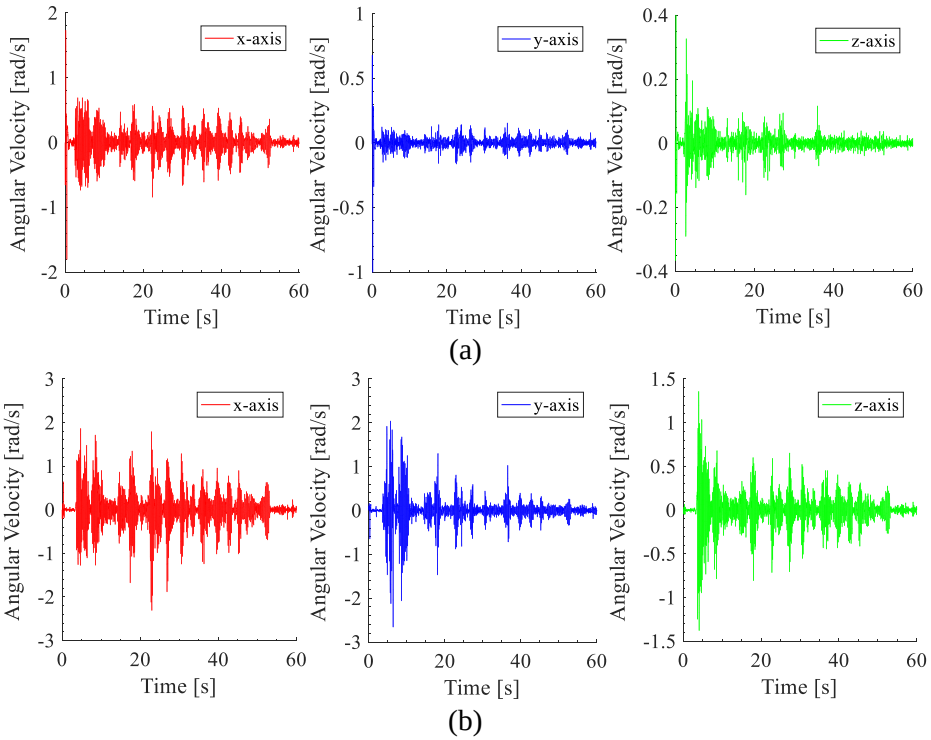

Figure 3.15: IMU x-, y-, and z-axis angular velocity signals measured at the (a) forearm and (b) palm of "Patient 5" for clinical "Task 2"

The PSD of the acceleration and angular velocity signals shown in Figure 3.14 and Figure 3.15, are depicted in Figure 3.16a and Figure 3.16b, respectively. The figures compare the forearm and palm behaviors in the frequency domain. Some forearm signals required amplification for a better comparison as the forearm tremor signals are much smaller than the palm signals. The PSD of acceleration and angular velocity signals for the forearm and palm of "Patient 5" show the same critical peak frequency, which occurs at 5.1 Hz for the 3 axes. The obtained frequency belongs to the PT frequency range 5–12 Hz [16].

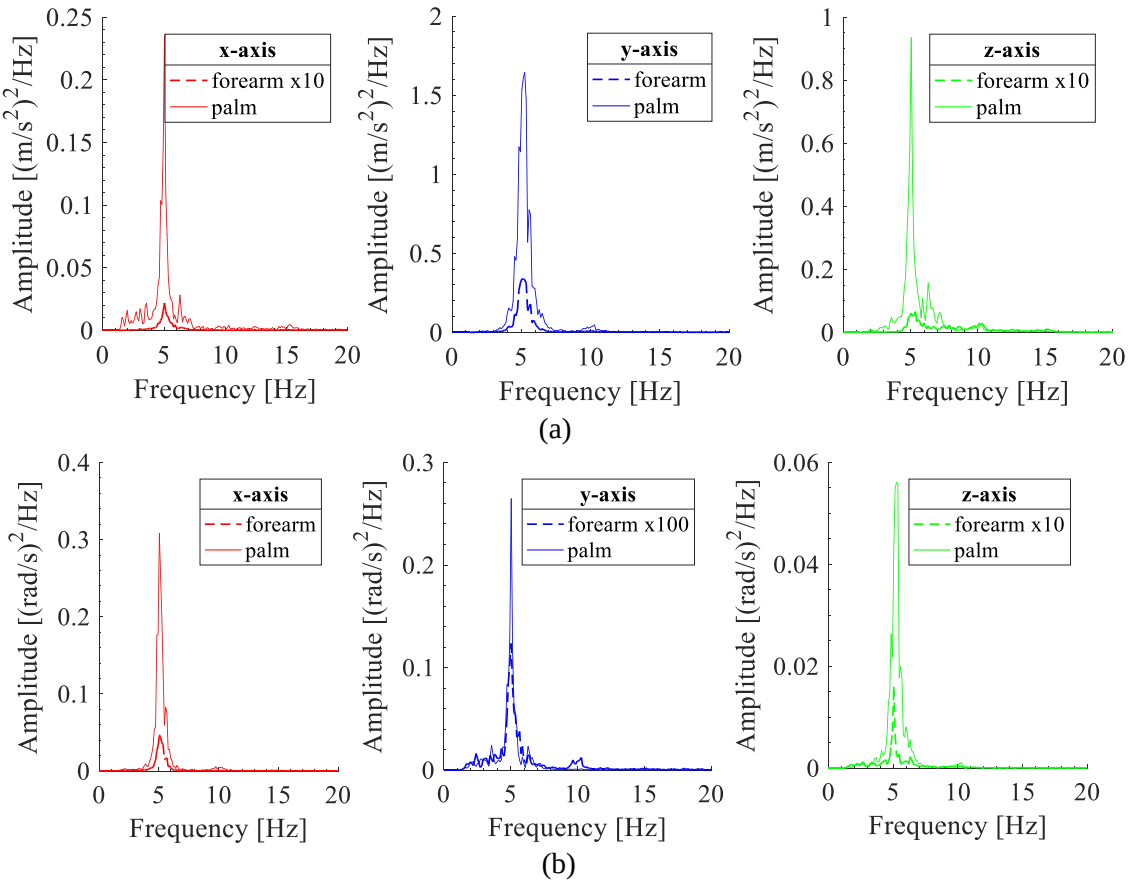

Figure 3.16: PSD of the x-, y-, and z-axis (a) acceleration and (b) angular velocity signals at the forearm and the palm of "Patient 5" for clinical "Task 2"

3.4.2.2. Physiological tremor

The physiological tremor measurements serve to analyze the tremor amplitude levels compared to that of the pathological tremor for the patient. Measurements are carried out for four healthy people ("Healthy 1", "Healthy 2", "Healthy 3", and "Healthy 4") with the same measurement conditions as for "Patient 5". The acceleration and angular velocity signals measured for "Healthy 1" are shown in Figure 3.8 and Figure 3.9.

Figure 3.17 shows the PSD of the y-axis acceleration signals of the four healthy people and of “Patient 5”. It shows that the tremor amplitude level of “Patient 5” is higher than those of the four healthy subjects. The peak amplitude at the forearm of “Patient 5” is 600 times higher than the maximum amplitude level of the healthy participants, while it is 1400 times higher at the palm.

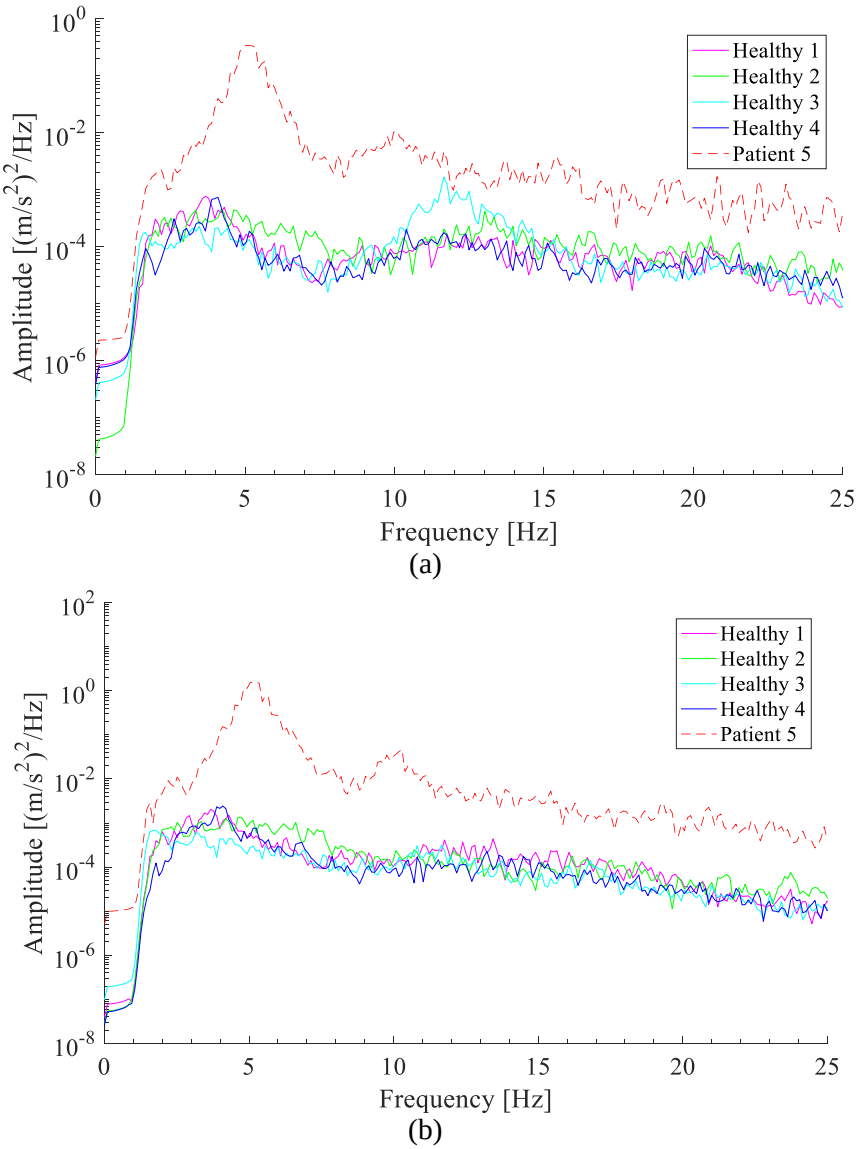

Figure 3.17: PSD of the y-axis acceleration signals at the (a) forearm and (b) palm of the four healthy participants and of “Patient 5”

Figure 3.18 shows the PSD of the y-axis angular velocity of the four healthy people and of “Patient 5”. It shows that the peak amplitude for the forearm of “Patient 5” is 50 times higher than the maximum amplitude level of the healthy participants, while it is 2100 times higher for the palm.

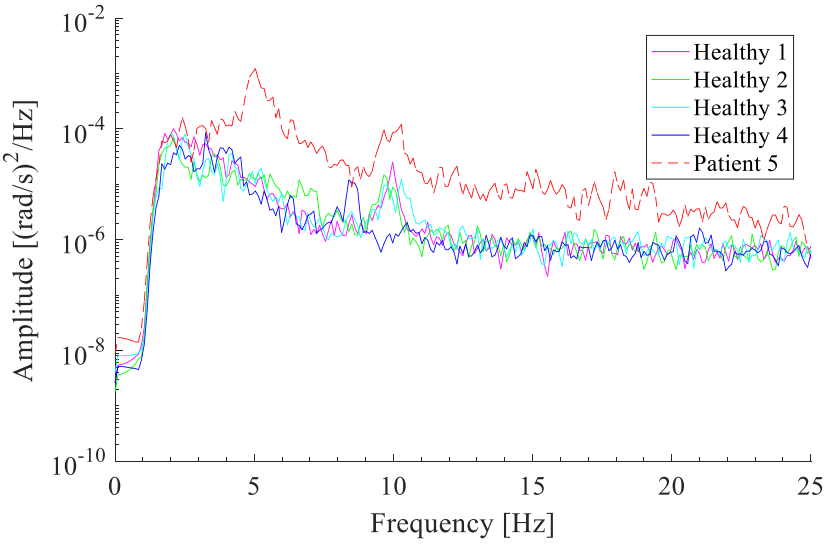

(a)

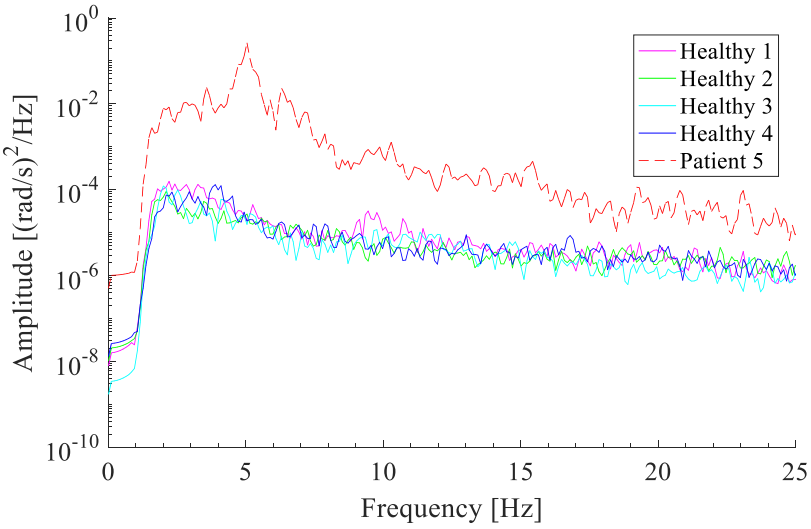

(b)

Figure 3.18: PSD of the y-axis angular velocity signals at the (a) forearm and (b) palm of the four healthy participants and of "Patient 5"

3.5. Tremor results at index finger for patients 1 to 4

3.5.1. Time signal analysis

The amplitudes of acceleration and displacement signals of the tremor are collected for the two postural clinical tests, repeated twice, for four different angular positions within three days.

3.5.1.1. Collected data from acceleration signals

Figure 3.19 presents the x-, y-, and z-axis absolute maximum and minimum tremor's acceleration amplitudes for each measurement for the "Task 1" and "Task 2" hand positions. In the set of measurements done for the patients, the dispersion of the results obtained for "Patient 1" and "Patient 3" is greater than obtained for "Patient 2" and "Patient 4". By comparing the absolute values of the maximum and minimum amplitudes within each measurement, we can deduce that they are not exactly equal. The same observation applies for each consecutive (not just the global maximum and minimum) peak-to-trough of the signals, which are asymmetrical.

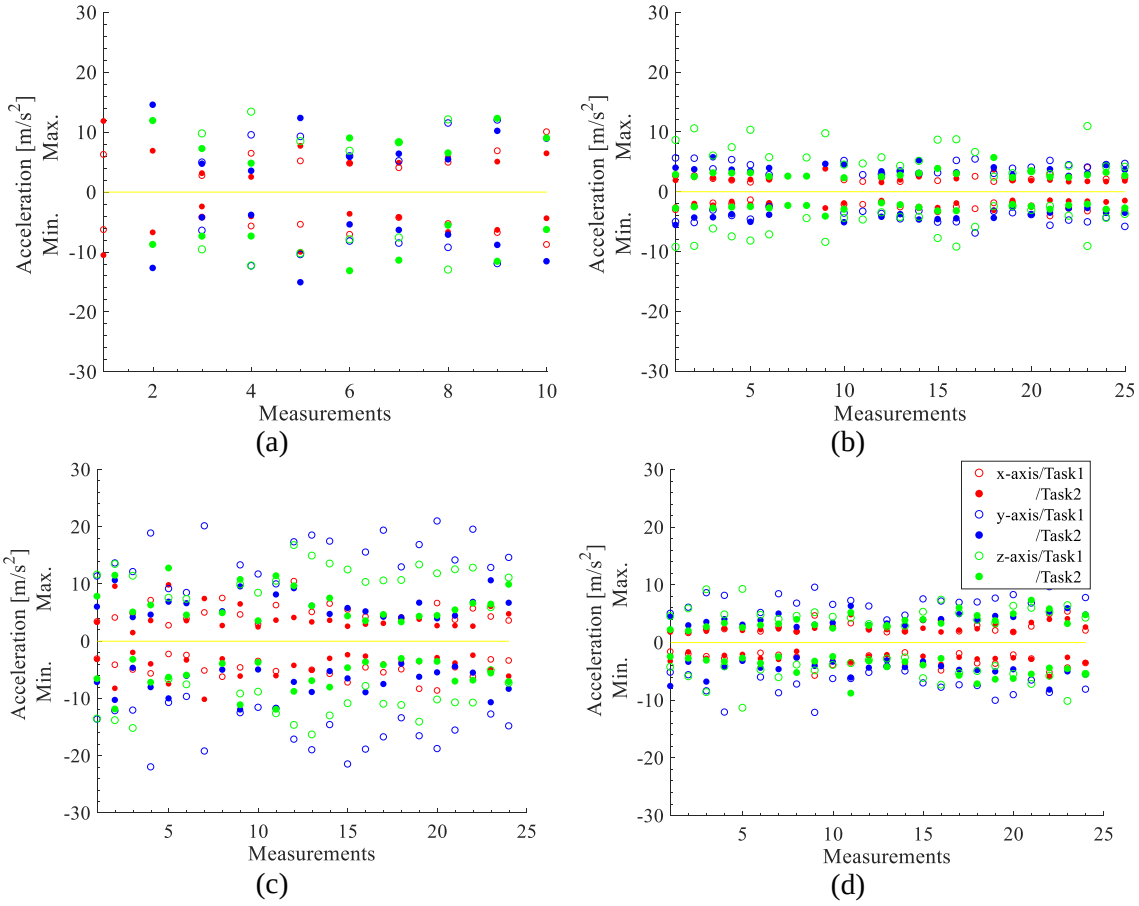

Figure 3.19: Maximum and minimum tremor's acceleration amplitude at the index finger for each measurement done for (a) "Patient 1", (b) "Patient 2", (c) "Patient 3", and (d) "Patient 4"

The acceleration results presented in Figure 3.19 for "Patient 1", "Patient 2", "Patient 3", and "Patient 4" for the two tested postural hand positions are summarized in Table 3.1, Table 3.2, Table 3.3, and Table 3.4, respectively. These tables provide the lowest and highest maximum and minimum (absolute values) acceleration amplitudes among the repeated measurements in the three axes, i.e. the range of variation of the amplitudes above

and below the origin. In addition, the mean and standard deviation (SD) of both highest and lowest amplitudes are calculated.

The acceleration data of "Patient 1" presented in Table 3.1 shows that the tremor amplitude is higher in "Task 2" position than in "Task 1" for the x-, and y-axis, but lower for the z-axis. The "Task 1" and "Task 2" highest amplitudes are presented in the z-axis and y-axis, respectively, with comparable levels.

Table 3.1: Maximum and minimum amplitudes of the acceleration signals at the index finger for "Patient 1"

Acceleration $[m/s^2]$		Patient 1					
		Task 1			Task 2		
		x	y	z	x	y	z
Maximum Amplitude	Lowest	2.7	4.9	6.8	2.5	3.5	4.8
	Highest	10.0	12.0	13.4	11.8	14.5	12.3
	Mean±SD	5.7±3.0	8.3±2.1	9.7±2.5	5.9±2.6	8.0±3.7	8.6±2.6
Minimum Amplitude	Lowest	4.2	6.4	7.6	2.5	3.9	5.6
	Highest	8.8	12.4	13.0	10.6	15.1	13.2
	Mean±SD	6.0±1.4	9.6±2.1	10.1±2.2	6.0±2.7	8.4±4.0	9.0±2.8

The acceleration amplitude for "Patient 2" presented in "Table 3.2" shows that the highest amplitude in "Task 1" for the z-axis is approximately the double of the highest amplitude of "Task 2" that occurs both along the y-, and z-axis. The y-axis amplitude in both tasks are comparable with a mean value around 4 m/s^2.

Table 3.2: Maximum and minimum amplitudes of the acceleration signals at the index finger for "Patient 2"

Acceleration $[m/s^2]$		Patient 2					
		Task 1			Task 2		
		x	y	z	x	y	z
Maximum Amplitude	Lowest	1.8	2.8	2.5	1.5	2.6	2.2
	Highest	4.0	5.6	11.0	4.0	5.7	5.7
	Mean±SD	2.3±0.6	4.2±1.0	6.1±2.6	2.2±0.7	3.8±0.8	3.0±0.7
Minimum Amplitude	Lowest	1.4	2.5	2.4	1.5	2.7	1.9
	Highest	4.1	7.0	9.3	3.2	5.6	4.2
	Mean±SD	2.6±0.6	4.4±1.0	5.7±2.4	2.1±0.5	4.1±0.8	2.7±0.5

"Patient 3" data provided in Table 3.3 show very high tremor amplitudes in comparison to the other patients. The tremor is more significant for "Task 1" than for "Task 2". The y-axis amplitudes and mean values of "Task 1" are the highest among all patients.

Table 3.3: Maximum and minimum amplitudes of the acceleration signals at the index finger for "Patient 3"

Acceleration $[m/s^2]$		Patient 3					
		Task 1			Task 2		
		x	y	z	x	y	z
Maximum Amplitude	Lowest	2.7	8.4	5.9	1.4	3.5	3.3
	Highest	10.4	20.9	16.73	9.8	10.6	12.7
	Mean±SD	5.1±1.8	14.9±3.7	11.3±2.6	4.1±2.1	6.2±2.1	6.7±2.9
Minimum Amplitude	Lowest	2.3	9.7	5.1	2.0	4.0	3.1
	Highest	8.7	22.0	16.3	10.2	12.0	12.0
	Mean±SD	5.0±1.7	15.3±3.5	11.0±3.1	4.5±2.0	7.4±2.4	6.3±2.7

Table 3.4 shows the collected acceleration data for "Patient 4". The acceleration amplitude along y-axis is the highest in "Task 1". The z-axis amplitudes are the highest for "Task 2", but comparable to those along y-axis of this postural task.

Table 3.4: Maximum and minimum amplitudes of the acceleration signals at the index finger for "Patient 4"

Acceleration $[m/s^2]$		Patient 4					
		Task 1			Task 2		
		x	y	z	x	y	z
Maximum Amplitude	Lowest	1.6	3.9	2.7	1.7	2.6	2.0
	Highest	5.3	9.6	9.2	4.8	6.3	7.3
	Mean±SD	2.7±1.1	7.0±1.5	5.1±1.7	2.5±0.8	4.0±1.0	3.8±1.3
Minimum Amplitude	Lowest	1.6	4.2	2.6	1.6	2.7	2.5
	Highest	5.8	12.2	11.4	6.0	8.2	8.8
	Mean±SD	3.1±1.1	7.5±2.1	5.5±2.1	2.9±0.9	4.7±1.4	4.3±1.7

3.5.1.2. Collected data from displacement signal

Figure 3.20 presents the x-, y-, and z-axis maximum and minimum tremor's displacement amplitudes for each measurement for the "Task 1" and "Task 2" hand positions, obtained after a double integration of the measured acceleration signals. A new

displacement amplitude range is obtained while the measurements are repeated. The displacement amplitudes range for "Patient 1" and "Patient 3", along the three axes and for both tasks, varies under an upper limit of about 2 cm. Results for those two patients are more dispersed. "Patient 2" and "Patient 4" displacement amplitudes range of the index finger tremor is less than 1 cm.

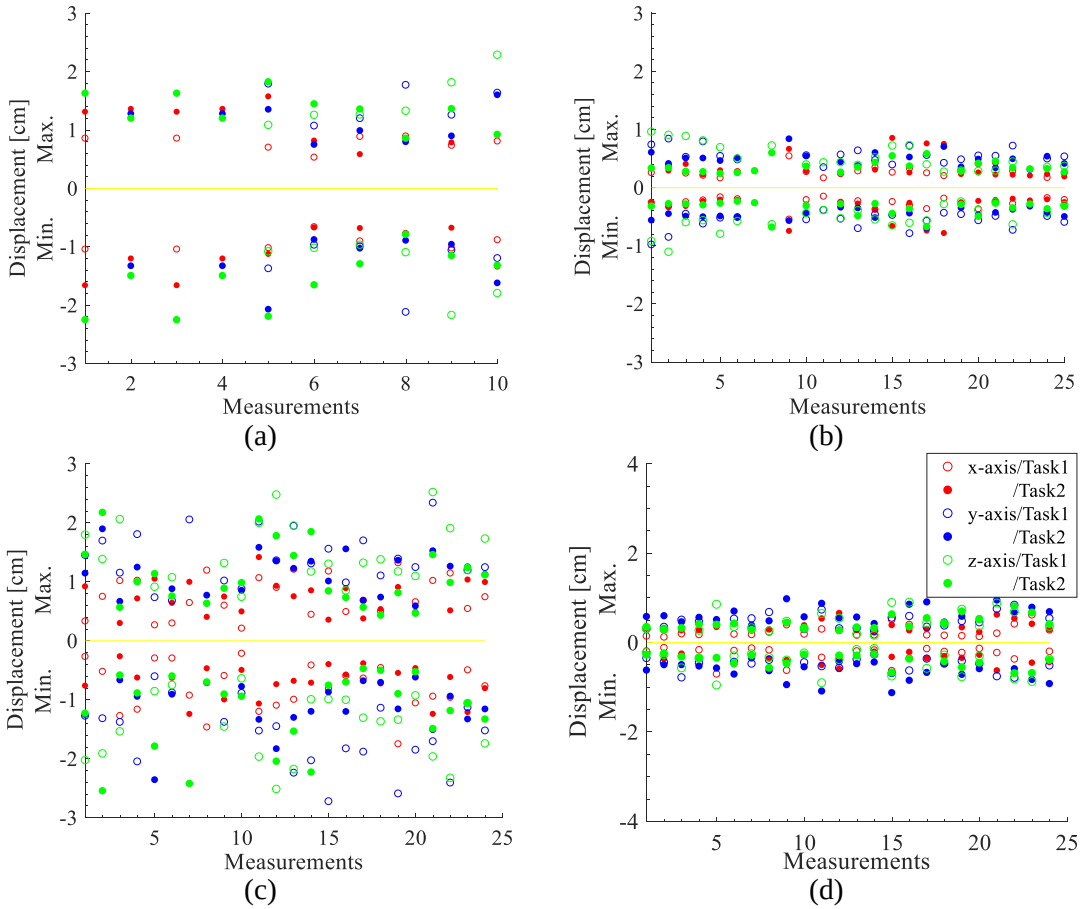

Figure 3.20: Maximum and minimum tremor's displacement amplitudes at the index finger for each measurement done for (a) "Patient 1", (b) "Patient 2", (c) "Patient 3", and (d) "Patient 4"

The results presented in Figure 3.20 for "Patient 1", "Patient 2", "Patient 3", and "Patient 4" for the two tested postural hand positions are summarized in Table 3.5, Table 3.6, Table 3.7, and Table 3.8, respectively. These tables provide the highest and lowest maximum and minimum (absolute values) displacement amplitudes among the repeated measurements in the three axes, i.e. the range of variation of the amplitudes above and below the origin. In addition, the mean and SD of the obtained results of both highest and lowest amplitudes are calculated.

Table 3.5 shows the displacement amplitude data for "Patient 1". The mean value of the displacement amplitudes in the three axes for both tasks lies between 0.8–1.6 cm.

Table 3.5: Maximum and minimum amplitudes of the displacement signals at the index finger for "Patient 1"

Displacement [cm]		Patient 1					
		Task 1			Task 2		
		x	y	z	x	y	z
Maximum Amplitude	Lowest	0.5	1.1	1.1	0.6	0.7	0.9
	Highest	0.9	1.8	2.3	1.6	1.6	1.8
	Mean±SD	0.8±0.1	1.5±0.3	1.5±0.5	1.1±0.3	1.1±0.3	1.3±0.3
Minimum Amplitude	Lowest	0.7	1.0	1.0	0.7	0.9	0.8
	Highest	1.0	2.1	2.2	1.7	2.1	2.3
	Mean±SD	1.0±0.1	1.3±0.4	1.4±0.5	1.1±0.4	1.3±0.4	1.6±0.5

Table 3.6 reflecting the results of "Patient 2" shows that all the average values of the displacement amplitudes are close to 0.5 cm. "Task 1" and "Task 2" tremor amplitude levels are very close to each other. All the amplitude mean values range between 0.3–0.6 cm.

Table 3.6: Maximum and minimum amplitudes of the displacement signals at the index finger for "Patient 2"

Displacement [cm]		Patient 2					
		Task 1			Task 2		
		x	y	z	x	y	z
Maximum Amplitude	Lowest	0.2	0.3	0.3	0.2	0.3	0.2
	Highest	0.5	0.8	1.0	0.8	0.8	0.6
	Mean±SD	0.3±0.1	0.6±0.1	0.5±0.2	0.6±0.2	0.5±0.1	0.4±0.1
Minimum Amplitude	Lowest	0.2	0.4	0.2	0.2	0.3	0.2
	Highest	0.5	1.0	1.1	0.8	0.7	0.7
	Mean±SD	0.3±0.1	0.6±0.2	0.5±0.2	0.3±0.2	0.5±0.1	0.4±0.1

In Table 3.7, the tremor displacement amplitudes for "Patient 3" are presented. The displacement amplitudes for "Patient 3" are higher than those of the other patients. Tremor amplitudes presented in "Task 1" higher than in "Task 2". The highest displacement amplitude value is 2.7 cm ("Task 1" in the y-axis). All the amplitude mean values range between 0.7–1.6 cm.

Table 3.7: Maximum and minimum amplitudes of the displacement signals at the index finger for "Patient 3"

Displacement $[cm]$		Patient 3					
		Task 1			Task 2		
		x	y	z	x	y	z
Maximum Amplitude	Lowest	0.2	0.7	0.7	0.3	0.6	0.4
	Highest	1.3	2.3	2.5	1.4	1.9	2.1
	Mean±SD	0.8±0.3	1.4±0.4	1.5±0.5	0.7±0.3	1.1±0.4	1.1±0.5
Minimum Amplitude	Lowest	0.2	0.6	0.6	0.3	0.6	0.5
	Highest	1.8	2.7	2.5	1.2	2.4	2.5
	Mean±SD	0.8±0.4	1.6±0.6	1.5±0.6	0.7±0.3	1.1±0.4	1.2±0.6

The displacement amplitudes for "Patient 4" are presented in Table 3.8. The obtained amplitudes values are very close to each other and are under 1.1 cm . The mean values ranges between 0.3–0.7 cm.

Table 3.8: Maximum and minimum amplitudes of the displacement signals at the index finger for "Patient 4"

Displacement $[cm]$		Patient 4					
		Task 1			Task 2		
		x	y	z	x	y	z
Maximum Amplitude	Lowest	0.1	0.3	0.2	0.2	0.4	0.3
	Highest	0.6	0.8	0.9	0.7	1.0	0.8
	Mean±SD	0.2±0.1	0.5±0.2	0.5±0.2	0.4±0.1	0.6±0.2	0.4±0.2
Minimum Amplitude	Lowest	0.1	0.3	0.1	0.2	0.4	0.2
	Highest	0.7	0.8	1.0	0.7	1.1	0.7
	Mean±SD	0.3±0.2	0.5±0.1	0.5±0.3	0.4±0.1	0.7±0.2	0.4±0.1

3.5.2. PSD analysis

The PSD of the acceleration signals are used to analyze the tremor behavior in the frequency domain. The tremor behavior of "Patient 1" is excluded from this analysis, since just few measurements are performed for this patient. In addition, the PSD of the measured signals for this patient provides unclear PSD information. Figure 3.21 shows the dominant peak's amplitude and its corresponding frequency obtained from the tremor measurements for the two clinical postural tasks and the three presented patients.

For “Patient 2”, both tasks show comparable dominant peak amplitudes, while dominant peaks for “Task 1” occur in a lower frequency range than for “Task 2”. “Patient 3” has very high peak amplitudes which are concentrated in a narrow range of frequencies. This frequency slightly changes for the different measurements done for “Task1”. The PT doesn’t affect “Patient 3” in “Task 2”, where no critical peaks are presented for these measurements. PSD data for “Patient 4” show that the tremor behavior is more significant for “Task 1”, and that the frequencies obtained for “Task 2” are in a higher frequency range. Figure 3.21b depicted the critical peaks amplitude and frequency distribution for the three presented patients and the tested postural positions. Each patient has different level of tremor amplitude. The peaks frequencies lie within a specific frequency range.

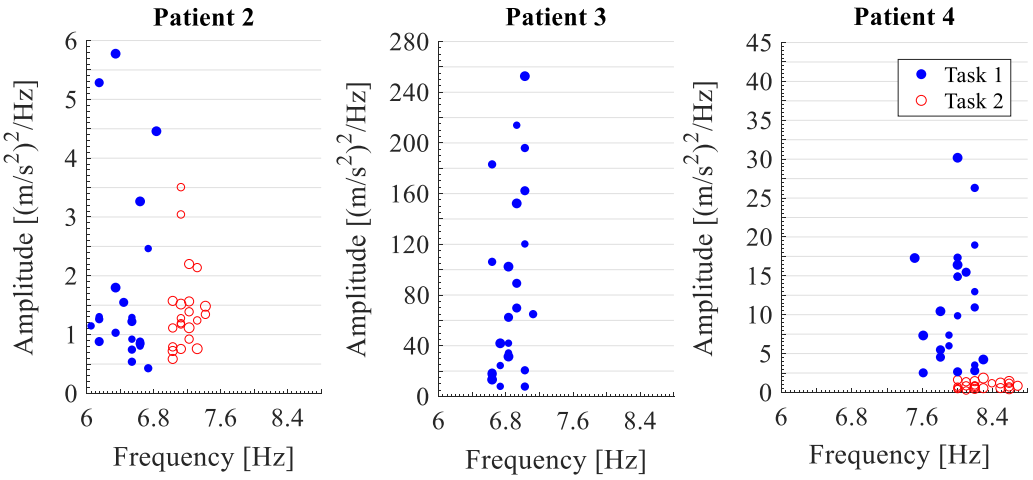

(a)

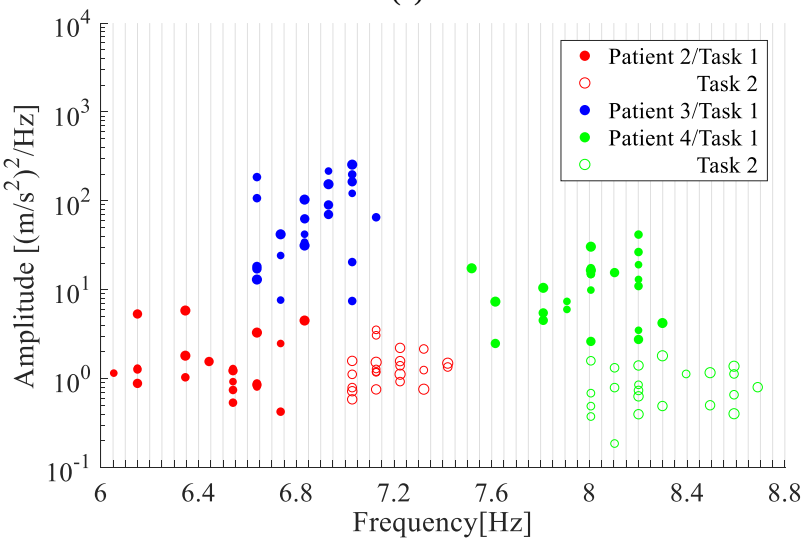

(b)

Figure 3.21: Dominant peak’s amplitude and its corresponding frequency for all datasets of (a) each patient and (b) all the patients for the two clinical tasks (● for “Task 1” and ○ for “Task 2”)

Table 3.9 summarizes the critical peaks amplitude and frequency distribution shown in Figure 3.21. The ranges of the amplitude and frequency values and their means with the SD are listed. The hand postural tremor frequencies for these three patients together are between 6.2–8.2 Hz for "Task 1", and 7.0–8.6 Hz for "Task 2". All the obtained frequencies lies within the range of PT [16]. "Task 1" seems to induce lower frequency ranges with higher amplitude ranges. "Patient 3" doesn't have PT in the "Task 2" hand position. "Patient 2" and "Patient 3" have PT with comparable frequency range in "Task 1" position, however, their tremor amplitudes are distinct. So, the frequency range alone can't indicate the severity of the patient's tremor. For a single patient, a maximum shift of 0.6 Hz in the critical frequency ranges is observed.

Figure 3.22 presents the occurrences of critical frequency of "Patient 2", "Patient 3", and "Patient 4" presented in Figure 3.21 and summarized by frequency ranges in Table 3.9.

Table 3.9: Dominant peaks frequency and amplitude statistical results for each patient for different clinical task tests

Data	Frequency $[Hz]$		Amplitude $[(m/s^2)^2/Hz]$	
	Range	Mean ± SD	Range	Mean ± SD
Patient 2 (Task 1)	6.2–6.7	6.5±0.2	0.4–3.3	1.2±0.7
Patient 2 (Task 2)	7.0–7.4	7.2±0.1	0.6–2.2	1.2±0.4
Patient 3 (Task 1)	6.6–7.0	6.8±0.1	7.4–213.6	77.1±65.3
Patient 4 (Task 1)	7.6–8.2	8.0±0.2	2.5–18.9	9.7±5.6
Patient 4 (Task 2)	8.0–8.6	8.3±0.2	0.18–1.8	0.6±0.4

Knowing the damping ratio of the muscles can be useful for an analytical model of the muscle's and its representation in the frequency domain. The damping ratio (ζ) is determined for the critical peaks of the PSD of the measured ECR and FCR signals. damping ratio is usually identified using the half-power bandwidth method for the frequency response function [122,123], however, it can be applied for the PSD of the signals [124]. The obtained results are represented in Figure 3.23. It shows that the damping ratio obtained from ECR and FCR muscles critical peaks varies between 1.5–3.5 %. The highest occurrence of damping ratio for ECR and FCR muscles are for values between 1.88–2.26 % and 1.9–2.3 %, respectively. The damping ratio of both muscles together has a mean and SD of 2.4±0.47%.

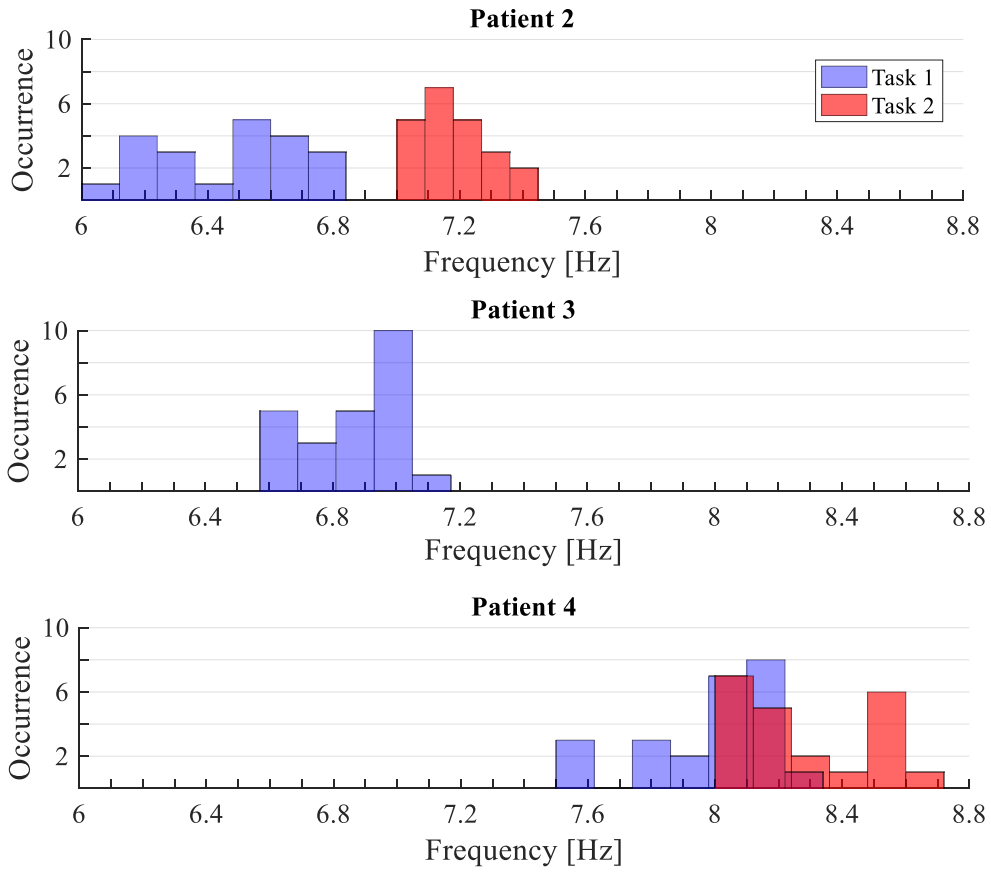

Figure 3.22: Number of occurrences of the critical frequency for two clinical position tests and three patients

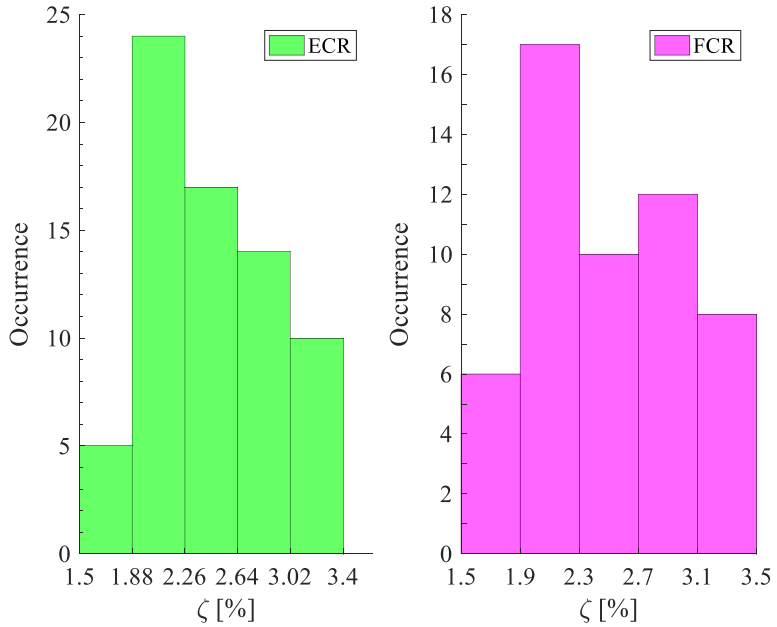

Figure 3.23: Number of occurrence for the calculated percentage of damping ratio for the critical peaks of the ECR and FCR muscles of "Patient 2", "Patient 3", and "Patient 4"

3.6. Tremor results at forearm and palm for healthy people and "Patient 5"

The results of the processed IMU measurements, the acceleration and angular velocity signals, at the forearm and the palm of the four healthy participants are used to provide the amplitude ranges for each and compare them to that of "Patient 5". Tremor acceleration, displacement, and angular displacement information are obtained from these measurements, in addition to an analysis of the physiological tremor behavior.

3.6.1. Time response analysis

Figure 3.24 compares the maximum and minimum acceleration amplitudes of the tremor for four healthy people, obtained with IMU measurements at their forearm and palm, and for the PT affected participant ("Patient 5"). Table 3.10 provides the highest maximum value (absolute maximum) and lowest minimum value (absolute minimum) for the data presented in Figure 3.24. In addition, Table 3.10 includes the calculated mean and SD for the highest maximum and lowest minimum (as absolute value). The maximum acceleration amplitudes of the healthy participants along the three axes are 0.5 m/s^2 for the forearm and the palm, which is approximately the minimum acceleration amplitude for "Patient 5". The maximum amplitude of the patient reaches 2.7 m/s^2 at the forearm and 7.0 m/s^2 at the palm along the y-axis.

The displacement results (double integrated) are provided by Figure 3.25 and Table 3.11. The highest maximum displacement value of the healthy participants along the three axes is 1.2 cm. However, the maximum value of "Patient 5" reaches 4.1 cm for the forearm and 7.2 mm for the palm in the y-axis.

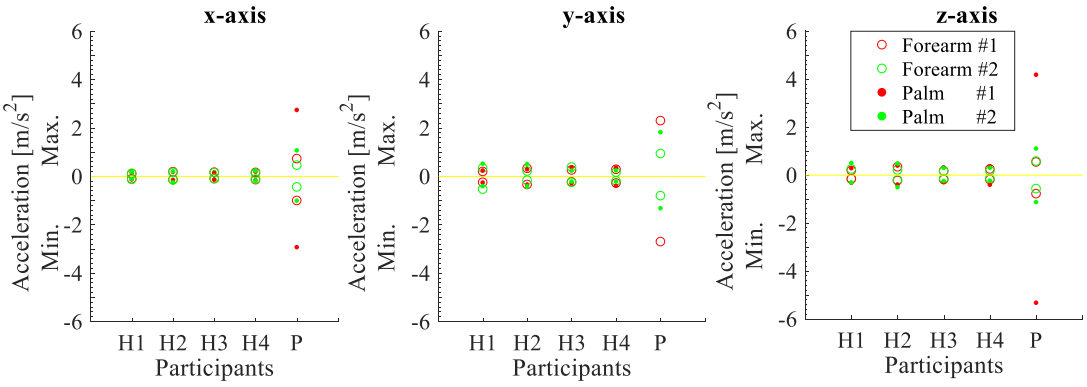

Figure 3.24: Maximum and minimum acceleration amplitudes along x-, y-, and z-axis of the tremor at the forearm and the palm of healthy people and a patient (H1, H2, H3, and H4 refer to "Healthy 1", "Healthy 2", "Healthy 3", and "Healthy 4", and P for "Patient 5")

Table 3.10: Absolute maximum and absolute minimum acceleration amplitudes at the forearm and the palm of healthy people and of "Patient 5"

Acceleration $[m/s^2]$		Forearm			Palm		
		x	y	z	x	y	z
Four Healthy	Maximum	0.2	0.5	0.3	0.3	0.5	0.5
	Minimum	-0.1	-0.2	-0.2	-0.1	-0.2	-0.3
	Mean±SD	0.1±0.0	0.3±0.1	0.2±0.1	0.2±0.0	0.3±0.1	0.4±0.1
"Patient 5"	Maximum	1.0	2.7	0.8	2.9	7.0	5.3
	Minimum	0.5	0.8	0.5	1.0	1.3	1.1
	Mean±SD	0.7±0.3	1.7±1.0	0.6±0.1	1.9±1.0	4.2±3.1	2.9±2.2

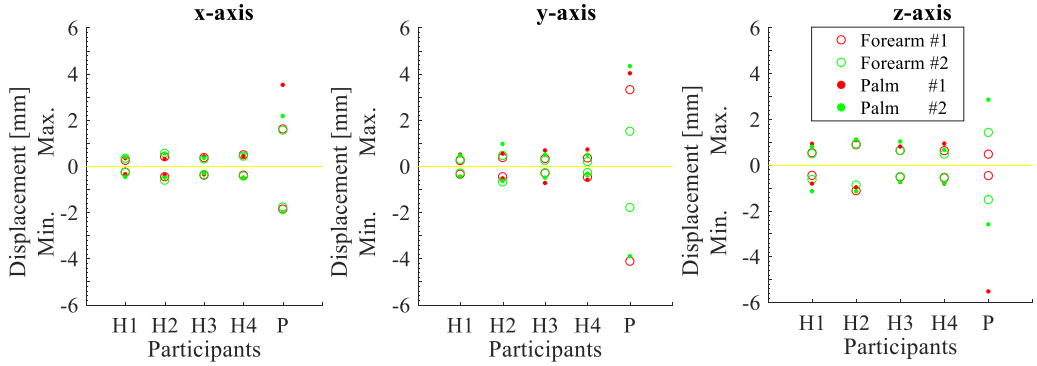

Figure 3.25: Maximum and minimum displacement amplitudes along x-, y-, and z-axis of the tremor at the forearm and the palm of healthy people and a patient (H1, H2, H3, and H4 refer to "Healthy 1", "Healthy 2", "Healthy 3", and "Healthy 4", and P for "Patient 5")

Table 3.11: Absolute maximum and absolute minimum displacement amplitudes at the forearm and the palm of healthy people and of "Patient 5"

Displacement $[mm]$		Forearm			Palm		
		x	y	z	x	y	z
Four Healthy	Maximum	0.6	0.7	1.1	0.6	1.0	1.2
	Minimum	-0.3	-0.2	-0.5	-0.3	-0.3	-0.7
	Mean±SD	0.4±0.1	0.4±0.1	0.7±0.2	0.4±0.1	0.6±0.1	0.9±0.2
"Patient 5"	Maximum	1.9	4.1	1.5	6.4	7.2	6.1
	Minimum	-1.6	-1.5	-0.5	-2.0	-3.9	-2.6
	Mean±SD	1.7±0.1	2.7±1.2	1.0±0.6	3.5±2.0	4.9±1.6	4.3±1.8

The results for the maximum and minimum angular displacement amplitudes of the tremor are provided by Figure 3.26 and Table 3.12. The angular displacement amplitudes

for the healthy people ranges between 0.1°–0.3° for the forearm and the palm and between 0.3°–4.6° for "Patient 5".

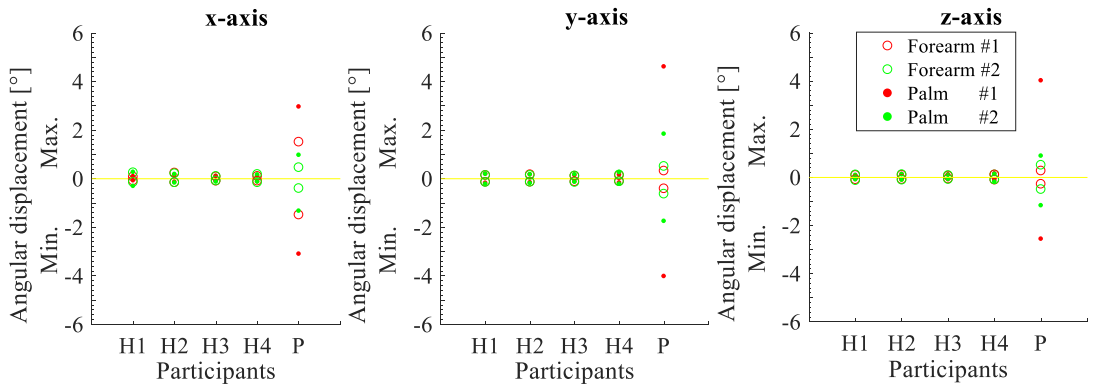

Figure 3.26: Maximum and minimum angular displacement amplitudes along x-, y-, and z-axis of the tremor at the forearm and the palm of healthy people and a patient (H1, H2, H3, and H4 refer to "Healthy 1", "Healthy 2", "Healthy 3", and "Healthy 4", and P for "Patient 5")

Table 3.12: Absolute maximum and absolute minimum angular displacement amplitudes at the forearm and the palm of healthy people and of "Patient 5"

Angular Displacement [°]		Forearm			Palm		
		x	y	z	x	y	z
Four Healthy	Maximum	0.3	0.2	0.1	0.3	0.3	0.2
	Minimum	-0.1	-0.1	-0.1	-0.1	-0.1	-0.1
	Mean±SD	0.1±0.1	0.1±0.0	0.1±0.0	0.1±0.1	0.2±0.0	0.1±0.0
"Patient 5"	Maximum	1.5	0.6	0.5	3.1	4.6	4.0
	Minimum	-0.4	-0.3	-0.3	-1.0	-1.8	-0.9
	Mean±SD	1.0±0.6	0.5±0.1	0.4±0.1	2.1±1.1	3.1±1.5	2.1±1.4

3.6.2. PSD analysis

The PSD of the acceleration signals measured by IMUs at the forearm and the palm simultaneously are shown in Figure 3.27. The involuntary tremor critical peak exists in some the healthy people, and is referred as the physiological tremor. "Healthy 1" has dominant peak at 9.45 Hz for the response of the forearm. At the palm, the critical peak of "Healthy 1", "Healthy 2", "Healthy 3", and "Healthy 4" occurs at 9.8 Hz, 9.7 Hz, 10.3 Hz and 8.4 Hz, respectively. Their tremor amplitude is very low, especially when compared to the pathological tremor amplitude as discussed for Figure 3.17. Figure 3.27 confirms that physiological tremor peak can occur between 8–12 Hz with a very low tremor amplitude [125].

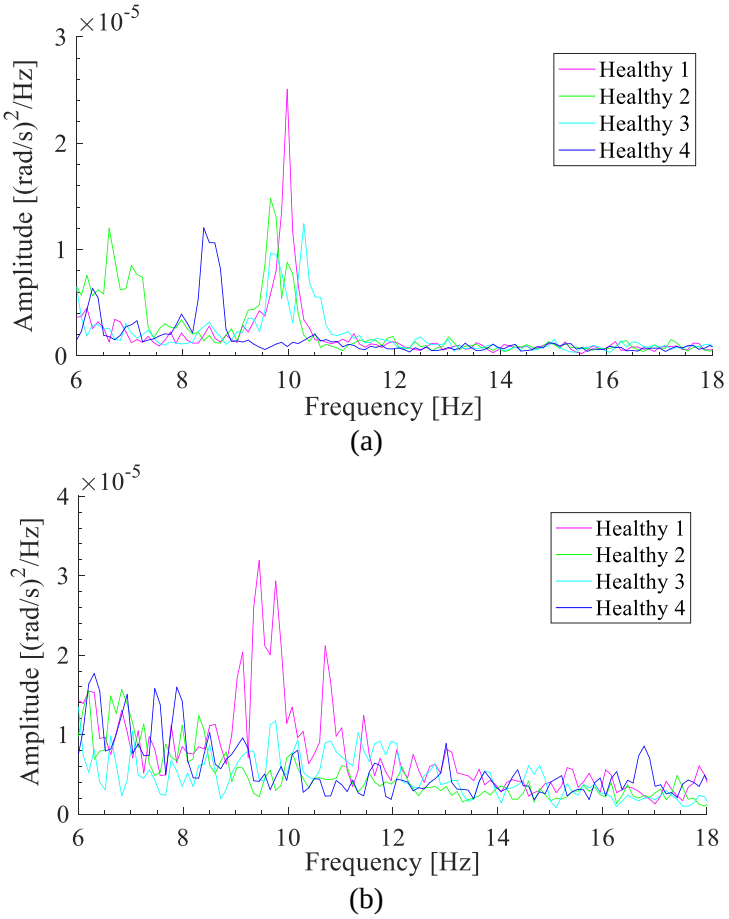

Figure 3.27: PSD of the Physiological tremor y-axis angular velocity measured by the IMU at the (a) forearm and (b) palm

3.7. Conclusion

A total of 166 tremor datasets are obtained for the four recruited patients. Each contains 3-axis acceleration signals at the index finger, and ECR and FCR forearm muscles signals for two different hand posture tasks. The tremor signals analysis indicates that the dominant peak present in the PSD of the acceleration measurements at the finger occurs at the same frequency as the operating frequency of the muscles, which is different, a priori, from the natural frequency of the upper limb. PT critical frequency for several measurements repeated for the four patients ranges between 6.2–8.2 Hz for extended arms while palms are raised, and 7.0–8.6 Hz for bent elbows while dorsum are facing each other. Each patient has its dominant frequency that changes within a 0.6 Hz range for the two afore mentioned hand positions. The value of the critical frequency doesn't reflect the severity level of the tremor of a patient as patients can have the same critical frequency but a different tremor amplitude level. The study also provides data related to the tremor acceleration and displacement amplitudes of the index finger obtained from each measurement repeated along three days. In addition, IMU measurements are repeated twice

to obtain the 3-axis acceleration and 3-axis angular velocity signals at the palm and forearm of four healthy people and a PT patient. The same dominant frequency obtained from the measurements at the forearm are present in the signals of the palm. The physiological tremor frequency of the four healthy participants ranges between 8.4–10.3 Hz. Besides, the difference in the level of tremor amplitude between the healthy people and the affected patient is clearly highlighted.

CHAPTER 4. DESIGN OF THE UPPER LIMB WITH OPTIMIZED TMDS

THIS chapter presents a biodynamic model of the upper limb that provides the behavior in flexion-extension of the proximal joints of the musculoskeletal system. The derivation of the equations of motion of the 3DOF model using the Lagrange formulation is presented. Then, the governing equations of the global system with an addition of multiple TMDs at the forearm or the palm segment are established. Two types of TMD are modeled: the pendulum and the cantilever-type. The fundamental frequency of the cantilever-type TMD is derived using Dunkerley's semi-analytical formula. An optimization strategy is proposed, taking into account the fact that the applied force contains driving frequencies distinct from the natural frequencies of the system, and its effect tested on a 1DOF classical system. The response of the 3DOF dynamic hand model is studied when it is excited by an analytical representation of the measured activity of the muscles of an ET patient, provided by EMG, or directly by the measured activity of the muscles. The TMD located at the palm segment is optimized to reduce the maximum angular displacement of the wrist joint. A parametric study is carried out to test the effect of TMD's position along the hand segment, the number of TMDs, and the TMD mass ratio on the reduction of the angular displacement.

Plan of Chapter 4

4.1. Introduction

This chapter proposes a musculoskeletal dynamic model of human upper limb used to design the tremor absorber device before being tested. Based on previous arm models [61,67,70] and valuable suggestions or assumptions, a mathematical model is built. Upper limbs positioned in the vertical plane can reflect most of our daily tasks. So, a 3DOF system is modeled in the vertical plane to reflect the flexion-extension planar motion at the proximal joints. Nevertheless, the dynamic modeling for hand-arm system in the vertical plane is not easily derived, neither solved. A MATLAB program is done to solve the non-linear dynamic equations. Then, the passive absorber is added in order to test its ability in reducing the response of the pathological tremor measured using the EMG signals. The optimization of the TMD is done to reach the best reduction of the flexion-extension motion in the wrist joint linearized system. The optimized TMD is tested when attached to the forearm and the palm segments. An analytical formulation is proposed to model the behavior of the muscle's signals in the frequency domain. The measured muscular signal of an ET patient is used as the excitation of the upper limb model. Finally, parametric study of the TMD is done to test the TMD performance for different number of TMD, positions along the segment, and mass ratios. The numerical design of the passive TMD is improved in order to operate even if the tremor frequency of the patient experiences some changes.

4.2. Upper limb model build-up

The modeled hand-arm system is described as a three-link system in the vertical plane consisting of the upper arm, forearm, and palm reflecting the flexion-extension angular displacement (as in Figure 2.12) at the shoulder, elbow, and wrist joints, respectively. The musculoskeletal model considers the skeletal and muscle dynamics. Tremor is produced by the passive muscles torques, from the viscoelastic behavior of its soft tissues [72], and the active torques generated by the muscles activity [61]. The modeled system is represented in Figure 4.1, where θ_i is the angular displacement, l_i the arm length, r_i position of the link's centroid, and m_i the mass concentrated at the centroid of the segment i, such that i =1, 2, and 3 represents the upper-arm, forearm, and the palm, respectively. k_i and c_i represents the stiffness and damper passive elements of the muscles, such that i =1, 2, and 3 refers to the shoulder, elbow, and wrist joints, respectively. The skeletal dynamic model is an extension of the model proposed by Jackson et al. [61] (also presented by Flanagan et al. [63] and Corradini et al. [64]) and Hirashima [70], by adding a separated palm link, to raise up from the 2DOF to a 3DOF model.

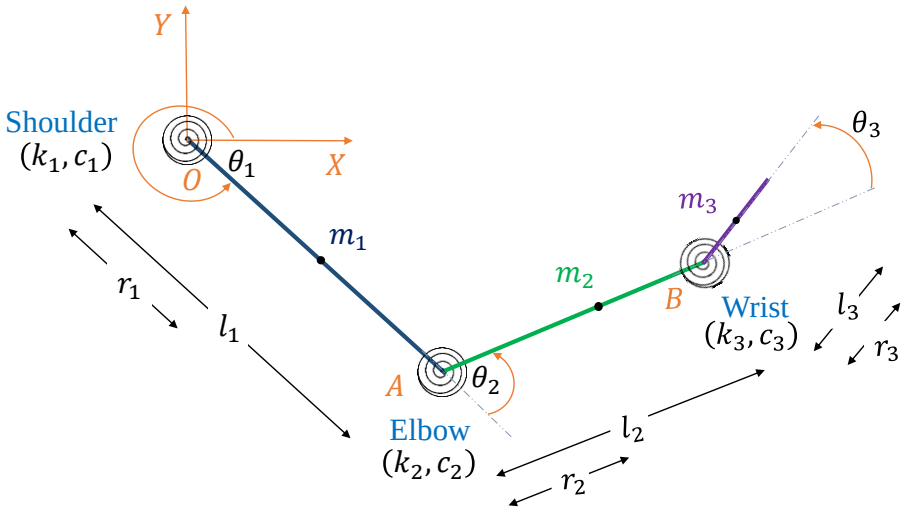

Figure 4.1: Biodynamic model of the upper limb in the vertical plane

The parameters used for the 3DOF system are listed in Table 4.1, represents the length and density of the hand-arms, and the position of centroid from the proximal joints which can be calculated as a percentage of the corresponding segment. These parameters were determined experimentally by Harless [126,127], who was the first to use the immersion method which allows the determination of the segments mass and centroid. The parameters determined by Harless [127] were directly used as a reference to size up the body segments parameters by several researchers [128-130], or used indirectly, by referring to some existing research works which were in fact based on the same parameters, such as in [131,132].

Table 4.1: Hand-arm parameters determined by Harless [127]

Right Hand	Length (cm)		Density (kg/m^3)		Centroid (m)	
Upper arm	l_1	36.4	D_1	1088.0	r_1	$0.427l_1$
Forearm	l_2	29.9	D_2	1108.6	r_2	$0.417l_2$
Palm	l_3	20.3	D_3	1112.6	r_3	$0.361l_3$

The parameters of in Table 4.1 are used to find the geometrical parameters of each segment, where the details are included in [133]. The system is pinned to the fixed trunk by shoulder joint. Hand segments are interconnected by a single DOF shoulder (pivot), elbow (hinge), and wrist (saddle) frictionless joints, having fixed axis of rotation [53-55]. The density of each segment is considered to be constant [134], i.e. the mass is uniformly distributed along each segment. The upper-arm, ulna, and radius are modeled as truncated cones, where the largest radius starts at the proximal and decreases gradually till reaching the distal end of each segment [135]. Using this geometry and the collected parameters, the

masses and mass moments of inertia of each segment are then calculated (Table 4.2). The obtained values lies within the range obtained experimentally in [127,130,135-138].

Table 4.2: Calculated hand arm parameters

Right Hand	Upper Arm		Forearm		Palm	
Mass (cm)	m_1	2.07	m_2	1.16	m_3	0.54
Inertia $(g.m^2/rad)$	I_1	55.67	I_2	19.00	I_3	1.28

4.2.1. Derivation of governing equations

In order to derive the equations of motion representing the behavior of the upper limbs, the kinematics of the system is determined. The human is not considered to be moving (fixed whole body centroid), so the modeled shoulder joint has zero translational velocity (v_0):

$$\vec{v}_0 = \vec{0} \tag{4.1}$$

This leads to a zero acceleration of the shoulder joint (no locomotion). The velocities at the centroid of the upper arm (v_1), forearm (v_2), and palm (v_3) are derived by taking into account the Coriolis effect resulting from the rotation of the reference frames [139]:

$$\vec{v}_1 = \vec{\dot{\theta}}_1 \times \vec{r}_1 \tag{4.2}$$

$$\vec{v}_2 = \vec{\dot{\theta}}_1 \times \vec{l}_1 + \left(\vec{\dot{\theta}}_1 + \vec{\dot{\theta}}_2\right) \times \vec{r}_2 \tag{4.3}$$

$$\vec{v}_3 = \vec{\dot{\theta}}_1 \times \vec{l}_1 + \left(\vec{\dot{\theta}}_1 + \vec{\dot{\theta}}_2\right) \times \vec{l}_2 + \left(\vec{\dot{\theta}}_1 + \vec{\dot{\theta}}_2 + \vec{\dot{\theta}}_3\right) \times \vec{r}_3 \tag{4.4}$$

where, $\dot{\theta}$ is the angular velocity, considered as positive counter-clockwise (CCW). The 1, 2, and 3 indices are related to the upper arm, forearm, and palm, respectively.

The Lagrange formulation is used to determine the equations of motion for the system modeled as a lumped parameter system. Since the system is non-conservative, the frictional moment is added and considered within the Rayleigh dissipation function [140]. It assumes that the damping coefficient is proportional to the velocity. The Lagrangian of a system, L, is defined by:

$$L = T - U \tag{4.5}$$

where, T and U are the kinetic and potential energies. Equation (4.5) is used to determine the dynamics of the system using the following equation:

$$\frac{d}{dt}\left(\frac{\partial L}{\partial \dot{q}_i}\right) - \frac{\partial L}{\partial q_i} + \frac{\partial \mathcal{R}}{\partial \dot{q}_i} = Q_i \quad ; \quad \mathcal{R} = \frac{1}{2} c \dot{q}_i^2 \tag{4.6}$$

where, q is the vector of the generalized coordinates of the system, i.e. the flexion-extension angular displacement vector $\theta = \{\theta_1 \quad ... \quad \theta_n\}^T$, where n is the number of DOF of the system. $\mathcal{R}$ is the Rayleigh dissipation function due to damping. Q_i is the generalized conservative moments.

By substituting $i = 1, 2,$ and 3 into (4.6), the governing equations of motion of the upper arm, forearm, and palm segments are obtained:

$$\frac{d}{dt}\left(\frac{\partial L}{\partial \dot{\theta}_1}\right) - \frac{\partial L}{\partial \theta_1} + \frac{\partial \mathcal{R}}{\partial \dot{\theta}_1} = Q_1 \tag{4.7}$$

$$\frac{d}{dt}\left(\frac{\partial L}{\partial \dot{\theta}_2}\right) - \frac{\partial L}{\partial \theta_2} + \frac{\partial \mathcal{R}}{\partial \dot{\theta}_2} = Q_2 \tag{4.8}$$

$$\frac{d}{dt}\left(\frac{\partial L}{\partial \dot{\theta}_3}\right) - \frac{\partial L}{\partial \theta_3} + \frac{\partial \mathcal{R}}{\partial \dot{\theta}_3} = Q_3 \tag{4.9}$$

The kinetic energy T, potential energy U, and Rayleigh dissipation function $\mathcal{R}$ for the system modeled in Figure 4.1, are respectively derived as:

$$\begin{aligned} T = &\left[\frac{1}{2} I_1 \dot{\theta}_1^2 + \frac{1}{2} m_1 v_1^2\right] + \left[\frac{1}{2} I_2 \left(\dot{\theta}_1 + \dot{\theta}_2\right)^2 + \frac{1}{2} m_2 v_2^2\right] \\ &+ \left[\frac{1}{2} I_3 \left(\dot{\theta}_1 + \dot{\theta}_2 + \dot{\theta}_3\right)^2 + \frac{1}{2} m_3 v_3^2\right] \end{aligned} \tag{4.10}$$

$$\begin{aligned} U = &\, m_1 g r_1 \sin\theta_1 + m_2 g r_2 \sin(\theta_1 + \theta_2) + m_2 g l_1 \sin\theta_1 \\ &+ m_3 g r_3 \sin(\theta_1 + \theta_2 + \theta_3) + m_3 g l_2 \sin(\theta_1 + \theta_2) \\ &+ m_3 g l_1 \sin\theta_1 + \frac{1}{2} k_1 \theta_1^2 + \frac{1}{2} k_2 \theta_2^2 + \frac{1}{2} k_3 \theta_3^2 \end{aligned} \tag{4.11}$$

$$\mathcal{R} = \frac{1}{2} c_1 \dot{\theta}_1^2 + \frac{1}{2} c_2 \dot{\theta}_2^2 + \frac{1}{2} c_3 \dot{\theta}_3^2 \tag{4.12}$$

where, v is the translational velocity at the centroid of the segment i, g is the gravitational acceleration constant.

Equations (4.10)–(4.12) lead to the non-linear equations of motion for the musculoskeletal system after their substitution into (4.7)–(4.9). The i-th junction equation, for each dynamically coupled non-linear equation of motion, has the form:

$$\sum_j M_{ij} \ddot{\theta}_j = \sum_j P_{ij} \dot{\theta}_i \dot{\theta}_k + \sum_j N_{ij} \dot{\theta}_i^2 + G_i + \left(T_{a_i} - T_{p_i}\right), \begin{cases} k = i + 1 \; for \; i < 3 \\ k = 1 \quad for \; i = 3 \end{cases} \tag{4.13}$$

where, $i, j = \{1,2,3\}$ such that i represents the row and j the column. $M = M(\theta, t)$ is the mass moment of inertia matrix. $\mathrm{G} = \mathrm{G}(\theta, t)$ is the vector of gravitational moment. $\theta = \{\theta_1 \quad \theta_2 \quad \theta_3\}^T$ is the angular displacement vector at the upper limb proximal joints (1: shoulder, 2: elbow, and 3: wrist joint). $\mathrm{P} = \mathrm{P}(\theta, t)$ and $\mathrm{N} = \mathrm{N}(\theta, t)$ are the matrices of the coefficients of non-linear terms $\dot{\theta}_i\dot{\theta}_k$ and $\dot{\theta}_i^2$. T_a is the active torque of the muscles, i.e. the tremor's driving torque. T_m is the passive torque of the muscles due to its passive elements (spring and damper).

The derived matrices M, P, N, and vector G of (4.13) are as follows:

$$\mathrm{M} = \begin{bmatrix} M_{11} & M_{12} & M_{13} \\ M_{12} & M_{22} & M_{23} \\ M_{13} & M_{23} & M_{33} \end{bmatrix}$$

where,

$$\begin{aligned} M_{11} &= I_1 + m_1 r_1^2 + m_2 l_1^2 + m_3(l_1^2 + l_2^2) + I_2 + m_2 r_2^2 + I_3 + m_3 r_3^2 \\ &\quad + 2l_1(m_2 r_2 + m_3 l_2)\cos\theta_2 + 2m_3 l_1 r_3 \cos(\theta_2 + \theta_3) \\ &\quad + 2m_3 l_2 r_3 \cos\theta_3 \\ M_{12} &= I_2 + m_2 r_2^2 + m_3 l_2^2 + I_3 + m_3 r_3^2 + l_1(m_2 r_2 + m_3 l_2)\cos\theta_2 \\ &\quad + m_3 l_1 r_3 \cos(\theta_2 + \theta_3) + 2m_3 l_2 r_3 \cos\theta_3 \\ M_{13} &= I_3 + m_3 r_3^2 + m_3 l_1 r_3 \cos(\theta_2 + \theta_3) + m_3 l_2 r_3 \cos\theta_3 \\ M_{22} &= I_2 + m_2 r_2^2 + m_3 l_2^2 + I_3 + m_3 r_3^2 + 2m_3 l_2 r_3 \cos\theta_3 \\ M_{23} &= I_3 + m_3 r_3^2 + m_3 l_2 r_3 \cos\theta_3 \\ M_{33} &= I_3 + m_3 r_3^2 \end{aligned} \tag{4.14}$$

$$\mathrm{N} = \begin{bmatrix} 0 & N_{12} & N_{13} \\ -N_{12} & 0 & N_{23} \\ -N_{13} & -N_{23} & 0 \end{bmatrix}$$

where,

$$\begin{aligned} N_{12} &= l_1(m_3 l_2 + m_2 r_2)\sin\theta_2 + m_3 l_1 r_3 \sin(\theta_2 + \theta_3) \\ N_{13} &= m_3 l_1 r_3 \sin(\theta_2 + \theta_3) + m_3 l_2 r_3 \sin\theta_3 \\ N_{23} &= m_3 l_2 r_3 \sin\theta_3 \end{aligned} \tag{4.15}$$

$$\mathrm{P} = \begin{bmatrix} P_{11} & P_{12} & P_{12} \\ 0 & P_{22} & P_{22} \\ P_{31} & 0 & 0 \end{bmatrix}$$

where,

$$\begin{aligned} P_{11} &= 2l_1(m_3 l_2 + m_2 r_2)\sin\theta_2 + 2m_3 l_1 r_3 \sin(\theta_2 + \theta_3) \\ P_{12} &= 2m_3 l_1 r_3 \sin(\theta_2 + \theta_3) + 2m_3 l_2 r_3 \sin\theta_3 \\ P_{22} &= 2m_3 l_2 r_3 \sin\theta_3 \\ P_{31} &= -2m_3 l_2 r_3 \sin\theta_3 \end{aligned} \tag{4.16}$$

$$\mathrm{G} = \begin{Bmatrix} G_1 \\ G_2 \\ G_3 \end{Bmatrix}$$

where,

$$\begin{aligned} G_1 &= -g[(m_1 r_1 + m_2 l_1 + m_3 l_1)\cos\theta_1 + (m_2 r_2 + m_3 l_2)\cos(\theta_1 + \theta_2) \\ &\quad + m_3 r_3 \cos(\theta_1 + \theta_2 + \theta_3)] \\ G_2 &= -g[(m_2 r_2 + m_3 l_2)\cos(\theta_1 + \theta_2) + m_3 r_3 \cos(\theta_1 + \theta_2 + \theta_3)] \\ G_3 &= -g[m_3 r_3 \cos(\theta_1 + \theta_2 + \theta_3)] \end{aligned} \tag{4.17}$$

These matrices can also be expressed as follows:

$$\mathrm{M} = \mathrm{M}_0 + \mathrm{M}_1 \cos\theta_2 + \mathrm{M}_2 \cos(\theta_2 + \theta_3) + \mathrm{M}_3 \cos\theta_3 \tag{4.18}$$

$$\mathrm{N} = \mathrm{N}_1 \sin\theta_2 + \mathrm{N}_2 \sin(\theta_2 + \theta_3) + \mathrm{N}_3 \sin\theta_3 \tag{4.19}$$

$$\mathrm{P} = \mathrm{P}_1 \sin\theta_2 + \mathrm{P}_2 \sin(\theta_2 + \theta_3) + \mathrm{P}_3 \sin\theta_3 \tag{4.20}$$

$$\mathrm{G} = \mathrm{G}_1 \cos\theta_1 + \mathrm{G}_2 \cos(\theta_1 + \theta_2) + \mathrm{G}_3 \cos(\theta_1 + \theta_2 + \theta_3) \tag{4.21}$$

where, $\mathrm{M_i}$, $\mathrm{N_i}$, and $\mathrm{P_i}$ are 3×3 matrices of constant elements, defined in (A.3)–(A.5), and $\mathrm{G_i}$ are 3×1 vectors of constant elements (A.6).

Group of similar muscles in the human upper limb can be considered to produce tremor when operating at the same driving frequency ω_{dr}, as reported by [33,35,59]. The active torque of the system, T_a, may be represented as:

$$T_{a_i} = T_{a_{i,max}} \sin\omega_{dr} t \tag{4.22}$$

where, $T_{a_{i,max}}$ is the amplitude of the active muscular torque. However, the torque T_a will be modeled depending on the tremor's datasets or used as a discrete vector containing measured muscle signal.

Concerning the passive of the muscle torque, T_m, 90% of the torque can be attributed to the elastic stiffness and 10% to the viscous stiffness [58,61,65], as shown in (2.2) and (2.3). The spring stiffness, ψ, ranges between $[0.1, 10]\ N.m/rad$ depending on the considered frictional effect (the frictional effect decreases with the increase of ψ) [61]. The spring stiffness of the muscles, can be chosen equal to $\psi = 5.74\ N.m/rad$, as proven by Goddard et al. [65].

The Voigt model of the muscle [72,74], presented in Figure 2.17b, is used in the designed musculoskeletal model of the upper limbs. The passive elements are represented by K and C, the total equivalent stiffness and damping matrices, such that:

$$\mathrm{K} = \begin{bmatrix} k_1 & 0 & 0 \\ 0 & k_2 & 0 \\ 0 & 0 & k_3 \end{bmatrix} \text{ and } \mathrm{C} = \begin{bmatrix} c_1 & 0 & 0 \\ 0 & c_2 & 0 \\ 0 & 0 & c_3 \end{bmatrix} \tag{4.23}$$

The passive torque of the muscle formulation is then:

$$T_{m_i} = k_i\theta_i + c_i\dot{\theta}_i \tag{4.24}$$

where, $\mathrm{K} = 0.9\psi \times I_n$ and $\mathrm{C} = 0.1\psi \times I_n$, with I_n the identity matrix and n the number of DOF of the primary system. So, (4.24) leads to:

$$T_{m_i} = \psi\left(0.9\theta_i + 0.1\dot{\theta}_i\right) \tag{4.25}$$

where, the passive torque of the system, T_{p_i}, presented in the non-linear differential equation of the upper limb (4.13) is the passive torque of the muscle, defined as:

$$T_{p_i} = T_{m_i} \tag{4.26}$$

The non-linear second order differential equation of motion (4.13) can be solved using the fourth or fifth order Runge-Kutta method (*ode45* built in function in MATLAB. So, it needs to be transformed into a first ordered differential equation using a suitable change of variable, to have the following form:

$$\mathrm{M_r}(\theta, t).\dot{y} = \mathrm{F_r}\left(\dot{\theta}, \theta, t\right), \qquad \text{such that } y = \begin{Bmatrix} \theta \\ \dot{\theta} \end{Bmatrix} \tag{4.27}$$

and,

$$\dot{y} = \mathrm{M_r}^{-1}\mathrm{F_r}, \qquad \text{such that } \mathrm{F_r} = \mathrm{P_r} + \mathrm{N_r} + \mathrm{G_r} + \left(\mathrm{T}_{a_r} - \mathrm{T}_{p_r}\right) \tag{4.28}$$

where,

$$\mathrm{M_r} = \begin{bmatrix} I_3 & 0_{3\times3} \\ 0_{3\times3} & \mathrm{M} \end{bmatrix}, \quad \mathrm{P_r} = \begin{bmatrix} 0_{3\times3} & 0_{3\times3} \\ 0_{3\times3} & \mathrm{P} \end{bmatrix} \begin{Bmatrix} 0_{3\times1} \\ \dot{\theta}_1\dot{\theta}_2 \\ \dot{\theta}_2\dot{\theta}_3 \\ \dot{\theta}_3\dot{\theta}_1 \end{Bmatrix}, \quad \mathrm{N_r} = \begin{bmatrix} 0_{3\times3} & 0_{3\times3} \\ 0_{3\times3} & \mathrm{N} \end{bmatrix} \begin{Bmatrix} 0_{3\times1} \\ \dot{\theta}^2 \end{Bmatrix},$$
$$\mathrm{G_r} = \begin{Bmatrix} 0_{3\times1} \\ \mathrm{G} \end{Bmatrix}, \quad \mathrm{T}_{a_r} = \begin{Bmatrix} 0_{3\times1} \\ \mathrm{T}_a \end{Bmatrix}, \quad T_{p_r} = \begin{bmatrix} 0_{3\times3} & -I_3 \\ \mathrm{K} & \mathrm{C} \end{bmatrix}.y \tag{4.29}$$

The *ode45* function uses the derived equation in (4.27) to find the solution $y = \{\theta_1 \quad \theta_2 \quad \theta_3 \quad \dot{\theta}_1 \quad \dot{\theta}_2 \quad \dot{\theta}_3\}^T$ of (4.13). In addition, the x- and y-axis global Cartesian coordinates of the end of each link (Figure 4.1) can then be, deduced according to the following equations:

- Link 1 (L1 subscript) for the upper-arm:

$$\begin{cases} x_{L1} = l_1 \cos\theta_1 \\ y_{L1} = l_1 \sin\theta_1 \end{cases} \tag{4.30}$$

- Link 2 (L2 subscript) for the forearm:

$$\begin{cases} x_{L2} = l_1 \cos\theta_1 + l_2 \cos(\theta_1 + \theta_2) \\ y_{L2} = l_1 \sin\theta_1 + l_2 \sin(\theta_1 + \theta_2) \end{cases} \tag{4.31}$$

- Link 3 (L3 subscript) for the palm:

$$\begin{cases} x_{L3} = l_1 \cos\theta_1 + l_2 \cos(\theta_1 + \theta_2) + l_3 \cos(\theta_1 + \theta_2 + \theta_3) \\ y_{L3} = l_1 \sin\theta_1 + l_2 \sin(\theta_1 + \theta_2) + l_3 \sin(\theta_1 + \theta_2 + \theta_3) \end{cases} \tag{4.32}$$

where, $l_1, l_2,$ and l_3 represents the length of the upper-arm, forearm, and palm segments, respectively.

4.2.2. Equations linearization

The governing equation of motion of the system (4.13) is a non-linear differential equation with high order and non-linear coefficients. The coefficients, $\mathrm{N}, \mathrm{P}, \mathrm{G},$ and, especially, M are time dependent matrices. So, the natural frequencies of the system (depending on M and K) are also time dependent. Solving such system would be of high difficulty [141] and may be a waste of time if the variations in system's properties with time are small. If the time dependent parameters change slightly, the linearization of these equations can be a good solution.

The non-linear differential equations (4.13) can be linearized using Taylor's series [142], following the next steps:

1. The vector x is defined to represent the independent variables and their derivatives as separated variables, so:

$$x = \{\ddot{\theta}_1 \quad \ddot{\theta}_2 \quad \ddot{\theta}_3 \quad \dot{\theta}_1 \quad \dot{\theta}_2 \quad \dot{\theta}_3 \quad \theta_1 \quad \theta_2 \quad \theta_3 \quad u_1 \quad u_2 \quad u_3\}^T \tag{4.33}$$

where, $u_1 = T_{a_1}(t)$, $u_2 = T_{a_2}(t)$, and $u_3 = T_{a_3}(t)$ are the muscular moments applied at the shoulder, elbow, and wrist joints, respectively, and $u = \{u_1 \quad u_2 \quad u_3\}^T$

2. The equation of motion is written in the form of $h(x) = \mathbf{0}$. By using (4.18)–(4.21), and (4.23):

$$
\begin{aligned}
h(x) = \begin{Bmatrix} h_1 \\ h_2 \\ h_3 \end{Bmatrix} &= \mathbf{0} \\
&= [\mathrm{M}_0 + \mathrm{M}_1 \cos\theta_2 + \mathrm{M}_2 \cos(\theta_2 + \theta_3) + \mathrm{M}_3 \cos\theta_3] \begin{Bmatrix} \ddot{\theta}_1 \\ \ddot{\theta}_2 \\ \ddot{\theta}_3 \end{Bmatrix} \\
&+ \begin{bmatrix} c_1 & 0 & 0 \\ 0 & c_2 & 0 \\ 0 & 0 & c_3 \end{bmatrix} \begin{Bmatrix} \dot{\theta}_1 \\ \dot{\theta}_2 \\ \dot{\theta}_3 \end{Bmatrix} + \begin{bmatrix} k_1 & 0 & 0 \\ 0 & k_2 & 0 \\ 0 & 0 & k_3 \end{bmatrix} \begin{Bmatrix} \theta_1 \\ \theta_2 \\ \theta_3 \end{Bmatrix} \\
&- [\mathrm{N}_1 \sin\theta_2 + \mathrm{N}_2 \sin(\theta_2 + \theta_3) + \mathrm{N}_3 \sin\theta_3] \begin{Bmatrix} \dot{\theta}_1^2 \\ \dot{\theta}_2^2 \\ \dot{\theta}_3^2 \end{Bmatrix} \\
&- [\mathrm{P}_1 \sin\theta_2 + \mathrm{P}_2 \sin(\theta_2 + \theta_3) + \mathrm{P}_3 \sin\theta_3] \begin{Bmatrix} \dot{\theta}_1\dot{\theta}_2 \\ \dot{\theta}_2\dot{\theta}_3 \\ \dot{\theta}_3\dot{\theta}_1 \end{Bmatrix} \\
&- [\mathrm{G}_1 \cos\theta_1 + \mathrm{G}_2 \cos(\theta_1 + \theta_2) + \mathrm{G}_3 \cos(\theta_1 + \theta_2 + \theta_3)] \\
&- \begin{Bmatrix} T_{a_1}(t) \\ T_{a_2}(t) \\ T_{a_3}(t) \end{Bmatrix}
\end{aligned}
\tag{4.34}
$$

3. The differential equation is linearized around x_0, which is called the operating point. x_0 must satisfy all the differential equations, such that $h(x_0) = \mathbf{0}$. The operating point is chosen to be the static equilibrium state of the system, which satisfies the following equation:

$$\mathrm{K}\theta_0 - \mathrm{G}(\theta, 0) = \mathrm{T}_a(0) \tag{4.35}$$

where, G and K are defined in (4.17) and (4.23) and $\theta_0 = \{\theta_1(0) \quad \theta_2(0) \quad \theta_3(0)\}^T$. Thus, x_0 becomes:

$$x_0 = [0 \quad 0 \quad 0 \quad 0 \quad 0 \quad 0 \quad \theta_1(0) \quad \theta_2(0) \quad \theta_3(0) \quad u_1(0) \quad u_2(0) \quad u_3(0)]^T \tag{4.36}$$

4. Finally, each term of the differential equations can be linearized using Taylor series by computing their differential functions. The Taylor series linearization formula for $h(x)$ about x_0 is described below:

$$h(x) = \mathbf{0} = \sum_{j=0}^{\infty} \left\{ \frac{1}{j!} \left[\sum_{k=1}^{n} (x_k - x_{k0}) \frac{\partial}{\partial x_k} \right]^j . h(x)|_{x=x_0} \right\} \tag{4.37}$$

By ignoring the high order terms, then,

$$
\begin{aligned}
h(x) = \mathbf{0} &\approx h(x_0) + \nabla h(x)|_{x=x_0} . \Delta x, \\
&\text{with } \Delta x = x - x_0 \text{ and } x = [x_1 \quad \dots \quad x_n]^T
\end{aligned}
\tag{4.38}
$$

Such that,

$$\nabla h(x) = \left[\frac{\partial h(x)}{\partial x_1} \quad \dots \quad \frac{\partial h(x)}{\partial x_n}\right] \text{ and } \Delta x = \{x_1 - x_1(0) \quad \dots \quad x_n - x_n(0)\}^T \tag{4.39}$$

where, $J = \nabla h(x)$ is the Jacobian matrix consisting of the partial derivative with respect to the system variables and n is the length of the vector x. In other words, the linearized equations of motion have the form:

$$h(x_0) + J|_{x=x_0}.\Delta x \approx \mathbf{0} \tag{4.40}$$

where, $h(x_0) = 0$ if x_0 satisfies the non-linear differential equation, such that:

$$\begin{aligned} h(x_0) = \mathbf{0} = \mathrm{K}\theta_0 \\ - \left[\mathrm{G}_1 \cos\theta_1(0) + \mathrm{G}_2 \cos\big(\theta_1(0) + \theta_2(0)\big)\right. \\ \left. + \mathrm{G}_3 \cos\big(\theta_1(0) + \theta_2(0) + \theta_3(0)\big)\right] - u(0) \end{aligned} \tag{4.41}$$

J and Δx of (4.40) which have to be computed and used for (4.34), are defined by:

$$J = \begin{bmatrix} \frac{\partial h_1}{\partial \ddot{\theta}_1} & \frac{\partial h_1}{\partial \ddot{\theta}_2} & \frac{\partial h_1}{\partial \ddot{\theta}_3} & \frac{\partial h_1}{\partial \dot{\theta}_1} & \frac{\partial h_1}{\partial \dot{\theta}_2} & \frac{\partial h_1}{\partial \dot{\theta}_3} & \frac{\partial h_1}{\partial \theta_1} & \frac{\partial h_1}{\partial \theta_2} & \frac{\partial h_1}{\partial \theta_3} & \frac{\partial h_1}{\partial u_1} & \frac{\partial h_1}{\partial u_2} & \frac{\partial h_1}{\partial u_3} \\ \frac{\partial h_2}{\partial \ddot{\theta}_1} & \frac{\partial h_2}{\partial \ddot{\theta}_2} & \frac{\partial h_2}{\partial \ddot{\theta}_3} & \frac{\partial h_2}{\partial \dot{\theta}_1} & \frac{\partial h_2}{\partial \dot{\theta}_2} & \frac{\partial h_2}{\partial \dot{\theta}_3} & \frac{\partial h_2}{\partial \theta_1} & \frac{\partial h_2}{\partial \theta_2} & \frac{\partial h_2}{\partial \theta_3} & \frac{\partial h_2}{\partial u_1} & \frac{\partial h_2}{\partial u_2} & \frac{\partial h_2}{\partial u_3} \\ \frac{\partial h_3}{\partial \ddot{\theta}_1} & \frac{\partial h_3}{\partial \ddot{\theta}_2} & \frac{\partial h_3}{\partial \ddot{\theta}_3} & \frac{\partial h_3}{\partial \dot{\theta}_1} & \frac{\partial h_3}{\partial \dot{\theta}_2} & \frac{\partial h_3}{\partial \dot{\theta}_3} & \frac{\partial h_3}{\partial \theta_1} & \frac{\partial h_3}{\partial \theta_2} & \frac{\partial h_3}{\partial \theta_3} & \frac{\partial h_3}{\partial u_1} & \frac{\partial h_3}{\partial u_2} & \frac{\partial h_3}{\partial u_3} \end{bmatrix}$$

$$\text{and } \Delta x = \begin{Bmatrix} \ddot{\theta}_1 - \ddot{\theta}_1(0) \\ \ddot{\theta}_2 - \ddot{\theta}_2(0) \\ \ddot{\theta}_3 - \ddot{\theta}_3(0) \\ \dot{\theta}_1 - \dot{\theta}_1(0) \\ \dot{\theta}_2 - \dot{\theta}_2(0) \\ \dot{\theta}_3 - \dot{\theta}_3(0) \\ \theta_1 - \theta_1(0) \\ \theta_2 - \theta_2(0) \\ \theta_3 - \theta_3(0) \\ u_1 - u_1(0) \\ u_2 - u_2(0) \\ u_3 - u_3(0) \end{Bmatrix} \tag{4.42}$$

By following these steps, the linearized equation of motion of the uncontrolled upper limb in the vertical plane of Figure 4.1, described in (4.34), becomes:

$$\begin{aligned}\left[\mathrm{M}_0+\mathrm{M}_1\cos\theta_2(0)+\mathrm{M}_2\cos\left(\theta_2(0)+\theta_3(0)\right)+\mathrm{M}_3\cos\theta_3(0)\right]\ddot{\theta}\\ =\Delta u-\mathrm{K}\Delta\theta-\mathrm{C}\dot{\theta}\\ -\left[\mathrm{G}_1[\sin\theta_1(0).\Delta\theta_1]+\mathrm{G}_2\left[\sin\left(\theta_1(0)+\theta_2(0)\right).(\Delta\theta_1+\Delta\theta_2)\right]\right.\\ \left.+\mathrm{G}_3\left[\sin\left(\theta_1(0)+\theta_2(0)+\theta_3(0)\right)(\Delta\theta_1+\Delta\theta_2+\Delta\theta_3)\right]\right]\end{aligned} \tag{4.43}$$

For $x_0=[0\quad 0\quad 0\quad 0\quad 0\quad 0\quad \theta_1(0)\quad \theta_2(0)\quad \theta_3(0)\quad u_1(0)\quad u_2(0)\quad u_3(0)]^T$ operating point that represent the static equilibrium state, such that the linearized mass matrix has the form:

$$\mathrm{M}=\mathrm{M}_0+\mathrm{M}_1\cos\theta_2(0)+\mathrm{M}_2\cos\left(\theta_2(0)+\theta_3(0)\right)+\mathrm{M}_3\cos\theta_3(0) \tag{4.44}$$

The variables in (4.43) can be rearranged using the variable defined as:

$$\mathrm{G_k}=[\mathrm{G_{k_1}}\quad \mathrm{G_{k_2}}\quad \mathrm{G_{k_3}}]$$

$$\text{such that,}\begin{cases}\mathrm{G_{k_3}}=\mathrm{G}_3\sin\left(\theta_1(0)+\theta_2(0)+\theta_3(0)\right)\\ \mathrm{G_{k_2}}=\mathrm{G}_2\sin\left(\theta_1(0)+\theta_2(0)\right)+\mathrm{G_{k_3}}\\ \mathrm{G_{k_1}}=\mathrm{G}_1\sin\theta_1(0)+\mathrm{G_{k_2}}\end{cases} \tag{4.45}$$

where the terms $\mathrm{G_{k_i}}$ are obtained from the linearization of the gravitational moment G and act as an additional stiffness coefficient to the system. $\mathrm{M_i}$ and $\mathrm{G_i}$ matrices are the same as those defined for the non-linear system (for details, see (A.3) and (A.6), respectively). The term defined in (4.45) helps to get a compact ordinary differential equation as follows:

$$\mathrm{M}\ddot{\theta}=-(\mathrm{K}+\mathrm{G_k})\Delta\theta-\mathrm{C}\dot{\theta}+\Delta u \tag{4.46}$$

Thus, equation (4.46) represents the linearized differential equation operating around the equilibrium position of the system. According to equation (4.46), the total passive torque of the system T_p, is the addition of the passive torque of the muscle T_m and a passive torque appears (4.46) after the linearization of the terms related to the gravitational potential energy $(\mathrm{G_k})$, it is defined as:

$$\mathrm{T}_p=\mathrm{T}_m+\mathrm{G_k}\Delta\theta=(\mathrm{G_k}+\mathrm{K})\Delta\theta+\mathrm{C}\dot{\theta} \tag{4.47}$$

Then, the governing equation of motion can be simply defined as:

$$\mathrm{M}\ddot{\theta}=\mathrm{F}_r,\qquad \mathrm{F}_r=\left(\mathrm{T}_a-\mathrm{T}_a(0)\right)-\mathrm{T}_p \tag{4.48}$$

where, F_r is the resultant moment acting on the system. The generalized equation to be solved by the *ode45* function is:

$$\begin{bmatrix} I_3 & 0_{3\times3} \\ 0_{3\times3} & \mathrm{M} \end{bmatrix} \begin{Bmatrix} \dot{\theta}_1 \\ \dot{\theta}_2 \\ \dot{\theta}_3 \\ \ddot{\theta}_1 \\ \ddot{\theta}_2 \\ \ddot{\theta}_3 \end{Bmatrix} = \begin{Bmatrix} 0 \\ 0 \\ 0 \\ T_{a_1} - T_{a_1}(0) \\ T_{a_2} - T_{a_2}(0) \\ T_{a_3} - T_{a_3}(0) \end{Bmatrix} - \begin{bmatrix} 0_{3\times3} & -I_3 \\ \mathrm{K} + \mathrm{G_k} & \mathrm{C} \end{bmatrix} \begin{Bmatrix} \theta_1 - \theta_1(0) \\ \theta_2 - \theta_2(0) \\ \theta_3 - \theta_3(0) \\ \dot{\theta}_1 \\ \dot{\theta}_2 \\ \dot{\theta}_3 \end{Bmatrix} \tag{4.49}$$

The Laplace transform of the linearized equation (4.43) can be calculated to obtain the response of the system in the frequency domain, such that $\mathcal{L}\{\theta(t)\} = \Theta(s) = \Theta$ and $s = j\omega$ with ω is the angular frequency. The Laplace transform of the variables vector of the system (4.33) is as follows:

$$\mathcal{L}\left\{\begin{bmatrix} \ddot{\theta}_1 \\ \ddot{\theta}_2 \\ \ddot{\theta}_3 \\ \dot{\theta}_1 \\ \dot{\theta}_2 \\ \dot{\theta}_3 \\ \theta_1 \\ \theta_2 \\ \theta_3 \\ u_1 \\ u_2 \\ u_3 \end{bmatrix}\right\} = \begin{bmatrix} s^2\Theta_1 - s\theta_1(0) - \dot{\theta}_1(0) \\ s^2\Theta_2 - s\theta_2(0) - \dot{\theta}_2(0) \\ s^2\Theta_3 - s\theta_3(0) - \dot{\theta}_3(0) \\ s\Theta_1 - \theta_1(0) \\ s\Theta_2 - \theta_2(0) \\ s\Theta_3 - \theta_3(0) \\ \Theta_1 \\ \Theta_2 \\ \Theta_3 \\ \mathcal{L}\{u_1\} \\ \mathcal{L}\{u_2\} \\ \mathcal{L}\{u_3\} \end{bmatrix} \tag{4.50}$$

The response of the system in the frequency domain is usually calculated for the forced response terms of the differential equations, and TMDs optimum parameters are calculated depending on its amplitude. So, the homogenous response terms of (4.43) will be removed. Thus, the Laplace transform of (4.43) gives:

$$\begin{aligned} s^2\big[\mathrm{M}_0 + \mathrm{M}_1\cos\theta_2(0) + \mathrm{M}_2\cos\big(\theta_2(0) + \theta_3(0)\big) + \mathrm{M}_3\cos\theta_3(0)\big]\Theta + \mathrm{K}\Theta \\ + s\mathrm{C}\Theta \\ + \big[\Theta_1\mathrm{G}_1\sin\theta_1(0) + (\Theta_1 + \Theta_2)\mathrm{G}_2\sin\big(\theta_1(0) + \theta_2(0)\big) \\ + (\Theta_1 + \Theta_2 + \Theta_3)\mathrm{G}_3\sin\big(\theta_1(0) + \theta_2(0) + \theta_3(0)\big)\big] - \mathcal{L}\{u\} = \mathbf{0} \end{aligned} \tag{4.51}$$

The variable defined in (4.45) is used to write the compact form of the governing equation of motion in the frequency domain:

$$\Theta = \mathrm{H}.\{\mathcal{F}\} \text{ such that } \mathrm{H} = (\mathrm{M}s^2 + \mathrm{C}s + \mathrm{K} + \mathrm{G_k})^{-1} \tag{4.52}$$

where, H is the transfer function of the system, and $\mathcal{F} = \mathcal{L}\{u\}$ is the Laplace of the input moment signal.

4.3. TMDs at the upper limb

Passive TMD is proposed to reduce the vibrational energy, produced by the muscular signals in the hand of the patients. The TMD parameters will be designed depending on the dynamic modeling of the upper limb provided in Figure 4.1. Thus, equations of motion of the global system, after the addition of the TMD(s), need to be derived. The TMD(s) can be placed at the forearm or the palm to study the provided reduction of the joint tremor.

4.3.1. Absorber at the forearm

The Lagrangian formulation (4.6) is used again to derive the equation of motion related to the upper limbs with m-TMDs placed at different positions along the forearm, as shown in Figure 4.2. It is applied using the velocity at the centroid of each TMD (v_{a_i}), defined as:

$$\vec{v}_{a_i} = \dot{\vec{\theta}}_1 \times \vec{l}_1 + \left(\dot{\vec{\theta}}_1 + \dot{\vec{\theta}}_2\right) \times \vec{d}_{a_i} + \left(\dot{\vec{\theta}}_1 + \dot{\vec{\theta}}_2 + \dot{\vec{\theta}}_{a_i}\right) \times \vec{r}_{a_i} \tag{4.53}$$

where, $i = \{1,2,\dots,m\}$ is on the number of TMD to be tested. a_i subscript refers to the i^{th} absorber. d_{a_i} is the distance from elbow joint to the TMD joint. r_{a_i} is the centroid position of the TMD measured from its joint. $\dot{\theta}_{a_i}$ is the angular displacement of the TMD.

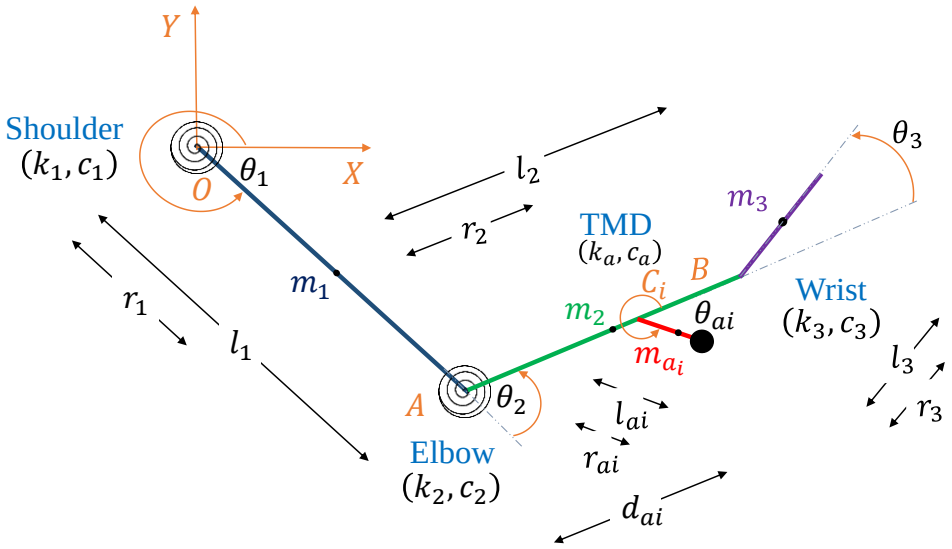

Figure 4.2: Upper limb model with TMD(s) placed at the forearm segment

The kinetic energy, gravitational potential energy, and Rayleigh dissipation function of the global system can be used to obtain the equations of motion of the system, defined as follows:

$$\begin{aligned} T = &\left[\frac{1}{2}I_1\dot{\theta}_1^2 + \frac{1}{2}m_1v_1^2\right] + \left[\frac{1}{2}I_2\left(\dot{\theta}_1 + \dot{\theta}_2\right)^2 + \frac{1}{2}m_2v_2^2\right] \\ &+ \left[\frac{1}{2}I_3\left(\dot{\theta}_1 + \dot{\theta}_2 + \dot{\theta}_3\right)^2 + \frac{1}{2}m_3v_3^2\right] \\ &+ \left[\frac{1}{2}I_{a_1}\left(\dot{\theta}_1 + \dot{\theta}_2 + \dot{\theta}_{a_1}\right)^2 + \frac{1}{2}m_{a_1}v_{a_1}^2\right] + \cdots \\ &+ \left[\frac{1}{2}I_{a_m}\left(\dot{\theta}_1 + \dot{\theta}_2 + \dot{\theta}_{a_m}\right)^2 + \frac{1}{2}m_{a_m}v_{a_m}^2\right] \end{aligned} \tag{4.54}$$

$$\begin{aligned} U = &m_1gr_1\sin\theta_1 + m_2gr_2\sin(\theta_1 + \theta_2) + m_2gl_1\sin\theta_1 \\ &+ m_3gr_3\sin(\theta_1 + \theta_2 + \theta_3) + m_3gl_2\sin(\theta_1 + \theta_2) \\ &+ m_3gl_1\sin\theta_1 + \frac{1}{2}k_1\theta_1^2 + \frac{1}{2}k_2\theta_2^2 + \frac{1}{2}k_3\theta_3^2 + m_{a_1}gl_1\sin\theta_1 \\ &+ m_{a_1}gd_{a_1}\sin(\theta_1 + \theta_2) + m_{a_1}gr_{a_1}\sin\left(\theta_1 + \theta_2 + \theta_{a_1}\right) \\ &+ \frac{1}{2}k_{a_1}\theta_{a_1}^2 + \cdots + m_{a_m}gl_1\sin\theta_1 + m_{a_m}gd_{a_m}\sin(\theta_1 + \theta_2) \\ &+ m_{a_m}gr_{a_m}\sin\left(\theta_1 + \theta_2 + \theta_{a_m}\right) + \frac{1}{2}k_{a_m}\theta_{a_m}^2 \end{aligned} \tag{4.55}$$

$$\mathcal{R} = \frac{1}{2}c_1\dot{\theta}_1^2 + \frac{1}{2}c_2\dot{\theta}_2^2 + \frac{1}{2}c_3\dot{\theta}_3^2 + \frac{1}{2}c_{a_1}\dot{\theta}_{a_1}^2 + \cdots + \frac{1}{2}c_{a_m}\dot{\theta}_{a_m}^2 \tag{4.56}$$

where, m_{a_i}, k_{a_i}, and c_{a_i} are the mass, stiffness and damping coefficient of the i^{th} TMD. θ_{a_i} is the angular displacement of the i^{th} TMD.

After linearizing, using (4.40), differential equations obtained by applying equation (4.6), the vector $\mathrm{G_k}$ defined as

$$\mathrm{G_k} = \begin{bmatrix} \mathrm{G_{k_1}} & \mathrm{G_{k_2}} & \mathrm{G_{k_3}} & \mathrm{G_{k_4}} & \cdots & \mathrm{G_{k_n}} \end{bmatrix}$$

with,

$$\begin{cases} \mathrm{G_{k_n}} = \mathrm{G_n}\sin\left(\theta_1(0) + \theta_2(0) + \theta_{a_m}(0)\right) \\ \mathrm{G_{k_{n-1}}} = \mathrm{G_{n-1}}\sin\left(\theta_1(0) + \theta_2(0) + \theta_{a_{m-1}}(0)\right) \\ \qquad\vdots \\ \mathrm{G_{k_4}} = \mathrm{G_4}\sin\left(\theta_1(0) + \theta_2(0) + \theta_{a_1}(0)\right) \\ \mathrm{G_{k_3}} = \mathrm{G_3}\sin\left(\theta_1(0) + \theta_2(0) + \theta_3(0)\right) \\ \mathrm{G_{k_2}} = \mathrm{G_2}\sin\left(\theta_1(0) + \theta_2(0)\right) + \mathrm{G_{k_3}} + \mathrm{G_{k_4}} + \cdots + \mathrm{G_{k_n}} \\ \mathrm{G_{k_1}} = \mathrm{G_1}\sin\theta_1(0) + \mathrm{G_{k_2}} \end{cases} \tag{4.57}$$

helps to obtain a compact form of the linearized equations, where n is the number of DOF of the global system formed of the 3DOF principle system and the m-TMDs (i.e. $n = m + 3$).

Compact equations for time and frequency domains, defined in (4.49) and (4.52), can then be obtained. The variables needed to compute these equations are the $n \times n$ $\mathrm{M_i}$ matrices and $n \times 1$ $\mathrm{G_i}$ vectors defined in appendices (B.5) and (B.6). The global angular

displacement vector of the global system becomes $\theta = [\theta_1 \quad \theta_2 \quad \theta_3 \quad \theta_{a_1} \quad \dots \quad \theta_{a_\mathrm{m}}]^T$, and the stiffness and damping matrices:

$$\mathrm{K} = \begin{bmatrix} k_1 & 0 & 0 & 0 & 0 & 0 \\ 0 & k_2 & 0 & 0 & 0 & 0 \\ 0 & 0 & k_3 & 0 & 0 & 0 \\ 0 & 0 & 0 & k_{a_1} & 0 & 0 \\ 0 & 0 & 0 & 0 & \ddots & 0 \\ 0 & 0 & 0 & 0 & 0 & k_{a_\mathrm{m}} \end{bmatrix} \tag{4.58}$$

$$\mathrm{C} = \begin{bmatrix} c_1 & 0 & 0 & 0 & 0 & 0 \\ 0 & c_2 & 0 & 0 & 0 & 0 \\ 0 & 0 & c_3 & 0 & 0 & 0 \\ 0 & 0 & 0 & c_{a_1} & 0 & 0 \\ 0 & 0 & 0 & 0 & \ddots & 0 \\ 0 & 0 & 0 & 0 & 0 & c_{a_\mathrm{m}} \end{bmatrix} \tag{4.59}$$

The x- and y-axis global Cartesian coordinates for the end of each absorber's link in Figure 4.2 can be deduced according to the following equations:

- Link a (L_a subscript) for the absorber placed at the forearm:

$$\begin{cases} x_{L_{a_i}} = x_{L_1} + d_{a_i}\cos(\theta_1 + \theta_2) + l_{a_i}\cos\left(\theta_1 + \theta_2 + \theta_{a_i}\right) \\ y_{L_{a_i}} = y_{L_1} + d_{a_i}\sin(\theta_1 + \theta_2) + l_{a_i}\sin\left(\theta_1 + \theta_2 + \theta_{a_i}\right) \end{cases} \tag{4.60}$$

where, $i = \{1,2, \dots, m\}$.

4.3.2. Absorbers at the palm

The effect of TMDs effect can also be tested when they are placed at the palm segment, as shown in Figure 4.3. The derivation of the equations of motion needs the computation of the velocity at the centroid position of each TMD, defined as:

$$\begin{aligned} \vec{v}_{a_i} = \dot{\vec{\theta}}_1 \times \vec{l}_1 + \left(\dot{\vec{\theta}}_1 + \dot{\vec{\theta}}_2\right) \times \vec{l}_2 + \left(\dot{\vec{\theta}}_1 + \dot{\vec{\theta}}_2 + \dot{\vec{\theta}}_3\right) \times \vec{d}_{a_i} \\ + \left(\dot{\vec{\theta}}_1 + \dot{\vec{\theta}}_2 + \dot{\vec{\theta}}_3 + \dot{\vec{\theta}}_{a_i}\right) \times \vec{r}_{a_i} \end{aligned} \tag{4.61}$$

where, $i = \{1,2, \dots, m\}$ is the number of TMD to be tested. a_i subscript refers to the i^{th} absorber. d_{a_i} is the distance from the wrist joint to the TMD joint. r_{a_i} is the centroid position of the TMD measured from its joint. $\dot{\theta}_{a_i}$ is the angular displacement of the TMD.

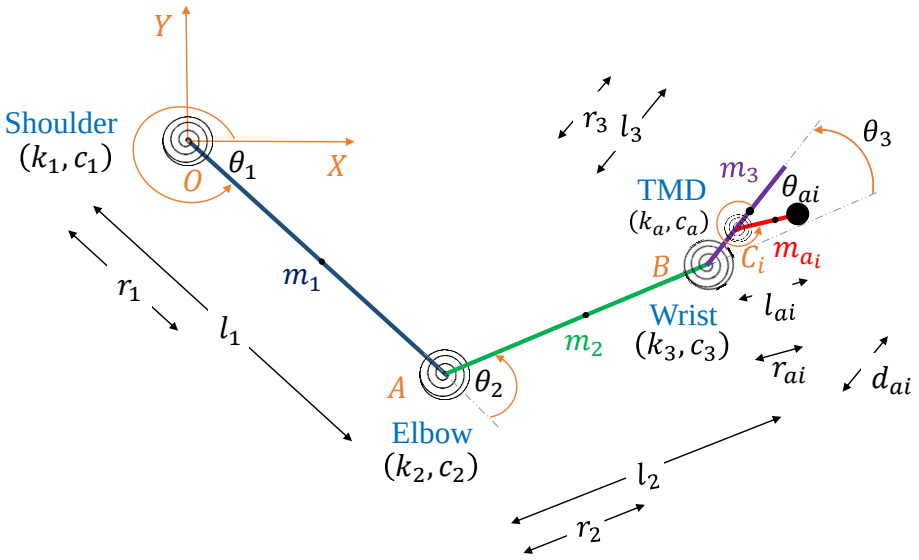

Figure 4.3: Upper limb model with TMD(s) placed at the palm segment

The kinetic and gravitational potential energies of the global system are defined as:

$$\begin{aligned} T = &\left[\frac{1}{2}I_1\dot{\theta}_1^2 + \frac{1}{2}m_1v_1^2\right] + \left[\frac{1}{2}I_2\left(\dot{\theta}_1 + \dot{\theta}_2\right)^2 + \frac{1}{2}m_2v_2^2\right] \\ &+ \left[\frac{1}{2}I_3\left(\dot{\theta}_1 + \dot{\theta}_2 + \dot{\theta}_3\right)^2 + \frac{1}{2}m_3v_3^2\right] \\ &+ \left[\frac{1}{2}I_{a_1}\left(\dot{\theta}_1 + \dot{\theta}_2 + \dot{\theta}_3 + \dot{\theta}_{a_1}\right)^2 + \frac{1}{2}m_{a_1}v_{a_1}^2\right] + \cdots \\ &+ \left[\frac{1}{2}I_{a_m}\left(\dot{\theta}_1 + \dot{\theta}_2 + \dot{\theta}_3 + \dot{\theta}_{a_m}\right)^2 + \frac{1}{2}m_{a_m}v_{a_m}^2\right] \end{aligned} \tag{4.62}$$

$$\begin{aligned} U = &\, m_1gr_1\sin\theta_1 + m_2gr_2\sin(\theta_1 + \theta_2) + m_2gl_1\sin\theta_1 \\ &+ m_3gr_3\sin(\theta_1 + \theta_2 + \theta_3) + m_3gl_2\sin(\theta_1 + \theta_2) \\ &+ m_3gl_1\sin\theta_1 + \frac{1}{2}k_1\theta_1^2 + \frac{1}{2}k_2\theta_2^2 + \frac{1}{2}k_3\theta_3^2 + m_{a_1}gl_1\sin\theta_1 \\ &+ m_{a_1}gd_{a_1}\sin(\theta_1 + \theta_2) + m_{a_1}gd_{a_1}\sin(\theta_1 + \theta_2 + \theta_3) \\ &+ m_{a_1}gr_{a_1}\sin\left(\theta_1 + \theta_2 + \theta_3 + \theta_{a_1}\right) + \frac{1}{2}k_{a_1}\theta_{a_1}^2 + \cdots \\ &+ m_{a_m}gl_1\sin\theta_1 + m_{a_m}gd_{a_m}\sin(\theta_1 + \theta_2) \\ &+ m_{a_m}gd_{a_m}\sin(\theta_1 + \theta_2 + \theta_3) \\ &+ m_{a_m}gr_{a_m}\sin\left(\theta_1 + \theta_2 + \theta_3 + \theta_{a_m}\right) + \frac{1}{2}k_{a_m}\theta_{a_m}^2 \end{aligned} \tag{4.63}$$

where, m_{a_i}, k_{a_i}, and c_{a_i} are the mass, stiffness and damping coefficient of the i^{th} TMD. θ_{a_i} is the angular displacement of the i^{th} TMD. The Rayleigh dissipation function is similar to that defined in (4.56).

The vector $\mathrm{G_k}$, used to obtain the compact form of the differential equations in the time and frequency domains, as in (4.49) and (4.52), is defined as:

$$\mathrm{G_k} = \begin{bmatrix} \mathrm{G_{k_1}} & \mathrm{G_{k_2}} & \mathrm{G_{k_3}} & \mathrm{G_{k_4}} & \cdots & \mathrm{G_{k_n}} \end{bmatrix}$$

such that,

$$\begin{cases} \mathrm{G_{k_n}} = \mathrm{G_n} \sin\left(\theta_1(0) + \theta_2(0) + \theta_3(0) + \theta_{a_m}(0)\right) \\ \mathrm{G_{k_{n-1}}} = \mathrm{G_{n-1}} \sin\left(\theta_1(0) + \theta_2(0) + \theta_3(0) + \theta_{a_{m-1}}(0)\right) \\ \qquad\qquad \vdots \\ \mathrm{G_{k_4}} = \mathrm{G_4} \sin\left(\theta_1(0) + \theta_2(0) + \theta_3(0) + \theta_{a_1}(0)\right) \\ \mathrm{G_{k_3}} = \mathrm{G_3} \sin\left(\theta_1(0) + \theta_2(0) + \theta_3(0)\right) + \mathrm{G_{k_4}} + \cdots + \mathrm{G_{k_n}} \\ \mathrm{G_{k_2}} = \mathrm{G_2} \sin\left(\theta_1(0) + \theta_2(0)\right) + \mathrm{G_{k_3}} \\ \mathrm{G_{k_1}} = \mathrm{G_1} \sin\theta_1(0) + \mathrm{G_{k_2}} \end{cases} \tag{4.64}$$

where, n is the number of DOF of the global system formed of the 3DOF principle system and the m-TMDs (i.e. $n = m + 3$). The $n \times n$ $\mathrm{M_i}$ matrices and $n \times 1$ $\mathrm{G_i}$ vectors of the upper limbs with m-TMDs placed at the palm are defined in (C.5) and (C.6). The global angular displacement vector of the global system is $\theta = [\theta_1 \quad \theta_2 \quad \theta_3 \quad \theta_{a_1} \quad \ldots \quad \theta_{a_\mathrm{m}}]^T$. The stiffness and damping coefficient matrices are similar to those defined in (4.58) and (4.59), respectively.

The x- and y-axis global Cartesian coordinates for the end of each absorber's link in Figure 4.3 can be deduced according to the following equations:

- Link a (L_a subscript), reflecting the absorber placed at the palm:

$$\begin{cases} x_{L_{a_i}} = x_{L1} + d_{a_i} \cos(\theta_1 + \theta_2 + \theta_3) + l_{a_i} \cos\left(\theta_1 + \theta_2 + \theta_3 + \theta_{a_i}\right) \\ y_{L_{a_i}} = y_{L1} + d_{a_i} \sin(\theta_1 + \theta_2 + \theta_3) + l_{a_i} \sin\left(\theta_1 + \theta_2 + \theta_3 + \theta_{a_i}\right) \end{cases} \tag{4.65}$$

where, $i = \{1,2, \ldots, m\}$.

4.4. Passive absorber design

As investigated in the previous chapter, the critical frequency of the patient can slightly shift with different task and hand positions along different days. So, it is not practical to design a new passive TMD for each time the critical frequency changes. In contrast, it is suggested to use the same TMD designs can operate at different frequencies. The cantilever-type TMD is proposed as the passive TMD to be used for this study, which is used to provide other natural frequencies by fixing its geometry and adjusting the position of the mass along the beam. As the upper-limb's dynamic model (Figure 4.1) is formed of three rotating rigid bodies connected together, it is convenient to put a TMD of the same type, i.e. a pendulum TMD as a first step.

4.4.1. Pendulum TMD

The passive vibration absorber proposed to reduce the response amplitude for the system is first modeled by a compound pendulum with torsional spring and damper (Figure 4.4), which is the TMD model considered in the derivation of the equations of motion for the upper limb with TMDs. It is composed of a light weight circular rod and a mass located at a small distance, d_{mass}, from the free end. This distance exists to ensure that the geometry of the mass is included entirely within the length of the pendulum, and not to increase the effective length of the pendulum.

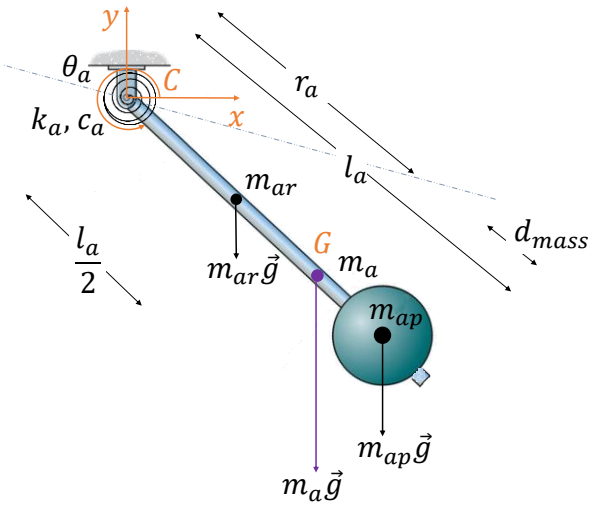

Figure 4.4: Compound pendulum TMD

The total mass of the pendulum TMD, m_a, is formed of the concentrated mass or point mass, m_{ap}, and the rod mass, m_{ar}. So, the total mass of the pendulum TMD at its centroid is:

$$m_a = m_{ap} + m_{ar} \tag{4.66}$$

The position of the TMD's centroid from the joint at point C, r_a, is defined by:

$$r_a = \frac{1}{m_a}\left[(l_a - d_{mass})m_{ap} + \frac{l_a m_{ar}}{2}\right] \tag{4.67}$$

where, l_a is the length of the absorber. The mass moment of inertia of the absorber with respect to the joint at point C, $I_{a/C}$,is:

$$I_{a/C} = m_{ap}(l_a - d_{mass})^2 + \frac{1}{3}m_{ar}l_a^2 \tag{4.68}$$

and with respect to the centroid at point G, $I_{a/G}$:

$$I_{a/G} = I_{a/C} - m_a r_a^2 \tag{4.69}$$

m_a, r_a and $I_{a/G}$ will be used later for the parameter optimization procedure of the pendulum TMD's, placed at the forearm or the palm of the dynamic upper limb model.

The governing equation of motion for the pendulum system of Figure 4.4 is derived using Newton's second law:

$$I_{a/C}\ddot{\theta}_a + k_a\theta_a + m_a g r_a \sin\theta_a + c_a\dot{\theta}_a = 0 \tag{4.70}$$

which is a non-linear differential equation. The same linearization process, by Taylor series expansion (4.40), is used to linearize this equation. The vector of independent variables for this equation is defined as $x = \{\ddot{\theta}_a \quad \theta_a\}^T$, where the rest condition $x_0 = \{\ddot{\theta}_a(0) \quad \theta_a(0)\}^T$ is an operating point for (4.70). Then, the linearized equation around x_0 is:

$$\begin{aligned} I_{a/C}\left(\ddot{\theta}_a - \ddot{\theta}_a(0)\right) + k_a\left(\theta_a - \theta_a(0)\right) + m_a g r_a \cos\theta_a(0)\,.\,(\theta_a - \theta_{0a}) \\ + c_a\left(\dot{\theta}_a - \dot{\theta}_a(0)\right) = 0 \end{aligned} \tag{4.71}$$

By taking $x_0 = \{0 \quad 0 \quad 0\}^T$, equation (4.71) becomes:

$$I_{a/C}\ddot{\theta}_a + (k_a + m_a g r_a)\theta_a + c_a\dot{\theta}_a = 0 \tag{4.72}$$

The natural angular frequency of the pendulum TMD, ω_a, and its damping ratio, ζ_a, are defined by:

$$\omega_a = \sqrt{\frac{k_a + m_a g r_a}{I_{a/C}}} \tag{4.73}$$

$$\zeta_a = \frac{c_a}{2 I_{a/c}\omega_a} \tag{4.74}$$

where, the total equivalent rotational stiffness coefficient of the system, k_{eq}, is:

$$k_{eq} = k_a + m_a g r_a \tag{4.75}$$

4.4.2. Cantilever-type TMD

Another possible modeling of an absorber which can provide a rotational motion, is the cantilever-type TMD. A cantilever Euler-Bernoulli beam serves to provide the stiffness and damping coefficients of the TMD and a mass is placed on the beam's longitudinal axis to obtain the cantilever-type TMD illustrated in Figure 4.5. This TMD

can be optimized to reduce the amplitude at the critical frequency of the patient's tremor, which depends on the muscles activity.

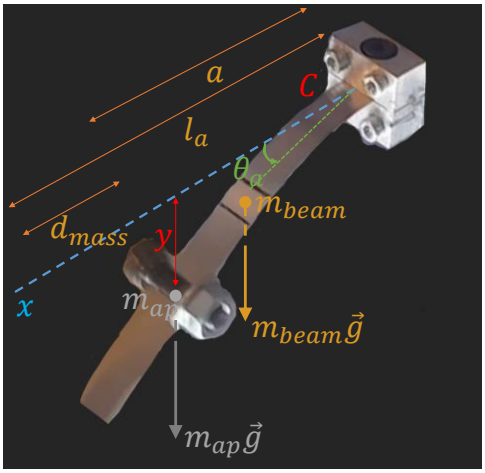

Figure 4.5: Cantilever-type TMD

The fundamental frequency of such continuous system can be calculated using Dunkerley's formula [143-145]. It approximates the fundamental frequency of a composite system as a function of the natural frequency of its components. The principle is based on the fact that the fundamental frequency of the system is very small compared to its high order natural frequencies. The approximated fundamental frequency is always smaller than the exact value.

Dunkerley's semi-empirical formula is applied to the Cantilever-type TMD by dividing the system, as shown in Figure 4.6, into Euler-Bernoulli cantilever beam and a massless rod with a mass attached at a position a. Dunkerley's formula is written as:

$$\frac{1}{\omega_a^2} \simeq \frac{1}{\omega_{ap}^2} + \frac{1}{\omega_{1_{beam}}^2} \tag{4.76}$$

where, ω_a is the fundamental angular frequency of the TMD system, ω_{ap} is the natural angular frequency of the concentrated mass mounted on the massless rod, and $\omega_{1_{beam}}$ is the fundamental angular frequency of the cantilever beam.

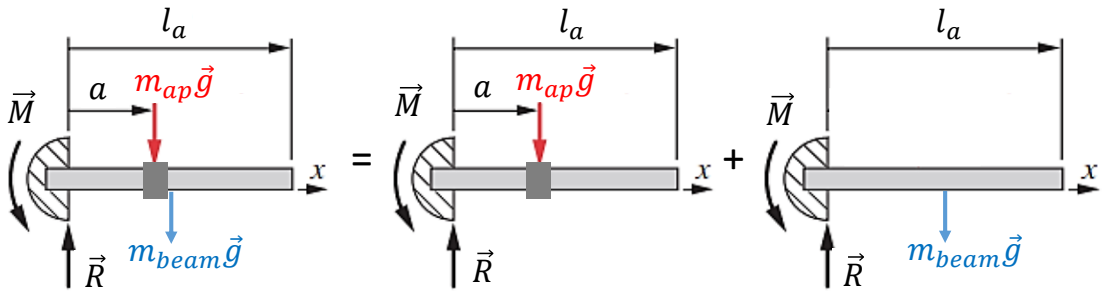

Figure 4.6: Decomposition of the compound cantilever-beam TMD

Total stiffness coefficient of the overall system in Figure 4.5 can't be extracted directly from the natural frequency formula obtained from (4.76). Providing two similar models for each part of the cantilever-type TMD with the same stiffness coefficient model for each, can help to obtain the total stiffness coefficient, k_x, and the effective mass, m_a, of this system. The natural angular frequency is required to have the form:

$$\omega_a = \sqrt{\frac{k_x}{m_a}} \tag{4.77}$$

The natural angular frequency ω_{ap} of a massless rod with a concentrated mass m_{ap} at a distance a from the fixed-end is:

$$\omega_{ap} = \sqrt{\frac{k_x}{m_{ap}}} \tag{4.78}$$

where, k_x represents the translational stiffness coefficient of such a system classically obtained by:

$$k_x = \frac{3E_{beam}I_0}{a^3} \tag{4.79}$$

where E_{beam} is the Young's modulus of the beam, and I_0 the cross-sectional area moment of inertia of the beam calculated as:

$$I_0 = \frac{1}{12} w_{beam} t_{beam}^3 \tag{4.80}$$

with t_{beam}, and w_{beam} are the thickness and the width of the beam, respectively. Then, the bending natural frequency of equation (4.78) becomes:

$$\omega_{ap} = \sqrt{\frac{3E_{beam}I_0}{m_{ap}a^3}} \tag{4.81}$$

The cantilever beam is vibrating transversally. The natural angular frequency $\omega_{n_{beam}}$ of the cantilever Euler-Bernoulli beam is expressed as:

$$\omega_{n_{beam}} = (\beta_n l_a)^2 \sqrt{\frac{E_{beam}I_0}{\rho_{beam} \times S_{beam} l_a^4}} = (\beta_n l_a)^2 \sqrt{\frac{E_{beam}I_0}{m_{beam} l_a^3}} \tag{4.82}$$

where, n is the mode number. $(\beta_n l_a)$ is a solution of the transcendental equation corresponding to boundary conditions studied, l_a and S_{beam} are the length and the cross-sectional area of the beam, and ρ_{beam} and m_{beam} are the density and mass of the beam.

So, the fundamental angular frequency of the beam is:

$$\omega_{1_{beam}} = (\beta_1 l_a)^2 \sqrt{\frac{E_{beam} I_0}{m_{beam} l_a^3}} \text{ with } (\beta_1 l_a) \simeq 1.875 \text{ for cantilever beam} \tag{4.83}$$

The cantilevered beam alone can also be modeled as a massless rod with an effective beam mass, $m_{eff_{beam}}$, placed at the position a, as it is the case for the concentrated load m_{ap}. In other words, the beam has the same stiffness coefficient k_x of equation (4.79). The effective mass of the beam, $m_{eff_{beam}}$, can be deduced using its natural frequency determined by equation (4.83) and the stiffness in equation (4.79), it is obtained as:

$$m_{eff_{beam}} = \frac{3}{(\beta_1 l_a)^4} \left(\frac{l_a}{a}\right)^3 m_{beam} \tag{4.84}$$

It is used to calculate the total mass defined in equation (4.77) as follows:

$$m_a = m_{ap} + \frac{3}{(\beta_1 l_a)^4} \left(\frac{l_a}{a}\right)^3 m_{beam}, \qquad \forall\, a \in [0, l_a] \tag{4.85}$$

Substituting (4.81) and (4.83) into (4.76), we get the natural frequency of the cantilever-type TMD (Figure 4.5):

$$\omega_a \simeq (\beta_1 l_a)^2 \sqrt{\frac{3 E_{beam} I_0}{3 m_{beam} l_a^3 + (\beta_1 l_a)^4 m_{ap} a^3}}, \qquad \forall\, a \in [0, l_a] \tag{4.86}$$

Its natural frequency expressed using k_x and m_a determined in (4.79) and (4.85), respectively, is:

$$\omega_a \simeq \sqrt{\frac{\frac{3 E_{beam} I_0}{a^3}}{m_{ap} + \frac{3}{(\beta_1 l_a)^4} \left(\frac{l_a}{a}\right)^3 m_{beam}}} \tag{4.87}$$

which provides a useful expression for the natural frequency already determined in (4.86). Since the cantilever-type TMD compound system is modeled at the end as a point mass placed at a distance a along the massless rod, then the centroid position r_a and the mass moment of inertia at the centroid I_a of the system are:

$$r_a = a \tag{4.88}$$

$$I_a = 0 \tag{4.89}$$

Note that the equivalent stiffness coefficient of the pendulum-type TMD in (4.73) includes the spring's stiffness coefficient, k_a, in addition to a stiffness resulting from the gravitational potential energy $m_a g r_a$. However, the natural frequency of the beam-type TMD has just the stiffness coefficient term. So, the stiffness coefficient of the beam that replace the pendulum's stiffness, in the derived equations of motion for the upper limb with TMD, and which will be optimized later, must maintain the natural frequency formular of the beam-type TMD.

To preserve the beam stiffness (4.79) after replacing the pendulum TMD by the beam TMD, and according to equation (4.75), the stiffness of the pendulum have to be replaced by:

$$k_a = \frac{E_{beam} I_0}{a} - m_a g r_a \tag{4.90}$$

Its effect can be more clear while substituting (4.90) in the single pendulum's differential equation (4.72) to left out by just the beam's stiffness value (4.79).

4.5. TMD optimization for classical system

The spring coefficient of an undamped absorber, for a given mass, is usually tuned to the undesired resonance frequency of the structure (or principle system). However, the natural frequency of the global system (primary system with TMD) is often not exactly equal to the natural frequency of the principle system after the addition of the TMD. The choice of the TMD's parameters needed to obtain the best attenuation is not obvious, as the highest damping added to the system does not necessarily cause an improvement in the amplitude reduction. As a result, the absorber's stiffness and damping coefficients have to be optimized in order to provide the best attenuation.

A MATLAB code has been programmed to solve the response of the modeled upper limb (Figure 4.1) and to calculate numerically the optimum TMD(s) parameters using the *fminsearch* built in function. The results obtained by such a program are first verified with the analytical formulas provided for 1DOF classical system. The equation of motion for the forced damped 1DOF structure with one TMD (Figure 4.7) is given by:

$$\begin{bmatrix} m_s & 0 \\ 0 & m_a \end{bmatrix} \begin{Bmatrix} \ddot{x}_s \\ \ddot{x}_a \end{Bmatrix} + \begin{bmatrix} c_s + c_a & -c_a \\ -c_a & c_a \end{bmatrix} \begin{Bmatrix} \dot{x}_s \\ \dot{x}_a \end{Bmatrix} + \begin{bmatrix} k_s + k_a & -k_a \\ -k_a & k_a \end{bmatrix} \begin{Bmatrix} x_s \\ x_a \end{Bmatrix} = \begin{Bmatrix} f(t) \\ 0 \end{Bmatrix} \tag{4.91}$$

where, m, k, and c are the mass, spring, and damper, respectively. The subscripts s and a correspond to the structure and the absorber, respectively. $f(t)$ is the external force applied on the structure. x_s and x_a are the displacement signals of the structure and the absorber, respectively. It can be written in the form:

$$\mathrm{M}\ddot{x} + \mathrm{C}\dot{x} + \mathrm{K}x = \mathrm{F}(t) \tag{4.92}$$

with,

$$\mathrm{M} = \begin{bmatrix} m_s & 0 \\ 0 & m_a \end{bmatrix}, \ \mathrm{C} = \begin{bmatrix} c_s + c_a & -c_a \\ -c_a & c_a \end{bmatrix}, \ \mathrm{K} = \begin{bmatrix} k_s + k_a & -k_a \\ -k_a & k_a \end{bmatrix}, \quad \text{and } \mathrm{F}(t) = \begin{Bmatrix} f(t) \\ 0 \end{Bmatrix} \tag{4.93}$$

where, $x = \{x_s \quad x_a\}^T$ is the displacement vector of the system. This system is assumed to operate with zero intial conditions.

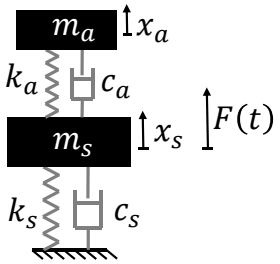

Figure 4.7: Diagram of a structure with damping and one TMD

The Laplace transform $\mathcal{L}$ can be applied to the differential equation (4.93) using:

$$X(j\omega) = \mathcal{L}\{x(t)\}, \qquad f(j\omega) = \mathcal{L}\{f(t)\}, \qquad \text{and} \quad \mathcal{F}(j\omega) = \mathcal{L}\{\mathrm{F}(t)\} \tag{4.94}$$

to obtain the equation in the frequency domain:

$$[-\omega^2\mathrm{M} + j\omega\mathrm{C} + \mathrm{K}]X(j\omega) = \mathcal{F}(j\omega) \tag{4.95}$$

where, $X = \{X_s \quad X_a\}^T$ with X_s and X_a the Laplace transforms of the structure and absorber displacements, respectively. The transfer function of the system, $\mathrm{H}(j\omega)$, is given by:

$$\mathrm{H}(j\omega) = \frac{X(j\omega)}{\mathcal{F}(j\omega)} = [-\omega^2\mathrm{M} + j\omega\mathrm{C} + \mathrm{K}]^{-1} \tag{4.96}$$

By substituting (4.93) in (4.96), we get:

$$\mathrm{H}(j\omega) = \frac{\begin{bmatrix} -\omega^2 m_a + k_a + j\omega c_a & k_a + j\omega c_a \\ k_a + j\omega c_a & -\omega^2 m_s + (k_s + k_a) + j\omega(c_s + c_a) \end{bmatrix}}{|-\omega^2 \mathrm{M} + j\omega \mathrm{C} + \mathrm{K}|} \tag{4.97}$$

The determinant is written as follows:

$$\begin{aligned} &|-\omega^2 \mathrm{M} + j\omega \mathrm{C} + \mathrm{K}| \\ &\quad = m_s m_a \omega^4 - [c_s c_a + m_a(k_s + k_a) + k_a m_s]\omega^2 + k_s k_a \\ &\quad + j[(k_s c_a + c_s k_a)\omega - (c_a(m_s + m_a) + c_s m_a)\omega^3] \end{aligned} \tag{4.98}$$

The frequency response function of the structure can be written as:

$$H_{11}(j\omega) = \frac{X_s(j\omega)}{f(j\omega)} = \frac{(k_a - \omega^2 m_a) + j\omega c_a}{|-\omega^2 \mathrm{M} + j\omega \mathrm{C} + \mathrm{K}|} \tag{4.99}$$

with, $f(j\omega)$ the Laplace transform of the force applied on the system.

In the following, calculations will be done for the study case defined by:

$$m_s = 10\ kg,\ \ k_s = 200\ N/m,\ \ c_s = 0.1k_s,\ \text{ and }\ f_0 = 1\ N \tag{4.100}$$

The natural frequency of the studied system is:

$$\omega_s = 4.47\ rad/s \quad \text{or} \quad 0.71\ Hz \tag{4.101}$$

4.5.1. Classical optimization procedure

It is not always possible to uncouple the equation of motion in (4.91) is not necessary to be in the modal coordinate system due to the unpredictable damping coefficient of the TMD [140]. Even if the damping coefficient of the structure satisfies the linear combination of its mass and stiffness matrices, this is not necessarily the case for the global system composed of the structure and TMD. Hence, the damping matrix of the global system doesn't satisfy the proportional damping condition stated below:

$$\mathrm{C} = \gamma \mathrm{M} + \lambda \mathrm{K} \tag{4.102}$$

where, γ and λ are constant values.

Due to this fact, the exponential approach was suggested to solve this problem and obtain the response of the structure by nearly most of the research works which intend to obtain the analytical solution of the optimized TMD's parameters [146-149].

Then, the harmonic forcing function exerted on the system can have the complex form:

$$f(j\omega) = f_0 e^{j\omega t} = f_0(\cos\omega t + j\sin\omega t) \tag{4.103}$$

and so, the particular response takes the form:

$$X(j\omega) = Ae^{j\omega t} \tag{4.104}$$

$A = \{A_s \quad A_a\}^T$ is the amplitude vector, such that A_s and A_a are the amplitudes of the particular response related to the structure and the absorber, respectively. Using (4.103) and (4.104), then the absolute value of $H(j\omega)$ in equation (4.96) becomes:

$$|\mathrm{H}(j\omega)| = \left|\frac{Ae^{j\omega t}}{f_0 e^{j\omega t}}\right| = \frac{A}{f_0} \tag{4.105}$$

The deflection δ_{st} of the structure under the static force f_0 is provided as:

$$\delta_{st} = \frac{f_0}{k_s} \tag{4.106}$$

which is used to define the magnification factor (also known as the amplification factor or the amplitude ratio), MF, which represents the dynamic to the static amplitude ratio, and is defined as:

$$MF = \frac{k_s A_s}{f_0} \; or \; \frac{A_s}{\delta_{st}} \tag{4.107}$$

The magnification factor defined in (4.105) is used with the modulus of the complex response function of equation (4.99) to obtain the following dimensionless equation [150]:

$$\frac{A_s}{\delta_{st}} = \sqrt{\frac{\left(1-\frac{r^2}{\beta^2}\right)^2 + 4\left(\zeta_a\frac{r}{\beta}\right)^2}{\left[\frac{r^4}{\beta^2} - \left(\frac{4\zeta_a\zeta_p}{\beta} + \frac{1}{\beta^2} + \mu + 1\right)r^2 + 1\right]^2 + \cdots \\ 4\left[r\left(\zeta_s + \frac{\zeta_a}{\beta}\right) - \frac{r^3}{\beta}\left(\zeta_a + \frac{\zeta_s}{\beta}\right) - \frac{r^3}{\beta}\zeta_a\mu\right]^2}} \tag{4.108}$$

such that,

$$\omega_s = \sqrt{\frac{k_s}{m_s}}, \qquad \omega_a = \sqrt{\frac{k_a}{m_a}}, \qquad \zeta_s = \frac{c_s}{2m_s\omega_s}, \qquad \zeta_a = \frac{c_a}{2m_a\omega_a}, \\ \mu = \frac{m_a}{m_s}, \qquad \beta = \frac{\omega_a}{\omega_s}, \qquad \text{and} \quad r = \frac{\omega}{\omega_s} \tag{4.109}$$

where, ω_s and ζ_s are the uncoupled natural angular frequency and damping ratio of the structure alone. ω_a and ζ_a are the decoupled natural frequency and the damping ratio of the absorber before being attached to the structure, respectively. μ is the mass ratio of the TMD's mass to the structure's mass. β is the ratio of the uncoupled natural angular frequencies (TMD's frequency ratio). r is the angular frequencies normalized to the uncoupled natural angular frequency of the structure. The TMD to be tested, is chosen to have:

$$\mu = 0.2 \tag{4.110}$$

4.5.1.1. Undamped structure

The undamped absorber ($\zeta_a = 0$) can be tuned to the driving frequency ($\beta = 1$) to reduce the maximum amplitude of the structure to zero, where the numerator in (4.118) vanishes as mentioned in Frahm [101]. However, when the TMD is damped, its numerator can't be exactly equal to zero. In this case, the TMD's parameters have to be optimized to obtain the maximum possible reduction. Den Hartog [146] was the first to identify the TMD's optimal parameters (β_{opt} and ζ_{opt}) for the undamped principle structure, where c_s in equation (4.92) is zero. The optimal parameters were obtained to minimize the structural maximum displacement amplitude of the structure, for $\zeta_s = 0$ in equation (4.108). Their determination is based on the existence of the two invariant points P and Q, which have the same amplification level regardless of the TMD's damping ratio ζ_a. The formulas obtained for β_{opt} and ζ_{opt} are:

$$\beta_{opt} = \frac{1}{1+\mu} \tag{4.111}$$

$$\zeta_{a,opt} = \sqrt{\frac{3\mu}{8(1+\mu)}} \tag{4.112}$$

For $\beta = \beta_{opt}$ and $\zeta_a = \zeta_{a,opt}$, the optimal parameters of the TMD obtained for the numerical values system chosen in equation (4.100), are calculated using equation (4.109) and listed in Table 4.3. The analytical optimal values are compared to the numerical ones obtained using the MATLAB code developed to optimize the parameters of the TMD(s) added to the modeled upper limb system. It shows that the analytical and numerical methods give almost the same results. The optimum frequency of the TMD in Table 4.3 is shifted from the natural frequency of the system given by (4.101), for which the optimum frequency ratio $\beta = 0.83$ is obtained to provide the maximum amplitude reduction for a damping value $\zeta_a = 0.25$.

Table 4.3: Optimal TMD's parameters obtained using Den Hartog [146] **analytical formulas compared to the one obtained by numerical simulations**

Optimal parameters $(c_p = 0)$	ω_a (rad/s)	β	ζ_a	k_a (N/m)	c_a (kg/s)
Den Hartog	3.727	0.833	0.2500	27.778	3.727
Numerical simulations	3.727	0.833	0.2504	27.772	3.732

The frequency responses of the structure without TMD, with tuned undamped TMD, and with the optimized TMD using the numerical values are compared and depicted in Figure 4.8a. The safe operational bandwidth of the tuned undamped TMD, where $MF \leq 1$, lies between $0.93\omega_s$ and $1.10\omega_s$. If the excitation frequency shifts within this range, the absorber will provide a protection for the system. If the operational frequency drifts to $0.80\omega_s$ or $1.25\omega_s$, which are the combined natural frequencies of the system, the system will experience resonance and fails. The TMD in this case will operate with very high amplitude especially at the combined system's frequencies, as shown in Figure 4.8b. In the case of the optimized TMD, a magnification factor between 2.9–3.3 is experienced by the structure when the driving frequencies are between $0.70\omega_s$ and $1.15\omega_s$, which reduces gradually elsewhere. This improvement in the system's response can be reached by the optimized TMD when operating with low amplitudes, as shown in Figure 4.8b.

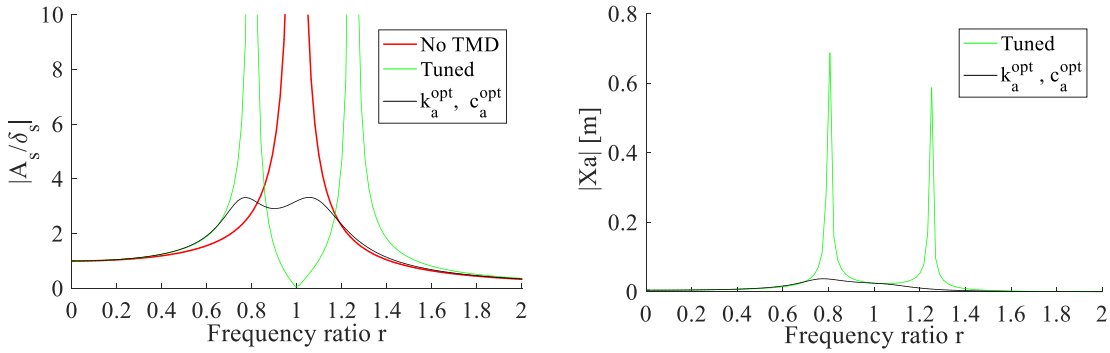

(a) (b)

Figure 4.8: Responses of the (a) structure and (b) absorber using the tuned absorber and the optimized TMD when the structure is undamped and subjected to a constant force

The response of the structure in equation (4.108) for different TMD's damping ratios ζ_a including the optimal damping, while its frequency ratio is fixed to the optimal value, is shown in Figure 4.9. The graph illustrates the two invariant points P and Q, which were used by Den Hartog [146] to obtain the analytical formulas in (4.111) and (4.112). The magnification factor at the level of these points is 3.31, which occurs at the driving frequencies $0.75\omega_s$ and $1.05\omega_s$. The TMD with the optimal damping ratio seems to be the best design choice.

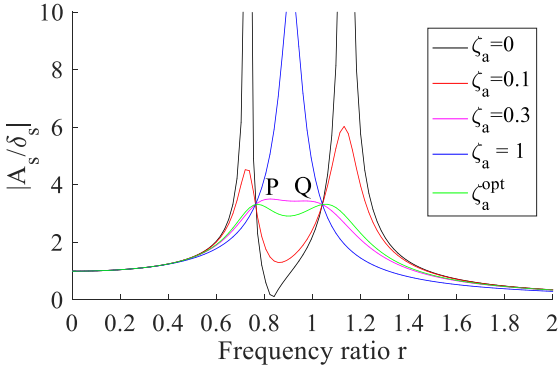

Figure 4.9: Response of the undamped structure subjected to a constant force using the optimized frequency ratio β=0.8333 for different damping ratio ζ_a

4.5.1.2. Damped structure

Ioi and Ikeda [147] derived the analytical formulas for the optimum TMD parameters (β_{opt} and ζ_{opt}) to minimize the response amplitude in equation (4.108) for the damped system, which are obtained as:

$$\beta_{opt} = \frac{1}{1+\mu} - (0.241 + 1.7\mu - 2.6\mu^2)\zeta_s - (1 - 1.9\mu + \mu^2)\zeta_s^2 \qquad (4.113)$$

$$\zeta_{opt} = \sqrt{\frac{3\mu}{8(1+\mu)}} + (0.13 + 0.12\mu + 0.4\mu^2)\zeta_s - (0.01 + 0.9\mu + 3\mu^2)\zeta_s^2 \qquad (4.114)$$

A comparison between the optimal parameters obtained by Ioi and Ikeda [147] and the numerical optimization for the considered system is shown in Table 4.4. Again, the parameters obtained numerically match with the analytical ones which needs derivation and much more effort, especially if the considered system is more complex.

Table 4.4: Optimal TMD's parameters obtained using Ioi and Ikeda [147] **analytical formulas compared to the ones obtained by numerical simulation**

Optimal parameters $(c_p = 0.1k_p)$	ω_a (rad/s)	β	ζ_a	k_a (N/m)	c_a (kg/s)
Ioi and Ikeda	3.102	0.694	0.273	19.25	3.38
Numerical simulation	3.088	0.690	0.275	19.06	3.40

It is more difficult to reach high amplitude reduction for a structure with damping. The tuned undamped TMD in Figure 4.10a shows safe operation within a narrow bandwidth, where the magnification factor increases extremely while approaching the combined system's resonance frequencies. However, the optimized TMD is better for

protecting the system from extreme amplifications in the amplitude for wider range of frequencies. The structure will experience magnification factor between 2.7–5.5 when the excitation frequencies varies from $0.84\omega_s$ to $1.17\omega_s$, and less outside this range. The optimized TMD can reduce the amplitude of the structure while operating at a very low amplitude compared to the tuned absorber, as shown in Figure 4.10b.

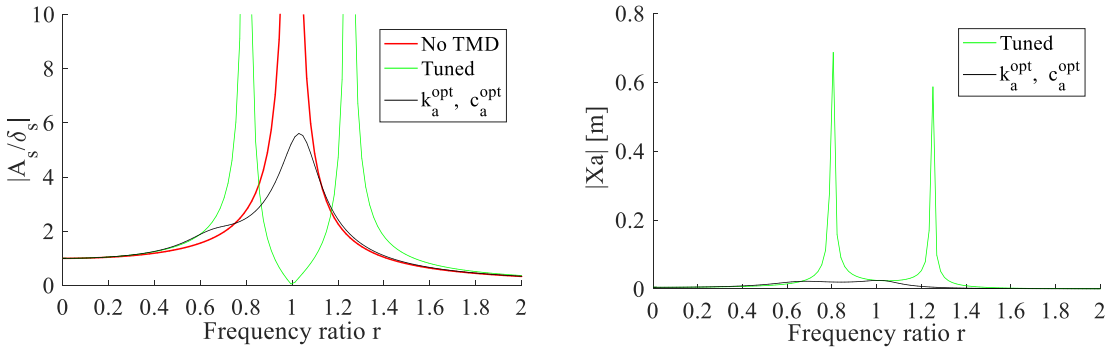

(a) (b)

Figure 4.10: Response of the (a) structure and (b) absorber using the tuned absorber and the optimized TMD when the structure is damped and subjected to a constant force

The effect of changes in the TMD's damping ratio, with the optimal TMD's frequency ratio fixed (Table 4.4), is represented in Figure 4.11. That the graphs intersect at two fixed points P and Q, whatever the damping ratio used. Unlike the undamped structure, the points P and Q have different amplitude level. The amplitudes are equal to 2.12 and 5.21, which occurs at $0.67\omega_s$ and $0.99\omega_s$ for points P and Q, respectively.

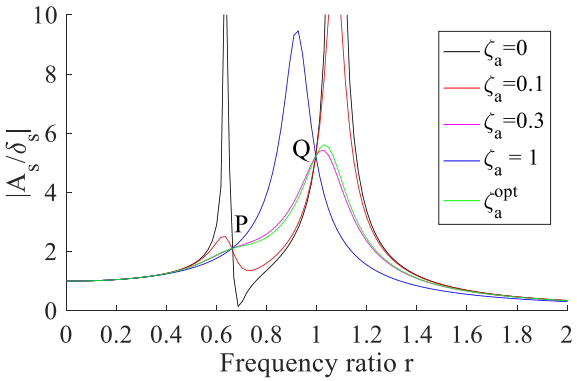

Figure 4.11: Response of the damped structure subjected to a constant force using the optimized frequency ratio β=0.6903 for different damping ratios ζ_a

The exponential approach procedure (equations (4.103) to (4.105)) is used to derive the magnification factor (4.108). It delivers a simple technique used to obtain the response amplitude when the force excites the structure at the resonance frequency. The analytical formulas of the optimum TMD's parameters provided by Den Hartog [146] and Ioi and Ikeda [147] were derived based on the minimization of this response amplitude, which is provided by (4.108). In addition, this method doesn't take into account the type of the

excitation force, but just its amplitude. However, some systems may operate at different frequencies, as it is the case for the involuntary tremor in Patient's upper limbs. The critical frequencies of the measured tremor signals were demonstrated to be the muscles driving frequencies, measured using EMG, which are not necessarily the natural frequencies of the upper limb.

It is difficult or nearly impossible to follow the same procedure, and obtain the magnification factor using the dimensionless parameters (as provided by (4.108)), for the dynamic model of the upper limb. Indeed, it is difficult to derive the amplification factor for the equation of motion obtained by (4.43), especially because of its non-diagonal mass matrix that includes more terms. Thus, as the muscular force has random motion having no specific analytical form, an alternative approach is needed. It is required to optimize the TMD's parameters for different type of excitation force and for any excitation frequency.

4.5.2. Optimization strategy

Improvements in the previous optimization steps are added to make it convenient more cases of studies. An example is shown for a sinusoidal applied force, of the form:

$$f(t) = f_0 \sin \omega_{dr} t \tag{4.115}$$

This force can be represented in the frequency domain as:

$$f(j\omega) = \frac{f_0 \omega_{dr}}{\omega_{dr}^2 - \omega^2} \tag{4.116}$$

such that, ω_{dr} is the driving frequency of the exciter that can be or not the natural frequency of the structure. Then, the displacement in the frequency domain is written as:

$$X(j\omega) = [-\omega^2 \mathrm{M} + j\omega \mathrm{C} + K]^{-\mathbf{1}} \times \frac{f_0 \omega_{dr}}{\omega_{dr}^2 - \omega^2} \tag{4.117}$$

Note that the forced response represented by equation (4.117) can have experience critical amplitudes when the frequency is at the natural frequency $(\omega = \omega_s)$, due to the first part related to the transfer function, and at the excitation frequency $(\omega = \omega_{dr})$, due to the excitation force type. This forced response is solved and optimized numerically using the MATLAB code developed to optimize the tremor absorber parameters.

Using the transfer function $\mathrm{H}(j\omega)$ defined in equations (4.96) or (4.97), the response of the system is written as:

$$X(j\omega) = \mathrm{H}(j\omega)\frac{f_0\omega_{dr}}{\omega_{dr}^2 - \omega^2} \tag{4.118}$$

So, the magnification factor of the structure is obtained as:

$$\left|\frac{\omega_s X_s(j\omega)}{\delta_{st}}\right| = \sqrt{\frac{\left(1-\frac{r^2}{\beta^2}\right)^2 + 4\left(\zeta_a\frac{r}{\beta}\right)^2}{\left[\frac{r^4}{\beta^2} - \left(\frac{4\zeta_a\zeta_p}{\beta} + \frac{1}{\beta^2} + \mu + 1\right)r^2 + 1\right]^2 + \cdots} \times \frac{\alpha}{\alpha^2 - r^2}} \tag{4.119}$$
$$\sqrt{4\left[r\left(\zeta_s + \frac{\zeta_a}{\beta}\right) - \frac{r^3}{\beta}\left(\zeta_a + \frac{\zeta_s}{\beta}\right) - \frac{r^3}{\beta}\zeta_a\mu\right]^2}$$

with,

$$\alpha = \frac{\omega_{dr}}{\omega_s} \tag{4.120}$$

defined as the system's frequency ratio. Note that α is the frequency ratio that occurs at the driving frequency of the system, which can be the natural frequency of the uncoupled system or a different excitation frequency.

4.5.2.1. Operation at resonance frequency

The response in (4.119) is optimized for the structure parameters considered by equation (4.100) with an excitation at natural frequency (which is defined in (4.101)). The new optimal parameters of the TMD obtained for the undamped and damped systems are shown in Table 4.5. They can be compared to those of Den Hartog [146] and Ioi and Ikeda [147], which are provided by Table 4.3 and Table 4.4, respectively. Table 4.5 shows that the optimal parameters are different from those obtained using the classical optimization procedure. When the Laplace transform of the force is considered, the optimal angular frequency of the TMD, ω_a, tends to be closer to the resonance frequency of the system, even if the structure is damped.

Table 4.5: Optimal TMD's parameters obtained numerically for the undamped and the damped systems when the TMD is operating at the resonance frequency

Optimal parameters	ω_a (rad/s)	β	ζ_a	k_a (N/m)	c_a (kg/s)
$c_p = 0$	4.41	0.986	0.046	38.86	0.80
$c_p = 0.1k_p$	4.45	0.994	0.008	39.54	0.15

The frequency response of the structure, with the optimized TMD, excited by a sinusoidal force at the resonance frequency is depicted in Figure 4.12. The system shows an unusual response behavior. When the Laplace transform of the force is considered within the response, a peak appears at the driving frequency, which is the natural frequency of the uncoupled system. The two other peaks, which normally exist, are at the combined system's natural frequencies. For the undamped system (Figure 4.12a), 0.5% of the response amplitude remains in the system at the first two peaks, which occurs at $0.79\omega_s$ and $0.99\omega_s$, and just 0.1% at the third peak at $1.24\omega_s$. The damped system's response in Figure 4.12b shows similar behavior, where 3.66% of the amplitude is visualized in the combined system at $0.82\omega_s$ and $1.01\omega_s$.

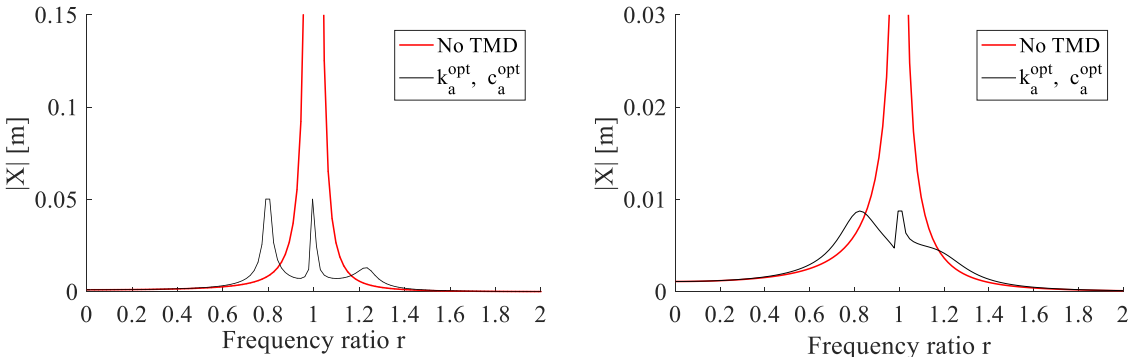

Figure 4.12: Response of the (a) undamped and (b) damped structure using the optimized TMD when subjected to a sinusoidal force operating at the resonance frequency

The existence of the two fixed points for the response provided in equation (4.119), is tested in Figure 4.13. It shows the response of the system for a fix optimal frequency (Table 4.4) with different the damping ratios around the optimal value. The Figure 4.13a shows the two points P and Q which are invariant for different damping ratios for the undamped system. These two points occur at the frequencies $0.83\omega_s$ and $1.13\omega_s$, which differs from that obtained using the classical optimization method. In addition, these two points are not on the same amplitude level anymore. For the damped system, Figure 4.13b shows that the graphs meet at two close frequencies, but they can't be considered as fixed. This fact makes it possible to derive the analytical formulas of the optimal parameters for the undamped system. However, it can be more complex when their is damping in the system exists.

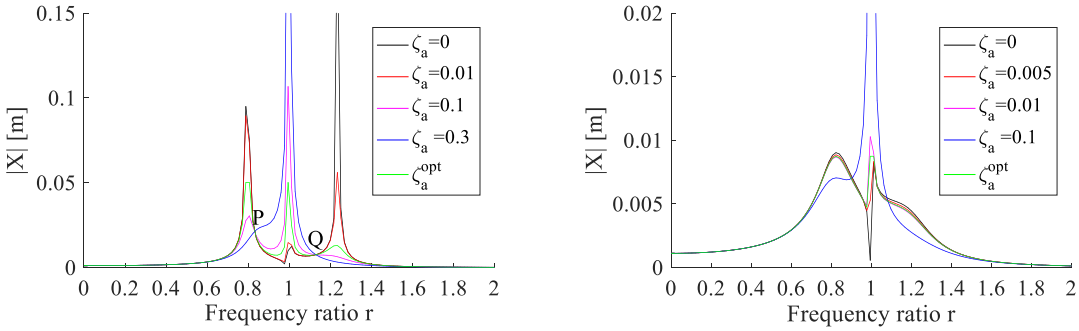

(a) (b)

Figure 4.13: Response of the system subjected to a sinusoidal force at the resonance frequency for different damping ratio ζ_a for the (a) undamped structure using the optimized frequency ratio β=0.9856 and (b) damped structure using the optimized frequency ratio β=0.9942

4.5.2.2. Operation at non-resonant frequency

The same structure's response as that obtained in equation (4.119), is feasible for a system with an excited at a frequency different from its natural frequency. The excitation frequency of the system is chosen as:

$$\omega_{dr} = 9.42\, rad/s \quad or \quad 1.5\, Hz \tag{4.121}$$

The optimal parameters of the TMD obtained for the undamped and damped system are found in Table 4.6. As for the Table 4.5, the TMD's optimal frequency is closer to the excitation frequency when the system is damped, while it is the opposite for the results obtained using the classical optimization in Table 4.3 and Table 4.4. Moreover, the optimal damping ratio obtained is smaller for the damped structure. So, the prediction of the TMD's parameters becomes more difficult when the driving frequency is equal to or different from the natural frequency, and for an undamped or damped structure. Using Table 4.6, the shifting in the TMD's optimal frequency can be now calculated using the following frequency ratio:

$$\frac{\omega_a}{\omega_{dr}} = \begin{cases} 1.12 & \text{for } c_p = 0 \\ 1.00 & \text{for } c_p = 0.1k_p \end{cases} \tag{4.122}$$

Table 4.6: Optimal TMD's parameters obtained numerically for the undamped and the damped systems when the TMD is operating at any frequency

Optimal parameters	ω_a (rad/s)	β	ζ_a	k_a (N/m)	c_a (kg/s)
$c_p = 0$	10.53	2.35	1.648e-08	221.8	6.9e-07
$c_p = 0.1k_p$	9.44	2.11	0.003	178.2	0.11

The frequency response of the structure with the optimized TMD, operating at a frequency different from the resonance frequency is shown in Figure 4.14. For, the undamped system (Figure 4.14a), a peak at the driving is has significant amplitude since the optimal damping ratio is very low. An additional frequency appears near the driving frequency due to the addition of the TMD to the structure and the natural frequency of the system is shifted. At both peaks, the amplitude is reduced. When the damping coefficient of the structure is considered, the peak amplitudes are reduced, especially at the natural frequency (Figure 4.14b). Two peaks with low amplitudes exist near the operating frequency of the system after the addition of the optimized TMD.

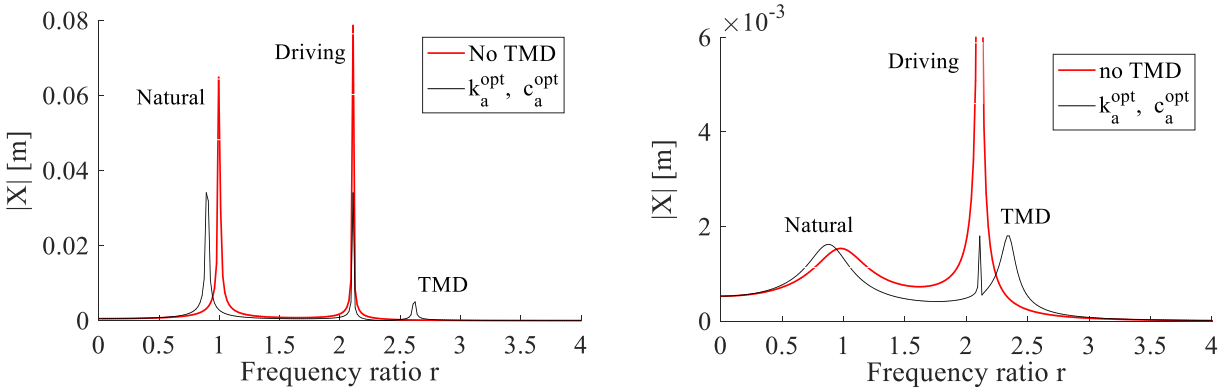

Figure 4.14: Response of the (a) undamped and (b) damped structure using the optimized TMD when subjected to a sinusoidal force operating at 1.5 Hz

The frequency response of the damped structure with an optimized TMD for different damping ratios ζ_a is depicted in Figure 4.15. It shows that the invariant points don't exist anymore. So, the derivation of the TMD's analytical model becomes more complex after considering the excitation force to reflect the actual response of the system under this type of load.

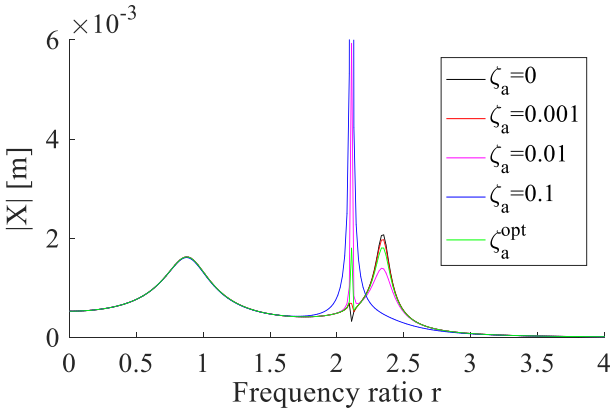

Figure 4.15: Response of the damped structure subjected to a sinusoidal force operating at 1.5 Hz using the optimized frequency of TMD for different damping ratio ζ_a

4.6. Input force of the dynamic model

The proposed dynamic model of the upper limbs (Figure 4.1) is excited by the measured muscular signal, i.e. the EMG dataset of a chosen patient is used as the active torque (equation (4.22)). The responses at the shoulder, elbow, and wrist proximal joints are solved numerically. The adjustment of the model's parameter such that the proximal joints responses have simultaneously the measured amplitude level was a difficult task. So, the muscle's voltage signal is scaled such that only the wrist joint response reaches the measured amplitude level and that the response of the shoulder and elbow joints have acceptable amplitude ranges. To reflect the measured tremor signals, the natural frequencies of the system are filtered. Later on, the filtered signal of the wrist joint is used to optimize the TMD parameters.

4.6.1. Patient's tremor

The EMG measurements of a new patient, "Patient 6" is shown in Figure 4.16a and Figure 4.16b, the PSD of these signals compared to the ones obtained from the finger's acceleration signals measured are shown in Figure 4.16c. Figure 4.16c reveals, as before, that the peaks present in the PSD acceleration signals reflect the muscles driving frequencies. The ECR and FCR muscles operate at the same frequencies which confirms to Raethje et al. [35]. The ECR signal presented in Figure 4.16a is used as an active torque at the proximal joints of the upper limb dynamic model.

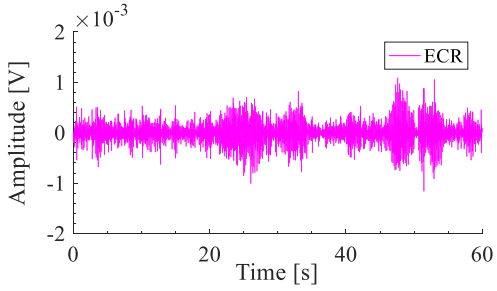

(a)

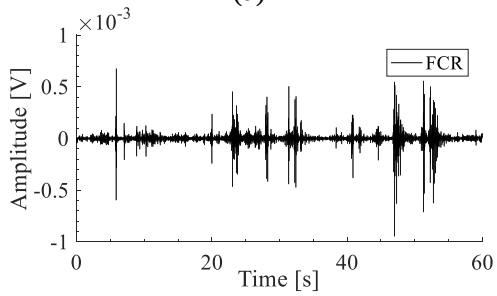

(b)

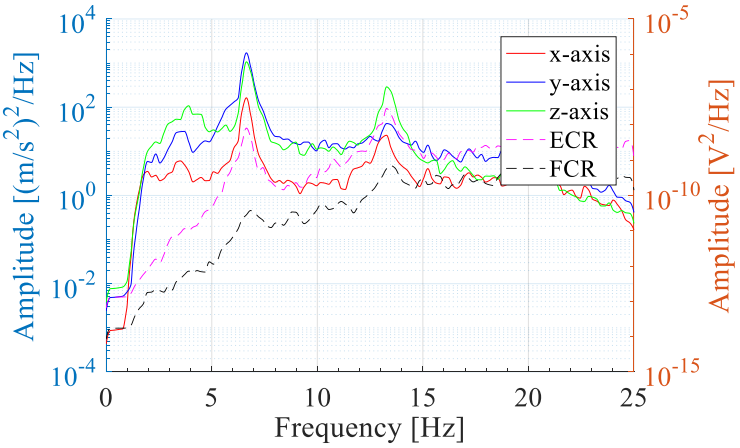

(c)

Figure 4.16: Electromyography recording of the (a) ECR and (b) FCR muscles, and (c) their PSD compared to the PSD of the x-, y-, and z-axis acceleration signals at the finger of "Patient 6"

The voltage signal of the ECR muscle will be scaled so that the dynamic system of the upper limb response reaches the angular displacement amplitude of the palm obtained using the IMU, to approach the active input moment of the ECR muscle. The angular velocity signal of the IMU $\dot{\theta}_y$ (Figure 4.17a) is integrated to obtain the angular displacement around the y-axis, θ_y, which is shown in Figure 4.17b. The displacement signal in the z-axis (vertical direction) is also presented in Figure 4.17c. The direction of the y- and z-axis of the IMU are already illustrated in Figure 3.2.

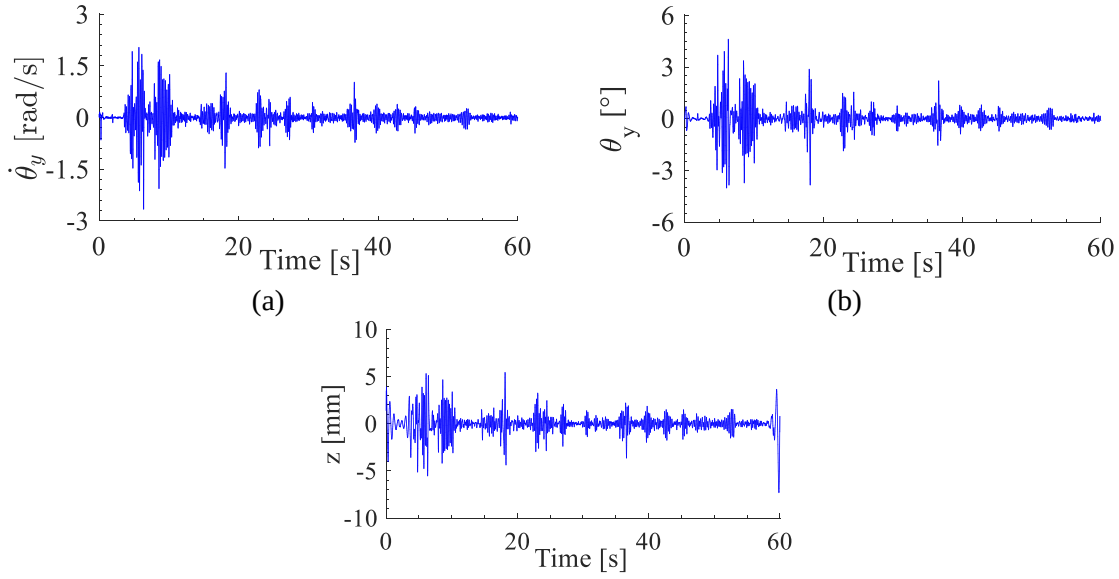

Figure 4.17: (a) Angular velocity, (b) angular displacement, and (c) vertical displacement signals obtained using the IMU

4.6.2. Response of the principle system

The response of the system excited at all its proximal joints by the ECR voltage signal of Figure 4.16a, without scaling, is depicted in Figure 4.18. The time signals of the flexion-extension angular displacement θ_1, θ_2, and θ_3 are obtained by solving (4.49), which correspond to the shoulder, elbow, and wrist joints, respectively. The time responses of the proximal joints are shown in Figure 4.18a. The PSD of the wrist joint response, presented in Figure 4.18b, shows peaks at frequencies corresponding to the natural frequencies of the system and others at driving frequencies of the muscle, obtained in Figure 4.16c. The natural frequencies of the designed principle system are:

$$f_s = \{0.75,\ \ 1.92,\ \ 4.01\}\, Hz \tag{4.123}$$

while the driving frequencies of the muscles are:

$$f_{dr} = \{6.63,\ \ 13.28\}\, Hz$$

The dominant frequency of such a system, as shown in Figure 4.18b, occurs at 6.63 Hz.

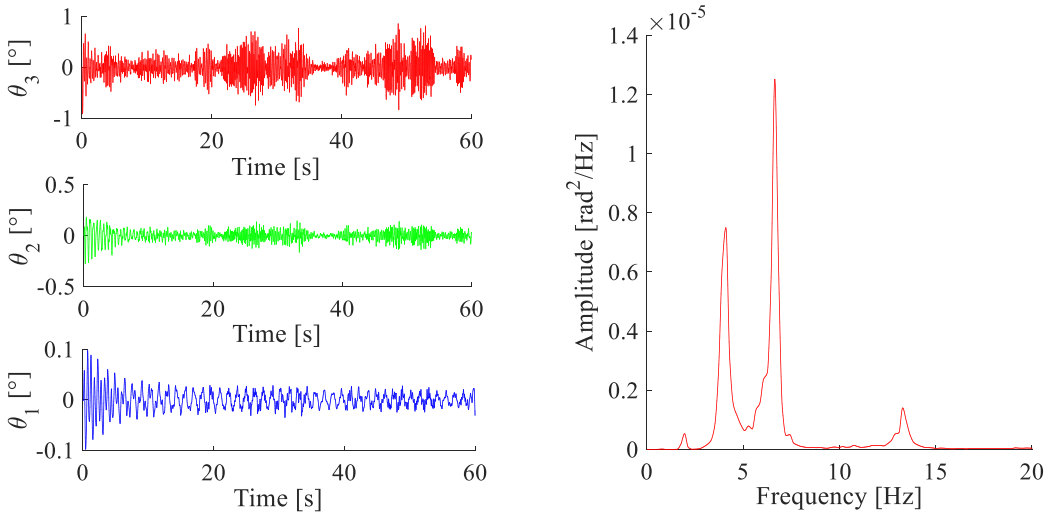

(a) (b)

Figure 4.18: (a) Angular displacement at the proximal joints and (b) PSD of the wrist joint angular displacement for the upper limb model excited by "Patient 6" muscular signal (not scaled)

The study concentrates on reducing the dominant peak of the wrist joint angular displacement which contributes to most of our daily tasks. The response amplitude is made to vary within a range of $\pm 5°$, similar to the measurement shown in Figure 4.17b, by scaling the ECR signal (Figure 4.19) to represent the active input torque for the system.

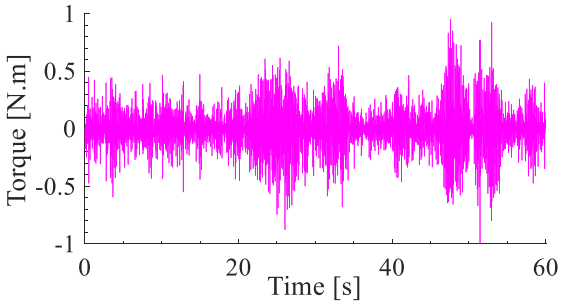

Figure 4.19: Scaled ECR signal used as an input torque to excite the dynamic model

Since the PSD of sensor's measurements of the hand tremor don't present the natural frequencies but just the driving frequencies (Figure 4.16), the natural frequencies of the upper limb model are filtered. The obtained responses of the proximal joints are presented in Figure 4.20a. The wrist joint response θ_3 in Figure 4.20a, has a similar amplitude level as θ_y in Figure 4.17b. The corresponding PSD is shown in Figure 4.20b.

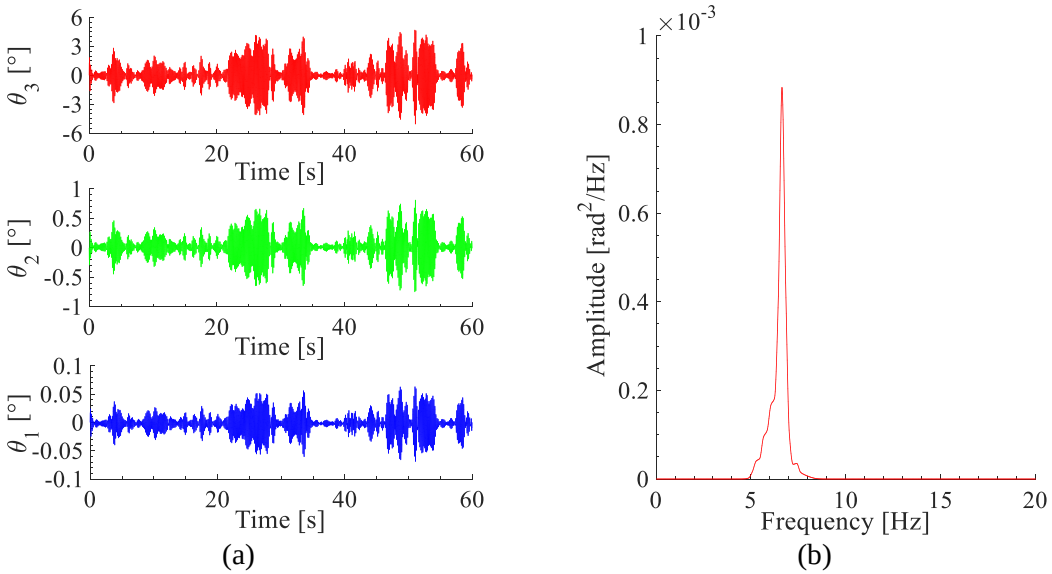

(a) (b)

Figure 4.20: (a) Filtered angular displacement at the proximal joints and (b) PSD of the wrist joint angular displacement for the upper limb model excited by "Patient 6" muscular signal (scaled)

The horizontal (x-axis) and vertical (y-axis) displacement response of the link ends, determined by equations (4.30) to (4.32) using the angular displacement of Figure 4.17a, are shown in Figure 4.21a and Figure 4.21b. The angular velocity of the modeled system obtained by solving (4.49) is shown in Figure 4.21c.

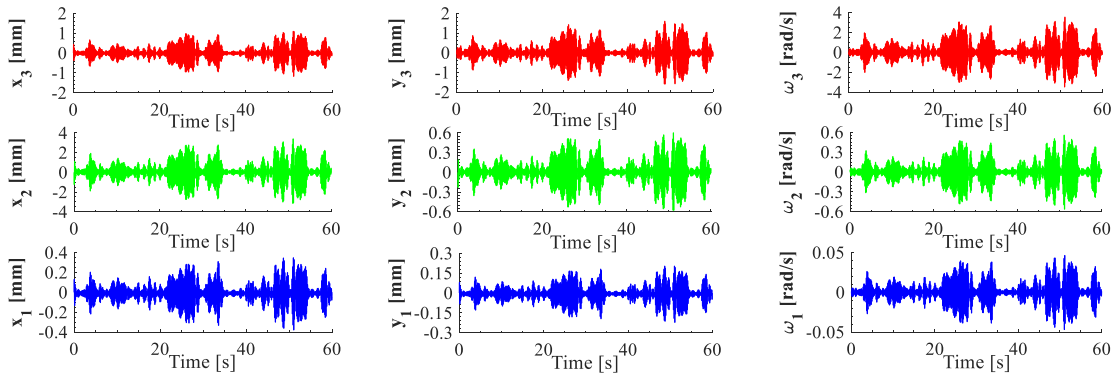

(a) (b) (c)

Figure 4.21: (a) Horizontal (x-axis) and (b) vertical (y-axis) displacements at the distal end of each segment and (c) angular velocity at the proximal joints, obtained by the upper limb model excited by "Patient 6" muscular signal (scaled)

4.7. Optimization steps

One or multiple TMD(s) are added to the upper limb system and optimized to reduce the angular displacement amplitude of the wrist joint. The measured muscle's signal is modeled and this model is used to excite the upper limb model. The experimental muscle's signals are also used directly as an inputs for the model to make it more realistic. The optimization steps followed are described below.

4.7.1. Optimization for the model of the muscle response

The equation of motion of the upper limb model (Figure 4.1) in the frequency domain, with TMD added to the forearm or palm segment, is represented as:

$$\Theta = [(\mathrm{M}s^2 + \mathrm{C}s + \mathrm{K} + \mathrm{G_k})^{-1}].\{\mathcal{F}\}, \quad \text{such that } \mathcal{F} = \{T_{a_1} \quad T_{a_2} \quad T_{a_3} \quad 0 \quad \dots \quad 0\}^T \tag{4.124}$$

where, $s = j\omega$. n is the number of DOF of the upper limb ($n = 3$), and m is the number of TMD. $\mathcal{F}$ is the $(n+m) \times 1$ vector representing the applied muscular torque. T_{a_i} is the active torque in the frequency domain, such that:

$$T_{a_i} = \mathcal{L}\{u_i\}. \tag{4.125}$$

u_i is the active input torque in the time domain. Since damping ratios obtained from of the ECR and FCR muscle response for several patients were measured (Figure 3.23) between 1.5–3.5%, the muscle's response shows an underdamped response behavior. Thus, the muscle motion is modeled as an underdamped system:

$$u(t) = u_0 e^{-j\zeta\omega_{dr}t} \sin(\omega_{d_m} t) \quad \text{where } \omega_{d_m} = \omega_{dr}\sqrt{1-\zeta^2} \tag{4.126}$$

where, u_0 is the amplitude of the torque. ζ is the damping ratio measured using the half-power bandwidth method [122,123]. ω_{dr} is the critical angular frequency of the peak. ω_{d_m} represents the damped angular frequency of the muscle. However, to get a response peak which occurs exactly at the critical frequency of the measured muscle's signal, the effect of the damping ratio at the operating frequency will be removed from (4.126). Therefore, the modeled signal of the muscles operating at two frequencies is represented as:

$$u(t) = u_{01} e^{-j\zeta_1 \omega_{dr_1} t} \sin\left(\omega_{dr_1} t\right) + u_{02} e^{-j\zeta_2 \omega_{dr_2} t} \sin\left(\omega_{dr_2} t\right) \tag{4.127}$$

This equation is used to fit the FFT of the measured ECR signal, presented in Figure 4.16a, and find the analytical formulation T_a (4.124) in the frequency domain. The subscripts 1 and 2 corresponds to the peak's number.

The Laplace transform of the signal defined in equation (4.127) is computed as follows:

$$\mathrm{T}_a = u_{01} \frac{\omega_{dr_1}}{s^2 + 2j\zeta_1 \omega_{dr_1} s + \omega_{dr_1}^2 (1 - \zeta_1^2)} + u_{02} \frac{\omega_{dr_2}}{s^2 + 2j\zeta \omega_{dr_2} s + \omega_{dr_2}^2 (1 - \zeta_2^2)} \tag{4.128}$$

The PSD of the measured ECR signal (Figure 4.16a) is scaled to the amplitude of the first critical peak of the fast Fourier transform (FFT) of the same ECR signal. The PSD of the ECR signal is used to obtain the parameters of analytical formulation (4.128) that can fit the FFT response of the ECR signal. The damping coefficients corresponding to the first and second peak of the PSD are calculated and peaks coordinates are obtained from Figure 4.22. The required parameters used to obtain the analytical formulation of the moment in (4.128) are:

$$u_{01} = 1.38\ N.mm,\ \ u_{02} = -3.22\ N.mm,\ \ \zeta_1 = 2.16\%,\ \ \zeta_2 = 1.15\%\,, \quad f_{dr_1} = 6.63\ Hz,\ \text{and}\ \ f_{dr_2} = 13.28\ Hz \tag{4.129}$$

Note that the calculated damping coefficients for the peaks of the PSD of the ECR muscle signal of "Patient 6" belong to the range 1.88–2.26% presented by Figure 3.23, which represents the damping ratios obtained for three patients after several measurements done for each. The formulated analytical input torque is shown in Figure 4.22. Thus, as a first approximation, the muscle's motion can be simply modeled by a second-order linear oscillation with additive dynamic noise, which can combine the representations obtained in [48, 51].

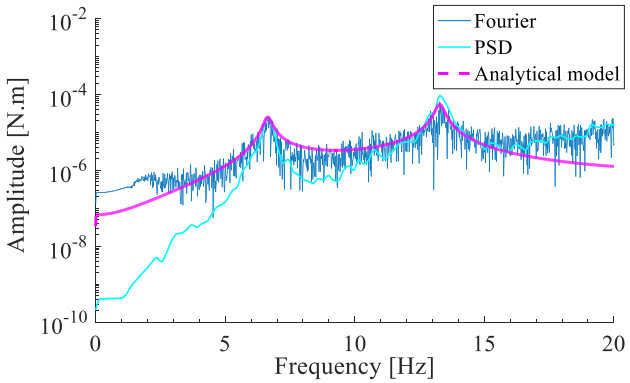

Figure 4.22: FFT, PSD, and fitting (analytical model) of the torque obtained for the measured ECR signal of "Patient 6"

The analytical modeling of the FFT of the ECR signal (Figure 4.22) is used as an input torque for the system's equation of motion in the frequency domain (equation (4.52)). The TMD is optimized when placed at the forearm segment of the upper limb to reduce the angular displacement critical amplitude of the wrist joint around the dominant peak. The frequency response using the Laplace transform in (4.52) of the proximal joints due to this input is presented in Figure 4.23a. All the proximal joints are excited with the same modeled torque. In Figure 4.23b, the response of the wrist joint signal due to an optimized TMD having 14.13 g mass is shown. The TMD is placed at 45% of the forearm segment length away from its proximal joint. The optimum parameters obtained for this TMD are:

$$d = 0.57\ mm, \qquad l_a = 5.3\ cm, \qquad \text{and} \qquad \zeta_a = 0.17\% \tag{4.130}$$

where, d is the diameter of the circular cross-section of the cantilever-type TMD.

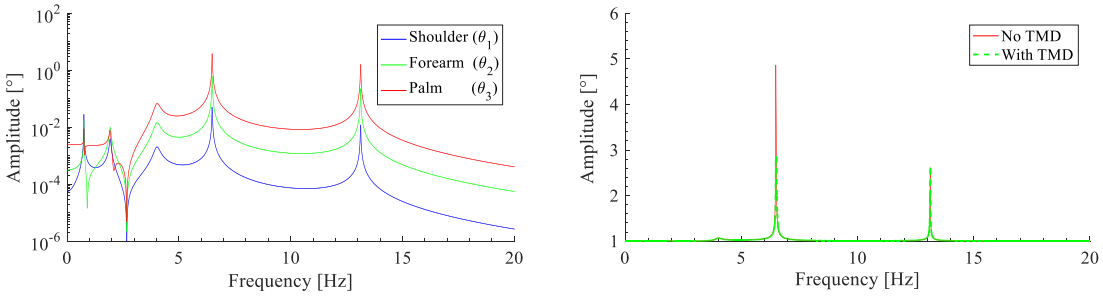

(a) (b)

Figure 4.23: Frequency response of (a) proximal joints signals without TMD and (b) wrist joint signal with optimized TMD located at the forearm for a system excited by the response of the ECR modeled analytically

4.7.2. Optimization for the measured muscle

The scaled time signal of the ECR muscles (Figure 4.19) is used as an input moment of the 3DOF principle system (equation (4.49)). Including the discrete dataset of the ECR

signal increases the simulation time to calculate the response of the system. The addition of TMDs increases the number of DOF of the system, and therefore, also the simulation time. A range is set for each TMD parameter x needed to be optimized using the function *fminsearch* in MATLAB, where x can be mainly the stiffness and damping coefficients of the TMD. The problem here comes from solving the time response several times for the parameter chosen by the program, starting from the initially specified value x_0 of the TMD parameters. When the iteration number exceeds a high value, a new initial parameter of the TMD is chosen and the operation is repeated again. It took more than 5 days waiting for the results of optimizing 1TMD in the time domain, but no convergence occurs. So, the optimization in the frequency domain seems to be a better solution.

The FFT of the muscle's signal is presented in Figure 4.24 and used as the active input moment to solve the equations of the system in the frequency domain. The frequency response is obtained from the Laplace transform of the ODE in (4.52). It is faster to solve the equations in the frequency domain than doing it in the time domain. So, the optimization process to minimize of the wrist joint amplitude is applied in the frequency domain.

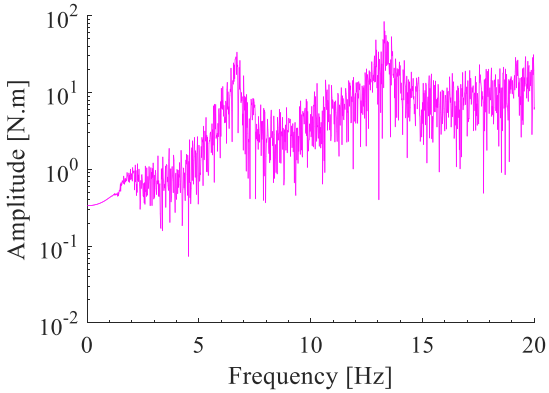

Figure 4.24: FFT of the scaled ECR signal

The following steps are used in the program to search for the optimal parameters of the TMD(s) x_{opti}:

1- The FFT of the ECR muscle signal is used as an input of the equation of motion (4.52). For a random set of optimal parameters x_i, the responses of the principle and global systems are solved, as shown in Figure 4.25a.
2- The inverse fast Fourier transform (IFFT) of the solved responses in frequency domain are used to obtain the corresponding time signals as shown in Figure 4.25b.
3- The PSD in Figure 4.25c are computed for the time signal (Figure 4.25b) filtered between 5.06 Hz and 7.23 Hz, representing the operational bandwidth around driving frequency (Figure 4.25a).

4- The reduction in the peak amplitude of the global system due to x_i is then calculated.

The program gives the optimal TMD parameters when it converges at the local minimum 'x_{opti}' needed to provide the minimum value of the wrist joint maximum amplitude.

Using this procedure, the time domain response due to the measured muscles signal of Figure 4.19 is optimized in an indirect way. After obtaining the optimal parameters, the time domain response can also be computed by solving (4.49) to compare the reduction produced by the optimized TMD in the time domain.

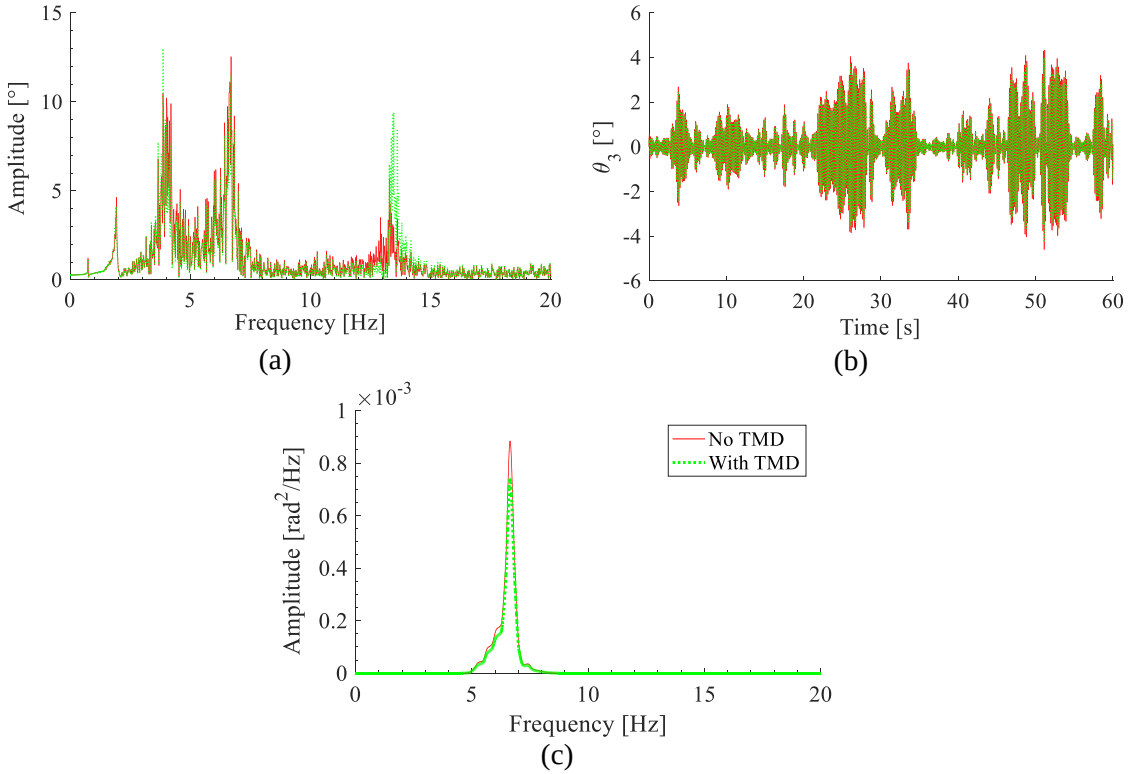

Figure 4.25: Steps used in the TMD optimization process (a) responses due to the FFT of the measured and scaled ECR signal (b) IFFT of the responses obtained in (a), and (c) PSD of the responses obtained in (b) before and after adding to the palm a TMD with randomly chosen parameters

4.8. Optimized TMD for the upper limb model

The cantilever-type TMD with circular cross-section is used to reduce the critical peak of "Patient 6". Its length l_a, damping ratio ζ_a, and diameter d are calculated numerically to reduce the maximum amplitude of the response, for a mass position set at 2 mm away from the free end of the beam:

$$a = l_a - 2\,mm \tag{4.131}$$

This is to take into account the width of the added mass, so that the mass is concentrated within the beam's length and not to cause any additional effective length.

The effect of a 14.13 g TMD, which corresponds to $\mu_a = 0.37\%$, is tested for the simulated response presented earlier in Figure 4.20. The effect of using 1TMD is shown in Figure 4.26, where its calculated optimum parameters are as follows:

$$d_{opti} = 0.82\,mm, \qquad l_a = 8.2\,cm, \qquad \text{and} \qquad \zeta_a = 2.5\% \tag{4.132}$$

This optimized TMD causes 84.9% reduction in the tremor amplitude at the wrist joint, reduced from 8.8×10^{-4} to $1.3 \times 10^{-4}\,rad^2/Hz$. The response in Figure 4.26a is compared to that obtained for an optimized TMD having a diameter equal to 0.79 mm, which is very close to the optimal one. A beam having this diameter will be used in the experimental study. No significant changes are observed for this TMD which have the following optimum parameters:

$$l_a = 7.7\,cm, \qquad \text{and} \qquad \zeta_a = 2.2\% \tag{4.133}$$

These TMDs having a low mass ratio were able to cause high reduction, which can also be visible in the wrist joint signal of Figure 4.26b.

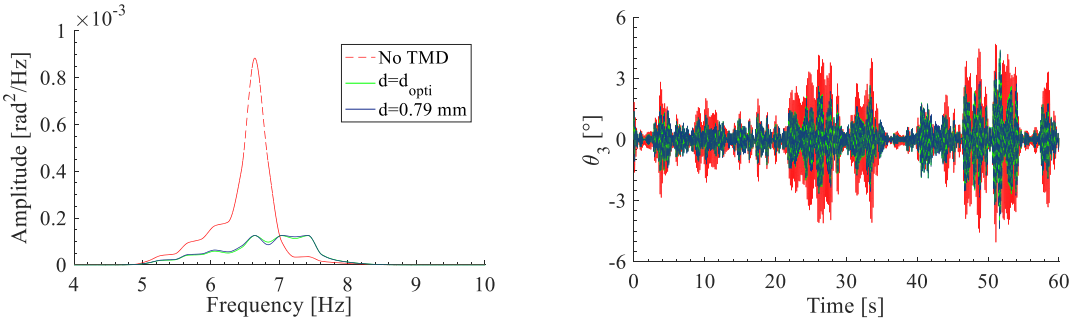

(a) (b)

Figure 4.26: Behavior of the wrist joint controlled by 14.13g optimized TMDs located at the palm having an optimized diameter d_{opti} and a diameter d=0.79 mm in the (a) frequency domain and (b) time domain

4.8.1. TMD parametric study

A parametric study is done to test the effect of increasing the number of TMDs (for the same total mass), the mass ratio, and the position of the TMDs along the segment. This study is done for the optimized TMDs having a 0.79 mm beam's diameter.

4.8.1.1. TMD position

The effect of the TMD position along the palm segment on its performance is studied for 1 and 2TMDs which have a total mass of 8.83 g and 14.13 g, corresponding to a mass ratio of 0.23% and 0.37%, respectively. Figure 4.27 shows changes in the performance of the 1TMD having a mass ratio of 0.23% when placed at 20%, 45%, 60%, and 100% of the palm segment length away from the wrist joint. The TMD provides its best performance at the position 100%, which can represent a sufficient desired reduction from the TMD. However, this position represents the finger tip of the patient, which is not suitable for hand use. So, the best position of the TMD must also be chosen by taking into account the patient's comfort even if the TMD performance is decreased. The lowest reduction (the difference between highest amplitude before and after the addition of the TMD) shown by the 8.83 g TMD in Figure 4.27 is 66.5%, when it is placed at 20% of the palm length. This can also be a good reduction produced by this light TMD.

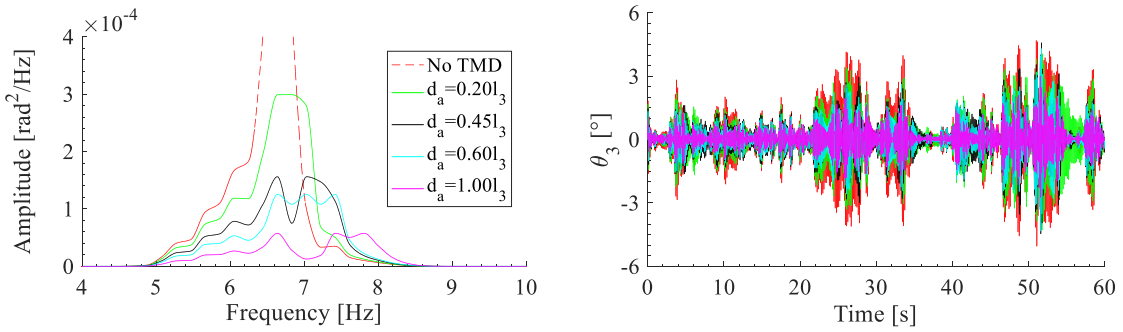

(a) (b)

Figure 4.27: Behavior of the wrist joint controlled by a 8.83 g optimized TMD with 0.79 mm beam's diameter located at the palm and placed at different positions d_a along the wrist joint in the (a) frequency domain and (b) time domain

The effect of the 1TMD with a 0.37% mass ratio is drawn in Figure 4.28. The 14.13 g TMD is able to reduce 68.8% of the wrist joint amplitude. The critical peak is about to vanish at the finger's tip, where a 96.5% reduction is produced at this position.

Figure 4.29 shows the behavior of the system with 2TMDs for different positions along the palm. Figure 4.29a and Figure 4.29b represent a TMD system of 0.23% and 0.37% total mass ratios, respectively. They show that the tremor amplitude decrease as the two TMD are placed away from the wrist joint. The 2TMDs cause 79.1% and 81.6% reduction when both are placed at position representing 20% and 60% of the palm length, respectively. It also shows that placing the 2TMDs at the same position provides better reduction than placing them in two different ones. For example, TMDs placed at $d_a = [0.45 \quad 0.60]l_3$ lead to a response that lies between the 2TMDs placed together at $d_a = 0.45l_3$ and $d_a = 0.60l_3$.

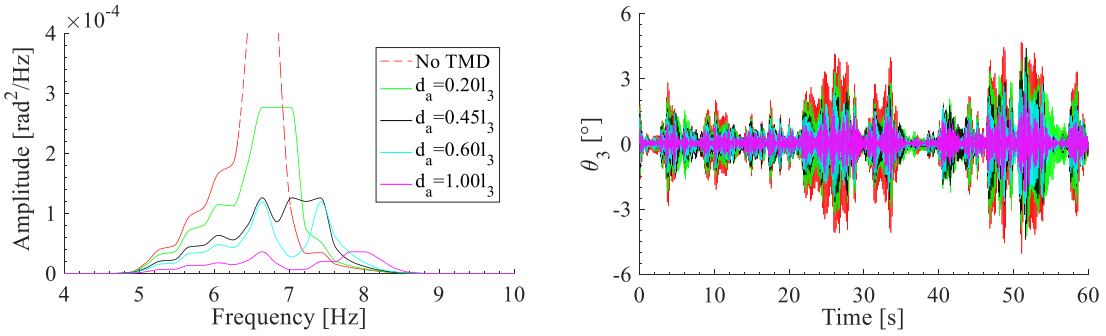

(a) (b)

Figure 4.28: Behavior of the wrist joint controlled by a 14.13 g optimized TMD with 0.79 mm beam's diameter located at the palm and placed at different positions d_a along the wrist joint in the (a) frequency domain and (b) time domain

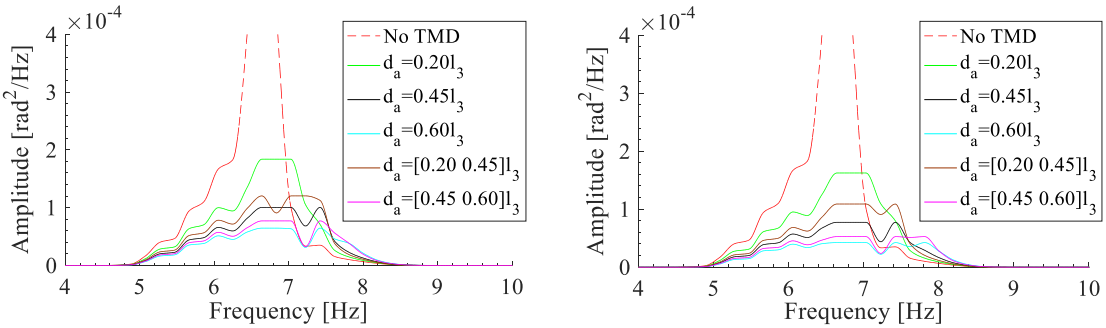

(a) (b)

Figure 4.29: PSD of the wrist joint signal controlled by 2 optimized TMDs with 0.79 mm beam's diameter located at the palm at different positions d_a along the wrist joint for a total mass of (a) 8.83 g and (b) 14.13 g

4.8.1.2. Number of TMD

The effect of the number of TMDs for the same mass ratio is tested in Figure 4.30 and Figure 4.31 for a TMD system having 0.23% and 0.37% mass ratio. The TMDs in these figures are placed on the palm segment at a position of 45% of its length away from the wrist joint. This distance can be a suitable position that doesn't disturb the patient. Increasing in the number of TMDs from 1 to 4, as shown in Figure 4.30a, causes an improvement in the tremor amplitude reduction from 82.5% to 94.1% for a TMD system with $\mu_a = 0.23\%$. The angular displacement in the time domain also shows better reduction for a higher number of TMDs, as presented in Figure 4.30b.

For the TMDs system having a total mass ratio of 0.37%, the increase in the number of TMDs from 1 to 4 causes a reduction of the undesired response amplitude from 85.8% to 97.0%, as shown in Figure 4.31a. The time response shows also good reduction in the tremor amplitude, as shown in Figure 4.31b.

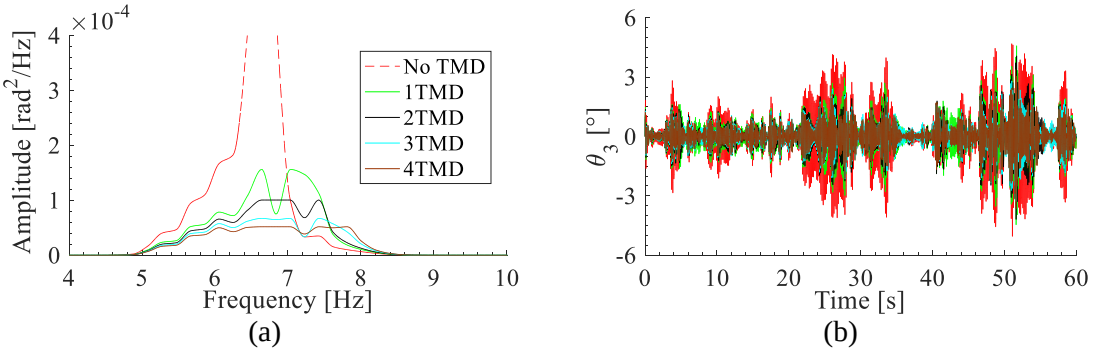

(a) (b)

Figure 4.30: Behavior of the wrist joint controlled by the 1–4 optimized TMDs located at the palm having a total mass of 8.83 g and 0.79 mm beam's diameter in the (a) frequency domain and (b) time domain

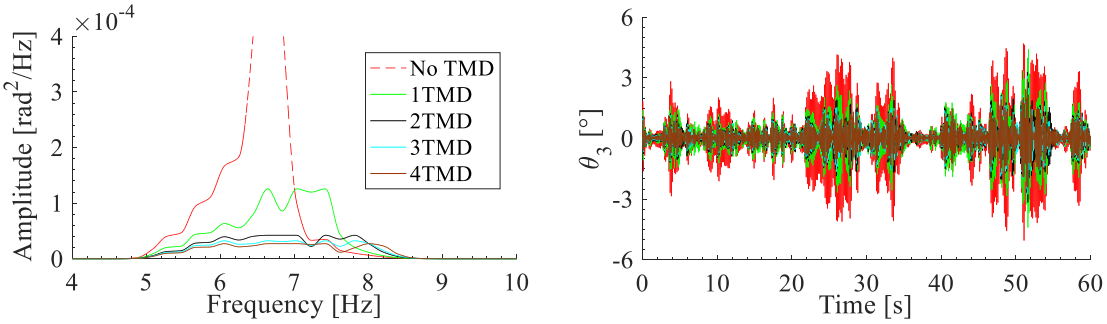

(a) (b)

Figure 4.31: Behavior of the wrist joint controlled by the 1–4 optimized TMDs located to the palm having a total mass of 14.13 g and 0.79 mm beam's diameter in the (a) frequency domain and (b) time domain

4.8.1.3. Mass ratio

A comparison between the 1 and 4TMDs having a total mass ratio of 0.23% and 0.37% is presented in Figure 4.32. It shows that increasing the number of TMDs for the same mass ratio causes more reduction over a wider range of frequencies (Figure 4.32a). The time domain response has also better response when each beam of the 4TMD system is holding a slightly higher mass, as shown in Figure 4.32b. Figure 4.32 shows the importance of increasing the total mass ratio for the same number of TMDs. Moreover, the amplitude reduction increases from 82.5% to 85.8% when the 1TMD total mass ratio increases from 0.23% to 0.37%. Similarly, for the 4TMDs, it increases from 94.1% to 97.0% when the mass ratio increases.

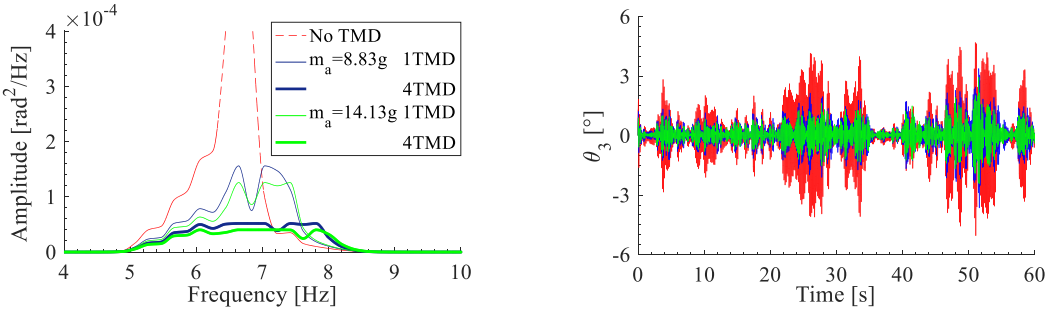

(a) (b)

Figure 4.32: Behavior of the wrist joint controlled by TMDs located at the palm having a total mass of 8.83 g and 14.13 g with 0.79 mm beam's diameter (a) 1 and 4 optimized TMDs in the frequency domain and (b) 4TMD in the time domain

4.8.1.4. Damping ratio

The effect of damping ratio of the TMD is studied in Figure 4.33 for 1, 2, and 3TMDs of same total mass of 14.13 g, with 0.79 mm cross-sectional diameter of the beam. The effect of decreasing the damping ratio is studied since the obtained optimum damping is higher than the damping ratio range of stainless steel, which will be used as the beam's material for the experiment. Figure 4.33 shows that the system is not sensitive to the changes in the damping ratio. Indeed, the changes in tremor amplitude due to the decrease of the damping ratio is more clear for the system with 1TMD (Figure 4.33a), its effect is less with 2TMD (Figure 4.33b), and the effect of TMD's damping ratio disappears for higher number of TMDs (Figure 4.33c for the 3TMDs).

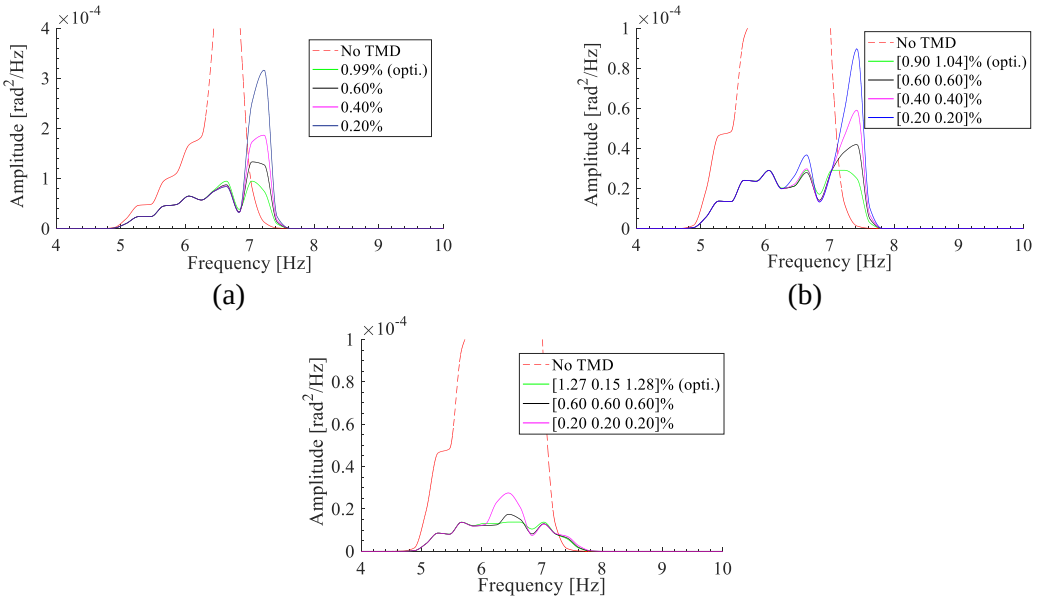

(a) (b)

(c)

Figure 4.33: Behavior of the wrist joint controlled by TMDs located at the palm having a total mass of 14.13 g with 0.79 mm beam's diameter for different values of damping ratio of the TMD for (a) 1TMD, (b) 2TMD, and (c) 3TMD

4.8.2. TMDs for the experimental testing

The behavior of a 0.79 mm beam's diameter TMD with a 14.13g mass attached along its length can be tested numerically for TMDs having fixed length of 9.1 cm, as such beams will be used in the experimental tests. The position of the mass along the beam a, and the damping coefficient c_a are the parameters to optimized. The behavior of the system with this TMD is depicted in Figure 4.34. It shows the behavior of the system with 1, 2, and 3TMDs, each holding a 14.13 g mass. The 1TMD is able to reduce 89.3% of the wrist joint amplitude, and the 3TMDs 98.4%, as shown in Figure 4.34a. High reduction is also clearly indicated in the time response for the three TMDs, as presented in Figure 4.34b.

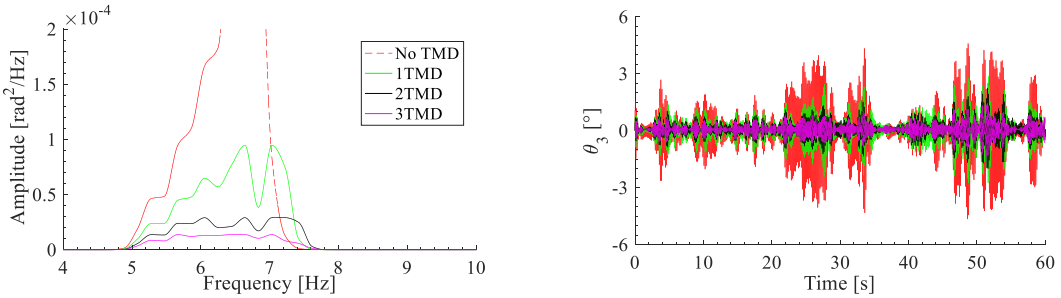

Figure 4.34: Behavior of the wrist joint controlled by the 1–3 optimized TMDs located at the palm with 9.1 cm long beams having 0.79 mm diameter and 14.13 g mass attached on each TMD in the (a) frequency domain and (b) time domain

The effect of the 3TMDs on the response of the distal ends of the upper limb segments in the x- and y-axis in addition to the angular velocity at the proximal joints are shown in Figure 4.35. The responses of the system after the addition of the 3TMDs are represented in black color. It shows that the TMD, designed to reduce the angular displacement of the wrist joint, is also able to decrease the displacement of the other joints.

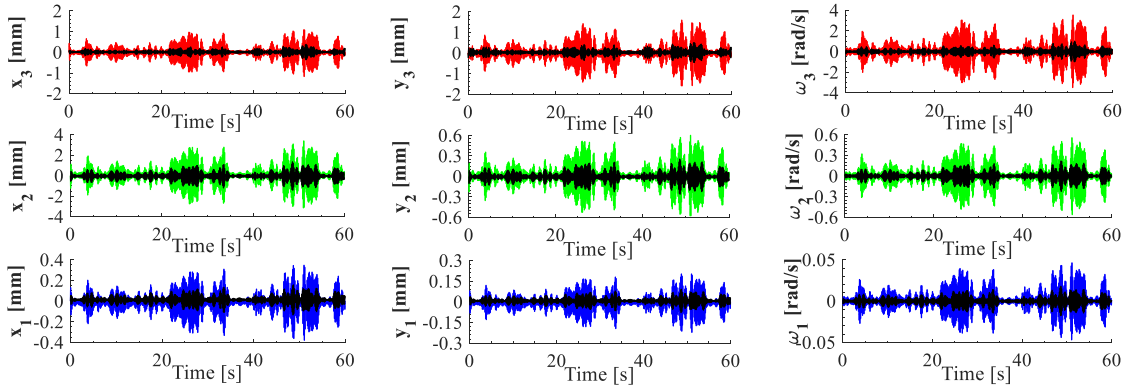

Figure 4.35: (a) Horizontal (x-axis) and (b) vertical (y-axis) displacements at the distal ends of each segment, and (c) angular velocity at the proximal joint obtained by the upper limb model with "Patient 6"excitation signal where black curves correspond to the system responses after adding the TMDs to the palm

The PSD of the responses presented in Figure 4.35, which are related to the palm segment and the wrist joint, are shown in Figure 4.36. The system shows reduced the x- and y-axis amplitudes, and angular velocity amplitude of the tremor in the frequency domain after the addition of the 3TMDs, with fixed diameters and lengths.

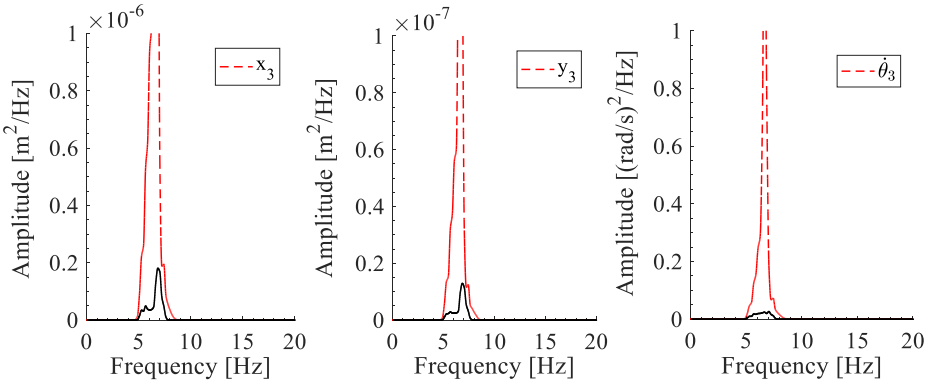

Figure 4.36: PSD of the x- and y-axis displacement signals at the distal end of the palm and the angular velocity at the wrist joint of the upper limb model excited with "Patient 6" muscle signal, where black curves correspond to the system responses after adding the TMDs

In Figure 4.37, the behavior of the 3TMDs, having 0.79 mm beam's diameter, 9.1 cm length and optimized to reduce the angular displacement amplitude of the wrist joint, is presented. TMD1, TMD2, and TMD3 represent the first, second, and third TMD used for this TMD system. These TMDs are designed to hold a mass of 14.13 g each and the position of the mass along the beam is optimized along with the beam's material's damping coefficient. It shows that the three beams have maximum angular displacements of 25°, 18°, and 17°, respectively.

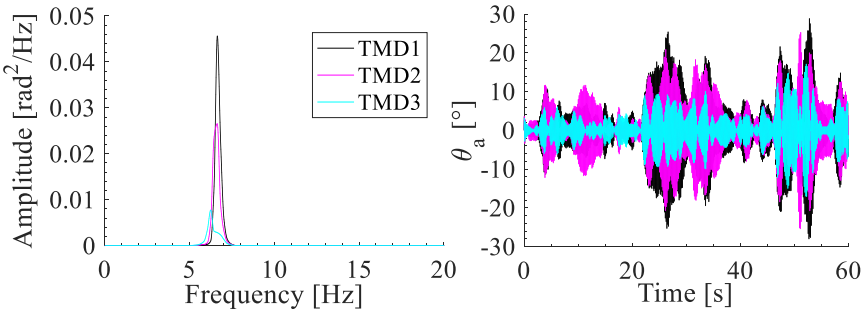

Figure 4.37: Behavior of the optimized 3TMDs attached to the palm to reduce the wrist joint amplitude where each cantilever-type TMD holds a 14.13 g mass and has a beam length of 9.1 cm with 0.79 mm diameter

4.9. Tremor frequency changes

The study done to test the TMD's performance considers that the critical frequency of the patients doesn't change. However, as proven in this study, the frequency of the

patient's tremor can vary in a 0.6 Hz range. The controller's type used in the study is passive, which is very sensitive to the changes in the system's frequency. Improvements in the passive controller's performance to make it suitable for the environmental changes is of high importance.

4.9.1. Shifted patient responses

A study is done aiming to adapt the TMDs parameters in a way that it can remain effective even if the critical frequency changes. The study starts by presenting in Figure 4.38 the PSD of the wrist joint that result from different shifted critical frequencies for "Patient 6". Seven main PSDs are shown in Figure 4.38a, the space between each peak is 0.1 Hz which lead to a 0.6 Hz interval width between the first and the seventh peak. This interval represents the frequencies between 6.33–6.93 Hz centered at 6.63 Hz, represented by the "0" in Figure 4.38. The frequency of 6.63 Hz is the frequency of the "Patient 6" critical peak. Then, the critical peak frequency is shifted to the left or the right with respect to the "0 peak" by subtraction or addition in the downsampled time step (i.e., the downsampled frequency), respectively. The shifted values are chosen to reach exactly a ± 0.1 Hz spaced between two consecutive internal peaks. The extreme peaks are +0.3 Hz or -0.3 Hz far away from the "0". Figure 4.38b shows additional arbitrary shifted peaks, represented by the dashed lines, between the 7 main peaks afore mentioned.

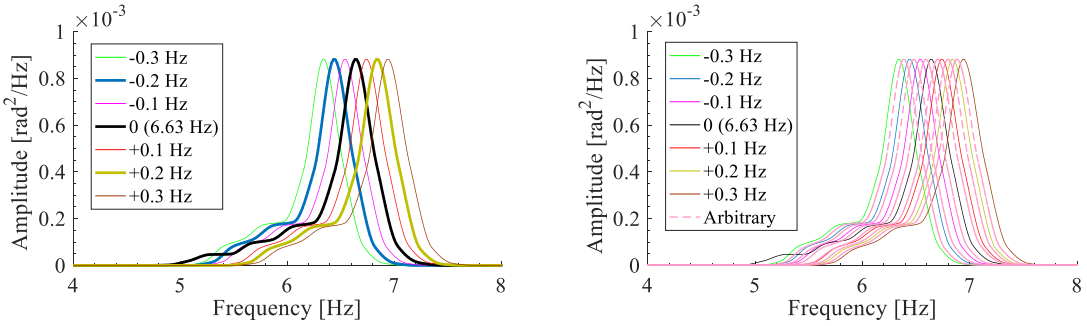

Figure 4.38: Seven equally spaced shifted peaks of the PSD of the wrist joint response along a 0.6 Hz frequency range, and (b) additional in-between shifted peaks

4.9.2. Optimized TMDs for shifted peaks

The 9.1 cm long cantilever-type TMD with a 0.79 mm cross-section diameter and a 14.13 g mass is used again to represent each single TMD's system considered hereafter. The optimization of the TMD concerns the optimization of the mass position along the beam and the optimization of the damping ratio. All the TMDs are placed at a distance $d_a = 0.45 l_3$, representing 45% of the palm segment length away from the wrist joint. Figure 4.39 represents the PSD of the response due to each input torque with shifted critical

peak (Figure 4.38a), before and after the addition of the optimized TMD(s). The result obtained by the addition of the optimized 1TMD, 2TMD, and 3TMD, which provides 89.3%, 96.7%, and 98.4% reduction in the tremor amplitude correspond to Figure 4.39a, Figure 4.39b, and Figure 4.39c, respectively.

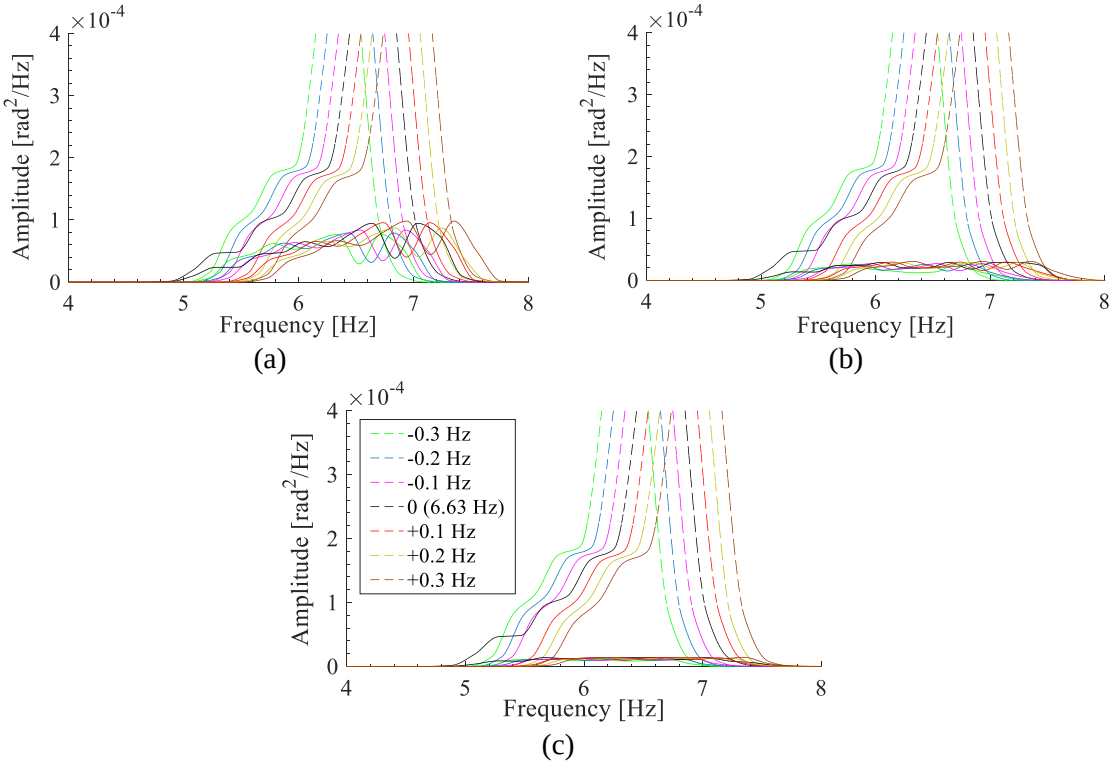

Figure 4.39: PSD of the wrist joint responses due to the optimization for each shifted peak of (a) 1TMD, (b) 2TMD, and (c) 3TMD placed at the palm

4.9.2.1. 1TMD effect

The optimum parameters associated with the 1TMD used to optimize each shifted peak in Figure 4.39a, are presented in Table 4.7. It shows that the position a of the mass changes within a range of ± 0.1 mm when the critical frequency changes is ± 0.1 Hz, and the optimum damping $\zeta_{a\ opti}$ ranges between 0.75–0.99%. The optimum frequency f_a of each TMD is not exactly equal to the critical peak frequency since both the principle system and the TMD includes damping.

Since the optimum parameters are close to each other, a TMD having the mean values for a and $\zeta_{a\ opti}$ of Table 4.7 is tested to reduce all the shifted peaks of Figure 4.39a. The result obtained with this TMD ($a = 7.5\ cm$ and $\zeta_a = 0.87\%$) for each peak is shown in Figure 4.40. This TMD works well at the "0". For the other critical frequencies, it causes an increase in the tremor's amplitude in comparison with the optimized TMD of Figure 4.39a. The amplitude slowly increases as the critical frequency is shifted to the left and a

critical increase is observed when shifted to the right. So, this TMD doesn't fit the requirements.

Table 4.7: Optimum parameters of the 1TMD systems (9.1 cm beam with 0.79 mm diameter and 14.13 g mass) used to optimize the response of the wrist joint for different critical frequency of "Patient 6" muscle signal

Critical Frequency	6.33 (Hz)	6.43 (Hz)	6.53 (Hz)	6.63 (Hz)	6.73 (Hz)	6.83 (Hz)	6.93 (Hz)	Mean
$a\ (cm)$	7.72	7.65	7.57	7.49	7.43	7.37	7.29	7.50
$\zeta_{a\ opti}\ (\%)$	0.75	0.79	0.83	0.99	0.95	0.84	0.94	0.87
$f_a\ (Hz)$	6.64	6.74	6.85	6.95	7.05	7.13	7.24	-

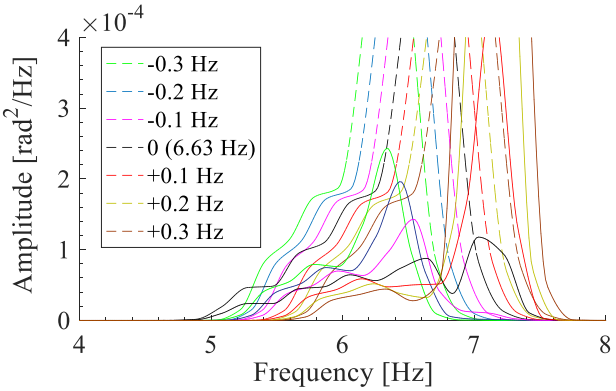

Figure 4.40: PSD of the wrist joint responses due to 1TMD with parameters chosen as the average values of those optimized for each shifted frequency

4.9.2.2. 2TMD effect

The number of TMDs used to optimize each shifted frequency needs to be increased. Table 4.8 lists the optimum parameters of the 2TMDs used to optimize the seven equally spaced shifted frequencies (Figure 4.39b). The presented data shows a variation between 7.4–7.9 cm for a and 0.50–1.18% for $\zeta_{a\ opti}$.

The mean value of the optimum parameters obtained in Table 4.8 for TMD1 and TMD2 are tested in Figure 4.41 and compared to the results obtained in Figure 4.39b for the optimized 2TMD used for each shifted frequency. A better response is observed in comparison to Figure 4.40 (1TMD with the average of the optimum values). Slight changes in the tremor amplitude is shown for the three peaks shifted to the left of "0". However, it increases gradually and critically for the other shifted peaks. This TMD system needs more improvements.

Table 4.8: Optimum parameters of the 2TMDs systems (9.1 cm beam with 0.79 mm diameters and a 14.13 g mass each) used to optimize the response of the wrist joint for different critical frequency of "Patient 6" muscle signal

Critical Frequency	a (cm)		$\zeta_{a\ opti}$ (%)		f_a (Hz)	
	TMD 1	TMD 2	TMD 1	TMD 2	TMD 1	TMD 2
6.33 Hz	7.90	7.82	0.51	0.50	6.43	6.52
6.43 Hz	7.87	7.72	0.81	0.61	6.47	6.65
6.53 Hz	7.78	7.64	0.75	0.63	6.57	6.75
6.63 Hz	7.68	7.56	0.64	1.18	6.70	6.86
6.73 Hz	7.61	7.49	0.59	0.65	6.79	6.95
6.83 Hz	7.57	7.43	0.79	0.57	6.85	7.03
6.93 Hz	7.47	7.35	0.59	0.67	6.98	7.15
Mean	7.70	7.60	0.67	0.69	-	-

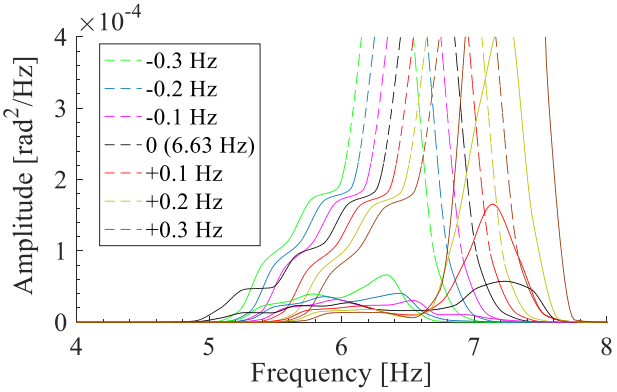

Figure 4.41: PSD of the wrist joint responses due to 2TMD with parameters chosen as the average values of those optimized for each shifted frequency

4.9.2.3. 3TMD effect

The optimum parameters of the 3TMD used for the responses presented in Figure 4.39c are listed in Table 4.9. The ranges for the optimum mass position and TMD damping ratio show to increase, where a ranges between 7.4–8.1 cm and $\zeta_{a\ opti}$ between 0.19–1.26%.

The PSD of the responses of the system with the 3TMD having average values of TMD1–3 (Table 4.9) are presented in Figure 4.42 and compared to those obtained with the optimized 3TMD (Figure 4.39c). It shows that this variation of the optimum parameters slightly affects the response and causes an acceptable increase in the tremor amplitude in comparison to the optimum response. The two peaks in the coupled system around the critical frequency have a minimum reduction of 91.0%, at the first peak, and 75.3%, at the second. This 3TMD system can be used to handle the frequency changes in the tremor of

the patient. Increasing the mass ratio together with the number of TMDs also improves the reduction.

Table 4.9: Optimum parameters of the 3TMDs systems (9.1 cm beam with 0.79 mm diameters and a 14.13 g mass each) used to optimize the response of the wrist joint for different critical frequency of "Patient 6" muscle signal

Critical Frequency	a (cm)			$\zeta_{a\ opti}$ (%)			f_a (Hz)		
	TMD 1	TMD 2	TMD 3	TMD 1	TMD 2	TMD 3	TMD 1	TMD 2	TMD 3
6.33 Hz	8.13	7.93	7.84	0.51	0.27	1.12	6.16	6.39	6.45
6.43 Hz	8.05	7.87	7.76	0.41	0.29	1.02	6.25	6.47	6.64
6.53 Hz	7.97	7.79	7.68	0.47	0.26	1.13	6.34	6.57	6.71
6.63 Hz	7.91	7.70	7.59	1.26	0.13	1.26	6.41	6.68	6.82
6.73 Hz	7.80	7.63	7.52	0.51	0.16	1.21	6.55	6.77	6.91
6.83 Hz	7.75	7.58	7.47	0.45	0.33	1.04	6.61	6.84	6.99
6.93 Hz	7.66	7.49	7.39	0.45	0.19	1.12	6.73	6.96	7.10
Mean	7.90	7.70	7.60	0.58	0.23	1.13	-	-	-

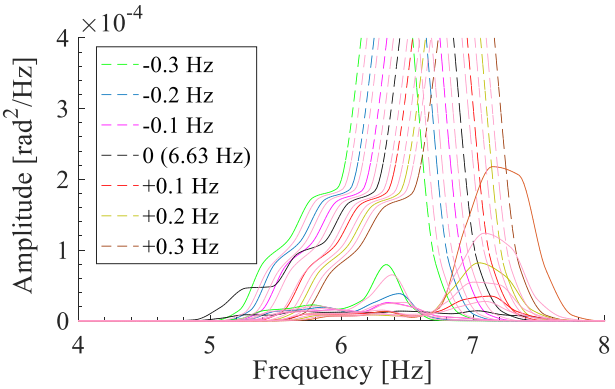

Figure 4.42: PSD of the wrist joint responses due to 3TMD with parameters chosen as the average values of those optimized for each shifted frequency

4.9.3. TMD system adapted for frequency shifting

Improvement in the system's response due to the 3TMD system (Figure 4.42) can be necessary to protect the system from critical behavior at the second induced peak (at almost 7 Hz), for which 75.3% reduction is obtained. The effect of the 7 optimized TMDs, one for each peak, whose parameters are provided in Table 4.7, can be tested by combining them into a single TMD system. The effect of this TMD system on the PSD of the responses of the wrist joint for each shifted frequency is shown in Figure 4.43. It provides a 95.3% minimum reduction for all the shifted frequencies, including the arbitrary frequencies which were added in Figure 4.38b. Although the considered TMD system provides an interesting mitigation effect, it loads the principle system with an additional mass of 98.9

g. However, the 98.9 g represents only a total mass ratio of 2.62%, which is a relatively low mass in comparison to those used by other researchers to design TMD for the tremor attenuation. Nevertheless, the objective of this study is to reach the highest possible reduction with a minimum number of TMDs and a lower total mass of the TMD system.

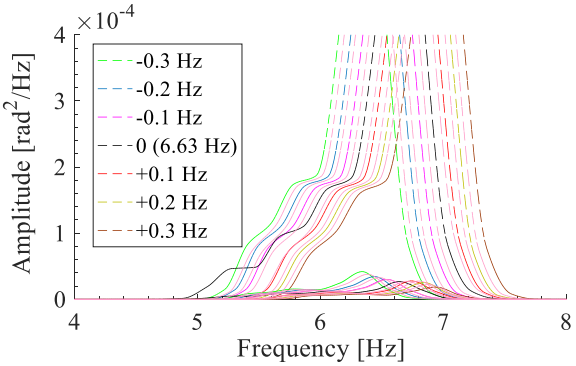

Figure 4.43: PSD of the wrist joint responses due to 7TMDs system, each TMD has the optimum parameters corresponding to each shifted peak

The study done in the thesis insures that 3TMDs of 14.13 g each represents the minimum requirement for the design of TMD system. The Figure 4.42 points out to the possibility of designing a 3TMD system (14.13 g each) that can reduce more the amplitude of the system. The Table 4.7 is used in order to select a set of 3TMDs out of the 7 presented ones. The TMDs are selected to correspond for the non-consecutive shifted frequencies. So, the optimum TMDs corresponding to the "0" response position, and the $\pm$0.2 Hz shifted responses, marked by thick lines in Figure 4.38b, are used. The TMDs optimized for the three mentioned frequencies, are considered now as the TMD system suitable for the tremor attenuation along a 0.6 Hz tremor frequency shifting.

Figure 4.44a shows the PSD of the "Patient 6" tremor response at the wrist joint due to the 3TMDs optimized at the 6.43, 6.63, and 6.83 Hz. This TMD system shows to be the best design to be considered. The amplitude reduction ranges between 90.0–98.6% for all the shifted responses, including the arbitrary ones. The masses of the TMD system are located at position a = 7.4, 7.5, and 7.6 cm and the optimum damping ratios are $\zeta_{a\ opti}$ = 0.84, 0.99, and 0.79%. The total mass ratio is equal to 1.12%. Figure 4.44b shows the PSD obtained with TMDs using the optimum positions a but a damping ratio of 0.33%.

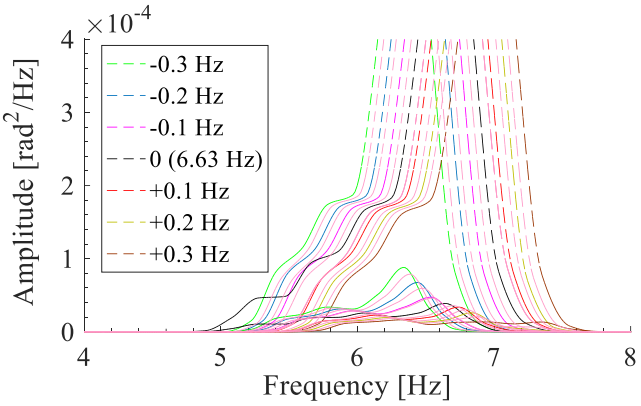

Figure 4.44: PSD of the wrist joint responses due to 3TMDs system, each TMD has the optimum parameters corresponding to -0.2 Hz, 0Hz, and +0.2 Hz shifted peaks with 0.33% damping ratio

4.10. Conclusion

The derived equation of motion for the upper limb represents a 3DOF dynamically coupled non-linear differential equation with non-linear coefficients of high degrees. Solving such a system required high effort, which can be simplified by its linearization since the time dependent matrices slightly change with time. Taylor series expansion is applied to linearize the multivariable system and the Laplace transform of the linearized system is done to obtain its response in the frequency domain. The derived system's response was able to reflect the tremor's behavior of an ET patient when it is excited by his measured ECR muscle signals.

The parametric study of the TMDs shows that the performance increases when they are located at the distal end of the palm segment. However, this location may not be practical for a daily use. TMDs placed on the palm segment near the wrist joint also provide very good reduction in the tremor amplitude, for a TMD system with a total mass ratio of 8.83 g or 14.13 g. When MTMD are used, it is better to place them at the same position along the hand segment than distributing them on different positions. Increasing the number of TMDs, while keeping the same total mass ratio, improves the mitigation effect of the TMD system. As expected, TMDs with higher total mass ratio are more effective in reducing the undesired tremor amplitude for the same number of TMDs. The natural frequency of the cantilever-type TMD, is obtained by using Dunkerley's formulation, and can be verified experimentally in the next chapter. The cantilever-type TMD having the same dimension as the one used for the experimental tests, was simulated to anticipate the reachable tremor reduction.

In order to test the robustness of a TMD system to excitation frequency changes, an optimization is done for the 1TMD, 2TMD, and 3TMD systems to reduce the tremor amplitude due to an excitation signal with initial frequency changes within a centered 0.6

Hz range. The optimum parameter of each TMD is provided. The ability of several TMD systems in reducing the tremor amplitude for different excitation signals with shifted frequency is tested using numerical simulations. It shows that to reduce the patient's response amplitude, minimum of 3TMDs is required. The used 3TMD system 9.1 cm long beams, and 0.79 mm cross-sectional diameter each. The damping ratio used for these 3TMDs is 0.33%, which will represent later the means value of the damping ratios of stainless steel beam with 14.13 g mass located at different position along the beam, calculated from the measurements. This TMD system was able to reduce 90.0–98.6% of the wrist joint tremor amplitude.

CHAPTER 5. EXPERIMENTAL TESTING OF PASSIVE TMDS

THIS chapter includes numerical design as well as fabrication of passive TMD suitable to operate within the postural frequency range of critical tremor. The cantilever type TMD is used, which can provide different operating frequency depending on the position of the proof mass along its beam. Semi-analytical formula of Dunkerley's equation used to approximate the natural frequency is verified experimentally for a TMD system with different mass positions. The effect of replacing the optimal damping ratio by a lower value deduced from the measurements is studied for several TMDs. The response of the system due to designed TMDs is obtained experimentally on a fabricated experimental arm and excited using the ECR signal provided by the mechanical shaker.

Plan of Chapter 5

5.1. Introduction

In this chapter, two TMDs are manufactured with different geometries. A rectangular and other a circular cross-section cantilever beam having the same length. Each beam has an attached mass which can be placed on different position along the beam to provide a new natural frequency for the TMD. The natural frequency of the TMD compound with different mass position was derived using Dunkerley's formula. The reliability of this equation in providing the exact value of the natural frequency is checked by experimental measurements using the Vibrometer. The equivalent damping coefficient of the fabricated TMD system is calculated for different mass position. Numerical simulation is done to test the performance of the fabricated TMD with the same dimensions and damping ratio values corresponding to the experimentally calculated ones. Shifting in the tremor's frequency of the patient is considered. The used range is taken from the experimental study done previously for different patients where several measurements were done under different conditions. The signals of the patient are used to excite the experimental-arm and test experimentally the behavior of 1, 2, and 3TMDs.

5.2. TMD frequency measurement

The results of the patient's tremor measurements, which are summarized in Table 3.9, indicates that the participants has PT that lies between 6.2–8.5 Hz. The patient chosen for the numerical study (Patient 6), whose tremor will be simulated experimentally, has dominant peak that occurs at 6.63 Hz. The TMD will be designed to reduce the tremor of this patient. For a chosen proof mass, (4.86) or (4.87) can be used to check the possibilities of designing a TMD able to have operating frequencies which can cover the participant's undesired frequency range. A light weight TMD with a chosen to reach the design requirements.

The optimum frequency of the TMD is calculated for a system excited by the patient's tremor signal which corresponds to a specific mass position 'a' along the beam. This frequency is evaluated using the derived formula of the TMD system found in (4.86). To check the reliability of this formula in specifying the correct mass position 'a', a comparison is done between the natural frequencies obtained analytically and experimentally for the fabricated TMD system.

The Portable Digital Vibrometer PDV-100 is used to measure the velocity signals of the TMD's beam for different screw positions along the beam, when excited by an initial displacement at its free end. The sensor's data are transmitted to LabVIEW software in order to acquire the velocity signals and its Fourier transform.

The PDV speed is specified using Table 5.1 where PDV scaling factor is applied to obtain the measured velocity signal. The measurements are processed for a sampling rate of 1706.67 Hz. The signal is downsampled to get a sampling frequency higher than twice of the maximum frequency to cover all the measured frequency range. The signal is filtered to obtain the processed signal before applying its FFT.

Table 5.1: Portable Digital Vibrometer PDV-100 scaling factor

Measurement range full scale (peak) mm/s	Scaling factor $(mm/s)/V$
20	5
100	25
500	125

The beam's natural frequency is represented by the analytical formula of the Euler-Bernoulli fixed-free beam found in (4.83). Measurements are done to verify the derived semi-analytical formula using Dunkerley's formula of the TMD system which includes the fundamental frequency of the beam in (4.83) and the frequency of the mass placed on a massless beam. The type of clamping used to fix the beam can cause changes in the material's effective Young's modulus 'E_{beam}'. Since the main objective is to verify the Dunkerley's formula for different mass position and not the fundamental frequency of the beam alone, the Young's modulus of the beam is chosen so that the frequency of the beam alone confirms with its analytical formulation. Thus, the calculated error between the measured frequency and the calculated frequency doesn't include the effect of the clamping type. The calculated of the natural frequency of the TMD for each mass position using the analytical formula corresponds to the linear systems. So before proceeding the calculations, wavelet transform is used to record the changes in the natural frequency of the fabricated TMD and check its linearity.

Measurements of the system's critical frequency and damping ratio calculations are done for different mass position along the beam, starting near its free end toward the fixed end position. The measured frequencies of the TMD are compared with the analytical formula derived in (4.86) using Dunkerley's method, and checked numerically using the finite element method (FEM). The proof mass is modeled as a concentrated load placed at the centroid position in both Dunkerley's and FEM methods.

5.2.1. Rectangular beam

To have an idea about the required TMD size needed to reach the patient's undesired frequency, Figure 5.1 is presented. It shows the effect of the TMD length 'l_a' and mass position 'a' geometrical parameters in the Dunkerley's equation of (4.86), on the

TMD's operating frequency 'f_a'. The range of operation of different selected rectangular beam TMDs when the position of the 8.83 g mass position is changed along the beam is presented. It tests the effect of the 5.5 to 9.1 cm long beams, which are 10 mm wide and 0.2 mm thick. The 7.5–9.1 cm long beams can operate between 5–9 Hz when the mass is placed at a distance 4.6–7.1 cm away from the fixed end. Shorter beams are able to operate within smaller range of frequencies.

A vertical line is drawn at the 6.63 Hz, which represents the tremor frequency of "Patient 6". Figure 5.1 shows that all the tested beam's length can achieve the required frequency of "Patient 6", except the 5.5 cm and 6 cm relatively short beams. On the other hand, long tested beams like the 9.1 cm, can achieve this frequency when the mass is placed at a=5.7 cm, where the remaining length of the beams is left as useless. If the critical frequency of "Patient 6" is fixed at 6.63 Hz with no shifting, the most suitable beam can be the 6.5 cm long where a=5.9 cm.

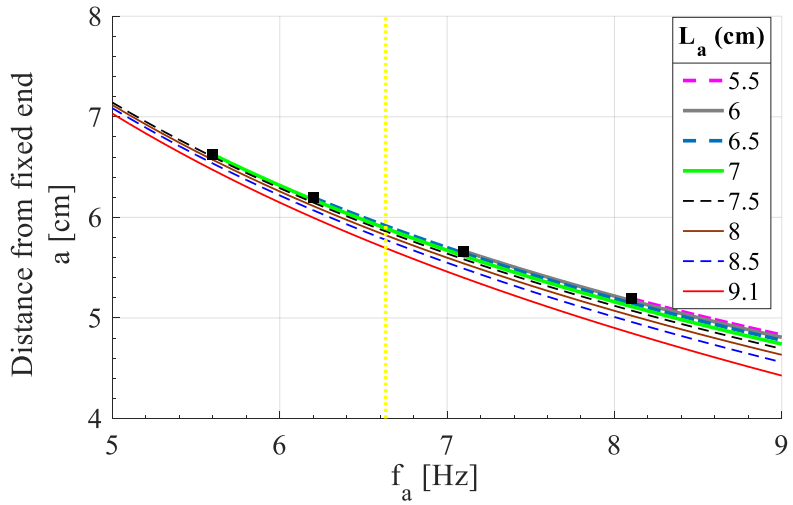

Figure 5.1: Operation frequency range of several 10 $mm \times 0.2\ mm$ rectangular beam TMD for different mass position

A rectangular cross-section stainless steel cantilever beam, is designed as shown in Figure 5.2a, to be 9.1 $cm \times 10\ mm \times 0.2\ mm$. An 8.83 g screw is designed as the proof mass of this TMD system and placed at different positions 'a' according to the following:

$$a = l_a - d_{meas} - \frac{d}{2} \tag{5.1}$$

where, l_a is the length of the beam. d_{meas} is the measured position of the mass away from the free end of the beam, where the minimum position to be considered is for the screw size included within the beam's length to prevent the addition of an effective length to the system. d is the diameter of the screw. The fabricated TMD system is shown in Figure 5.2b.

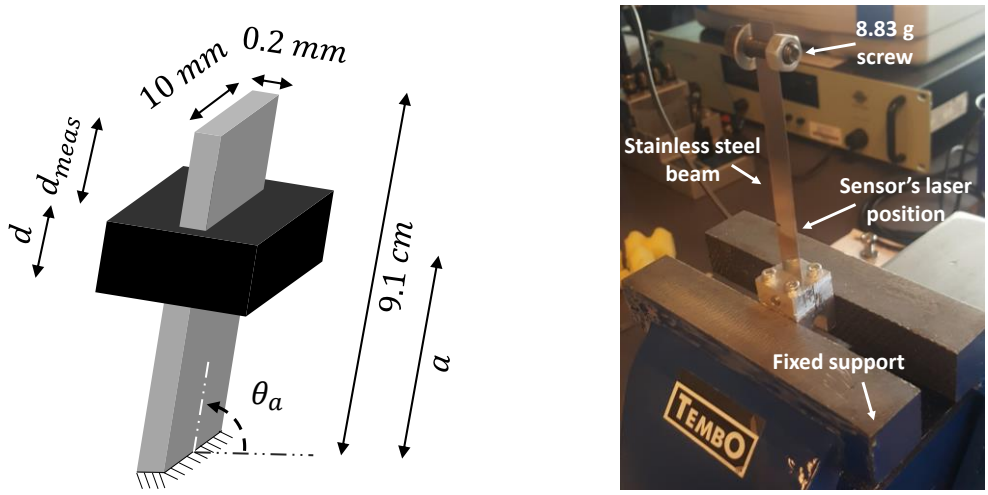

(a) (b)

Figure 5.2: Fabricated rectangular beam cantilever-type TMD

The measured and processed signal for the rectangular cross-sectional cantilever-type TMD of Figure 5.2 is shown in Figure 5.3 and Figure 5.4. The incident ray of the PDV strikes the beam at a position of 2.1 cm away from its fixed end. The PDV speed is set at 100 mm/s, and the signal length is 60 s. The signal is downsampled by a ratio of 25 to obtain the sampling frequency 68 Hz.

The measured signal for the beam alone before adding the mass and its FFT are shown in Figure 5.3a and Figure 5.3b, respectively. The stainless steel beam in Figure 5.3a behaves as an underdamped system. Its damping ratio is measured graphically using the half-power bandwidth method [122,123]. The percentage of damping ratio and critical frequency is obtained from the FFT response in Figure 5.3b, to be 0.0018 (0.18%) and 18.45 Hz, respectively. Using its measured frequency and the frequency formula of the Euler-Bernoulli beam in (4.83), the E_{beam} is calculated to be 180.3 GPa. This shows that the clamping used, weaken the material's stiffness.

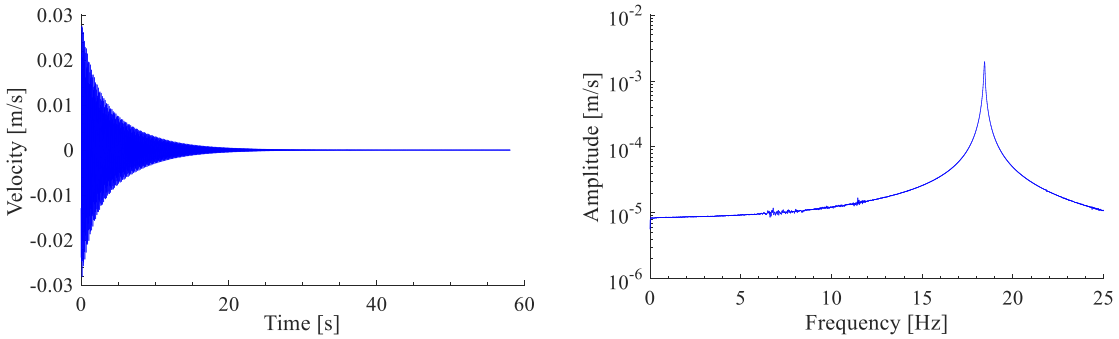

(a) (b)

Figure 5.3: (a) Velocity signal and (b) its Fourier transform measured by the Vibrometer for the rectangular beam alone

The processed velocity signal of the beam after placing the 8.83 g mass to the $d_{meas} = 2.4$ mm is shown in Figure 5.4a. Its FFT in Figure 5.4b shows the measured damping coefficient and the natural frequency of the TMD system to be 0.21% and 3.65 Hz, respectively. It shows that the addition of the mass, causes an increase in the overall system's damping ratio, which is different from that obtained by its beam alone without the need of adding an external damper. The calculated fundamental frequency using Dunkerley's formula at this position is 3.81 Hz. Similar measurements are done for different mass positions along the beam.

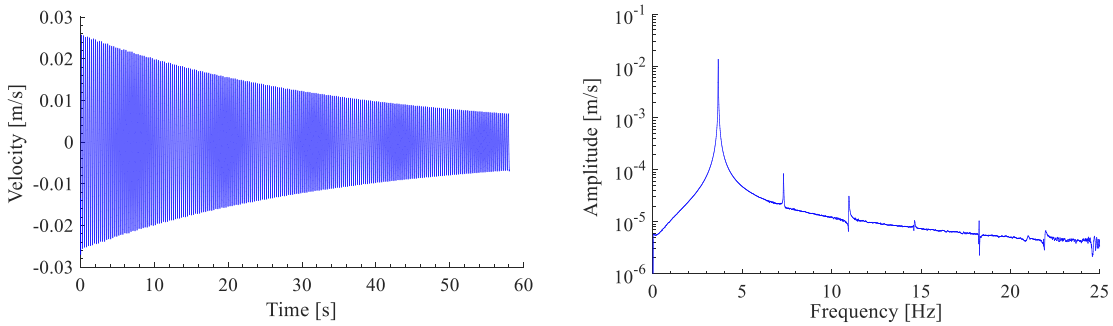

(a) (b)

Figure 5.4: (a) Velocity signal and (b) its Fourier transform measured by the Vibrometer for the rectangular beam with the 8.83 g screw placed at its free end

The wavelet transforms extracted from the velocity signal of the rectangular beam while the screw is placed near the free end position presented in Figure 5.4a, is shown in Figure 5.5. The variation of the natural frequency is analyzed within the interval [4.6, 54] s, where the rest represents changes in the natural frequencies due to the edge effect. Slight changes are realized at the beginning when the amplitude of the oscillation was still high. However, this variation in the natural frequency corresponds only to a small value of 0.22% that represents a linear system.

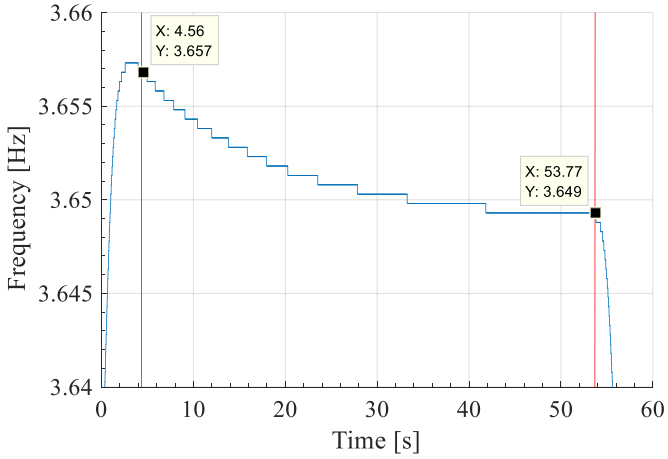

Figure 5.5: Wavelet transform for the natural frequency of the rectangular beam with 8.83 g screw placed at its free end

The beam is divided into 1820 2D-elements in the FEM calculations of the TMD's natural frequency. The measurement results are presented in Figure 5.6. The left y-axis of Figure 5.6 shows the natural frequency obtained using the experimental, FEM, and Dunkerley's methods, while the right y-axis shows the percentage of error in the natural frequency between the FEM and Dunkerley's methods, and the experimental results. The results presented in Figure 5.13 show that the analytical method and numerical methods give exactly the same frequency for the mass placed near the free end of the beam. These frequencies starts to have different values at the position $a = 6.2\,cm$. This difference increases while the frequency of the TMD system increases, i.e. the position of the mass 'a' is decreasing. The highest percentage of error obtained in comparison with the frequencies calculated experimentally is 4.7%, which occurs near the free end of the beam.

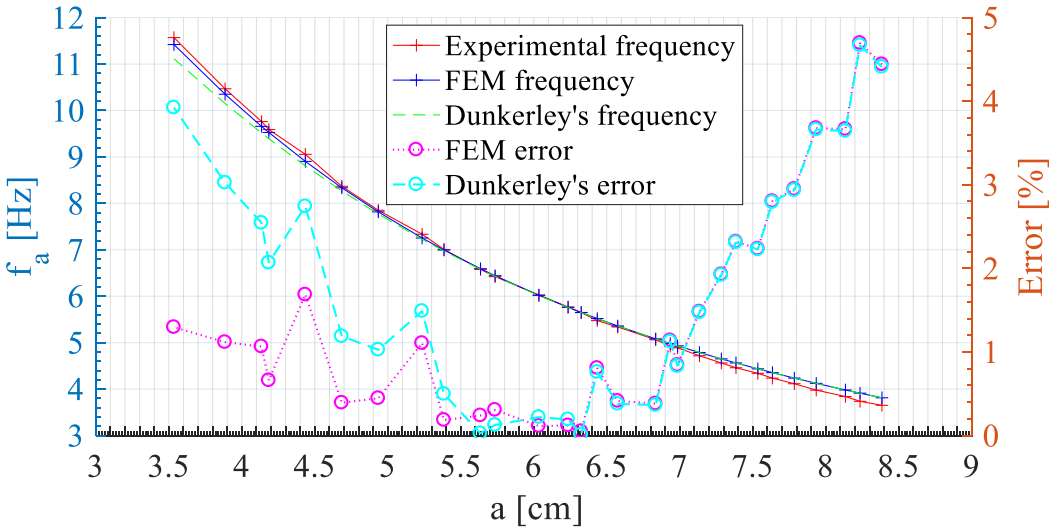

Figure 5.6: The calculated Dunkerley's and FEM fundamental frequency of the TMD with their percentage of error compared to the frequency obtained experimentally for different mass position along the rectangular beam

The damping ratio of the beam TMD's system are calculated graphically using its response in the frequency domain, for different mass position along the beam's longitudinal axis. These results are depicted in Figure 5.7. It shows that the system provides different percentage of damping ratios distributed between 0.15–0.29% for each mass position along the beam. The mean percentage of damping ratio of the data provided in Figure 5.7 is 0.22%.

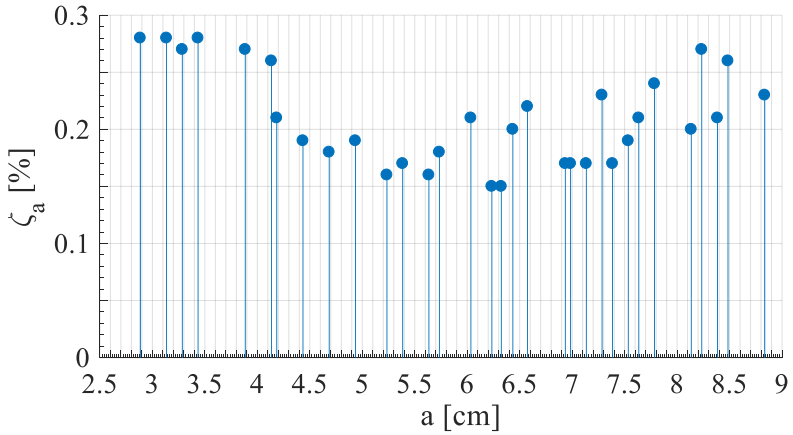

Figure 5.7: Variation of TMD's systems equivalent percentage of damping ratio for different mass position along the rectangular beam

5.2.2. Circular beam

Figure 5.8 shows the range of operation of a specific circular beam TMDs, obtained by changing the proof mass position along its beam. For the 9.1 cm long beams, the 0.75 mm diameter is suitable to operate all over the PT range (5–12 Hz [16]), and the 0.79 mm diameter as well. The 0.85 mm diameter is enough for "Patient 6" by taking into account a 0.6 Hz shifting in the frequency due to the change of the hand position, as already summarized in Table 3.9.

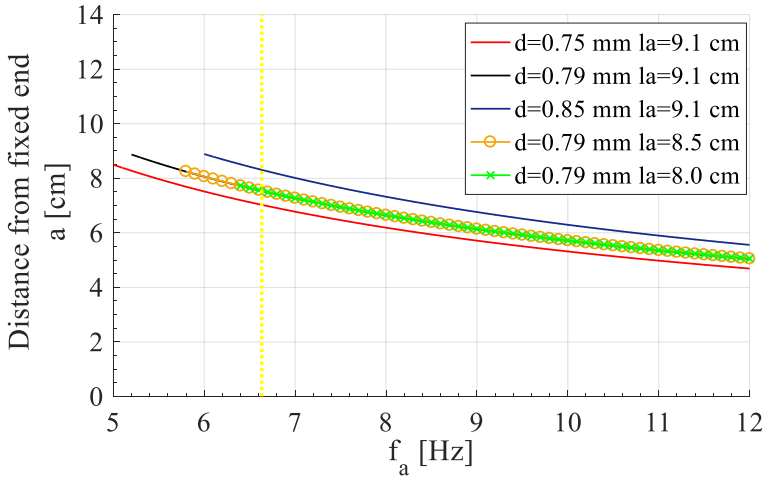

Figure 5.8: Operation frequency range of several circular beam TMD for different mass position

Table 5.2 shows the calculated position of the mass 'a' needed to reach the minimum frequency in range of the PT for different beam's length having 0.79 mm diameter, deduced from Figure 5.8. The operation frequency 'f_a' of the TMD increases when the position of the mass 'a' is lower than the provided values for each TMD. Note that the position 'a' in the table represents the position of the centroid for the attached

mass, when it is just touching the free end of the beam. Using Figure 5.8, these TMDs can reach the frequency of "Patient 6" when the mass is placed at $a = 7.5\ cm$.

Table 5.2: Maximum mass position needed to reach the minimum operating frequency for the 14.13 g TMDs with different beam's length

Beam's length	8 cm	8.5 cm	9.1 cm
$a\ (cm)$	7.7	8.2	8.9
$f_a\ (Hz)$	6.4	5.8	5.2

The fabricated circular beam cantilever-type TMD with a 14.13 g proof mass is shown in Figure 5.9. The beam is 9.1 cm long with a cross-sectional beam's diameter of 0.79 mm. The same equation in (5.1) is used to measure the position of the centroid 'a' for attached mass. It serves to calculate the natural frequency using Dunkley's formula.

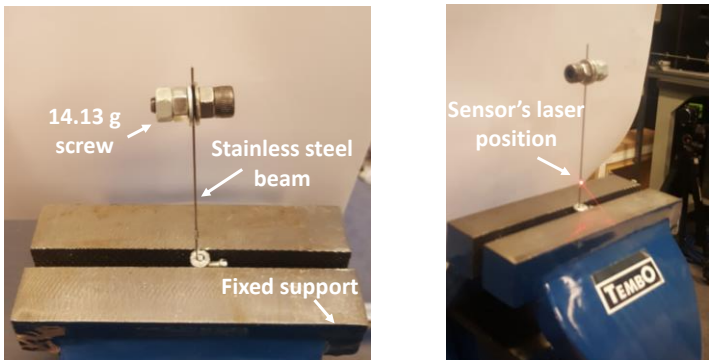

Figure 5.9: Fabricated circular beam cantilever-type TMD

The measured and processed signal for the circular cross-sectional cantilever-type TMD of Figure 5.9 are shown in Figure 5.10 and Figure 5.11. The incident ray of the PDV strikes the beam at a position of 1.5 cm away from its fixed end. The PDV speed is set at 20 mm/s, and the signal length is 10 s. The signal is downsampled by a ratio of 10 to obtain the sampling frequency 170 Hz.

The measured signal for the beam alone before adding the mass and its FFT are shown in Figure 5.10a and Figure 5.10b, respectively. The percentage of damping ratio and fundamental frequency are obtained from the FFT response in in Figure 5.10b, to be 0.14% and 67.3 Hz, respectively. Using its measured frequency and the frequency formula of the Euler-Bernoulli beam in (4.83), the E_{beam} is calculated to be 200 GPa. The obtained Young's modulus is approximately equal to the actual value of the stainless steels, which reflect a perfect clamping that does not affect the real E_{beam} value of the free-free beam.

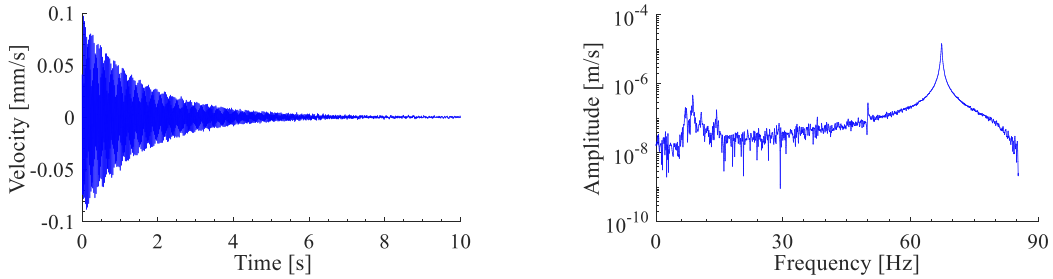

(a) (b)

Figure 5.10: (a) Velocity signal and (b) its Fourier transform measured by the Vibrometer for the circular beam alone

The behavior of the 14.13 g screw when placed in contact with the free end of the beam ($d_{meas} = 0$), is shown in Figure 5.11. The processed time signal at this position is shown in Figure 5.11a for a 60 s long signal. The critical frequency of the TMD system is presented by the frequency response in Figure 5.11b, and shows a value equal to 5.60 Hz. The frequency using Dunkerley's formula at this position is 5.63 Hz, which is very close to the value obtained experimentally. The percentage of damping ratio of this TMD system is calculated to be 0.27%. Similar measurements are done for different mass positions along the beam.

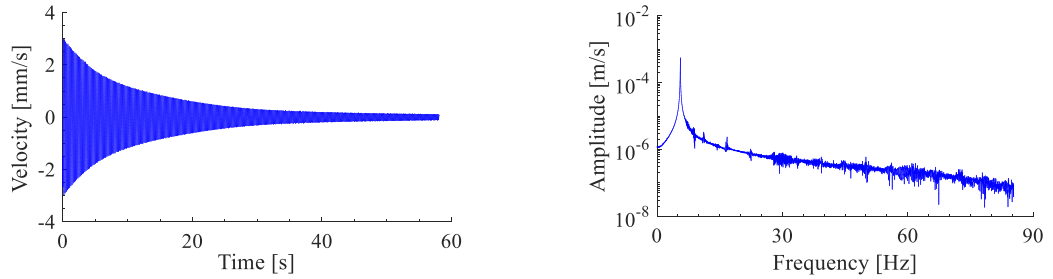

(a) (b)

Figure 5.11: (a) Velocity signal and (b) its Fourier transform measured by the Vibrometer for the circular beam with the 14.13 g screw placed at its free end

The wavelet transforms extracted from the velocity signal of the circular beam while the screw is placed at the free end position presented in Figure 5.11a, is shown in Figure 5.12. The variation of the natural frequency is analyzed within the interval [2.8, 55] s. Relatively higher variation is observed for the circular beam than the rectangular one presented by Figure 5.5. The variation in its natural frequency is just of 0.59% which represents a linear system.

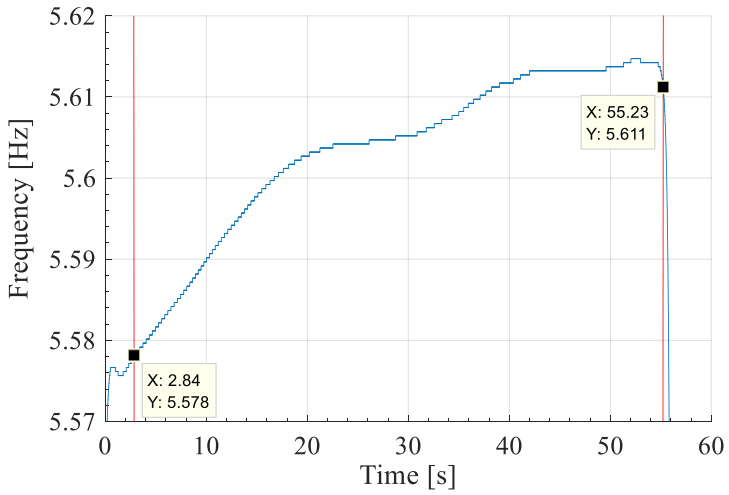

Figure 5.12: Wavelet transform for the natural frequency of the circular beam with 14.13 g screw placed at its free end

The beam is divided into 910 2D-elements in the FEM calculations of the TMD's natural frequency. The measurement results are presented in Figure 5.13. The left y-axis of Figure 5.13 shows the natural frequency obtained using the experimental, FEM, and Dunkerley's methods, while the right y-axis shows the percentage of error in the natural frequency between the FEM and Dunkerley's methods, and the experimental results. The results presented in Figure 5.13 show that the analytical values match with the numerical ones. Both methods give natural frequencies which slightly change from the measured frequency. The highest error with the experimental method is observed at the free end of the beam, with a value of 0.65%.

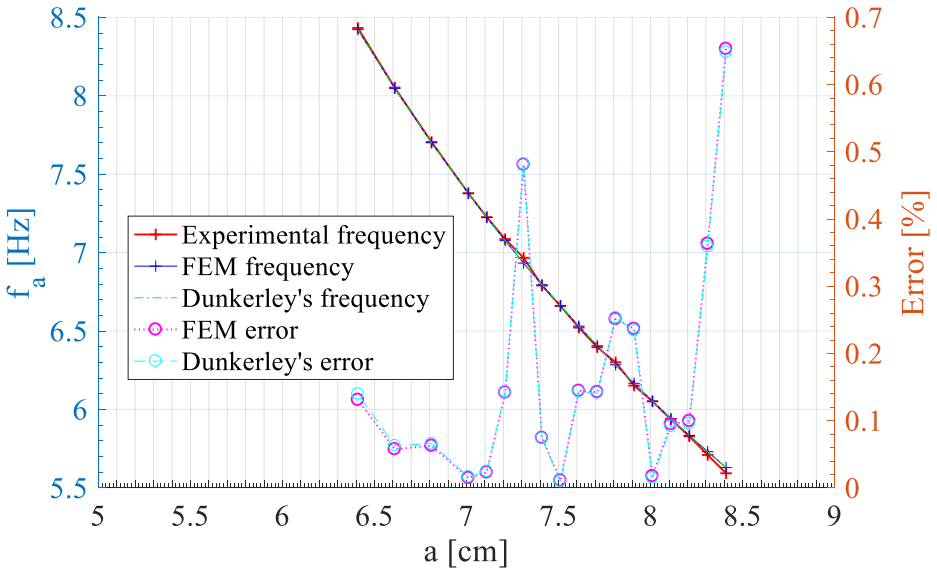

Figure 5.13: The calculated Dunkerley's and FEM fundamental frequency of the TMD with their percentage of error compared to the frequency obtained experimentally for different mass position along the circular beam

The damping coefficients values of the beam TMD's system are calculated graphically using its response in the frequency domain, for different mass position along the beam's longitudinal axis. These results are shown in Figure 5.14. It shows that the system provides different percentage of damping ratios distributed between 0.26–0.46% for each mass position along the beam. The mean percentage of damping ratio of the data provided in Figure 5.14 is 0.33%.

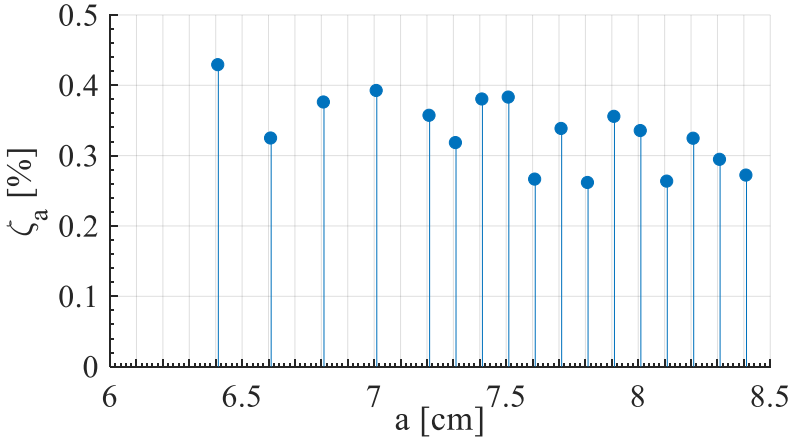

Figure 5.14: Variation of TMD's systems equivalent percentage of damping ratio for different mass position along the circular beam

5.3. TMDs with measured damping

The numerical study was done to obtain the required parameters needed to design the TMD. A parametric study for the TMD is done to test the effect of each parameter of the TMD's performance. Accordingly, TMDs sized and fabricated. Experiments are done to check the natural frequency for the TMDs and the damping ratio is calculated graphically for each mass position along the beam. A small study is done again to see the performance of the fabricated circular beam TMD having the used dimensions and obtained damping ratios from the experiment, it is done for TMDs placed at the palm of the forearm.

5.3.1. At palm

The optimum TMD's mass position 'a' and damping ratio '$\zeta_{a\ opti}$' obtained for the 1, 2, and 3TMDs used in the system's response of Figure 4.34, are listed in Table 5.3. The 9.1 cm beams are used with a 0.79 mm diameter, where each beam is holding a 14.13 g mass. After optimizing the TMD's mass position 'a', the measured damping ratio '$\zeta_{a\ meas}$' at this position can be selected using Figure 5.14. Their corresponding values for the TMDs of Figure 4.34, are also shown by Table 5.3.

Table 5.3: Optimum parameters of the 1, 2, and 3TMDs at the palm having 0.79 mm diameter and 9.1 cm length along with the measured damping ratio corresponding to each optimum mass position used for "Patient 6" signals

Number of TMDs	1TMD	2TMD		3TMD		
$a\ (cm)$	7.49	7.68	7.56	7.91	7.70	7.59
$\zeta_{a\ opti}$ (%)	0.99	0.64	1.18	1.26	0.13	1.26
$\zeta_{a\ meas}$ (%)	0.35	0.38	0.31	0.33	0.38	0.37

The behavior of the wrist joint after the addition of 1, 2, and 3TMDs, with the optimized damping ratio '$\zeta_{a\ opti}$' were shown in Figure 4.33. Their response due to the replacement by the measured damping ratios '$\zeta_{a\ meas}$', which are provided by Table 5.3, is shown in Figure 5.15. It can be deduced from the study for the variation of the damping ratio in Figure 4.33, that effect of replacing '$\zeta_{a\ opti}$' by '$\zeta_{a\ meas}$' become less visible as the number of TMDs increases. The 1, 2, and 3 TMDs with the measured damping ratios, were able to reduce 91.3%, 97.2%, 97.5% of the tremor's amplitude.

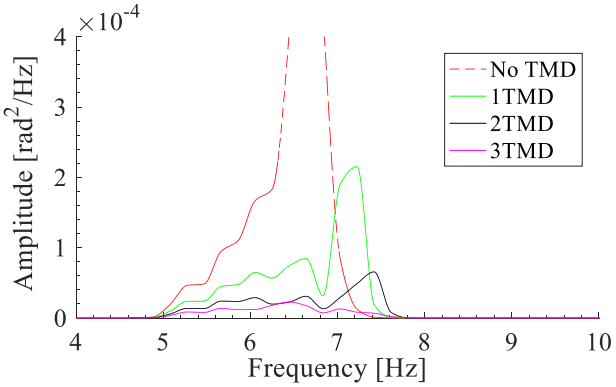

Figure 5.15: Behavior of the wrist joint controlled by 1-3TMDs with the measured damping ratio '$\zeta_a\ meas$' for 9.1 cm long beams having 0.79 mm diameter and 14.13 g mass attached on each TMD at the palm

5.3.2. At forearm

It can be interesting to check the reduction provided by the TMDs inserted to the forearm segment. The same TMD system is used, where each beam has 9.1 cm length and 0.79 mm diameter, and is holding 14.13 g mass. Table 5.4 shows the optimum TMD mass position with its corresponding damping ratio from Figure 5.14 for 1, 2, and 3TMDs placed at the forearm segment. These TMDs are placed at a distance 80% of the forearm length away from the elbow joint and have an optimized mass position along the TMD's beam's length.

Table 5.4: Optimum mass position of the 1, 2, and 3TMDs at the forearm having 0.79 mm diameter and 9.1 cm length along with the measured damping ratio corresponding to each position used for "Patient 6" signals

Number of TMDs	1TMD	2TMD		3TMD		
$a\ (cm)$	7.7	7.7	7.6	7.9	7.7	7.6
$\zeta_{a\ meas}$ (%)	0.38	0.38	0.38	0.33	0.38	0.37

Figure 5.16 shows the response of the wrist joint when the TMDs are placed at the forearm. The 1TMD in Figure 5.16a provides an increase in the tremor's reduction from 53.1% to 42.2% while the TMD approached the wrist joint, for the distance between 20–80% of the forearm length 'd_a' measured from its proximal joint. For the For the tMD's parameters shown in Table 5.4, the behavior due to increasing the number of TMDs at the forearm is shown in Figure 5.16b. The 1, 2, and 3 TMDs are able to reduce 51.2%, 71.1%, 78.1% of the wrist joint tremor amplitude when placed at the distance $d_a = 0.80 l_3$.

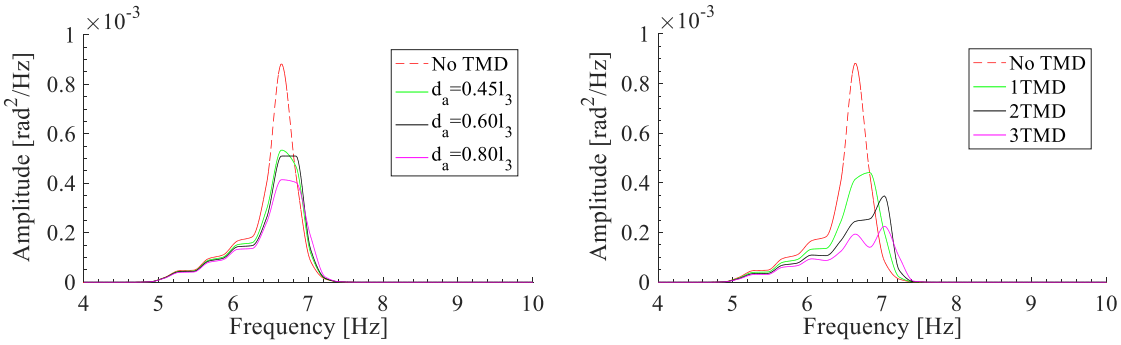

Figure 5.16: Behavior of the wrist joint controlled by (a) 1TMD, (b) 2TMDs, and (c) 3TMDs with optimized damping ratio '$\zeta_a\ opti$' compared to that replaced by the corresponding measured damping ratio '$\zeta_a\ meas$' for 9.1 cm long beams having 0.79 mm diameter and 14.13 g mass attached on each TMD at the forearm

5.4. Performance of TMDs experimentally

Before testing the performance of the designed TMD on the hand of the patient, the experimental-arm (Part 1) shown in Figure 5.17 is used to emulate the PT. The hand segment is fabricated as a fixed-free rigid steel beam with the dimensions $33\ cm \times 1.8\ cm \times 0.5\ cm$.

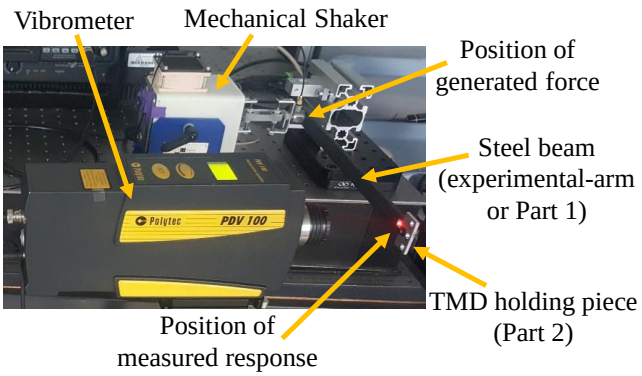

Figure 5.17: Experimental setup used to test the behavior of the TMD with simulated tremor signal

The ECR signal of "Patient 6" used in the numerical study for the TMD optimization, is generated by the mechanical shaker form the signal implemented on LabVIEW as shown in Figure 5.18. A 2V amplification is applied for the raw ECR signal. The excitation force is applied to the experimental-arm at a distance 4.8 cm away from the fixed end using the mechanical shaker. Vibrometer PDV-100 is used to measure the response of the experimental-arm, where the incident ray hits the beam at a distance 2 cm away from its free end. The Vibrometer also provides the signal of the excitation force exerted on the experimental arm.

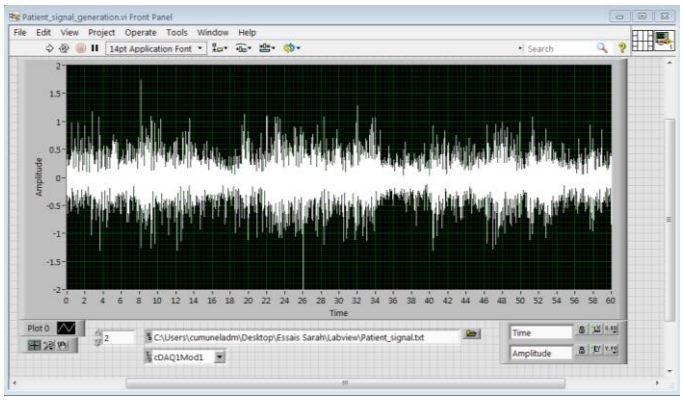

Figure 5.18: Simulated ECR signal of "Patient 6" implemented on the LabVIEW and transmitted to the mechanical shaker

A comparison between the PSD of the simulated ECR signal and the measured ECR signal of "Patient 6" is shown. The PSDs are normalized to the amplitude of the first peak. It shows that the ECR signal provided by the mechanical shaker converges to the measured signal and specially at the first critical frequency, the frequency of concern for this study, which is simulated to be 6.64 Hz.

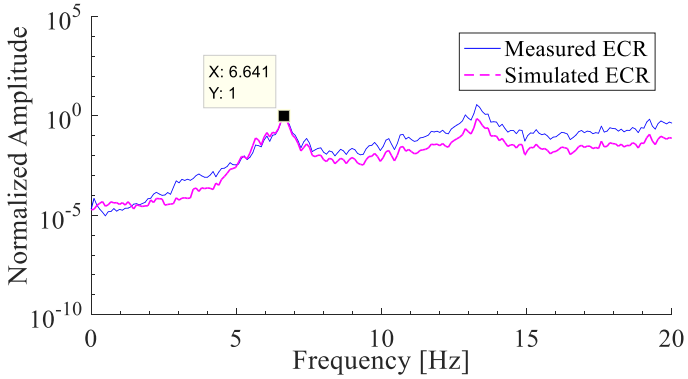

Figure 5.19: Normalized PSD of the measured and simulated ECR signal for "Patient 6" provided by the mechanical shaker

The PSD of the measured and simulated ECR signals are shown again in Figure 5.20a in addition to the response of the experimental-arm alone, but without "Part 2" shown in Figure 5.17. The signal corresponding to the experimental-arm response is shown in Figure 5.20b. The response of the system varies approximately between ± 0.1 V.

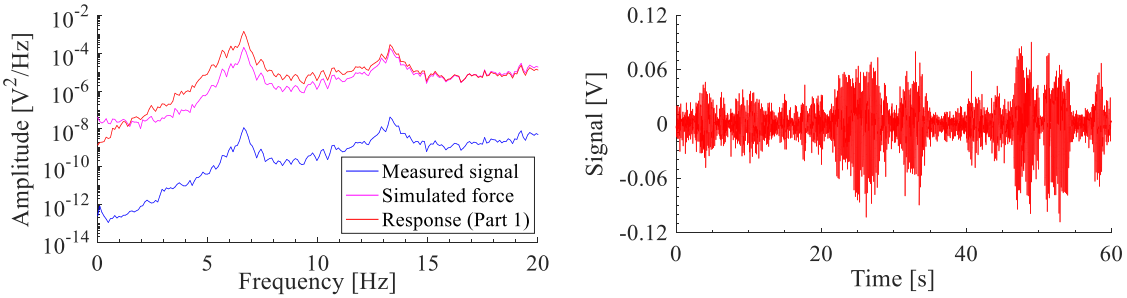

(a) (b)

Figure 5.20: (a) Measured and simulated PSDs of tremor signals in addition for the PSD for the response of the experimental-arm and (b) its tremor signal in the time domain

Three TMD's are used for the experimental testing, each have 0.79 mm diameter and are 9.1 cm long as the one shown in Figure 5.21a. Each time the TMD is used, its frequency is checked by the Vibrometer's measurements, while it is placed in the required direction of vibration as shown in Figure 5.21b, before it is attached to the system. The three TMDs are prepared to be placed together on a small symmetrical piece (Part 2) shown in Figure 5.21c, and fixed to the free end of the experimental-arm. The TMD beams are placed at the positions 'I', 'II', and 'III' of Figure 5.21c, where each beam holds 13.69 g, 13.80 g, and 13.74 g screw and corresponds respectively to the mentioned positions. These screws are made to have masses close to the one used in the numerical study, which was 14.13 g. The 13.69 g and 13.80 g TMD have 9.1 cm long beam each, while the 13.74 g has a close length of 9.25 cm. The masses with the corresponding beam length are always used together, where their placement along 'Part 2' is also fixed during the experiment.

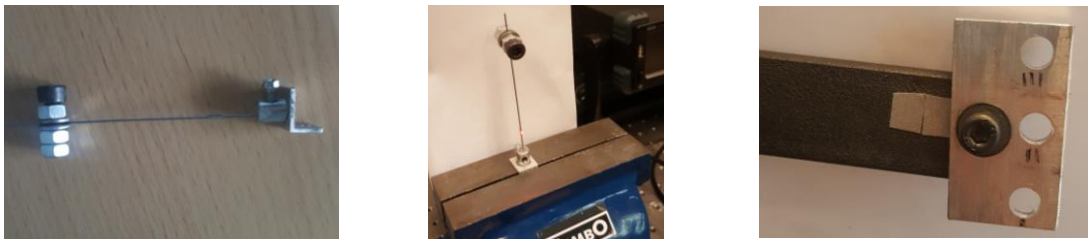

(a) (b) (c)

Figure 5.21: (a) TMD used for the experimental study having 0.79 mm diameter, and (b) TMD's natural frequency measurements, and (c) TMD's piece 'Part 2' used to hold 3TMD when attached to the experimental-arm 'Part 1'

The effect of the TMD's holder on the response of the experimental-arm is studied in Figure 5.22. It shows the PSD for the signal of the experimental-arm (Part 1) with and without the TMD's holder part (Part 2). In addition, to the response of the experimental-arm with 1TMD when Part 2 is added and removed. The 13.80 g mass is tested while it is attached to the beam at the position 'II' on "Part 2" of attached directly to "Part 1". Figure 5.22 shows that the addition of "Part 2" slightly affect the response of the system with or without the TMD. The TMD position is chosen to provide fundamental frequency close to the first excitation frequency (6.64 Hz). The mass placed at a distance $d_{meas} = 0.97\ cm$, which was defined for (5.1) to be the distance away from the beam's free end, leads to the TMD's frequency of 6.63 Hz.

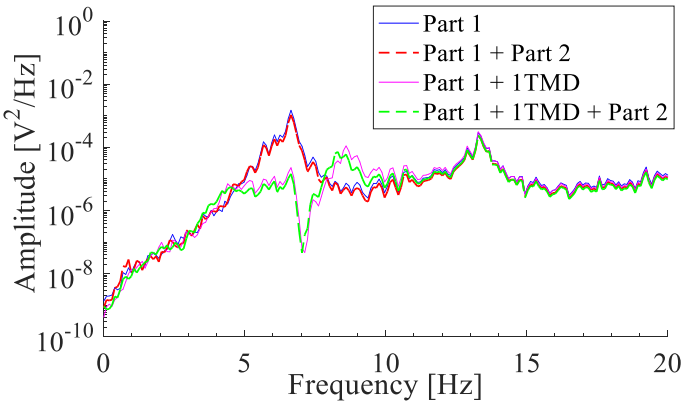

Figure 5.22: PSD of the experimental-arm (Part 1) response with and without the TMD holder (Part 2) when the TMD is attached to Part 1 directly or to Part 2

The effect of adding the small piece used to hold the TMDs can be neglected, so it will be kept attached to the experimental arm while testing the performance of the TMD. Figure 5.23 shows again the response of the system with and without the 1TMD having $f_{a\ meas}$ =6.63 Hz. The 13.80 g light TMD (placed at 'I') causes improved behavior for the system around the critical frequency in Figure 5.23a, but increased in the amplitude at higher frequencies. This phenomenon was observed in the numerical study for the system with 1TMD in Figure 5.15 after replacing the optimum damping ratio by the measured one,

which is much lower. The TMD causes some improvements in the response of the system in the time domain as shown in Figure 5.23b.

For the low damping ratio provided by the stainless steel material of the TMD beam holding a light mass, the TMD in Figure 5.23a causes 95% average reduction of in the tremor amplitude between 5.47–8.00 Hz and 93% amplification in the amplitudes between 8.00–9.08 Hz. However, the new critical peak of the global system observed at 8.30 Hz has 93% lower amplitude than the principle system's critical peak at 6.64 Hz.

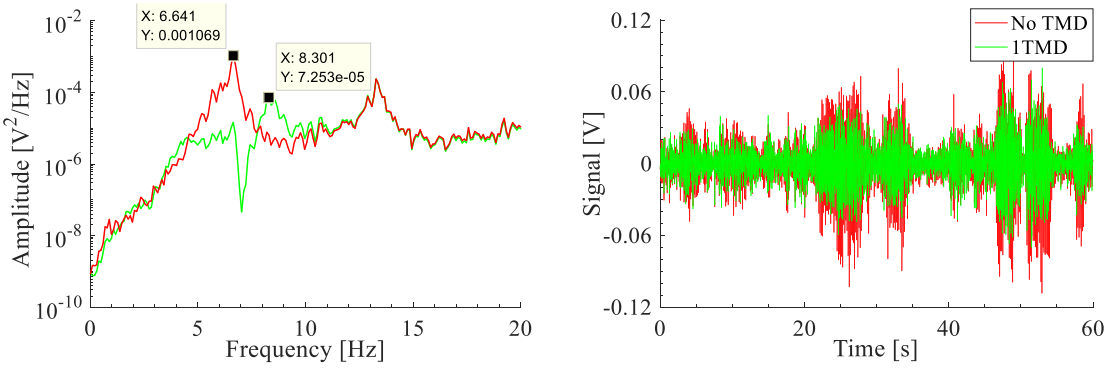

(a) (b)

Figure 5.23: Response of the system with 1TMD with 6.63 Hz frequency in (a) frequency and (b) time domains while 'Part 2' is attached

The TMD's optimum frequency may not be the driving frequency of the system, which represents the tuning condition of the undamped global system. The presence of damping in the system can cause shifting in the best frequency of the TMD as obtained numerically for the optimized 1TMD parameters shown in Table 5.3. The measured natural frequency ($f_{a\,meas}$) of the 13.80 g TMD corresponding to each d_{meas} is presented in Figure 5.24a, and used while placing the TMD at the position 'I' as shown in Figure 5.24b. Measurements are each 0.20 cm distance between the positions of the mass, starting from the end of the beam at $d_{meas} = 0$ cm ($f_{a\,meas} = 5.52$ Hz) until reaching $d_{meas} = 1.60$ cm ($f_{a\,meas} = 7.57$ Hz).

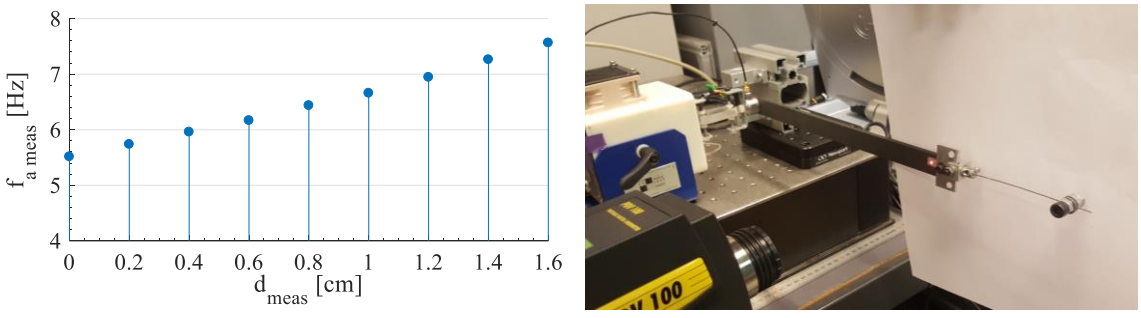

(a) (b)

Figure 5.24: (a) Frequency of 13.80 g TMD for different mass position obtained from the measurements and (b) 1TMD attached to the system at 'II'

The response of the system for different TMD's 13.80 g mass position (d_{meas}) is shown in Figure 5.25. In Figure 5.25a, as the mass moves from $d_{meas} = 0.00$ cm to $d_{meas} = 0.80$ cm, the amplitude of the system around the critical peak was decreasing until reaching good level of reduction at 0.80 cm. In contrast, as the mass position moves from 0.80 cm to 1.60 cm, which are shown in Figure 5.25a, the amplitude of the system around the critical frequency was increasing. Attaching the TMD to the system caused an additional peak to its response, with an amplified amplitude. This additional peak is shifting to the right with a lower amplitude while the TMD's frequency is increasing. Hence, no perfect response was obtained for the behavior all over the PT range, however, a position that compromise between reduced and amplified amplitudes can be chosen. It can be deduced that the best position for the 13.80 g used TMD, lied between the positions 0.80–1.00 cm away from the free end, which corresponds to the frequencies between 6.44–6.66 Hz (using Figure 5.24a). This range in fact represents the frequencies around the critical frequency of the system and includes the TMD's closest position used for its tuning in Figure 5.23a. So, the 13.80 TMD provides the causes the good response for the system while its frequency is set to 6.63 Hz (or the 0.97 cm).

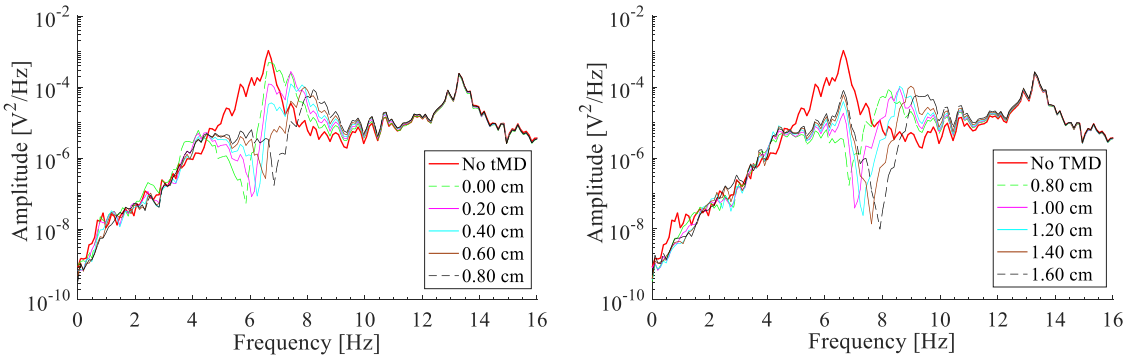

(a) (b)

Figure 5.25: Response of the system due to 1TMD for different mass position 'd_{meas}' measured from the free end of the beam

In order to study the effect of increasing the number of TMDs, the 13.69 g and 13.47 g TMDs are added to the experimental-arm and placed on 'Part 2' at the positions 'I' and 'III', respectively. The 13.80 g TMD is removed from 'II' to form the 2TMD system (Figure 5.26a) or added to have the 3TMD system (Figure 5.26b), where the 1TMD system (Figure 5.24b) is again the 13.80 g TMD placed at 'I'.

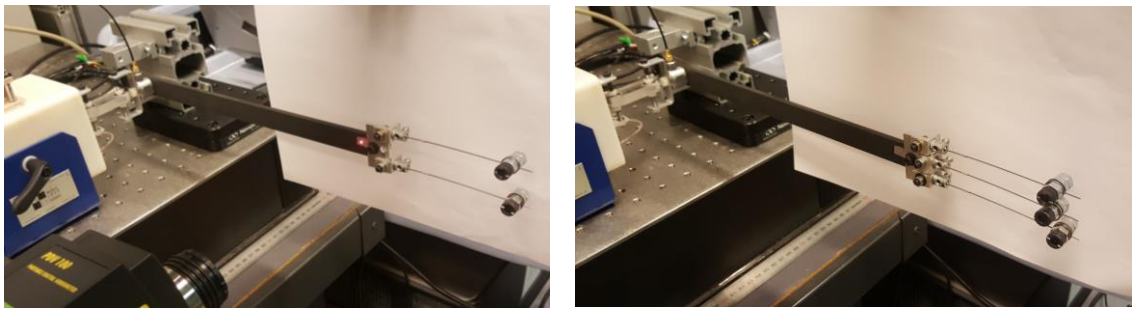

(a) (b)

Figure 5.26: (a) 2TMD and (b) 3TMD attached to the system

Table 5.5 recalls again the optimum parameters obtained in the numerical study for the 1, 2, and 3TMDs each holding 14.13 g mass. The calculated optimum natural frequency (f_a) for each TMD is provided in addition to its corresponding measured frequencies $(f_{a\,meas})$, interpolated using Figure 5.13, at the optimum mass positions (a) obtained in the numerical study. The effect of these TMD on the response of the system is checked experimentally using the manufactured TMDs. The TMD position which can provide the nearest TMD frequencies to the one approximated using the numerical study, are also shown in Table 5.5 and used for the experimental testing.

Table 5.5: 1, 2, and 3TMD optimal frequencies obtained from the numerical study and their corresponding nearest frequencies to be used in the experimental work

Number of TMDs		1TMD	2TMD		3TMD		
Numerical study	$f_a \quad (Hz)$	6.95	6.70	6.86	6.42	6.68	6.82
	$f_{a\,meas}\,(Hz)$	6.69	6.23	6.44	6.15	6.41	6.55
Experimental work	$d_{meas}\,(cm)$	1.08	0.5	0.80	0.45	0.80	0.92
	$f_{a\,meas}\,(Hz)$	6.68	6.21	6.41	6.18	6.41	6.52

The behavior of the system using the 1, 2, and 3TMD systems provided in Table 5.5 for the experimental work, are shown in Figure 5.27. The addition of TMDs causes more reduction in the response around the critical frequency (Figure 5.27a) when the 2TMD system is used, but not a considerable improvement with the 3TMD system. However, it didn't reduce the amplitude at the new critical peak added to the system as the result obtained numerically in Figure 5.15. The addition of the TMDs (or increasing the total mass of the system) causes improves its response in the time domain (Figure 5.27b).

Depending on the results deduced from Figure 5.25, where the best 1TMD position was between 0.80–1.00 cm to provide TMD with frequencies around the critical frequency (6.44–6.66), a new set of 3TMDs are tested. The frequencies of the old 3TMD system studies in Figure 5.27 is shown again in Table 5.6 and named as 'Set#1'. A new set 'Set#2' of 3TMDs is tested for just changing the TMD position of the beam placed at 'I' in 'Set#1', by another with an increased frequency.

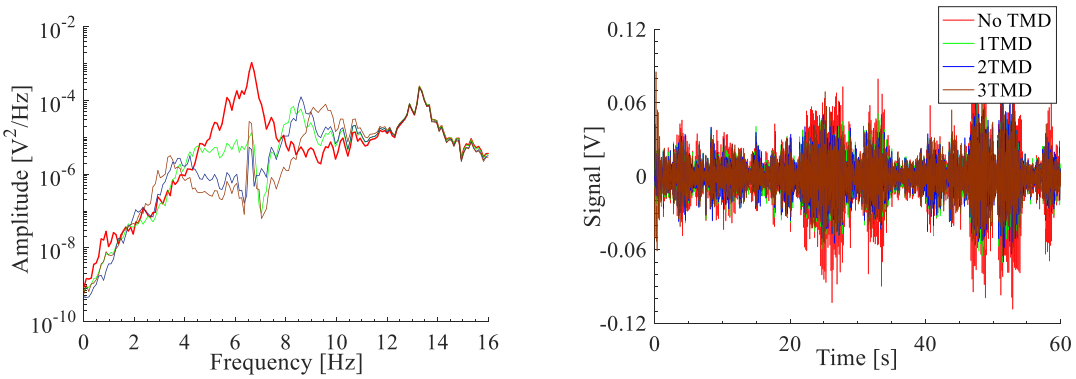

Figure 5.27: Response of the system due to 1, 2, and 3TMD systems corresponding to the numerical study in the (a) frequency and (b) time domains

Table 5.6: 3TMD system corresponding to the numerical study (Set#1) and another chosen randomly (Set#2) to have frequencies around the critical frequency of the system

Number of TMDs		3TMD		
Set#1	$d_{meas}\ (cm)$	0.45	0.80	0.92
	$f_{a\ meas}\ (Hz)$	6.18	6.41	6.52
Set#2	$d_{meas}\ (cm)$	0.85	0.85	0.92
	$f_{a\ meas}\ (Hz)$	6.61	6.55	6.52

The response of the system with 'Set#1' is compares to that when 'Set#2' is used (Figure 5.28). It shows this change has slight effect on the additional induced critical peak on the system, however, it solved the weakness due to presented for 'Set#1' around the driving frequency. A comparison with the 1TMD used in Figure 5.23, where its frequency was 6.63 Hz, is also shown here. It reveals that the 'Set#2' 3TMD highly improves the response in comparison with the 1TMD around the driving frequency, but didn't cause an important change in the behavior around the new frequency. The response with 'Set#2' was repeated 5 times, where the response the system was the same in all the measurements except of very slight changes at the low frequency below 2 Hz.

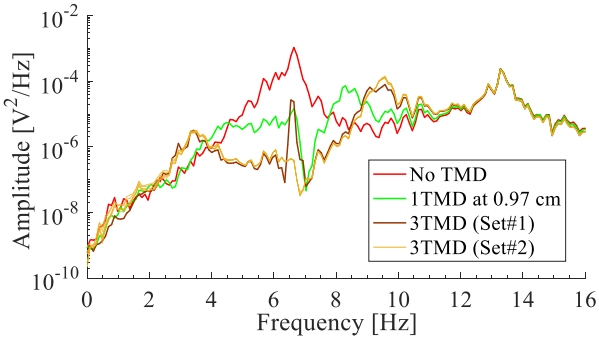

Figure 5.28: Response of the system due to 1TMD having 6.63 Hz, 3TMD system corresponding to the numerical study (Set#1), and another 3TMD system chosen randomly (Set#2) with repeated measurements

5.5. Conclusion

Two cantilever beam with a screw attached to each are manufactured to represent the TMDs, both are made of stainless steel beam having 9.1 cm length. The cross section of a rectangular beam have the dimensions $0.2\ mm \times 10\ mm$ holding 8.83 g screw, and the circular have a $0.79\ mm$ diameter holding 14.13 g screw. Both are sized to provide the PT range of frequencies for different mass position. Wavelet transform insures that both fabricated TMD systems have linear behavior. The natural frequency formula derived previously using Dunkerley's formula is checked is verified experimentally by measuring the velocity signal for each mass position using the Vibrometer. The rectangular beam TMD displays an error with the experimentally determined frequencies that doesn't exceed 4.7%, and for the circular TMD it is almost below 0.65% for different mass positions along the beam. The damping ratio of the beam alone was calculated using the FFT of its measured velocity signal. It shows that the addition of the mass changes the damping ratio provided by the beam's material, which changes randomly within a specific range for different mass positions. The provided damping after the addition of the mass increases when a higher mass is used.

An experimental setup is prepared to test the performance of the TMD experimentally before applying it to the hand of the patient. The measured behavior of the system after the addition of 1TMD is qualitatively similar to that obtained numerically, where the stainless steel TMD having low damping ratio causes the addition of new critical peak for the global system. It was difficult to find the optimum frequency of the TMD which can reduce the amplitude all over the frequency range, but a TMD frequency frequency around the critical frequency was chosen to compromise between its effect on the response amplitudes of the system. On the other hand, the 3TMD was not able to reduce the effect of this peak experimentally as shown in the numerical study. The response of the system was improved while choosing 3TMD with frequencies around the critical frequency of the system.

CHAPTER 6. GENERAL CONCLUSION AND PERSPECTIVES

The objective of the thesis is to provide a reliable model of the upper limb to reflect the tremor motion of PT patients, which can be used for tremor control strategies. Medical and surgical treatments can be replaced with tremor control devices designed to reduce the amplitude at the critical frequency of the tremor. The challenging task of this work is to design a passive controller, therefore without smart elements as for an active controller, sufficiently robust to changes in the critical frequency. For that purpose, the response of patients should be analyzed to adapt the parameters of the model to the patient's tremor behavior and to design the passive vibration controller.

The work done in the thesis provides information about pathological tremor of the PT type related to the PD or ET patient, for clinical tests with the upper limbs held against gravity. Characterization of the tremor's motion and the muscle's activity of the different segments of the upper limb is carried out by monitoring the tremor for different patients. The tremor measurements are repeated several time for four patients, with different postural positions of the hand: two postural tasks with four different joint angles. The obtained results are used to improve the biodynamic model of the upper limb and specify the range of displacements. The muscle signal is used as a realistic input to the model. The modeling of the upper limb serves to simulate numerically and design an absorber to reduce the amplitude of the tremor.

The patients monitored have a dominant frequency that is between 6 and 9 Hz. The level of tremor amplitude is different for each patient and is not related to the range of the tremor frequency. The different tasks and the number of measurements allow to characterize the range of variation of the dominant frequency for each patient, which is at most equal to 0.6 Hz. The shifting in the dominant frequency can be due to the change in the level of activation of the agonist and antagonist muscles that affects the spring-type properties of the muscles. Knowing this range of variation is required to design the vibration absorber.

The amplitudes of acceleration and displacement of PT patients are obtained, for each measurement, using a triaxial accelerometer. Information is also provided on acceleration, displacement, angular velocity, and angular displacement for the PT patient and healthy people using IMU measurements. The level of tremor amplitude for the pathological and physiological tremors is compared. The frequency of physiological tremor for the healthy participants is between 8 and 12 Hz and is characterized by very low amplitudes, in agreement with the range mentioned by other researchers.

The damping ratios and frequencies of the dominants peaks present in the PSD of the EMG signal of the muscle are identified for each patient. The identified values help to construct an analytical model of the muscle's signal, as two harmonic oscillators with additional dynamic noise. The EMG signal of the muscle is used directly as an input torque to excite the model of the upper limb. This signal is scaled in order to reach the required amplitude of the response of the upper limb system.

The PSD of the acceleration's measurement of the tremor motion has the same dominant frequencies as those present in the PSD of the EMG measurement of the muscles. The natural frequencies of the upper limb are not observable on the PSD of acceleration signals nor on that of EMG measurements. Single joint muscles are represented at the modeled proximal joint of each upper limb system. The muscle's passive elements (i.e the stiffness and damping), determining the natural frequency of the model, were chosen depending on ranges provided experimentally by other researchers. The natural frequencies related to the upper limb model, present in the PSD of the system's numerical solutions, are filtered to focus the optimization process only on the first dominant frequency of a patient's signal. The IMU measurements detected the same oscillation frequencies in the forearm and palm, which means that the same muscle group generates oscillations in different segments of the arm. An active input torque is added to the proximal joint of each segment in the upper limb model.

The model of human upper limb is derived using the Lagrangian formulation, then linearized to obtain the ordinary differential equations governing the dynamics of the model. The upper limb is modeled by three rigid bodies located in the vertical plane: the upper arm, forearm, and hand. The additional complexity of this model comes from the separation of the hand from the forearm segment. The response of the system represents the unidirectional angular motion of flexion-extension at the shoulder, elbow, and wrist joints. The mechanical parameters of the model are adjusted so that the angular displacement of the joints and the in-plane displacements of the distal ends of the hand segments are within a reasonable range, deduced from the conducted experiments. The study of the upper limb model focused on modeling the response of the wrist joint and analyzing its angular displacement.

Equations of motion are derived to describe the behavior of the system with MTMDs attached to the forearm or hand segment of the upper limb model. Since the upper limb segments are modeled as compound pendulums, the same formalism is used to design the TMD. Equations of motion for the system with MTMDs added are derived and the parameters to be optimized are specified. The pendulums require optimization of three independent variables, which are the length and the damping and stiffness coefficients.

A simple design is proposed for the mechanical vibration absorber: a cantilever beam with a mass located along the beam. The natural frequency of this compound TMD

system including a distributed mass (beam) and a concentrated mass is simply derived by knowing the deflection of the cantilever beam with each of these two masses at the position of the mass. This method refers to the Dunkerley's semi-analytical formulation that calculates an approximation of the natural frequency of the system by knowing the natural frequency of each part. The total mass of the TMD system at the location of the attached mass is the addition of the attached mass and the effective mass of the beam. Unlike the pendulum, the length of this cantilever-type TMD provides the stiffness of the TMD. Thus, to use the same code as for the pendulum TMD, the equivalent stiffness of the pendulum in the equations of motion is adapted to the beam's stiffness.

In the current work, the driving frequency of the muscle, represented by the frequency at the dominant peak of the PSD of acceleration measurements, is different from the natural frequencies of the upper limb. However, conventionally, the optimal parameters of the TMD are calculated analytically to attenuate the amplitude close to a resonant frequency. The optimization program, developed in the thesis to obtain the mechanical parameters of the TMD, was first tested on a classical system operating at the resonance frequency and the results are compared with those obtained analytically by other researchers. The frequency representation obtained for the response of the system contains the natural frequencies and also the driving frequencies.

In order to optimize the TMD parameters to reduce the amplitude of the angular displacement of the wrist joint, induced by the measured ECR signal excitation, different optimization steps are followed, the optimization being done in the frequency domain. As the manufactured TMD can operate at frequencies different from those calculated analytically and the damping ratio is not optimal, a cantilever beam with rectangular cross-section is optimized for different frequencies in the frequency range of the PT, by adjusting the position of the mass along the beam. The fundamental frequency calculated using Dunkerley's equation is compared to the frequency identified from the measurements and a good agreement is obtained. The variation of the equivalent damping ratio of the TMD system by changing the mass position, using the same beam's material and geometry, is identified.

Due to its geometry, the motion of the rectangular beam TMD is unidirectional. However, since the PT patient has a multidirectional motion, a change in the geometry of the TMD is necessary in order to be able to reduce the amplitude of the tremor in different directions. Thus, a circular cross-section is used for the beam of the TMD. The reliability of the Dunkerley's equation is also examined for such a system, for which greater consistency is observed between the analytical and experimental results. The damping ratio of the circular beam TMD is also provided for different mass positions.

A numerical study of the circular beam TMD is carried out to test its ability to sufficiently reduce the amplitude of the angular displacement in the wrist joint. A

parametric study has shown that the TMD is more effective when located at the hand than at the forearm segment. Its performance increases when placed away from the wrist joint along the hand segment. When the absorber is located on the forearm segment, a greater reduction in the amplitude of the tremor is obtained when it is placed closer to the wrist joint. MTMDs perform better when placed in the same position along the hand segment than distributing them in different positions. The distribution of the mass among multiple TMDs results in an increase in the performance of the TMDs' system compared to the use of a STMD having the same total mass. The TMD(s) system can be more efficient when its total mass increases for the same number of TMDs. Most researchers who have used passive or active controllers with a mass-spring-damper representation, have designed these controllers with a mass that doesn't exceed 120g. Although the total masses of the TMD tested in the thesis were very small (8.83 g and 14.13 g), they were sufficient to obtain numerically a suitable reduction in the amplitude of the tremor.

A 3TMDs' system with a total mass of 43 g (14.3g each at optimal positions around 9.1 cm along the beam) was tested numerically. The optimal damping ratios of each TMD were replaced by those obtained from the experimental measurements. The optimal diameter of each TMD was also replaced by the actual value of the beam diameter, which was very close. When the excitation of the system is effected by the measured muscular signal, the reduction in the amplitude of the wrist joint obtained numerically by such a TMD system is important. This system is very effective in reducing the vertical and horizontal displacements at the distal end of each segment of the upper limb. This 3TMD system seems to be suitable for carrying out experiments on PT patients.

A comparison between the numerical and experimental results for different TMD systems is presented. The 1TMD system showed qualitatively similar behavior between numerical and experimental results, whereas the 3TMD system didn't perform as well as expected from the numerical study. The addition of TMD to an experimental rigid body, used to reflect the motion of a patient's hand, causes an additional peak in the PSD for the global system and needs to be treated. The results obtained for the experimental 3TMD system, with a total mass of 41g, are promising but the attenuation was not as important as predicted by the numerical results. However, the attenuation is still satisfactory, especially since the damping ratio due to the material (stainless steel) of the beam is very low compared to the optimal damping ratio calculated numerically. The results should be improved by slightly increasing the mass of the TMD system.

As a future work, the response of the system with the passive TMD will be tested experimentally for different critical frequencies of the excitation in order to characterize the robustness of this absorber. The material of the beam will be modified from stainless steel to 3D printed material (ABS), with a square cross-section, in order to increase the damping ratio of the TMD and to study the influence on the response of the system. Due to the low Young's modulus provided by the ABS, which can be designed with low cost

material, shorter beams are obtained. The numerical study can be extended to test the effect of TMDs optimization for a larger frequency range, and not focused only on the critical peaks, in order to reduce the effect of new critical frequencies on the global system.

In addition, the experimental arm with rectangular cross-section will be replaced by a tube to position the TMD(s) in different orientations from that of the excitation and thus test the ability of the TMD system for multidirectional excitations, which will occur for the experimental tests with the patient. Another problem in experimental tests with patients is the transfer of energy from the upper limb to the TMD, passing through the skin where part of the vibrational energy can be dissipated. To anticipate the effect of the skin, an elastomer will be placed between the tube, representing the hand segment, and the TMD fixation to take into account the effect off the patient's epidermis, dermis, and subcutaneous tissue. A bracelet will also be designed to keep the TMDs attached in different directions around the tube.

According to future results, if an appropriate reduction is observed experimentally and the concept of passive absorbers as beam system worked well, then the cantilever beams could be replaced by a passive bracelet system providing a rotational counteracting motion against the hand tremor. A first fixed stage of the bracelet, made of ABS material, can be attached to the forearm and connected to a rotational second stage providing the TMD's mass. The stages can be connected together by spring-like elements, which can be thin rectangular rounded beams.

APPENDIX

APPENDIX A. UPPER LIMB PRINCIPLE SYSTEM

This appendix provides the matrices and vectors related to the upper-limb principle non-linear system of the upper limb, which are used to calculate the response of the system. The terms $\mathrm{M_i}$ and $\mathrm{G_i}$ are exactly those used in the linearized system of the upper limb, and have the general form:

$$\mathrm{M_i} = \begin{bmatrix} M_{11} & M_{12} & M_{13} \\ M_{12} & M_{12} & M_{23} \\ M_{13} & M_{13} & M_{13} \end{bmatrix}_i \tag{A.1}$$

$$\mathrm{G_i} = \begin{Bmatrix} G_1 \\ G_2 \\ G_2 \end{Bmatrix}_i \tag{A.2}$$

The non-linear mass matrix M of the principle system is:

$$\mathrm{M} = \mathrm{M_0} + \mathrm{M_1}\cos\theta_2 + \mathrm{M_2}\cos(\theta_2 + \theta_3) + \mathrm{M_3}\cos\theta_3 \tag{A.3}$$

where,

$$\mathrm{M_0} = \begin{bmatrix} M_{11} & M_{12} & M_{13} \\ M_{12} & M_{12} & M_{23} \\ M_{13} & M_{13} & M_{13} \end{bmatrix}_0$$

$$M_{11} = (I_1 + m_1 r_1^2) + (I_2 + m_2 r_2^2) + (I_3 + m_3 r_3^2) + m_2 l_1^2 + m_3(l_1^2 + l_2^2)$$
$$M_{12} = (I_2 + m_2 r_2^2) + (I_3 + m_3 r_3^2) + m_3 l_2^2$$
$$M_{13} = (I_3 + m_3 r_3^2)$$

$$\mathrm{M_1} = l_1(m_2 r_2 + m_3 l_2)\begin{bmatrix} 2 & 1 & 0 \\ 1 & 0 & 0 \\ 0 & 0 & 0 \end{bmatrix}$$

$$\mathrm{M_2} = m_3 l_1 r_3 \begin{bmatrix} 2 & 1 & 1 \\ 1 & 0 & 0 \\ 1 & 0 & 0 \end{bmatrix}$$

$$\mathrm{M_3} = m_3 l_2 r_3 \begin{bmatrix} 2 & 2 & 1 \\ 2 & 2 & 1 \\ 1 & 1 & 0 \end{bmatrix}$$

The non-linear matrix N of the principle system is:

$$\mathrm{N} = \mathrm{N}_1 \sin\theta_2 + \mathrm{N}_2 \sin(\theta_2 + \theta_3) + \mathrm{N}_3 \sin\theta_3$$

where,

$$\mathrm{N}_1 = l_1(m_3 l_2 + m_2 r_2)\begin{bmatrix} 0 & 1 & 0 \\ -1 & 0 & 0 \\ 0 & 0 & 0 \end{bmatrix}$$

$$\mathrm{N}_2 = m_3 l_1 r_3 \begin{bmatrix} 0 & 1 & 1 \\ -1 & 0 & 0 \\ -1 & 0 & 0 \end{bmatrix} \quad \text{(A.4)}$$

$$\mathrm{N}_3 = m_3 l_2 r_3 \begin{bmatrix} 0 & 0 & 1 \\ 0 & 0 & 1 \\ -1 & -1 & 0 \end{bmatrix}$$

The non-linear matrix P of the principle system is:

$$\mathrm{P} = \mathrm{P}_1 \sin\theta_2 + \mathrm{P}_2 \sin(\theta_2 + \theta_3) + \mathrm{P}_3 \sin\theta_3$$

where,

$$\mathrm{P}_1 = 2l_1(m_2 r_2 + m_3 l_2)\begin{bmatrix} 1 & 0 & 0 \\ 0 & 0 & 0 \\ 0 & 0 & 0 \end{bmatrix}$$

$$\mathrm{P}_2 = 2m_3 l_1 r_3 \begin{bmatrix} 1 & 1 & 1 \\ 0 & 0 & 0 \\ 0 & 0 & 0 \end{bmatrix} \quad \text{(A.5)}$$

$$\mathrm{P}_3 = 2m_3 l_2 r_3 \begin{bmatrix} 0 & 1 & 1 \\ 0 & 1 & 1 \\ -1 & 0 & 0 \end{bmatrix}$$

The non-linear vector G of the principle system is:

$$\mathrm{G} = \mathrm{G}_1 \cos\theta_1 + \mathrm{G}_2 \cos(\theta_1 + \theta_2) + \mathrm{G}_3 \cos(\theta_1 + \theta_2 + \theta_3)$$

where,

$$\mathrm{G}_1 = -g(m_1 r_1 + m_2 l_1 + m_3 l_1)\begin{Bmatrix}1\\0\\0\end{Bmatrix} \tag{A.6}$$

$$\mathrm{G}_2 = -g(m_2 r_2 + m_3 l_2)\begin{Bmatrix}1\\1\\0\end{Bmatrix}$$

$$\mathrm{G}_3 = -g m_3 r_3 \begin{Bmatrix}1\\1\\1\end{Bmatrix}$$

APPENDIX B. UPPER LIMB WITH MTMD AT FOREARM

This appendix provides the matrix M and vector G for the upper-limb principle system with MTMD placed at the forearm, which are used to calculate the response of the linearized system. The terms $\mathrm{M_i}$ and $\mathrm{G_i}$ are exactly those used in the linearized system of the upper limb with MTMD at the forearm, and have the general form:

$$\mathrm{M_i} = \begin{bmatrix} M_{11} & M_{12} & M_{13} & M_{14} & M_{15} & M_{16} & \cdots & M_{1n} \\ & M_{22} & M_{23} & M_{24} & M_{25} & M_{26} & \cdots & M_{2n} \\ & & M_{33} & M_{34} & M_{35} & M_{36} & \cdots & M_{3n} \\ & & & M_{44} & M_{45} & M_{46} & \cdots & M_{4n} \\ & & & & M_{55} & M_{56} & \cdots & M_{5n} \\ & & & & & M_{66} & & M_{6n} \\ & & & & & & \ddots & \vdots \\ & & & & & & & M_{nn} \end{bmatrix}_i \tag{B.1}$$

$$\mathrm{G_i} = \begin{Bmatrix} G_1 \\ G_2 \\ G_3 \\ G_{a_1} \\ G_{a_2} \\ \vdots \\ G_{a_m} \end{Bmatrix}_i \tag{B.2}$$

Recall that, $n = m + 3$.

The same M matrix ($\mathrm{M_{uncontrolled}}$) and G vector ($\mathrm{G_{uncontrolled}}$) determined for the principle system in (A.3) and (A.6), are used for the upper-limb system when m-TMDs are added. Before using them, their dimensions must be increased as follows:

$$\mathrm{M_{uncontrolled}} = \begin{bmatrix} \mathrm{M} & 0_{m\times m} \\ 0_{m\times m} & 0_{m\times m} \end{bmatrix} \tag{B.3}$$

$$\mathrm{G_{uncontrolled}} = \begin{Bmatrix} \mathrm{G} \\ 0_{m\times 1} \end{Bmatrix} \tag{B.4}$$

The non-linear matrix M of the upper limbs with m-TMD at forearm is:

$$\begin{aligned} \mathrm{M} = \mathrm{M}_{\mathrm{uncontrolled}} + \mathrm{M}_0 + \mathrm{M}_1 \cos\theta_2 + \mathrm{M}_2 \cos(\theta_2 + \theta_3) + \mathrm{M}_3 \cos\theta_3 \\ + \left[\mathrm{M}_4 \cos\left(\theta_2 + \theta_{a_1}\right) + \mathrm{M}_5 \cos\theta_{a_1}\right] \\ + \left[\mathrm{M}_6 \cos\left(\theta_2 + \theta_{a_2}\right) + \mathrm{M}_7 \cos\theta_{a_2}\right] + \cdots \\ + \left[\mathrm{M}_{2\mathrm{m}+2} \cos\left(\theta_2 + \theta_{a_m}\right) + \mathrm{M}_{2\mathrm{m}+3} \cos\theta_{a_m}\right] \end{aligned} \tag{B.5}$$

where,

$$\mathrm{M}_0 = \begin{bmatrix} M_{11} & M_{12} & 0 & M_{14} & M_{15} & \cdots & \cdots & M_{1n} \\ & M_{12} & 0 & M_{14} & M_{15} & \cdots & \cdots & M_{1n} \\ & & 0 & 0 & 0 & 0 & \cdots & 0 \\ & & & M_{14} & 0 & 0 & \cdots & 0 \\ & & & & M_{15} & 0 & & \vdots \\ & & & & & \ddots & \ddots & \vdots \\ & & & & & & \ddots & 0 \\ & & & & & & & M_{1n} \end{bmatrix}_0$$

$$M_{11} = \left[\left(I_{a_1} + m_{a_1} r_{a_1}^2\right) + m_{a_1}\left(l_1^2 + d_{a_1}^2\right)\right] + \cdots + \left[\left(I_{a_m} + m_{a_m} r_{a_m}^2\right) + m_{a_m}\left(l_1^2 + d_{a_m}^2\right)\right]$$

$$M_{12} = \left[\left(I_{a_1} + m_{a_1} r_{a_1}^2\right) + m_{a_1} d_{a_1}^2\right] + \cdots + \left[\left(I_{a_m} + m_{a_m} r_{a_m}^2\right) + m_{a_m} d_{a_m}^2\right]$$

$$M_{14} = \left(I_{a_1} + m_{a_1} r_{a_1}^2\right)$$

$$M_{15} = \left(I_{a_2} + m_{a_2} r_{a_2}^2\right)$$

$$M_{1n} = \left(I_{a_m} + m_{a_m} r_{a_m}^2\right)$$

$$\mathrm{M}_1 = \left(m_{a_1} l_1 d_{a_1} + \cdots + m_{a_m} l_1 d_{a_m}\right) \begin{bmatrix} 2 & 1 & 0 & 0 & 0 & \cdots & 0 \\ & 0 & 0 & 0 & 0 & \cdots & 0 \\ & & 0 & 0 & 0 & \cdots & 0 \\ & & & 0 & 0 & \cdots & 0 \\ & & & & 0 & & \vdots \\ & & & & & \ddots & \vdots \\ & & & & & & 0 \end{bmatrix}$$

$$M_2 = 0$$

$$M_3 = 0$$

$$\mathrm{M}_4 = m_{a_1} l_1 r_{a_1} \begin{bmatrix} 2 & 1 & 0 & 1 & 0 & \cdots & 0 \\ & 0 & 0 & 0 & 0 & \cdots & 0 \\ & & 0 & 0 & 0 & \cdots & 0 \\ & & & 0 & 0 & \cdots & 0 \\ & & & & 0 & & \vdots \\ & & & & & \ddots & \vdots \\ & & & & & & 0 \end{bmatrix}$$

$$\mathrm{M}_5 = m_{a_1} d_{a_1} r_{a_1} \begin{bmatrix} 2 & 2 & 0 & 1 & 0 & \cdots & 0 \\ & 2 & 0 & 1 & 0 & \cdots & 0 \\ & & 0 & 0 & 0 & \cdots & 0 \\ & & & 0 & 0 & \cdots & 0 \\ & & & & 0 & & \vdots \\ & & & & & \ddots & \vdots \\ & & & & & & 0 \end{bmatrix}$$

$$\mathrm{M}_6 = m_{a_2} l_1 r_{a_2} \begin{bmatrix} 2 & 1 & 0 & 0 & 1 & \cdots & 0 \\ & 0 & 0 & 0 & 0 & \cdots & 0 \\ & & 0 & 0 & 0 & \cdots & 0 \\ & & & 0 & 0 & \cdots & 0 \\ & & & & 0 & & \vdots \\ & & & & & \ddots & \vdots \\ & & & & & & 0 \end{bmatrix}$$

$$\mathrm{M}_7 = m_{a_2} d_{a_2} r_{a_2} \begin{bmatrix} 2 & 2 & 0 & 0 & 1 & 0 & \cdots & 0 \\ & 2 & 0 & 0 & 1 & 0 & \cdots & 0 \\ & & 0 & 0 & 0 & 0 & \cdots & 0 \\ & & & 0 & 0 & 0 & \cdots & 0 \\ & & & & 0 & 0 & \cdots & 0 \\ & & & & & 0 & & \vdots \\ & & & & & & \ddots & \vdots \\ & & & & & & & 0 \end{bmatrix}$$

$$\mathrm{M}_{2\mathrm{m}+2} = m_{a_m} l_1 r_{a_m} \begin{bmatrix} 2 & 1 & 0 & 0 & \cdots & 0 & 1 \\ & 0 & 0 & 0 & 0 & \cdots & 0 \\ & & 0 & 0 & 0 & \cdots & 0 \\ & & & 0 & 0 & \cdots & 0 \\ & & & & 0 & & \vdots \\ & & & & & \ddots & \vdots \\ & & & & & & 0 \end{bmatrix}$$

$$\mathrm{M}_{2\mathrm{m}+3} = m_{a_m} d_{a_m} r_{a_m} \begin{bmatrix} 2 & 2 & 0 & 0 & \cdots & 0 & 1 \\ & 2 & 0 & 0 & \cdots & 0 & 1 \\ & & 0 & 0 & 0 & \cdots & 0 \\ & & & 0 & 0 & \cdots & 0 \\ & & & & 0 & & \vdots \\ & & & & & \ddots & \vdots \\ & & & & & & 0 \end{bmatrix}$$

The non-linear vector G of the upper limbs with m-TMD at forearm is:

$$\begin{aligned} \mathrm{G} = \mathrm{G}_{\mathrm{uncontrolled}} &+ \mathrm{G}_1 \cos\theta_1 + \mathrm{G}_2 \cos(\theta_1 + \theta_2) + \mathrm{G}_3 \cos(\theta_1 + \theta_2 + \theta_3) \\ &+ \mathrm{G}_4 \cos\left(\theta_1 + \theta_2 + \theta_{a_1}\right) + \mathrm{G}_5 \cos\left(\theta_1 + \theta_2 + \theta_{a_2}\right) + \cdots \\ &+ \mathrm{G}_{\mathrm{m+3}} \cos\left(\theta_1 + \theta_2 + \theta_{a_m}\right) \end{aligned} \tag{B.6}$$

where,

$$\mathrm{G}_1 = -g\left(m_{a_1} l_1 + m_{a_2} l_1 + \cdots + m_{a_m} l_1\right) \begin{Bmatrix} 1 \\ 0 \\ \vdots \\ 0 \end{Bmatrix}$$

$$\mathrm{G}_2 = -g\left(m_{a_1} d_{a_1} + m_{a_2} d_{a_2} + \cdots + m_{a_m} d_{a_m}\right) \begin{Bmatrix} 1 \\ 1 \\ 0 \\ \vdots \\ 0 \end{Bmatrix}$$

$$\mathrm{G}_3 = 0$$

$$\mathrm{G}_4 = -g\left(m_{a_1} r_{a_1}\right) \begin{Bmatrix} 1 \\ 1 \\ 0 \\ 1 \\ 0 \\ \vdots \\ 0 \end{Bmatrix}, \qquad \mathrm{G}_5 = -g\left(m_{a_2} r_{a_2}\right) \begin{Bmatrix} 1 \\ 1 \\ 0 \\ 0 \\ 1 \\ \vdots \\ 0 \end{Bmatrix}$$

$$\mathrm{G}_{\mathrm{n}} = -g\left(m_{a_m} r_{a_m}\right) \begin{Bmatrix} 1 \\ 1 \\ 0 \\ \vdots \\ 0 \\ 1 \end{Bmatrix}$$

APPENDIX C. UPPER LIMB WITH MTMD AT PALM

This appendix provides the matrix M and vector G for the upper-limb system with MTMD placed at the palm, which are used to calculate the response of the linearized system. The terms $\mathrm{M_i}$ and $\mathrm{G_i}$ are exactly those used in the linearized system of the upper limb with MTMD at the palm, and have the general form:

$$\mathrm{M_i} = \begin{bmatrix} M_{11} & M_{12} & M_{13} & M_{14} & M_{15} & M_{16} & \cdots & M_{1n} \\ & M_{22} & M_{23} & M_{24} & M_{25} & M_{26} & \cdots & M_{2n} \\ & & M_{33} & M_{34} & M_{35} & M_{36} & \cdots & M_{3n} \\ & & & M_{44} & M_{45} & M_{46} & \cdots & M_{4n} \\ & & & & M_{55} & M_{56} & \cdots & M_{5n} \\ & & & & & M_{66} & & M_{6n} \\ & & & & & & \ddots & \vdots \\ & & & & & & & M_{nn} \end{bmatrix}_i \tag{C.1}$$

$$\mathrm{G_i} = \begin{Bmatrix} G_1 \\ G_2 \\ G_3 \\ G_{a_1} \\ G_{a_2} \\ \vdots \\ G_{a_m} \end{Bmatrix}_i \tag{C.2}$$

Recall that, $n = m + 3$.

The same matrix M ($\mathrm{M_{uncontrolled}}$) and vector G ($\mathrm{G_{uncontrolled}}$) determined for the principle system in (A.3) and (A.6), are used for the upper-limb system when m-TMDs are added. Before using them, their dimensions must be increased as follows:

$$\mathrm{M_{uncontrolled}} = \begin{bmatrix} \mathrm{M} & 0_{m\times m} \\ 0_{m\times m} & 0_{m\times m} \end{bmatrix} \tag{C.3}$$

$$\mathrm{G_{uncontrolled}} = \begin{Bmatrix} \mathrm{G} \\ 0_{m\times 1} \end{Bmatrix} \tag{C.4}$$

The non-linear matrix M of the upper limbs with m-TMD at palm is:

$$\begin{aligned}\mathrm{M} = \mathrm{M}_{\text{uncontrolled}} &+ \mathrm{M}_0 + \mathrm{M}_1\cos\theta_2 + \mathrm{M}_2\cos(\theta_2+\theta_3) + \mathrm{M}_3\cos\theta_3 \\ &+ \left[\mathrm{M}_4\cos\left(\theta_3+\theta_{a_1}\right) + \mathrm{M}_5\cos\theta_{a_1}\right. \\ &\left.+ \mathrm{M}_6\cos\left(\theta_2+\theta_3+\theta_{a_1}\right)\right] \\ &+ \left[\mathrm{M}_7\cos\left(\theta_3+\theta_{a_2}\right) + \mathrm{M}_8\cos\theta_{a_2}\right. \\ &\left.+ \mathrm{M}_9\cos\left(\theta_2+\theta_3+\theta_{a_2}\right)\right] + \cdots \\ &+ \left[\mathrm{M}_{3\mathrm{m}+1}\cos\left(\theta_3+\theta_{a_m}\right) + \mathrm{M}_{3\mathrm{m}+2}\cos\theta_{a_m}\right. \\ &\left.+ \mathrm{M}_{3\mathrm{m}+3}\cos\left(\theta_2+\theta_3+\theta_{a_m}\right)\right]\end{aligned} \tag{C.5}$$

where,

$$\mathrm{M}_0 = \begin{bmatrix} M_{11} & M_{12} & M_{13} & M_{14} & M_{15} & \cdots & \cdots & M_{1n} \\ & M_{12} & M_{13} & M_{14} & M_{15} & \cdots & \cdots & M_{1n} \\ & & M_{13} & M_{14} & M_{15} & \cdots & \cdots & M_{1n} \\ & & & M_{14} & M_{15} & \cdots & \cdots & M_{1n} \\ & & & & M_{15} & & & \vdots \\ & & & & & \ddots & & \vdots \\ & & & & & & \ddots & \vdots \\ & & & & & & & M_{nn} \end{bmatrix}_0$$

$$\begin{aligned} M_{11} &= \left[\left(I_{a_1} + m_{a_1}r_{a_1}^2\right) + m_{a_1}\left(l_1^2 + l_2^2 + d_{a_1}^2\right)\right] \\ &\quad + \left[\left(I_{a_2} + m_{a_2}r_{a_2}^2\right) + m_{a_2}\left(l_1^2 + l_2^2 + d_{a_2}^2\right)\right] + \cdots \\ &\quad + \left[\left(I_{a_m} + m_{a_m}r_{a_m}^2\right) + m_{a_m}\left(l_1^2 + l_2^2 + d_{a_m}^2\right)\right] \\ M_{12} &= \left[\left(I_{a_1} + m_{a_1}r_{a_1}^2\right) + m_{a_1}\left(l_2^2 + d_{a_1}^2\right)\right] + \left[\left(I_{a_2} + m_{a_2}r_{a_2}^2\right) + m_{a_2}\left(l_2^2 + d_{a_2}^2\right)\right] + \cdots \\ &\quad + \left[\left(I_{a_m} + m_{a_m}r_{a_m}^2\right) + m_{a_m}\left(l_2^2 + d_{a_m}^2\right)\right] \\ M_{13} &= \left[\left(I_{a_1} + m_{a_1}r_{a_1}^2\right) + m_{a_1}d_{a_1}^2\right] + \left[\left(I_{a_2} + m_{a_2}r_{a_2}^2\right) + m_{a_2}d_{a_2}^2\right] + \cdots \\ &\quad + \left[\left(I_{a_m} + m_{a_m}r_{a_m}^2\right) + m_{a_m}d_{a_m}^2\right] \\ M_{14} &= \left(I_{a_1} + m_{a_1}r_{a_1}^2\right) \\ M_{15} &= \left(I_{a_2} + m_{a_2}r_{a_2}^2\right) \\ M_{1n} &= \left(I_{a_m} + m_{a_m}r_{a_m}^2\right) \end{aligned}$$

$$\mathrm{M}_1 = \left(m_{a_1}l_1l_2 + m_{a_2}l_1l_2 + \cdots + m_{a_m}l_1l_2\right)\begin{bmatrix} 2 & 1 & 0 & 0 & 0 & \cdots & 0 \\ & 0 & 0 & 0 & 0 & \cdots & 0 \\ & & 0 & 0 & 0 & \cdots & 0 \\ & & & 0 & 0 & \cdots & 0 \\ & & & & 0 & & \vdots \\ & & & & & \ddots & \vdots \\ & & & & & & 0 \end{bmatrix}$$

$$\mathrm{M}_2 = \left(m_{a_1} l_1 d_{a_1} + m_{a_2} l_1 d_{a_2} + \cdots + m_{a_m} l_1 d_{a_m}\right) \begin{bmatrix} 2 & 1 & 1 & 0 & 0 & \cdots & 0 \\ & 0 & 0 & 0 & 0 & \cdots & 0 \\ & & 0 & 0 & 0 & \cdots & 0 \\ & & & 0 & 0 & \cdots & 0 \\ & & & & 0 & & \vdots \\ & & & & & \ddots & \vdots \\ & & & & & & 0 \end{bmatrix}$$

$$\mathrm{M}_3 = \left(m_{a_1} l_2 d_{a_1} + m_{a_2} l_2 d_{a_2} + \cdots + m_{a_m} l_2 d_{a_m}\right) \begin{bmatrix} 2 & 2 & 1 & 0 & 0 & \cdots & 0 \\ & 2 & 1 & 0 & 0 & \cdots & 0 \\ & & 0 & 0 & 0 & \cdots & 0 \\ & & & 0 & 0 & \cdots & 0 \\ & & & & 0 & & \vdots \\ & & & & & \ddots & \vdots \\ & & & & & & 0 \end{bmatrix}$$

$$\mathrm{M}_4 = m_{a_1} l_2 r_{a_1} \begin{bmatrix} 2 & 2 & 1 & 1 & 0 & \cdots & 0 \\ & 2 & 1 & 1 & 0 & \cdots & 0 \\ & & 0 & 0 & 0 & \cdots & 0 \\ & & & 0 & 0 & \cdots & 0 \\ & & & & 0 & & \vdots \\ & & & & & \ddots & \vdots \\ & & & & & & 0 \end{bmatrix}$$

$$\mathrm{M}_5 = m_{a_1} r_{a_1} d_{a_1} \begin{bmatrix} 2 & 2 & 2 & 1 & 0 & \cdots & 0 \\ & 2 & 2 & 1 & 0 & \cdots & 0 \\ & & 2 & 1 & 0 & \cdots & 0 \\ & & & 0 & 0 & \cdots & 0 \\ & & & & 0 & & \vdots \\ & & & & & \ddots & \vdots \\ & & & & & & 0 \end{bmatrix}$$

$$\mathrm{M}_6 = m_{a_1} l_1 r_{a_1} \begin{bmatrix} 2 & 1 & 1 & 1 & 0 & \cdots & 0 \\ & 0 & 0 & 0 & 0 & \cdots & 0 \\ & & 0 & 0 & 0 & \cdots & 0 \\ & & & 0 & 0 & \cdots & 0 \\ & & & & 0 & & \vdots \\ & & & & & \ddots & \vdots \\ & & & & & & 0 \end{bmatrix}$$

$$\mathrm{M}_7 = m_{a_2} l_2 r_{a_2} \begin{bmatrix} 2 & 2 & 1 & 0 & 1 & 0 & \cdots & 0 \\ & 2 & 1 & 0 & 1 & 0 & \cdots & 0 \\ & & 0 & 0 & 0 & 0 & \cdots & 0 \\ & & & 0 & 0 & 0 & \cdots & 0 \\ & & & & 0 & 0 & \cdots & 0 \\ & & & & & 0 & & \vdots \\ & & & & & & \ddots & \vdots \\ & & & & & & & 0 \end{bmatrix}$$

$$\mathrm{M}_8 = m_{a_2} r_{a_2} d_{a_2} \begin{bmatrix} 2 & 2 & 2 & 0 & 1 & 0 & \cdots & 0 \\ & 2 & 2 & 0 & 1 & 0 & \cdots & 0 \\ & & 2 & 0 & 1 & 0 & \cdots & 0 \\ & & & 0 & 0 & 0 & \cdots & 0 \\ & & & & 0 & 0 & \cdots & 0 \\ & & & & & 0 & & \vdots \\ & & & & & & \ddots & \vdots \\ & & & & & & & 0 \end{bmatrix}$$

$$\mathrm{M}_9 = m_{a_2} l_1 r_{a_2} \begin{bmatrix} 2 & 1 & 1 & 0 & 1 & 0 & \cdots & 0 \\ & 0 & 0 & 0 & 0 & 0 & \cdots & 0 \\ & & 0 & 0 & 0 & 0 & \cdots & 0 \\ & & & 0 & 0 & 0 & \cdots & 0 \\ & & & & 0 & 0 & \cdots & 0 \\ & & & & & 0 & & \vdots \\ & & & & & & \ddots & \vdots \\ & & & & & & & 0 \end{bmatrix}$$

$$\mathrm{M}_{3\mathrm{m}+1} = m_{a_m} l_2 r_{a_m} \begin{bmatrix} 2 & 2 & 1 & 0 & 0 & \cdots & 0 & 1 \\ & 2 & 1 & 0 & 0 & \cdots & 0 & 1 \\ & & 0 & 0 & 0 & 0 & \cdots & 0 \\ & & & 0 & 0 & 0 & \cdots & 0 \\ & & & & 0 & 0 & \cdots & 0 \\ & & & & & 0 & & \vdots \\ & & & & & & \ddots & \vdots \\ & & & & & & & 0 \end{bmatrix}$$

$$\mathrm{M}_{3\mathrm{m}+2} = m_{a_m} r_{a_m} d_{a_m} \begin{bmatrix} 2 & 2 & 2 & 0 & 0 & \cdots & 0 & 1 \\ & 2 & 2 & 0 & 0 & \cdots & 0 & 1 \\ & & 2 & 0 & 0 & \cdots & 0 & 1 \\ & & & 0 & 0 & 0 & \cdots & 0 \\ & & & & 0 & 0 & \cdots & 0 \\ & & & & & 0 & & \vdots \\ & & & & & & \ddots & \vdots \\ & & & & & & & 0 \end{bmatrix}$$

$$\mathrm{M}_{3\mathrm{m}+3} = m_{a_m} l_1 r_{a_m} \begin{bmatrix} 2 & 1 & 1 & 0 & 0 & \cdots & 0 & 1 \\ & 0 & 0 & 0 & 0 & 0 & \cdots & 0 \\ & & 0 & 0 & 0 & 0 & \cdots & 0 \\ & & & 0 & 0 & 0 & \cdots & 0 \\ & & & & 0 & 0 & \cdots & 0 \\ & & & & & 0 & & \vdots \\ & & & & & & \ddots & \vdots \\ & & & & & & & 0 \end{bmatrix}$$

The non-linear G of the upper limbs with m-TMD at palm is:

$$\begin{aligned} G = \mathrm{G}_{\text{uncontrolled}} &+ \mathrm{G}_1 \cos\theta_1 + \mathrm{G}_2 \cos(\theta_1 + \theta_2) + \mathrm{G}_3 \cos(\theta_1 + \theta_2 + \theta_3) \\ &+ \mathrm{G}_4 \cos\left(\theta_1 + \theta_2 + \theta_3 + \theta_{a_1}\right) \\ &+ \mathrm{G}_5 \cos\left(\theta_1 + \theta_2 + \theta_3 + \theta_{a_2}\right) + \cdots \\ &+ \mathrm{G}_{\mathrm{m+3}} \cos\left(\theta_1 + \theta_2 + \theta_3 + \theta_{a_m}\right) \end{aligned} \tag{C.6}$$

where,

$$\mathrm{G}_1 = -g\left(m_{a_1} l_1 + m_{a_2} l_1 + \cdots + m_{a_m} l_1\right) \begin{Bmatrix} 1 \\ 0 \\ \vdots \\ 0 \end{Bmatrix}$$

$$\mathrm{G}_2 = -g\left(m_{a_1} l_2 + m_{a_2} l_2 + \cdots + m_{a_m} l_2\right) \begin{Bmatrix} 1 \\ 1 \\ 0 \\ \vdots \\ 0 \end{Bmatrix}$$

$$\mathrm{G}_3 = -g\left(m_{a_1} d_{a_1} + m_{a_2} d_{a_2} + \cdots + m_{a_m} d_{a_m}\right) \begin{Bmatrix} 1 \\ 1 \\ 1 \\ 0 \\ \vdots \\ 0 \end{Bmatrix}$$

$$\mathrm{G}_4 = -g\left(m_{a_1} r_{a_1}\right) \begin{Bmatrix} 1 \\ 1 \\ 1 \\ 1 \\ 0 \\ \vdots \\ 0 \end{Bmatrix}, \qquad \mathrm{G}_5 = -g\left(m_{a_2} r_{a_2}\right) \begin{Bmatrix} 1 \\ 1 \\ 1 \\ 0 \\ 1 \\ 0 \\ \vdots \\ 0 \end{Bmatrix}$$

$$\mathrm{G}_{\mathrm{n}} = -g\left(m_{a_m} r_{a_m}\right) \begin{Bmatrix} 1 \\ 1 \\ 1 \\ 0 \\ \vdots \\ 0 \\ 1 \end{Bmatrix}$$

BIBLIOGRAPHY

[1] Mansfield, N. J. (2005). Human response to vibration. CRC Press.

[2] Deuschl, G., Bain, P., & Brin, M. (1998). Consensus statement of the Movement Disorder Society on tremor. *Movement Disorders*, 13(S3), 2-23.

[3] Almeida, M. F. S., Cavalheiro, G. L., Pereira, A. A., & Andrade, A. O. (2010). Investigation of age-related changes in physiological kinetic tremor. *Annals of Biomedical Engineering*, 38(11), 3423-3439.

[4] Rocon, E., Belda-Lois, J. M., Ruiz, A. F., Manto, M., Moreno, J. C., & Pons, J. L. (2007). Design and validation of a rehabilitation robotic exoskeleton for tremor assessment and suppression. *IEEE Transactions on Neural Systems & Rehabilitation Engineering*, 15(3), 367-378.

[5] O'Suilleabhain, P. E., & Matsumoto, J. Y. (1998). Time-frequency analysis of tremors. *Brain*, 121(11), 2127-2134.

[6] Calzetti, S., Baratti, M., Gresty, M., & Findley, L. (1987). Frequency/amplitude characteristics of postural tremor of the hands in a population of patients with bilateral essential tremor: implications for the classification and mechanism of essential tremor. *Journal of Neurology, Neurosurgery & Psychiatry*, 50(5), 561-567.

[7] Elble, R. J. (1986). Physiologic and essential tremor. *Neurology*, 36(2), 225-231.

[8] Elble, R. J., Higgins, C., & Hughes, L. (1992). Longitudinal study of essential tremor. *Neurology*, 42(2), 441-443.

[9] Elble, R. J., Higgins, C., Leffler, K., & Hughes, L. (1994). Factors influencing the amplitude and frequency of essential tremor. *Movement Disorders*, 9(6), 589-596.

[10] Parkinson, J. (1997). An Essay on the Shaking Palsy (Sherwood, Neely, and Jones, London, 1817); *MH Polymeropoulos, et al. Science*, 276, 2045-2047.

[11] Baker, M. G., & Graham, L. (2004). The journey: Parkinson's disease. *British Medical Journal*, 329(7466), 611-614.

[12] Phwa, R., Lyons, K. E., & Koller, W. (2007). *Handbook of Parkinson's Disease*, 4th ed. (pp. 53-59). CRC Press. New York, NY, USA.

[13] Grimaldi, G., & Manto, M. (2010). Neurological tremor: sensors, signal processing and emerging applications. *Sensors*, 10(2), 1399-1422.

[14] Dai, H., Zhang, P., & Lueth, T. C. (2015). Quantitative assessment of parkinsonian tremor based on an inertial measurement unit. *Sensors*, 15(10), 25055-25071.

[15] Elble, R., & Deuschl, G. (2011). Milestones in tremor research. *Movement Disorders*, 26(6), 1096-1105.

[16] Morrison, S., Kerr, G., & Silburn, P. (2008). Bilateral tremor relations in Parkinson's disease: Effects of mechanical coupling and medication. *Parkinsonism & Related Disorders*, 14(4), 298-308.

[17] Koller, R. L., & Watts, W. C. (1997). Movement Disorders: neurologic principles and practice. New York. NY, McGraw-Hill Corporation.

[18] Brennan, K. C., Jurewicz, E. C., Ford, B., Pullman, S. L., & Louis, E. D. (2002). Is essential tremor predominantly a kinetic or a postural tremor? A clinical and electrophysiological study. *Movement disorders: official journal of the Movement Disorder Society*, 17(2), 313-316.

[19] Elble, R. J. (2000). Essential tremor frequency decreases with time. *Neurology*, 55(10), 1547-1551.

[20] Louis, E. D., & Ferreira, J. J. (2010). How common is the most common adult movement disorder? Update on the worldwide prevalence of essential tremor. *Movement Disorders*, 25(5), 534-541.

[21] Louis, E. D., & Ottman, R. (2014). How many people in the USA have essential tremor? Deriving a population estimate based on epidemiological data. *Tremor & other Hyperkinetic Movements*, 4, 259-262.

[22] Lyons, K. E., & Pahwa, R. (2005). Handbook of essential tremor and other tremor disorders. CRC Press, Taylor & Francis.

[23] McAuley, J. H., & Marsden, C. D. (2000). Physiological and pathological tremors and rhythmic central motor control. *Brain*, 123(8), 1545-1567.

[24] Barker, R. and Burn, D. J. (2004). Tremor. *Advance in Clinical Neuroscience & Rehabilitation*, 4(1), 13-14.

[25] Smaga, S. (2003). Tremor-Problem-Oriented Diagnosis. *American Family Physician*, 68, 1545-1552.

[26] Taheri, B., Case, D., & Richer, E. (2014). Robust controller for tremor suppression at musculoskeletal level in human wrist. *IEEE Transactions on Neural Systems and Rehabilitation Engineering*, 22(2), 379-388.

[27] Reich, S. (1995). Common disorders of movement: Tremor and Parkinson's disease. In Principles of Ambulatory Medicine, 4th ed., Williams and Wilkins: Baltimore, MA, USA. 1217-1229.

[28] Bhidayasiri, R. (2005). Differential diagnosis of common tremor syndromes. *Postgraduate Medical Journal*, 81(962), 756-762.

[29] Huen, D., Liu, J., & Lo, B. (2016, June) An integrated wearable robot for tremor suppression with context aware sensing. *In: 2016 IEEE 13th International conference on wearable and implantable body sensor networks (BSN)*, San Francisco, CA, 312-317.

[30] Hess, C. W., & Pullman, S. L. (2012). Tremor: clinical phenomenology and assessment techniques. *Tremor & other Hyperkinetic Movements*, *2, 1-15*.

[31] Pullman, S. L., Goodin, D. S., Marquinez, A. I., Tabbal, S., & Rubin, M. (2000). Clinical utility of surface EMG: report of the therapeutics and technology assessment subcommittee of the American Academy of Neurology. *Neurology*, 55(2), 171-177.

[32] Elble, R. J., & Koller, W. C. (1990). Unusual forms of tremor. Tremor, The Johns Hopkins University Press, Baltimore, 154-157.

[33] Hunker, C. J., & Abbs, J. H. (1990). Uniform frequency of parkinsonian resting tremor in the lips, jaw, tongue, and index finger. *Movement Disorders*, *5*(1), 71-77.

[34] Hurtado, J. M., Gray, C. M., Tamas, L. B., & Sigvardt, K. A. (1999). Dynamics of tremor-related oscillations in the human globus pallidus: a single case study. *Proceedings of the National Academy of Sciences*, USA, 96(4), 1674-1679.

[35] Raethjen, J., Lindemann, M., Schmaljohann, H., Wenzelburger, R., Pfister, G., & Deuschl, G. (2000). Multiple oscillators are causing parkinsonian and essential tremor. *Movement Disorders*, 15(1), 84-94.

[36] Rovini, E., Maremmani, C., & Cavallo, F. (2017). How wearable sensors can support Parkinson's disease diagnosis and treatment: a systematic review. *Frontiers in Neuroscience*, 11, 555.

[37] Crawford, P., & Zimmerman, E. E. (2011). Differentiation and diagnosis of tremor. *American family physician*, 83(6), 697-702.

[38] Hauser, R. A., Friedlander, J., Zesiewicz, T. A., Adler, C. H., Seeberger, L. C., O'Brien, C.F., Molho, E.S., & Factor, S.A. (2000). A home diary to assess functional status in patients with Parkinson's disease with motor fluctuations and dyskinesia. *Clinical Neuropharmacology*, 23(2), 75-81.

[39] Wong, W. Y., Wong, M. S., & Lo, K. H. (2007). Clinical applications of sensors for human posture and movement analysis: a review. *Prosthetics & Orthotics International*, 31(1), 62-75.

[40] Grimaldi, G., & Manto, M. (2008). Tremor: from pathogenesis to treatment. *Synthesis Lectures on Biomedical Engineering*, *3*(1), 1-212.

[41] Zhou, H., Hu, H., & Tao, Y. (2006). Inertial measurements of upper limb motion. *Medical & Biological Engineering & Computing*, 44(6), 479-487.

[42] Rahimi, F., Samotus, O., Lee, J., & Jog, M. (2015). Effective management of upper limb parkinsonian tremor by incobotulinumtoxinA injections using sensor-based biomechanical patterns. *Tremor & other Hyperkinetic Movements*, 5, 1-13.

[43] Buki, E., Katz, R., Zacksenhouse, M., & Schlesinger, I. (2017). Vib-bracelet: a passive absorber for attenuating forearm tremor. *Medical & Biological Engineering & Computing*, 56(5), 923-930.

[44] Dai, H., Otten, B., Mehrkens, J. H., D'Angelo, L. T., & Lueth, T. C. (2013). A novel glove monitoring system used to quantify neurological symptoms during deep-brain stimulation surgery. *IEEE Sensors Journal*, 13(9), 3193-3202.

[45] Abbasi, M., Afsharfard, A., Arasteh, R., & Safaie, J. (2018). Design of a noninvasive and smart hand tremor attenuation system with active control: a simulation study. *Medical & Biological Engineering & Computing*, 56(7), 1315-1324.

[46] Timmer, J., Lauk, M., Pfleger, W., & Deuschl, G. (1998). Cross-spectral analysis of physiological tremor and muscle activity. *Biological Cybernetics*, 78(5), 349-357.

[47] Timmer, J. (1998). Modeling noisy time series: physiological tremor. *International Journal of Bifurcation & Chaos*, 8(7), 1505-1516.

[48] Timmer, J., Häussler, S., Lauk, M., & Lücking, C. H. (2000). Pathological tremors: Deterministic chaos or nonlinear stochastic oscillators?. *Chaos: An Interdisciplinary Journal of Nonlinear Science*, 10(1), 278-288.

[49] Gresty, M., & Buckwell, D. (1990). Spectral analysis of tremor: understanding the results. *Journal of Neurology, Neurosurgery & Psychiatry*, 53(11), 976-981.

[50] Gao, J. B., & Tung, W. W. (2002). Pathological tremors as diffusional processes. *Biological Cybernetics*, 86(4), 263-270.

[51] Gao, J. B. (2004). Analysis of amplitude and frequency variations of essential and Parkinsonian tremors. *Medical & Biological Engineering & Computing*, 42(3), 345-349.

[52] Buckwell, D., & Gresty, M. A. (1995). Analysis of tremor waveforms in Findley, L. J., and Koller, W. C. (Eds.): Handbook of tremor disorders (pp. 145-164). Marcel Dekker, New York.

[53] Seireg, A., & Arvikar, R. J. (1973). A mathematical model for evaluation of forces in lower extremeties of the musculo-skeletal system. *Journal of Biomechanics*, 6(3), 313-326.

[54] Chao, E. Y. & An, K. N. (1978). Determination of internal forces in human hand. *Journal of the Engineering Mechanics Division*, 104, 255-272.

[55] Zajac, F. E. & Gordon, M. E. (1989). Determining muscle's force and action in multi-articular movement. *Exercise & Sport Sciences Reviews*, 17, 187-230

[56] Hogan, N. (1985). Impedance Control - an Approach to Manipulation. Theory. *Journal of Dynamic Systems Measurement & Control*, 107(1), 1-24.

[57] Cnockaert, J. C., Lensel, G., & Pertuzon, E. (1975). Relative contribution of individual muscles to the isometric contraction of a muscular group. *Journal of Biomechanics*, 8(3), 191-197.

[58] Wright, V., & Johns, R. J. (1960). Physical factors concerned with the stiffness of normal and diseased joints. *Bulletin of the Johns Hopkins Hospital*, 106, 215-231.

[59] Deuschl, G., Raethjen, J., Lindemann, M., & Krack, P. (2001). The pathophysiology of tremor. *Muscle & Nerve*, 24(6), 716-735.

[60] Murray, M. P., Sepic, S. B., & Barnard, E. J. (1967). Patterns of sagittal rotation of the upper limbs in walking. *Physical Therapy*, 47(4), 272-284.

[61] Jackson, K. M., Joseph, J. T., & Wyard, S. J. (1978). A mathematical model of arm swing during human locomotion. *Journal of Biomechanics*, 11(6), 277-289.

[62] Kibble, T. W. B (1966). Classical Mechanics. McGraw-Hill, New York.

[63] Flanagan, J. R., Feldman, A. G., & Ostry, D. J. (1992). Equilibrium trajectories underlying rapid target-directed arm movements. *Advances in Psychology*, 87, 661-675.

[64] Corradini, M. L., Gentilucci, M., Leo, T., & Rizolatti, G. (1992). Motor control of voluntary arm movement. *Biological Cybernetics*, 57(1), 347-360.

[65] Goddard, R., Dowson, D., Longfield, M. & Wright, V. (1969). In Lubrication and Wear in Joints (Edited by Wright, V.) (pp. 134-139). Sector Publishing, London.

[66] Maia, N. M. M., & e Silva, J. M. M. (1997). *Theoretical and experimental modal analysis* (pp. 480-488). Taunton: Research Studies Press.

[67] Hashemi, S. M., Golnaraghi, M. F., & Patla, A. E. (2004). Tuned vibration absorber for suppression of rest tremor in Parkinson's disease. *Medical & Biological Engineering & Computing*, 42(1), 61-70.

[68] Hosseini, R., Firoozbakhsh, K., & Naseri, H. (2014). Optimal design of a vibration absorber for tremor control of arm in Parkinson's disease. *Journal of Computational & Applied Research in Mechanical Engineering*, 3(2), 85-95.

[69] Rahnavard, M., Hashemi, M., Farahmand, F., & Dizaji, A. F. (2014). Designing a hand rest tremor dynamic vibration absorber using H2 optimization method. *Journal of Mechanical Science and Technology*, 28(5), 1609-1614.

[70] Hirashima, M. (2011). Induced acceleration analysis of three-dimensional multi-joint movements and its application to sports movements. In *Theoretical biomechanics*. IntechOpen.

[71] NASA, H. (2010). *NASA Human Integration Design Handbook (HIDH)-NASA* (Vol. 3407). SP-2010.

[72] Yamaguchi, G. T. (2001). *Dynamic Modeling of Musculoskeletal Motion*. USA. Springer.

[73] Hill, A. V. (1938). The heat of shortening and the dynamic constants of muscle. *Proceedings of the Royal Society of London B: Biological Sciences*, 126(843), 136-195.

[74] Kazi, S., Mailah, M., Mansour, T. M., & Zain, Z. M. (2013). Active control method for postural tremor via iterative learning algorithm. *Latest Trends in Circuits, Control and Signal Processing*, (11), 103-109.

[75] Adeli, H., & Jiang, X. (2008). Intelligent infrastructure: neural networks, wavelets, and chaos theory for intelligent transportation systems and smart structures. CRC press, Taylor & Francis, Boca Raton.

[76] Adeli, H., & Kim, H. (2009). Wavelet-based vibration control of smart buildings and bridges. CRC Press, Taylor & Francis, Boca Raton.

[77] Adeli, H., & Saleh, A. (1999). Control, optimization, and smart structures: high-performance bridges and buildings of the future. John Wiley & Sons, New York.

[78] Koprinkova-Hristova, P. (2010). Backpropagation through time training of a neuro-fuzzy controller. *International Journal of Neural Systems*, 20(5), 421-428.

[79] Chen, J. P., Webster, R. S., Hathaway, M. D., Herrick, G. P., & Skoch, G. J. (2009). High performance computing of compressor rotating stall and stall control. *Integrated Computer-Aided Engineering*, 16(1), 75-89.

[80] Theodoridis, D., Boutalis, Y., & Christodoulou, M. (2010). Indirect adaptive control of unknown multi variable nonlinear systems with parametric and dynamic uncertainties using a new neuro-fuzzy system description. *International Journal of Neural Systems*, 20(2), 129-148.

[81] Bachmann, H., Pretlove, A. J., & Rainer, J. H. (1995). Vibrations induced by people. In *Vibration Problems in Structures* (pp. 1-28). Birkhäuser Basel.

[82] Rocon, E., Belda-Lois, J. M., Sanchez-Lacuesta, J. J., & Pons, J. L. (2004). Pathological tremor management: Modelling, compensatory technology and evaluation. *Technology & Disability*, 16(1), 3-18.

[83] Duval, C. (2006). Rest and postural tremors in patients with Parkinson's disease. *Brain Research Bulletin*, 70(1), 44-48.

[84] Forssberg, H., Ingvarsson, P. E., Iwasaki, N., Johansson, R. S., & Gordon, A. M. (2000). Action tremor during object manipulation in Parkinson's disease. *Movement Disorders*, 15(2), 244-254.

[85] Wenzelburger, R., Raethjen, J., Löffler, K., Stolze, H., Illert, M., & Deuschl, G. (2000). Kinetic tremor in a reach-to-grasp movement in Parkinson's disease. *Movement Disorders*, 15(6), 1084-1094.

[86] Jankovic, J., Schwartz, K. S., & Ondo, W. (1999). Re-emergent tremor of Parkinson's disease. *Journal of Neurology, Neurosurgery & Psychiatry*, 67(5), 646-650.

[87] Symans, M. D., & Constantinou, M. C. (1999). Semi-active control systems for seismic protection of structures: a state-of-the-art review. *Engineering Structures*, 21(6), 469-487.

[88] Dyke, S. J., Spencer Jr, B. F., Quast, P., Sain, M. K., Kaspari Jr, D. C., & Soong, T. T. (1996). Acceleration feedback control of MDOF structures. *Journal of Engineering Mechanics*, 122(9), 907-918.

[89] Soong, T. T. (1990). Active structural control: Theory and Practice. Longman Scientific and Technical, Wiley, New York.

[90] Soong, T. T., Reinhorn, A. M., Wang, Y. P., & Lin, R. C. (1991). Full-scale implementation of active control. I: Design and simulation. *Journal of Structural Engineering*, 117(11), 3516-3536.

[91] De Oliveira, L. P., Varoto, P. S., Sas, P., & Desmet, W. (2009). A state-space modeling approach for active structural acoustic control. *Shock & Vibration*, 16(6), 607-621.

[92] Jovanović, M. M., Simonović, A. M., Zorić, N. D., Lukić, N. S., Stupar, S. N., & Ilić, S. S. (2013). Experimental studies on active vibration control of a smart composite beam using a PID controller. *Smart Materials & Structures*, 22(11), 115038.

[93] Guo, S. X., & Li, Y. (2013). Non-probabilistic reliability method and reliability-based optimal LQR design for vibration control of structures with uncertain-but-bounded parameters. *Acta Mechanica Sinica*, 29(6), 864-874.

[94] Shan, J., Liu, H. T., & Sun, D. (2005). Slewing and vibration control of a single-link flexible manipulator by positive position feedback (PPF). *Mechatronics*, 15(4), 487-503.

[95] Lin, J., & Liu, W. Z. (2006). Experimental evaluation of a piezoelectric vibration absorber using a simplified fuzzy controller in a cantilever beam. *Journal of Sound & Vibration*, 296(3), 567-582.

[96] Leblanc, J. (2005). *Design proposal for a mechanical tremor suppression device.* Master's Thesis, Tufts University, Medford, MA.

[97] Stone, N., Kaiser, K., & White, R. D. (2006, November). Autotuning of a PID controller for an active vibration suppression device for the treatment of essential tremor. In *ASME 2006 international mechanical engineering congress and*

exposition, pp.855-861, Chigaco, Illinois, USA (pp. 855-861). American Society of Mechanical Engineers.

[98] Bennett, D. J., Hollerbach, J. M., Xu, Y., & Hunter, I. W. (1992). Time-varying stiffness of human elbow joint during cyclic voluntary movement. *Experimental Brain Research*, 88(2), 433-442.

[99] Lopez, M. J. E., & Morales, Á. L. R. (2019, October). Postural Tremor Reduction System Design for Parkinson's Disease Patients. In *Latin American Conference on Biomedical Engineering* (pp. 1191-1199). Springer, Cham.

[100] Gebai, S., Hammoud, M., Hallal, A., & Khachfe, H. (2016). Tremor Reduction at the Palm of a Parkinson's Patient Using Dynamic Vibration Absorber. *Bioengineering*, 3(3), 18-39.

[101] Frahm H (1909) Device for damped vibrations of bodies. Patent 989, USA.

[102] Den Hartog J. P., Ormondroyd, J. (1928). The theory of the dynamic vibration absorber. *Journal of Applied Mechanics*, 50(7), 9-22.

[103] Sun, J. Q., Jolly, M. R., & Norris, M. A. (1995). Passive, adaptive and active tuned vibration absorbers—a survey. *Journal of Vibration & Acoustics*, 117(B), 234-242.

[104] Kareem, A., Kijewski, T., & Tamura, Y. (1999). Mitigation of motions of tall buildings with specific examples of recent applications. *Wind & Structures*, 2(3), 201-251.

[105] Snowdon, J. C., Wolfe, A. A., & Kerlin, R. L. (1984). The cruciform dynamic vibration absorber. *The Journal of the Acoustical Society of America*, 75(6), 1792-1799.

[106] Zuo, L., & Nayfeh, S. A. (2006). The two-degree-of-freedom tuned-mass damper for suppression of single-mode vibration under random and harmonic excitation. *Journal of Vibration & Acoustics*, 128(1), 56-65.

[107] Zainulabidin, M. H., & Jaini, N. (2012). Transverse vibration of a beam structure attached with dynamic vibration absorbers: Experimental analysis. *International Journal of Engineering & Technology*, 12(6), 82-86.

[108] Igusa, T., & Xu, K. (1994). Vibration control using multiple tuned mass dampers. *Journal of Sound & Vibration*, 175(4), 491-503.

[109] Brennan, M. J. (1997). Characteristics of a wideband vibration neutralizer. *Noise Control Engineering Journal*, 45(5), 201-207.

[110] Zuo, L., & Nayfeh, S. A. (2005). Optimization of the individual stiffness and damping parameters in multiple-tuned-mass-damper systems. *Journal of Vibration & Acoustics*, 127(1), 77-83.

[111] Zuo, L. (2009). Effective and robust vibration control using series multiple tuned-mass dampers. *Journal of Vibration and Acoustics*, 131(3), 031003.

[112] Wang, P. W., & Cheng, C. C. (2006). Design of vibration absorbers for structures subject to multiple-tonal excitations. *Journal of Vibration & Acoustics*, 128(1), 106-114.

[113] Snowdon, J. C. (1974). Dynamic vibration absorbers that have increased effectiveness. *Journal of Engineering for Industry*, 96(3), 940-945.

[114] Asami, T., & Nishihara, O. (1999). Analytical and experimental evaluation of an air damped dynamic vibration absorber: design optimizations of the three-element type model. *Journal of Vibration & Acoustics*, 121(3), 334-342.

[115] Anh, N. D., Nguyen, N. X., & Hoa, L. T. (2013). Design of three-element dynamic vibration absorber for damped linear structures. *Journal of Sound & Vibration*, 332(19), 4482-4495.

[116] Joshi, A. S., & Jangid, R. S. (1997). Optimum parameters of multiple tuned mass dampers for base-excited damped systems. *Journal of Sound & Vibration*, 202(5), 657-667.

[117] Jangid, R. S. (1999). Optimum multiple tuned mass dampers for base-excited undamped system. *Earthquake Engineering & Structural Dynamics*, 28(9), 1041-1049.

[118] Li, C. (2000). Performance of multiple tuned mass dampers for attenuating undesirable oscillations of structures under the ground acceleration. *Earthquake Engineering & Structural Dynamics*, 29(9), 1405-1421.

[119] Li, C. (2002). Optimum multiple tuned mass dampers for structures under the ground acceleration based on DDMF and ADMF. *Earthquake Engineering & Structural Dynamics*, 31(4), 897-919.

[120] Hall WD (1991) Hand-held gyroscopic device. Patent 5,058,571, USA.

[121] Kotovsky, J., & Rosen, M. J. (1998). A wearable tremor-suppression orthosis. *Journal Of Rehabilitation Research & Development*, 35(4), 373-387.

[122] Casiano, M. J. (2016). Extracting damping ratio from dynamic data and numerical solutions. Marshal Space Flight Center, Huntsville, Alabama, USA.

[123] Wu, B. (2015). A correction of the half-power bandwidth method for estimating damping. *Archive of Applied Mechanics*, 85(2), 315-320.

[124] Sawaki, Y., Rajesh, R., Simon, Ó., & Dipendra, G. (2017). System identification of a residential building in Kathmandu using aftershocks of 2015 Gorkha earthquake and triggered noise data. In International Conference on Earthquake Engineering and Structural Dynamics, pp. 233-247. Springer, Cham, 2017.

[125] Cathers, I., O'Dwyer, N., & Neilson, P. (2006). Entrainment to extinction of physiological tremor by spindle afferent input. *Experimental Brain Research*, 171(2), 194-203.

[126] Harless, E. (1858). Textbook of plastic anatomy, Part III. Stuttgart, German.

[127] Harless, E. (1860). The static moments of human limbs. Treatises of the Math.-Phys. *Class of the Royal Academy of Science of Bavaria*, 8, 69-96.

[128] R, Contini R., & Bluestein, M. (1966). Body segment parameters. Tech. Rept. 116.03, New York University, School of Engineering and Science, Research Division.

[129] Contini, R. (1972). Body segment parameters, Part II. *Artificial Limbs*, 16(1), 1-19.

[130] Clauser, C. E., McConville, J. T., & Young, J. W. (1969). Weight, volume, and center of mass of segments of the human body. Wright-Patterson Air Fotce Base, Ohio (NTIS NO. AD-710 622) Antioch Coll Yellow Springs OH.

[131] Gebai, S., Cumunel, G., Hammoud, M., & Foret, G. (2019, August). Passive Absorber to Reduce the Upper-Limbs Involuntary Tremor. 24 Congrès Français de Mécanique, (pp. 3528-3537). Brest.

[132] Velandia, C., Celedón, H., Tibaduiza, D. A., Torres-Pinzón, C., & Vitola, J. (2016) Design and control of an exoskeleton in rehabilitation tasks for lower limb. In *2016 XXI Symposium on Signal Processing, Images & Artificial Vision (STSIVA)* (pp. 1-6). IEEE.

[133] Gebai, S., & Hammoud, M. (2016). *A novel design of tuned vibration absorber for tremor in hand of parkinsonian patients.* Master Thesis, Lebanese International University.

[134] Bernstein, N. A., Salzgeber, O. A., Pavlenko, P. P., & Gurvich, N. A. (1936). Determination of location of the centers of gravity and mass of the limbs of the living human body. *All-Union Institute of Experimental Medicine*, Moscow.

[135] Pandis, P. (2013). Musculoskeletal biomechanics of the shoulder in functional activities, Doctoral dissertation, Imperial College London.

[136] Zatsiorsky, V. M., Seluyanov, V. N., & Chugunova, L. G. (1990). Methods of determining mass-inertial characteristics of human body segments. In G.G. Chernyi & S.A. Regirer, Contemporary Problems of Biomechanics (pp.272-291). CRC Press. USA.

[137] De Leva, P. (1996). Adjustments to Zatsiorsky-Seluyanov's segment inertia parameters. *Journal of Biomechanics,* 29(9), 1223-1230.

[138] Lemay, M. A., & Crago, P. E. (1996). A dynamic model for simulating movements of the elbow, forearm, and wrist. *Journal of Biomechanics*, 29(10), 1319-1330.

[139] Hibbler, R.C. (2006). Engineering Mechanics: Principles of Statics and Dynamics. Pearson Press.

[140] Inman, D.J. (2008) Engineering Vibrations. Upper Saddle River, NJ: Virginia Tech, Prentice Hall.

[141] Storer, D. M. (1991). Dynamic analysis of nonlinear structures using higher order frequency response functions, Doctoral dissertation, Ph. D. Thesis, University of Manchester.

[142] Skaflestad, B. (2006). Newton's method for systems of non-linear equations, 3-7.

[143] Dunkerley, S. (1894). VIII. On the whirling and vibration of shafts. *Philosophical Transactions of the Royal Society of London*.(A.), 185, 279-360.

[144] Atzori, B. (1974). Dunkerley's formula for finding the lowest frequency of vibration of elastic systems. *Journal of Sound Vibration*, 36, 563-564.

[145] Jeffcott, H. H. (1918). The periods of lateral vibration of loaded shafts. The rational derivation of Dunkerley's empirical rule for determining whirling speeds. Proceedings of the Royal Society of London. *Series A, Containing Papers of a Mathematical and Physical Character*, 95(666), 106-115.

[146] Den Hartog, J. P. (1974). Mechanical vibrations, McGraw-Hill, New York.

[147] Ioi, T., & Ikeda, K. (1978). On the dynamic vibration damped absorber of the vibration system. *Bulletin of Journal of Software Maintenance & Evolution*, 21(151), 64-71.

[148] Krenk, S. (2005). Frequency analysis of the tuned mass damper. *Journal of Applied Mechanics*, 72(6), 936-942.

[149] Warburton, G. B. (1982). Optimum absorber parameters for various combinations of response and excitation parameters. *Earthquake Engineering & Structural Dynamics*, 10(3), 381-401.

[150] Liu, K., & Coppola, G. (2010). Optimal design of damped dynamic vibration absorber for damped primary systems. *Transactions of the Canadian Society for Mechanical Engineering*, 34(1), 119-135.